
Doctoral Dissertations

Student Theses and Dissertations

Spring 2024

A structure from motion photogrammetric method for continuously measuring and tracking the deformations of soils during triaxial testing

Xiaolong Xia

Missouri University of Science and Technology

Follow this and additional works at: https://scholarsmine.mst.edu/doctoral_dissertations



Part of the [Civil Engineering Commons](#)

Department: Civil, Architectural and Environmental Engineering

Recommended Citation

Xia, Xiaolong, "A structure from motion photogrammetric method for continuously measuring and tracking the deformations of soils during triaxial testing" (2024). *Doctoral Dissertations*. 3284.
https://scholarsmine.mst.edu/doctoral_dissertations/3284

This thesis is brought to you by Scholars' Mine, a service of the Missouri S&T Library and Learning Resources. This work is protected by U. S. Copyright Law. Unauthorized use including reproduction for redistribution requires the permission of the copyright holder. For more information, please contact scholarsmine@mst.edu.

A STRUCTURE FROM MOTION PHOTOGRAMMETRIC METHOD FOR
CONTINUOUSLY MEASURING AND TRACKING THE DEFORMATIONS OF
SOILS DURING TRIAXIAL TESTING

by

XIAOLONG XIA

A DISSERTATION

Presented to the Graduate Faculty of the
MISSOURI UNIVERSITY OF SCIENCE AND TECHNOLOGY

In Partial Fulfillment of the Requirements for the Degree

DOCTOR OF PHILOSOPHY

in

CIVIL ENGINEERING

2022

Approved by:

Dr. Xiong Zhang, Advisor

Dr. Wen Deng

Dr. Guney Olgun

Dr. Jenny Liu

Dr. Zhaozheng Yin

© 2022

Xiaolong Xia

All Rights Reserved

PUBLICATION DISSERTATION OPTION

This dissertation consists of the following six articles, formatted in the style used by the Missouri University of Science and Technology:

Paper I, found on pages 11-42, has been published in *Acta Geotechnica* (SPRINGER).

Paper II, found on pages 43-77, is intended for submission to *Acta Geotechnica* (SPRINGER).

Paper III, found on pages 78-107, is intended for submission to the *Journal of Geotechnical and Geoenvironmental Engineering* (American Society of Civil Engineers (ASCE)).

Paper IV, found on pages 108-132, is intended for submission to the *Journal of Geotechnical and Geoenvironmental Engineering* (American Society of Civil Engineers (ASCE)).

Paper V, found on pages 133-193, has been published in *Geotextile and Geomembranes* (ELSEVIER).

Paper VI, found on pages 194-223, is intended for submission to *Geotextile and Geomembranes* (ELSEVIER).

ABSTRACT

Measuring soil deformation characteristics during triaxial testing is an important part of characterizing the stress-strain behavior of both saturated and unsaturated soils. The total and local deformations and volume changes of a soil specimen are indispensable parameters that need to be measured and are of great significance for understanding volume change and shear strength characteristics of the soil. Over the past several decades, numerous efforts have been made to measure the soil deformations during triaxial testing. However, it remains a great challenge for researchers to measure the volume-changes of unsaturated soils due to the existence of the air phase.

This research presents a structure from motion photogrammetric method for continuously measuring the 3-D deformations of both saturated and unsaturated soils during triaxial testing. The proposed method has the following advantages: (a) it can continuously measure and track the soil deformations during the whole testing process; (b) it is highly automatic and user-friendly. The method has been implemented into an efficient computer program which can process the images and videos files rapidly; (c) it is low cost. The whole multi-camera system costs only about \$ 2K;(d) it can measure the complete 3-D deformations/strain distribution of the soil specimen; In addition to the triaxial test soil specimen measurement, a multi-camera-based method has also been developed to measure and track the 3-D full-field displacements/strains of geosynthetics in tensile test. It can identify any localized strains at any location within the geosynthetics specimen.

ACKNOWLEDGMENTS

I would like to express my wholeheartedly gratitude and appreciation to my advisor, Dr. Xiong Zhang, for providing consistent guidance, advice, and encouragement to support my Ph.D. studies. I am deeply grateful for the great opportunities and wonderful working environment offered by Dr. Zhang. It has been a great privilege and a pleasure to have worked with him. I would like to thank all my committee members: Dr. Wen Deng, Dr. Guney Olgun, Dr. Jenny Liu, and Dr. Zhaozheng Yin, for their insightful suggestions during my Ph.D. studies. My special appreciation goes to Dr. Yin for his invaluable research advice and guidance.

I would like to extend my thanks to the geotechnical research group at Missouri S&T: Drs. Junnan Cao, Chuang Lin, Chao Zeng, Beshoy Riad (former PhD students), Hanli, Javad, Sara, Chuanjun, Qingqing, Robert, Ahmad, Mahtab, and Elieh, for their generous help and warm friendship. In addition, I also received great help from the staff working in the CARE department, Greg, Jeffrey, John, Jeannie, David, and Robyn.

I would like to wholeheartedly thank my beloved wife, Fei, for her love, understanding, support, and sacrifice. I feel blessed and grateful for having her as my helper. I would like to thank my parents, sister, and parents-in-law for their unconditional love and support.

I would like to thank my Lord Jesus for his abundant love, mercy, and grace. My appreciation also goes to brothers and sisters in the church for their prayers, love, and encouragement.

TABLE OF CONTENTS

	Page
PUBLICATION DISSERTATION OPTION	iii
ABSTRACT.....	iv
ACKNOWLEDGMENTS	v
LIST OF ILLUSTRATIONS	xv
LIST OF TABLES	xix
 SECTION	
1. INTRODUCTION.....	1
1.1. PROBLEM STATEMENT.....	1
1.1.1. Soil Deformation Measurement in the Triaxial Test.....	1
1.1.2. Target Identification in Photogrammetry.....	3
1.1.3. Continuous Full-Field Deformation Measurement for Geosynthetics.	5
1.2. RESEARCH OBJECTIVES AND METHODOLOGY	8
1.3. DISSERTATION OUTLINE	9
 PAPER	
I. A TABLE METHOD FOR CODED TARGET DECODING WITH APPLICATION TO 3-D RECONSTRUCTION OF SOIL SPECIMENS DURING TRIAXIAL TESTING	11
ABSTRACT.....	11
1. INTRODUCTION.....	12
2. PROPOSED METHODOLOGY	17
3. PROCEDURES OF THE PROPOSED METHOD.....	21

3.1. STAGE 1: IMAGE ACQUISITION AND CODED TARGET RECOGNITION.....	21
3.1.1. Experimental Setup.	21
3.1.2. Image Acquisition.	23
3.1.3. Deep Learning-Aided Coded Target Recognition.....	23
3.2. STAGE 2: CODED TARGET IDENTIFICATION AND APPLYING THE TABLE METHOD	25
3.2.1. Coded Target Identification.....	25
3.2.1.1. Image binarization.	25
3.2.1.2. CT contour identification.....	25
3.2.1.3. Ellipse fitting and CT center determination.....	27
3.2.1.4. CT contour normalization.....	28
3.2.1.5. Signature-based CT contour representation and decoding.	29
3.2.2. Applying the Table Method.	29
3.2.2.1. Detect and remove the incorrect IDs.	30
3.2.2.2. Interpolation/extrapolation.....	33
3.2.2.3. Assign correct IDs to the missing CTs.	33
3.2.2.4. Search for the CTs near the predicted locations for missing CTs.....	34
3.2.2.5. Determine the accurate centroid of the missing CTs.....	34
3.3. STAGE 3: APPLICATION TO 3-D RECONSTRUCTION AND VOLUME MEASUREMENT OF SOILS SAMPLES	34
4. EXPERIMENTAL VALIDATION OF THE PROPOSED METHOD.....	35

4.1. COMPARISON OF THE CT RECOGNITION AND IDENTIFICATION RESULTS OBTAINED BY THE PROPOSED METHOD AND SOFTWARE.....	35
4.2. IMPLEMENTATION OF THE PROPOSED METHOD INTO 3-D RECONSTRUCTION OF SOIL SPECIMEN	38
5. CONCLUSIONS	39
REFERENCES.....	40
II. IMPROVED TABLE METHOD FOR CODED TARGET IDENTIFICATION WITH APPLICATION TO PHOTOGRAMMETRIC ANALYSIS OF SOIL SPECIMEN DURING TRIAXIAL TESTING.....	43
ABSTRACT	43
1. INTRODUCTION.....	44
2. RELATIVE WORK	50
2.1. SHAPE AND STRUCTURAL DESCRIPTOR METHODS.....	51
2.2. TEMPLATE MATCHING.....	53
2.3. DEEP CONVOLUTIONAL NEURAL NETWORK-BASED METHODS	53
3. PROPOSED METHODOLOGY	55
4. PROCEDURES OF THE PROPOSED METHOD.....	57
4.1. IMAGE ACQUISITION AND BLOB ANALYSIS	57
4.1.1. Experimental Setup.	57
4.1.2. Image Acquisition.	57
4.1.3. Image Idealization.	58
4.1.4. Image Binarization.	58
4.1.5. Blob Analysis.	61
4.1.6. Coded Target Identification.....	62

4.2. APPLICATION OF IMPROVED TABLE METHOD	63
4.2.1. Step 1: Detect and Remove the Outlier IDs Using RANSAC Algorithm.....	64
4.2.2. Step 2: Interpolation.	65
4.2.3. Step 3: Assign Correct IDs to the Missing CTs.	65
4.2.4. Step 4: Search for the CTs Near the Predicted Locations for Missing CTs.....	67
4.2.5. Step 5: Determine the Accurate Centroid of the Missing CTs.....	67
4.3. RENUMBERING THE CT IDS.....	68
4.4. 3-D RECONSTRUCTION OF SOIL SPECIMEN	69
5. EXPERIMENTAL VALIDATION OF THE PROPOSED METHOD.....	72
6. CONCLUSIONS	73
REFERENCES.....	75
III. A STRUCTURE FROM MOTION PHOTOGRAMMETRIC METHOD FOR RECONSTRUCTING THE 3-D MODELS OF SOILS DURING TRIAXIAL TESTING.....	78
ABSTRACT	78
1. INTRODUCTION.....	79
2. METHOD.....	82
2.1. STRUCTURE FROM MOTION WORKFLOW	82
2.1.1. Image Acquisition and Feature Point Extraction.	82
2.1.2. 3-D Scene Reconstruction.	83
2.2. DIFFERENCES BETWEEN THE PROPOSED METHOD AND SFM.....	84
2.2.1. Feature Points vs. Coded Targets.	85

2.3. A CUSTOMIZED SFM PHOTOGRAMMETRIC METHOD	88
2.3.1. Triaxial Test Setup.	88
2.3.2. Image Acquisition Procedure.	90
2.3.3. Code Target Recognition.....	91
2.3.3.1. Blob analysis.....	92
2.3.3.2. Blob filtering.....	92
2.3.4. Coded Target Identification.....	93
2.3.4.1. Initial ID determination.	93
2.3.4.2. Outlier detection.	93
2.3.5. Interpolation.	94
2.3.6. 3-D Model Generation.....	95
2.3.7. Outlier Rejection by Using Reprojection Error.....	100
2.3.8. Post-Processing and Absolute Volume Determination.	102
3. VALIDATION OF THE PROPOSED METHOD.....	103
4. CONCLUSIONS	104
REFERENCES.....	106
IV. USE OF LOW-COST SECURITY CAMERAS TO MEASURE AND TRACK THE VOLUME-CHANGES OF SOILS DURING TRIAXIAL TESTING	108
ABSTRACT	108
1. INTRODUCTION.....	109
2. PROPOSED METHOD	112
2.1. MULTI-CAMERA SYSTEM SETUP AND SECURITY CAMERA DESCRIPTION	112

2.1.1. Field of View and Image Distortion.....	114
2.1.2. Image Resolution.....	115
2.2. THE CODED TARGET/SOLID DOT DESIGN FOR THE TRIAXIAL TEST	115
2.3. PROCEDURES FOR THE PROPOSED METHOD.	117
2.3.1. Video Acquisition.....	118
2.3.2. Initialization of the Target Locations in 2-D Images and 3-D Space...	118
2.3.3. Tracking the Target Locations in 2-D Images and 3-D Space	124
3. PRELIMINARY RESULTS AND DISCUSSION	126
3.1. INITIAL 3-D RECONSTRUCTION RESULTS	126
3.2. POSTPROCESSING AND RAY TRACING RESULTS	127
3.3. CONTINUOUS 3-D DEFORMATIONS.....	128
4. CONCLUSION	130
REFERENCES.....	131
V. A MULTI-CAMERA BASED PHOTOGRAMMETRIC METHOD FOR THREE-DIMENSIONAL FULL-FIELD DISPLACEMENT MEASUREMENTS OF GEOSYNTHETICS DURING TENSILE TEST.....	133
ABSTRACT	133
1. INTRODUCTION.....	134
2. LITERATURE REVIEW	136
2.1. METHODS FOR MEASURING DISPLACEMENT/STRAIN OF GEOSYNTHETICS.	136
2.1.1. Crosshead Extension Method.....	136
2.1.2. Contact Extensometer.....	137

2.1.3. Strain Gauge.....	138
2.1.4. LVDT.....	138
2.2. METHODS THAT CAN POTENTIALLY BE USED FOR MEASURING DISPLACEMENT/STRAIN OF GEOSYNTHETICS	139
2.2.1. Video Extensometer.....	139
2.2.2. Laser Extensometer.....	140
2.2.3. Image-Based Tracking Techniques.....	140
2.2.4. Conventional Photogrammetry.....	142
3. THEORETICAL BASIS OF THE PROPOSED METHOD.....	143
3.1. DETERMINATION OF THE 3-D POSITIONS AND ORIENTATIONS OF THE CAMERAS.....	144
3.2. A MID-POINT METHOD FOR 3-D RECONSTRUCTION OF MOVING GEOGRIDS DURING TENSILE TESTS	148
4. EXPERIMENTAL DESIGN.....	153
4.1. SPECIMEN PREPARATION AND TEST METHOD.....	153
4.2. CAMERA CALIBRATION AND IMAGE IDEALIZATION	156
4.3. DETERMINATION OF THE OPTIMAL CAMERA STATIONS AND ORIENTATIONS.....	158
4.4. DATA COLLECTION REGARDING THE TENSILE TEST ON THE GEOGRID SPECIMEN	162
5. RESULTS AND DISCUSSION	163
5.1. VALIDATION OF ACCURACY OF THE PROPOSED METHOD.....	163
5.2. COMPARISON OF THE ACTUAL AND THE PREDESIGNED CAMERA STATIONS AND SHOOTING DIRECTIONS.....	167
5.3. EVALUATION OF THE FULL-FIELD DISPLACEMENT OF GEOGRIDS.....	167

5.4. EVALUATION OF THE FULL-FIELD STRAIN IN GEOGRIDS	176
5.5. EVALUATION OF THE MODULUS DISTRIBUTION OF THE GEOGRIDS.....	182
5.6. EVALUATION OF THE PLANAR ASSUMPTION	184
6. CONCLUSIONS	188
REFERENCES	192
VI. A LOW-COST PHOTOGRAMMETRIC METHOD FOR MEASURING AND TRACKING THE CONTINUOUS 3-D FULL-FIELD DEFORMATIONS OF GEOSYNTHETICS DURING TENSILE TEST	194
ABSTRACT	194
1. INTRODUCTION.....	195
2. MATERIALS AND METHOD	198
2.1. SPECIMEN PREPARATION AND TEST METHOD.....	198
2.2. CAMERA CALIBRATION AND IMAGE DISTORTION CORRECTION	201
2.3. VIDEO ACQUISITION	203
2.4. AUTOMATIC RECOGNITION AND DECODING OF CTS AND SOLID DOTS.....	204
2.5. MULTI-CAMERA-BASED STRUCTURE FROM MOTION PHOTOGRAMMETRY.....	206
2.6. TRACKING THE PIXEL COORDINATES AND 3-D LOCATIONS OF THE SOLID DOTS.....	209
3. RESULTS AND DISCUSSION	211
3.1. VALIDATION OF ACCURACY OF THE PROPOSED METHOD.....	211
3.2. EVALUATION OF THE FULL-FIELD DISPLACEMENT OF GEOGRIDS.....	211

3.3. EVALUATION OF THE FULL-FIELD STRAINS IN THE GEOGRID SPECIMEN	214
3.4. EVALUATION OF THE PLANAR ASSUMPTION	217
4. CONCLUSIONS	219
REFERENCES	222
SECTION	
2. CONCLUSIONS AND RECOMMENDATIONS.....	224
2.1. CONCLUSIONS	224
2.1.1. A Table Method for Coded Target Decoding.	225
2.1.2. Development of a Single-Camera-Based SfM Photogrammetric Method.....	225
2.1.3. Development of a Multi-Security Camera System to Continuously Measure the Soil Deformations.	226
2.1.4. Continuous 3-D Full-Field Displacements/Deformations Measurement for Geosynthetics.	227
2.2. RECOMMENDATIONS.....	228
BIBLIOGRAPHY	230
VITA.....	233

LIST OF ILLUSTRATIONS

PAPER I	Page
Figure 1. An example of unsatisfactory coded target recognition results.....	14
Figure 2. Schematic plot of the proposed table method.....	19
Figure 3. Flowchart and procedure of the proposed method.	22
Figure 4. Coded target recognition and identification results.....	26
Figure 5. The proposed coded target identification method..	28
Figure 6. Identify outlier coded target IDs using table method..	30
Figure 7. 3-D reconstruction results using the target recognition data..	38
PAPER II	
Figure 1. Triaxial test system.....	48
Figure 2. Coded target detection results using deep learning method.	48
Figure 3. Schematic plot of the RANSAC algorithm	55
Figure 4. Procedure of the proposed method.	59
Figure 5. CT recognition using embedding criterion.....	63
Figure 6. Identifying wrong CT IDs.	66
Figure 7. ID results before and after applying the improved table method	67
Figure 8. Renumbering the CT IDs on the membrane.....	70
Figure 9. Interpolation of solid dots on the membrane.....	72
Figure 10. 3-D results using the input obtained from the proposed method.....	74

PAPER III

Figure 1. Structure from Motion pipeline	82
Figure 2. Comparison of point correspondences..	86
Figure 3. The procedures for the proposed method	89
Figure 4. Triaxial test setup	89
Figure 5. CT Recognition and decoding results.....	91
Figure 6. Flowchart for the RANSAC algorithm for detecting outlier CTs	95
Figure 7. Schematic plot of the growing of 3-D reconstruction	97
Figure 8. Incremental 3-D reconstruction.	98
Figure 9. Reprojection error.....	100
Figure 10. Outlier removal based on reprojection errors for individual image points ...	101
Figure 11. Postprocessing- ray tracing for determining 3-D points on specimen in water.....	102
Figure 12. The reconstructed 3-D models of the acrylic cell and soil specimen.	103

PAPER IV

Figure 1. Multi-camera system setup for the proposed method.....	112
Figure 2. Camera calibration images for security cameras.....	115
Figure 3. Coded target and solid dot stripes posted on the triaxial cell	116
Figure 4. Flowchart for the proposed multi-camera photogrammetric method.....	119
Figure 5. Schematic representation of the video processing.....	120
Figure 6. Automatic recognition and identification of the solid dots on the acrylic cell and membrane.	121
Figure 7. Schematic plot of the target tracking method.....	125

Figure 8. 3-D reconstruction results in the air for the first frames.	127
Figure 9. 3-D models of the acrylic cell and soil specimen.....	128
Figure 10. 3-D models of unconfined compression test soil specimen at different axial deformations.....	129
PAPER V	
Figure 1. Principles of the proposed photogrammetric method.....	145
Figure 2. Geogrid tensile test setup and the geogrid specimen.....	153
Figure 3. Determination of the camera stations and shooting directions.....	160
Figure 4. 3-D models of the geogrid specimen and the camera stations.	161
Figure 5. Comparison of the displacements obtained by machine-controlled bottom clamp movements and the proposed method.....	165
Figure 6. Comparison of the actual and predesigned camera stations and shooting directions for camera	168
Figure 7. Displacement-time relationship curves of the geogrid specimen.....	170
Figure 8. Images of the observed localized slip and failure of the geogrid specimen....	173
Figure 9. Comparison of the vertical strains obtained by the extensometer and the proposed photogrammetric method	177
Figure 10. Contour plots of the strain distribution at different times during the tensile test.....	180
Figure 11. Load-strain curves of the geogrid specimen at different locations.....	182
Figure 12. Contour plot of the modulus distribution of the test geogrid specimen	184
Figure 13. Histogram plot of the modulus distribution of the test geogrid.....	185
Figure 14. 3-D models of the geogrid specimen at different times	186
Figure 15. R-squared and rotational angles of the best-fit planes of the geogrid specimen over time.	189

PAPER VI

Figure 1. Multi-Camera System Setup for the Tensile Test.	201
Figure 2. IDs Design for the Coded Targets and Solid Dots.	203
Figure 3. Image processing results for solid dot recognition.	205
Figure 4. Automatic decoding of solid dots.	207
Figure 5. Structure from Motion (SfM) process	209
Figure 6. Tracking the solid dot pixel coordinates.	210
Figure 7. 3-D models for the geogrid specimen and surveillance cameras at the initial moment.	212
Figure 8. Comparison of the displacements obtained by the bottom clamp movements and the proposed method.	212
Figure 9. Displacement-time Relationship Curves for Rib A.	214
Figure 10. Changes in full-field strains in geogrid specimen L3 over time.	216
Figure 11. Changes in the 3-D models and R-squared of the fitting planes for the geogrid specimen over time.	218
Figure 12. Changes in the R-squared of the fitting planes for the geogrid specimen during the entire tensile test.	219

LIST OF TABLES

PAPER I	Page
Table 1. Training data statistics.	24
Table 2. The pseudo code of the proposed algorithm for identifying outlier CT IDs.	31
Table 3. Comparison of CT recognition and identification results obtained by PhotoModeler and the proposed method.	36
PAPER III	
Table 1. Comparison between conventional SfM and the proposed method.	85
Table 2. Differences between coded targets and feature points.	87
Table 3. Coded target ID numbers for different coded target stripes.	90
Table 4. Validation of the program on different image sets.	105
PAPER IV	
Table 1. The multi-camera system information.	113
Table 2. The predesigned ID lookup table.	118
PAPER V	
Table 1. Properties of the test geogrid specimen.	155
Table 2. Parameters of the cameras used in this study.	157
PAPER VI	
Table 1. Properties of the Tested Geogrid Specimens.	199

Table 2. Summary of the Information Regarding the 4K UHD NVR Multi-Camera System.	200
Table 3. Camera Calibration Parameters.	202

SECTION

1. INTRODUCTION

1.1. PROBLEM STATEMENT

Triaxial tests have been widely used to evaluate stress-strain behavior for geomaterial. In the past few decades, several methods have been developed to measure the volume changes of unsaturated soil specimens during triaxial tests. Literature review indicates that all existing methods can only measure the soil volume during static tests and until now it remains a major challenge for researchers to measure the continuous volume changes of soil specimens during dynamic triaxial testing. This research developed a structure from motion photogrammetry based multiple camera system for measuring the volume changes of soil specimen during dynamic triaxial testing.

1.1.1. Soil Deformation Measurement in the Triaxial Test. Measuring the deformation properties of soils in the triaxial test is essential in understanding the stress-strain behavior of soils. During the past several decades, many research efforts have been made to develop alternative methods for measuring global and local deformational properties of both saturated and unsaturated soils during triaxial testing.

The double cell system (Bishop and Donald, 1961), also known as suction-controlled triaxial apparatus, is a widely accepted method for measuring the volume-changes of unsaturated soils. However, this method suffers several limitations, such as high-cost, only total volume-change measurement, and water absorption effect. Romero et al. (1997) used laser scanner to measure the deformations of the soils. It is non-contact

and localized deformations can be made. However, the high-cost setup and sophisticated installation procedures limited the application of this method. Macari et al. (1997) proposed an alternative method which uses digital image analysis (DIA) with refraction correction to measure the localized deformations of the specimen. The measurement accuracy is 0.2-0.3 mm, and it is low-cost. However, this method requires accurate control of camera position, and several assumptions need to be made. For example, this method assumes that the camera shooting direction is exactly perpendicular to the specimen which is impossible to satisfy in actual practice. White et al. (2003) proposed a digital image correlation (DIC) method to measure the volume-changes of soils. The DIC method has gained a lot of interest and popularity in soil deformation measurements (Liu & Iskander, 2004; DeJong et al., 2006, Take., 2015). However, this method cannot be used in triaxial tests since it cannot consider the influence of refraction.

In most recent years, the photogrammetry-based method has gained increasing interest in soil deformation measurements. Zhang et al., (2015) extended the photogrammetric method from one to multiple optical media to measure both the total and localized deformations for unsaturated soils during triaxial testing. In this method, the refraction has been properly handled and corrected by using mathematically rigorous equations. The point accuracy in the air and volume measurement accuracy have been reported to be less than 0.076 mm and better than 0.25%, respectively. Only one commercially available digital camera is needed to take images around the triaxial test apparatus from any arbitrary locations and orientations. Li and Zhang., (2019) discussed the factors influencing the accuracy of the photogrammetry-based deformation measurement method. Salazar et al. (2015) performed photogrammetric measurements of

soil volume in triaxial tests using an internal camera monitoring system.

Photogrammetric analysis was performed to monitor the deformation of the specimen during triaxial testing. Li et al. (2019) proposed and evaluated a new photogrammetry-based method for simultaneous measurement of soil water retention and shrinkage curves. The authors reported that comparing with the conventional methods, the new method can significantly reduce the time required for measuring the soil water retention and shrinkage curves. Fayek et al. (2020) developed a photogrammetry-based method to determine the top and bottom boundaries between the soil specimen, and the top and bottom pedestals. Based on that, the absolute volume of soil specimens in triaxial tests can be determined.

While the photogrammetry-based method has many merits over the existing methods, one limitation is the inability to continuously measure the deformations of the soil specimens during dynamic test, such as triaxial test, in which the soil specimen is continuously deforming. In Zhang et al. (2015), only one camera was used, and the method requires the test to be paused when taking images. However, for many tests, such as the triaxial tests on soils, the soil deformations are continuous. As a result, the tests cannot be paused during the test. Not to mention using this method to perform dynamic tests. Therefore, there is a clear need to develop a system which can continuously measure the 3-D full-field deformations of soil specimens during triaxial testing.

1.1.2. Target Identification in Photogrammetry. One of the main tasks of photogrammetry is to identify the homologous points in multiple images, which is commonly referred to as the corresponding problem (Knyaz & Sibiryakov, 1998; Ahn et al., 2001). Coded targets (CTs), often placed on the surfaces of the objects to be

measured, have been widely used as a reliable method for solving the corresponding problem in photogrammetry for high-accuracy 3-D measurements. CT has been widely used in photogrammetry to facilitate the automated 3-D measurements due to its low cost (Farnandez et al., 2013), and subpixel target center coordinates determination (Knyaz & Sibiriyakov, 1998). In addition, the CTs can be easily attached to any objects to be measured, from metallic to fragile materials (Farnandez et al., 2013). CTs have also been used in the photogrammetry-based method (Zhang et al., 2015; Salazar et al., 2015; Li et al., 2019; Fayek et al., 2020).

The overall measuring performance and the resulting accuracy levels of photogrammetry are directly linked to the quality of the image point determination (Ahn et al., 2001; Shorts et al., 2003). In the case of coded target-based photogrammetry, the image point determination depends largely on the performance of automatic recognition and identification of CTs. Therefore, accurate recognition and identification of CTs are of great importance in photogrammetric 3-D measurements. Over the past several decades, many research efforts have been made to develop reliable CT recognition and identification algorithms. These algorithms can be mainly categorized into two groups: shape and structural descriptor methods (Farnandez et al., 2013; Hattoris et al., 2000; Forbes et al., 2002; Xia et al., 2012; Nyarko., 2016), and template matching methods (Van et al., 1993; Barazzetti & Scaioni, 2010).

Despite the availability of many CT recognition and identification algorithms, as pointed out by many authors, CT recognition and identification are still challenging since CTs were often subjected to a great perspective deformation, freely rotated with regard to image frames, and displayed very large-scale differences (Bernat & Tokarczyk, 2013).

Mendikute and Zatarain (2012) pointed out that many CTs cannot be recognized by the photogrammetry system when the CT orientation with respect to the camera axis is larger than 45° . While unrecognized (missing) CTs may not have a significant influence on the subsequent photogrammetric analysis as long as a sufficient number of CTs are identified, false CT identification results can lead to inaccurate 3-D reconstruction results or even failure of 3-D reconstruction (Cheng et al., 2014). Therefore, manual correction is often required to correct the false CT identification results, which is tedious, prone to error, and inefficient. This deviates the original idea of CT as a rapid and automatic method to address the corresponding problem. Given the significance of CT recognition and identification in the photogrammetric method, there is a great need to develop a highly efficient and accurate method to take full advantage of the CTs.

At present, nearly all existing CT recognition and identification methods exhaustively search the entire image to detect CTs and compute ID numbers of each individual CT candidate, based solely upon the CT recognition and identification algorithms. The “brute force” state-of-practice did not take full advantage of the prior knowledge of the geometric arrangement of the CTs. In fact, at almost any time when CTs are used, the ID numbers and geometric locations of the CTs are carefully prescribed ahead of time instead of being arbitrarily posted to obtain the best representation of the targeted objects to be reconstructed.

1.1.3. Continuous Full-Field Deformation Measurement for Geosynthetics.

Geosynthetics have been extensively used as a reinforcement for a variety of geotechnical applications, such as soil stabilization, mechanically reinforced retaining walls and slopes, etc. The modulus and tensile strength are indispensable parameters in the design

applications of geosynthetics. The wide-width tensile test or grab tensile test is usually used to determine the tensile strength, failure strain, and deformation modulus of geosynthetics. The continuous and complete measurements of the displacements of geosynthetics at all locations (also referred to as full-field displacement) during tensile tests are essential for the above-mentioned purposes and provide important information about the mechanical behavior of the geosynthetics. However, the conventional mechanical strain measurement systems can only measure displacements/strains at a few locations with limited ranges. The inability to detect zones of varying strains and identify potential local failure zones as well as the inaccurate determination of strains may lead to either an unconservative design of the structure or possible catastrophic failures (Aydilek et al., 2004).

Over the past decade, numerous efforts have been made to develop alternative methods for displacement/strain measurements of geosynthetics during tensile tests. Crosshead extension method is commonly used to measure the overall deformations of geosynthetics by measuring the separation distance between the two tension grips. Skochdopole et al. (2) performed a tensile test on woven and knit geotextiles and geogrids using the crosshead extension method. It was pointed out that the measured strain obtained by this method was actually a combination of seating and specimen elongation. In addition, no information about the localized strains can be provided as this method only measures the overall displacements/strains of geosynthetics. Contact extensometer is also commonly used to provide accurate strain measurements. The use of extensometer requires the attachment of extensometer to the specimen at limited number of predesigned locations. In addition, the extensometer needs to be removed during the

test to avoid being damaged which will limit the measurement ranges of the extensometer. Strain gauge is another widely used contact method that has been used to measure the displacements/strains of geosynthetics. The measured strains by strain gauge are easily influenced by many factors, such as the strain gauge weight, data logger, quality of bonding between the strain gauge and the specimen (3). LVDT has also been extensively used in the displacement measurements. However, the additional weight of LVDT can lead to inaccurate measured strains in the geosynthetics. All the abovementioned contact methods can only measure the displacements/strains of geosynthetics at limited locations with limited measurement ranges. Aydilek et al. (2004) pointed out that the inability to detect zones of varying strains and identify potential failure zones as well as the inaccurate determination of strains may lead to either an unconservative design of the structure or possible catastrophic failures.

There are methods developed for other purposes but can potentially be used for measuring the varying displacement/strain of geosynthetics with larger measurement ranges. Jones (2000) used a non-contact image-based video extensometry technique to measure the strain of geotextiles during tensile test. It was reported that this method had accuracy values in the range of 86%-100 compared to the extensometer. Many researchers used image-based tracking techniques to track the movements of particles (Raschke et al.,1996; Paikowsky & Xi, 2000; Alshibli & Sture, 2000). Aydilek et al. (4) measured the strain distribution in geosynthetics during tensile test using an image-based method tracking method. However, the abovementioned image-based tracking methods often use 2-D images captured from a single camera and it is usually required to make an assumption that the specimen is initially planar and must maintain as a plane during the

test. Additional assumptions that the shooting direction should be exactly perpendicular to the specimen and the camera positions can be accurately controlled are also required. However, all these assumptions are nearly impossible to achieve. Moreover, these methods used zoom-lens and failed to perform camera calibration which can also lead to inaccurate or unreliable results. It was found that all existing methods had limitations. Thus, it remains a major challenge for researchers to develop alternative methods to continuously measure the three-dimensional (3-D) full-field displacement/strain of geosynthetics during tensile tests.

1.2. RESEARCH OBJECTIVES AND METHODOLOGY

The main objective of this research was to develop a structure from motion photogrammetric method that can continuously measure the 3-D soil deformations during triaxial testing. The new method has included the following features: 1) is able to measure and track the continuous deformations of soil specimen during the whole testing process; 2) is highly efficient, automatic, and user-friendly; 3) is low-cost and 4) can achieve sub-pixel precision 3-D results.

The advances in computer vision have offered great potential in the photogrammetric techniques. Recent developments in the computer vision algorithms have made it possible to reconstruct the three-dimensional models of a soil specimen using two dimensional images with a technique called Structure from Motion (SfM). This technique uses collections of 2-D images taken from a moving camera to reconstruct the 3-D model of the object. In this paper, a customized SfM photogrammetric method has been developed for reconstructing the 3-D models and measuring the volume-changes of

soils specimens in triaxial test. To facilitate the automatic target identification in the photogrammetric method, a table method has been proposed for coded target decoding by taking full advantage of the predesign geometric information regarding the coded targets. Then, the SfM photogrammetric method has been extended to consider multi-cameras and continuously measure the soil deformations during triaxial testing. Inexpensive security cameras are used to reduce the cost. In addition to the SfM photogrammetric method that is used in triaxial test, a multi-camera photogrammetric method has also been developed to continuously measure and track the 3-D full-field displacements/strains of the geosynthetics in the tensile test. All the abovementioned approaches have been implemented into efficient computer programs to reduce the time for processing the images/videos files. A series of unconfined compression tests, triaxial tests, and tensile tests have been conducted to demonstrate the effectiveness and merits of the proposed methods.

1.3. DISSERTATION OUTLINE

This dissertation contains three sections. Section 1 includes a brief introduction of the problem, primary objective, methodology, and the scope of work. Paper section includes six journal papers that present the developments of :1) a table method for coded target decoding; 2) a single-cameras-based SfM photogrammetric method, and 3) a multi-security camera system for dynamic test, such as triaxial test. The proposed methods can be used to measure the volume-changes of both saturated and unsaturated soils during both static and dynamic testing. The proposed multi-security camera system has been further developed for tensile test on geosynthetics. In this research, a low-cost security

camera system has been developed for continuously measuring and tracking the complete 3-D displacements/strains of geosynthetics. Section 3 summarizes the work has been accomplished, and major findings, conclusions, and recommendations for future research.

PAPER**I. A TABLE METHOD FOR CODED TARGET DECODING WITH APPLICATION TO 3-D RECONSTRUCTION OF SOIL SPECIMENS DURING TRIAXIAL TESTING**

Xiaolong Xia¹, Xiong Zhang², Sara Fayek³, and Zhaozheng Yin⁴

¹Ph.D. candidate, Department of Civil, Architectural, and Environmental Engineering, Missouri University of Science and Technology, Rolla, MO 65409-0030. Email: xxrkq@umsystem.edu

²(Corresponding author) Professor, Department of Civil, Architectural, and Environmental Engineering, Missouri University of Science and Technology, Rolla, MO 65409-0030. Email: zhangxi@umsystem.edu

³Ph.D. candidate, Department of Civil, Architectural, and Environmental Engineering, Missouri University of Science and Technology, Rolla, MO 65409-0030. Email: sfgbd@umsystem.edu

⁴Associate Professor, Department of Computer Science, Stony Brook University, Stony Brook, NY 11794. Email: zyin@cs.stonybrook.edu

ABSTRACT

Photogrammetry-based method is gaining popularity in many fields. One of the main tasks of photogrammetry is to identify the homologous points in multiple images, which is commonly referred to as the corresponding problem. Coded targets are often placed on the surfaces of the targeted objects and have been widely used as a reliable method for solving the corresponding problem in photogrammetry for high-accuracy three-dimensional measurements. Automated recognition and identification of coded targets are of great importance in the coded target-based photogrammetry. However, false

coded target identifications are inevitable due to large perspective distortion, unfavorable lighting conditions, and low-resolution, low-quality images, etc. As a result, manual corrections are often required, which are tedious, prone to error, and inefficient. In this paper, a faster R-CNN-based method has been proposed to recognize coded targets. Then, a table method has been developed to automatically identify and reject the falsely identified coded targets by taking advantages of the prior knowledge of the geometric arrangement of the coded targets. Based on that, missing coded targets can be recovered using either interpolation or extrapolation method. The effectiveness and accuracy of the proposed method are validated by implementing it into three-dimensional reconstruction of soil specimens during triaxial testing in geotechnical engineering. Experimental validation results indicate that the proposed method can achieve accurate and efficient coded target recognition and identification.

1. INTRODUCTION

Close-range photogrammetry has been extensively used as an effective technique for precise three-dimensional (3-D) measurements in many different fields, such as engineering, architecture, and surveying. Recently, photogrammetry-based method has also gained increasing interest in geotechnical engineering. For example, Zhang et al. [1] extended the photogrammetric method from one to multiple optical media to measure both the total and localized deformations for unsaturated soils during triaxial testing. Figure 1a shows a modified design for Zhang et al. [1]'s method. In this method, a conventional triaxial test apparatus for saturated soils was utilized for triaxial tests on

unsaturated soils. Only one commercially available digital camera was needed to take images of the triaxial tests from any arbitrary locations and orientations. Li and Zhang [2] discussed the factors influencing the accuracy of the photogrammetry-based deformation measurement method. Salazar et al. [3] performed photogrammetric measurements of soil volume in triaxial tests using an internal camera monitoring system. Photogrammetric analysis was performed to monitor the deformation of the specimen during triaxial testing. Li et al. [4] proposed and evaluated a new photogrammetry-based method for simultaneous measurement of soil water retention and shrinkage curves. The authors reported that comparing with the conventional methods, the new method can significantly reduce the time required for measuring the soil water retention and shrinkage curves. Fayek et al. [5] developed a photogrammetry-based method to determine the top and bottom boundaries between the soil specimen, and the top and bottom pedestals. Based on that, the absolute volume of soil specimens in triaxial tests can be determined.

One of the main tasks of photogrammetry is to identify the homologous points in multiple images, which is commonly referred to as the corresponding problem [6-7]. Coded targets (CTs), often placed on the surfaces of the objects to be measured, have been widely used as a reliable method for solving the corresponding problem in photogrammetry for high-accuracy 3-D measurements. Figure 1b shows the structure of a typical Ringed Automatically Detected (RAD) coded target. In Figure 1b, a central dot is surrounded by a unique code band with bit positions at equally spaced angular intervals. Each interval can be either black or white (0/1 or vice versa), forming a binary sequence that is unique for each coded landmark. Each CT has a unique band pattern that

corresponds to an identification (ID) number. The process of determining the ID number of the CT is also referred as the decoding process, or CT identification. The center of the

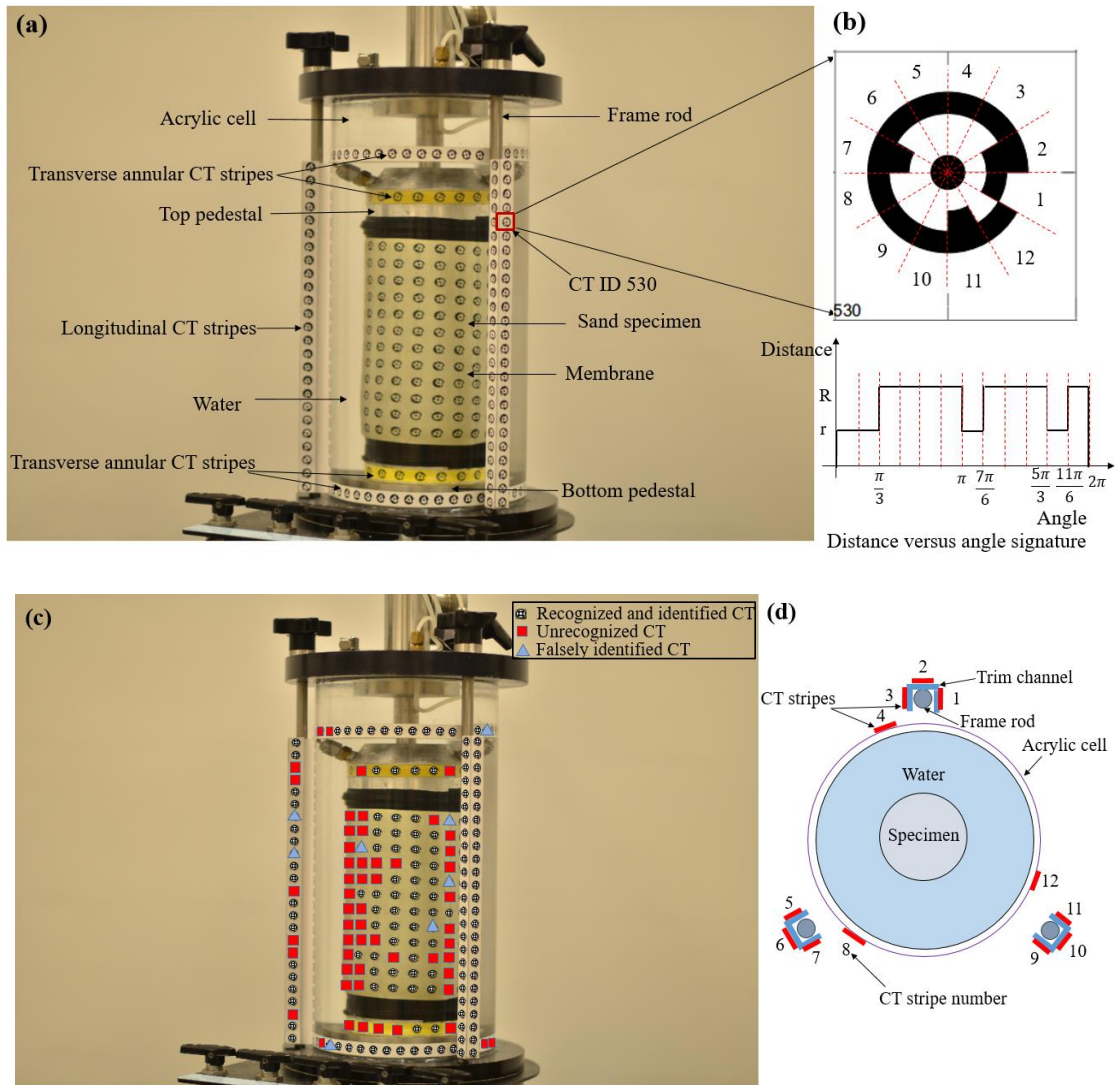


Figure 1. An example of unsatisfactory coded target recognition results. (a) Setup of the triaxial test system; (b) A typical coded target design; (c) coded target recognition results obtained from a commercial software; and (d) the cross-section of the triaxial cell system.

location of point of interest. CT has been widely used in photogrammetry to facilitate the automated 3-D measurements due to its low cost [8], and subpixel target center

coordinates determination [6]. In addition, the CTs can be easily attached to any objects to be measured, from metallic to fragile materials [8]. As shown in Figure 1a and Figure 1d, multiple longitudinal and transverse CT stripes were attached to the acrylic cell and frame rods. The membrane that placed on the soil specimen was also printed with CTs.

The overall measuring performance and the resulting accuracy levels of photogrammetry are directly linked to the quality of the image point determination [7, 9]. In the case of coded target-based photogrammetry, the image point determination depends largely on the performance of automatic recognition and identification of CTs. Therefore, accurate recognition and identification of CTs are of great importance in photogrammetric 3-D measurements. Over the past several decades, many research efforts have been made to develop reliable CT recognition and identification algorithms. These algorithms can be mainly categorized into two groups: shape and structural descriptor methods [8, 10-13], and template matching methods [14-15].

Despite the availability of many CT recognition and identification algorithms, as pointed out by many authors, CT recognition and identification are still challenging since CTs were often subjected to a great perspective deformation, freely rotated with regard to image frames, and displayed very large-scale differences [16]. Mendikute and Zatarain [17] pointed out that many CTs cannot be recognized by the photogrammetry system when the CT orientation with respect to the camera axis is larger than 45° . Figure 1c shows an example of unsatisfactory CT recognition and identification results obtained by a well-known commercial photogrammetric software called PhotoModeler. In Figure 1c, circular points represent CTs that had been both correctly recognized and identified, while the square and triangular points represent unrecognized and falsely identified CTs,

respectively. Out of the 197 CTs, only 69.5% of the CTs had been correctly recognized and identified. 27.9% of the CTs were unrecognized, and 4.1% of the CTs were falsely identified. While unrecognized (missing) CTs may not have a significant influence on the subsequent photogrammetric analysis as long as a sufficient number of CTs are identified, false CT identification results can lead to inaccurate 3-D reconstruction results or even failure of 3-D reconstruction [18]. Therefore, manual correction is often required to correct the false CT identification results, which is tedious, prone to error, and inefficient. This deviates the original idea of CT as a rapid and automatic method to address the corresponding problem. Given the significance of CT recognition and identification in the photogrammetric method, there is a great need to develop a highly efficient and accurate method to take full advantage of the CTs.

Convolutional Neural Networks (CNNs) have shown to be a powerful tool for image recognition and classification. Recently, CNNs have been adopted into the civil engineering community with applications in civil infrastructural defects detection [19-21], and structural analysis [22-24]. Limited research efforts have been devoted to utilizing the CNN-based method for CT recognition.

At present, nearly all existing CT recognition and identification methods exhaustively search the entire image to detect CTs and compute ID numbers of each individual CT candidate, based solely upon the CT recognition and identification algorithms. The “brute force” state-of-practice did not take full advantage of the prior knowledge of the geometric arrangement of the CTs. In fact, at almost any time when CTs are used, the ID numbers and geometric locations of the CTs are carefully prescribed

ahead of time instead of being arbitrarily posted to obtain the best representation of the targeted objects to be reconstructed.

In this paper, a faster R-CNN-based method was proposed to recognize RAD CTs as an initial attempt. Then, a table method was developed to fully utilize the geometric constraints on the CT arrangement with image processing. The method can automatically identify and reject false CT ID numbers with extremely high efficiency and accuracy after the preliminary CT identification is performed in a normal photogrammetric analysis. After that, the missing CTs were recovered by either interpolation or extrapolation technique based on the geometric constraints without any decoding process for the missing CTs, which significantly reduced the computational efforts while maintaining high accuracy of the analysis results.

2. PROPOSED METHODOLOGY

A simple example is shown in Figure 2 to demonstrate the principle of the proposed method. Figure 2a shows a design pattern of a 3-D reconstruction project with four-row and four-column of CTs. The sixteen CTs are numbered with IDs from one to sixteen. Figure 2a is a predesigned CT look-up table, which shows the geometric arrangement. Figure 2a contains the information regarding the relative location of each CT with respect to other CTs. Figure 2b shows the preliminary recognition and identification results of the CT IDs. The numbers outside the parentheses represent the computed IDs of the identified CTs, while the numbers inside the parentheses represent the pixel coordinates of the identified CTs. As can be seen in Figure 2, two IDs, 6 and 12

in Figure 2a were mistakenly identified as 15 and 2 in Figure 2b, which were marked with bold fonts. In addition, there were seven CTs (2, 4, 5, 9, 10, 13, and 15 in Figure 2a) that were not recognized, which were marked with shaded areas in Figure 2b. Results in Figure 2b were representative since it included some missing CTs and mistakenly identified CTs as well.

To implement the proposed table method, the outliers CT IDs have to be identified and removed first. To identify these two outlier IDs, a normalized distance is defined first by the following equation:

$$D_{i,j} = \frac{\sqrt{(X_I - X_J)^2 + (Y_I - Y_J)^2}}{\sqrt{(R_I - R_J)^2 + (C_I - C_J)^2}} \quad (1)$$

where $D_{i,j}$ = the normalized distance between CT (point) I and point J,

X_I, Y_I = pixel coordinates of CT I, which are denoted by the numbers inside the parentheses in Figures 2b and 2c,

X_J, Y_J = pixel coordinates of CT J, which are denoted by the numbers inside the parentheses in Figures 2b and 2c,

R_I, C_I = row number and column number of CT I, which can be obtained from Figure 2 directly, and

R_J, C_J = row number and column number of CT J, which can also be obtained from Figure 2.

For example, according to Figure 2, the pixel coordinates of CT 7, (X_7, Y_7) , are (300,200). The row number and column number of CT 7, (R_7, C_7) , are (2,3). The pixel coordinates of CT (point) 8, (X_8, Y_8) , are (400,200). The row number and column number

Column \ Row	1	2	3	4
1	1	2	3	4
2	5	6	7	8
3	9	10	11	12
4	13	14	15	16

(a)

Column \ Row	1	2	3	4
1	1(100, 100)		3(200, 100)	
2		15(200, 200)	7(300, 200)	8(400, 200)
3			11(300, 300)	2(400, 300)
4		14(200, 400)		16(400, 400)

(b)

Column \ Row	1	2	3	4
1	1(100, 100)	2(200, 100)	3(300, 100)	4(400, 100)
2	5(100, 200)	6(200, 200)	7(300, 200)	8(400, 200)
3	9(100, 300)	10(200, 300)	11(300, 300)	12(400, 300)
4	13(100, 400)	14(200, 400)	15(300, 400)	16(400, 400)

(c)

Figure 2. Schematic plot of the proposed table method. (a) Predesigned CT look-up table; (b) preliminary CT IDs and pixel coordinates results. The numbers outside the parentheses represent the computed IDs of the identified CTs, while the numbers inside the parentheses represent the pixel coordinates of the identified CTs. Bold font indicates falsely identified CT IDs, and shaded areas represent unrecognized CTs; and (c) CT IDs and pixel coordinates results after applying the table method. Bold font indicates corrected identified CT IDs, and shaded areas represent recovered CTs.

of CT 8, (R_8, C_8) , are (2,4). Therefore, it is easy to compute the normalized distance between CTs 7 and 8 using Equation 1, $D_{i,j} = 100$.

By using Equation 1, the computed normalized distances between any two correctly identified CTs, for example, CT 1 and any other CTs except the outlier CTs 2 and 15, $D_{1,3}, D_{1,7}, D_{1,8}, D_{1,11}, D_{1,14}, D_{1,16}$, were all the same value 100. 100 was the average normalized spacing of any two adjacent CTs. However, the computed normalized distances between CT 1 and two outlier CTs, and $D_{1,15}, D_{1,2}$ were 39 and 361, respectively, which were significantly different than 100. Therefore, by evaluating the normalized distances, it was easy to identify the two outlier CTs.

After the outlier CTs had been identified and discarded, the next step of the table method was to recover the missing CTs using the interpolation/extrapolation technique. For example, the pixel coordinates of CT 2 could be easily interpolated using the pixel coordinates of CTs 1 and 3, while the pixel coordinates of CT 4 could be readily extrapolated using the pixel coordinates of CTs 3, 7, and 8. Theoretically, a minimum of two correct CTs which did not belong to the same row and the same column were sufficient to infer both the IDs and the estimated pixel coordinates of all the other neighboring CTs. This is attributed to the fact that the table method takes advantage of the prior knowledge of the geometric arrangement of the CTs and the accurate preliminary ID and pixel coordinate results after outlier IDs rejection. The IDs of the recovered CTs can be readily known from the look-up table in Figure 2a. For example, the IDs of the two rejected CTs are 6 and 12, respectively. The ID and estimated pixel coordinate results for the recovered CTs were shown in Figure 2c. Once the estimated pixel coordinates were known as shown in Figure 2c, a new search could be performed in

the neighborhood of the estimated pixel coordinates to find the missing CTs. If the missing CT was successfully found, the ID of the missing CT was assigned directly to the CT without any ID computation process, and the accurate pixel coordinates of the missing CT could also be refined using well-established image processing techniques. Please note that although the example in Figure 2 is very simple with equally spaced rows and columns, this same concept can be easily applied to more realistic and more complex scenarios, as demonstrated in the following sections.

3. PROCEDURES OF THE PROPOSED METHOD

This section aims at describing the procedure of the proposed method. To perform 3-D reconstruction for the system as shown in Figure 1, three stages of analyses are needed: stage 1-image acquisition and CT recognition; stage 2-image processing and CT identification; and stage 3-post-processing and 3-D reconstruction. The flowcharts for each stage's analyses are shown in Figure 3. Due to the limited space, this section mainly focuses on stage 2 as shown in Figure 3, which demonstrates how the proposed table method is applied to automatically identify outlier CT IDs and recover missing CTs in a realistic scenario.

3.1. STAGE 1: IMAGE ACQUISITION AND CODED TARGET RECOGNITION

3.1.1. Experimental Setup. The experimental setup followed that used by Zhang et al. [1] with some modifications and is shown in Figure 1a and Figure 1d. Three longitudinal CT stripes (with CT IDs ranging from 501 to 800) were attached to each of

the three frame rods. Three longitudinal CT stripes and two (at the top and bottom) transverse circular CT stripes (with CT IDs ranging from 801 to 893) were attached to the acrylic cell. Two small annular CT stripes were attached to the top and bottom pedestals for top and bottom plane determination as proposed by Fayek et al. [4]. The membrane was printed with CTs (with IDs ranging from 1 to 300, but only 52 to 255 are visible in this paper due to installation). The four different sub-elements in the triaxial cell images (as shown in Figure 1b), namely longitudinal stripes, transverse circular stripes on the acrylic cell, small transverse annular stripes on pedestals, and membrane represent four different

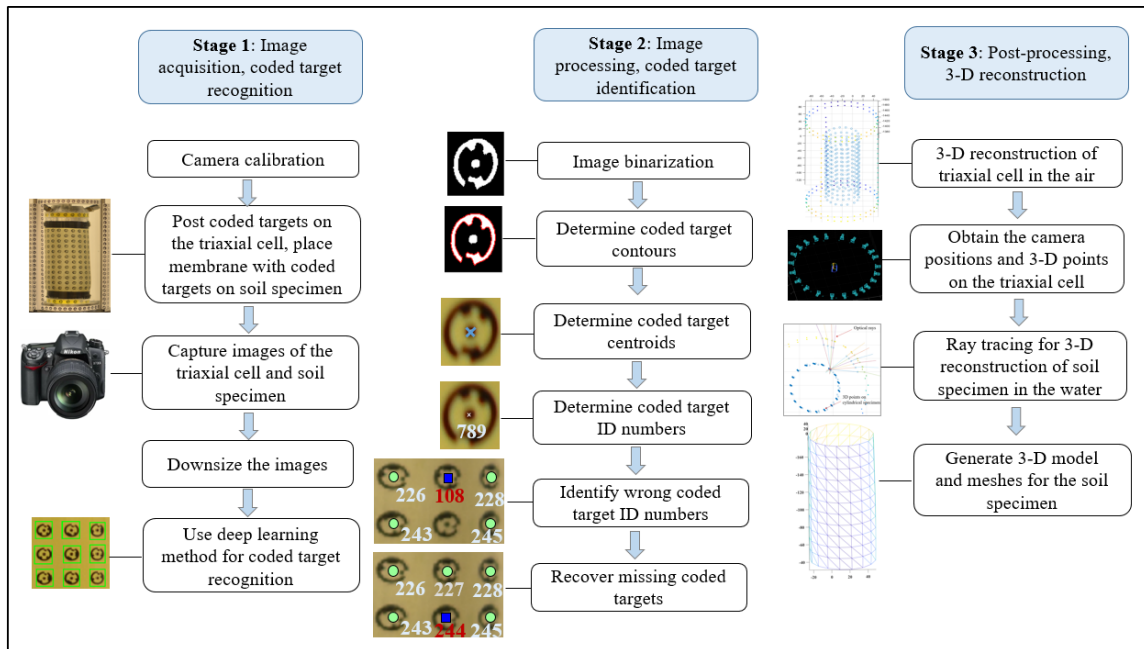


Figure 3. Flowchart and procedure of the proposed method.

situations regarding the geometric arrangement of CTs. The longitudinal CT stripes represent the linearly distributed CTs since the CTs on longitudinal stripes are always

distributed in a linear line regardless of the perspective deformation. The transverse annular stripes on the acrylic cell are curved and represent annularly distributed CTs. The transverse annular stripes on the top and bottom pedestals are inside the acrylic cell and immersed in water and are thus more complicated. The membrane is even more complicated since there is not only the refraction, possible scratches on the acrylic cell, damaged CTs on the membrane, but also the soil deformation during the triaxial testing. Due to light refraction, the CTs on the membrane in the images are distorted significantly. The refraction induced distortion of CT results in unavoidable false CT recognitions and identifications. The CTs in Figure 1 cover a large range of different scenarios. This is the reason why it is used as a representative example to demonstrate the implementation of the proposed method.

3.1.2. Image Acquisition. A commercial Nikon D7000 digital camera was used for image acquisition. Images of the triaxial test in the lab environment were captured both before and after triaxial loadings under normal lighting conditions. All the images have number of 4928 by 3264 pixels.

3.1.3. Deep Learning-Aided Coded Target Recognition. The CT recognition and identification were performed on a desktop PC (Intel Core E5-1603 v3 CPU, 2.80GHz, 64-bit operating system). After the images were collected, image preprocessing was operated on each image. The first step of image preprocessing is resizing the original images. The purpose of this operation is to reduce computational time. All the training images were downsized by 16 times. The second step of image preprocessing is to manually crop the original images into sub-elements, e.g., longitudinal stripes, larger transverse annular stripes, smaller transverse annular stripes, and membrane. These sub-

elements were also shown in Figure 1b. Ground truth labeling was performed on these sub-elements images. The training data statistics were listed in Table 1. A total of 167 CT stripes with 3459 CTs were utilized as training data. The ground truth data were prepared using the MATLAB Image Labeler app.

Table 1. Training data statistics.

	Number of Stripes	Number of CTs
Longitudinal stripes	20	1102
Transverse annular stripes (larger)	50	710
Transverse annular stripes (smaller)	77	416
Membrane	20	1231

These training data were then fed to the PC to train a faster R-CNN CT detector. Faster R-CNN consists of four parts: the convolution (Conv) layers, region proposal network (RPN), region of interest (RoI) pooling, and classification and regression. The Conv layer is responsible for extracting features from an image. The input is the whole image and the output is the feature maps. RoI pooling converts different sized inputs to fixed-length outputs. The classification and regression layer outputs the exact location of the CTs and the candidate regions to which the CTs respectively belongs in the image in terms of x , y , w , and h . Here x and y represent the coordinates of the upper left corner of the candidate area box, and w and h represent the width and height of the candidate area, respectively.

There are four steps for each training process. Step 1 is to train a Region Proposal Network (RPN); step 2 is to train a fast R-CNN Network using the RPN from step 1 and

extract region proposals from all the training images; step 3 is to re-train RPN using weight sharing with fast R-CNN; and step 4 to re-train fast R-CNN using updated RPN.

Figure 4a presents an example of CT recognition results using the faster R-CNN-based method. Out of the 200 CTs in the image, 175 CTs have been correctly recognized, indicating that faster R-CNN has the potential to achieve accurate CT recognition.

3.2. STAGE 2: CODED TARGET IDENTIFICATION AND APPLYING THE TABLE METHOD

3.2.1. Coded Target Identification. After the CTs have been recognized, the next phase is to decode each CT with its associated ID number and determine the accurate center of the CTs. A region of interest (ROI) that surrounds the CT was cropped based on the CT recognition results that obtained in the previous stage. All the operations in this phase will be performed over CT ROI area (Figure 5a). To decode the CTs, the following steps were performed sequentially:

3.2.1.1. Image binarization. The original CT ROI image patch was first converted into a grayscale CT image. After that, a locally adaptive threshold for the grayscale CT image patch was computed based on the local mean intensity in the neighborhood of each pixel. Then, image binarization was performed by replacing all values above the locally adaptive threshold with 1s and setting all other values to 0s.

Figure 5b shows a binary CT image.

3.2.1.2. CT contour identification. Blob analysis, as a common image processing technique, was performed to identify outlier blobs and the wanted blobs. In image processing, a blob means a connected area in an image. Typically, a small blob is

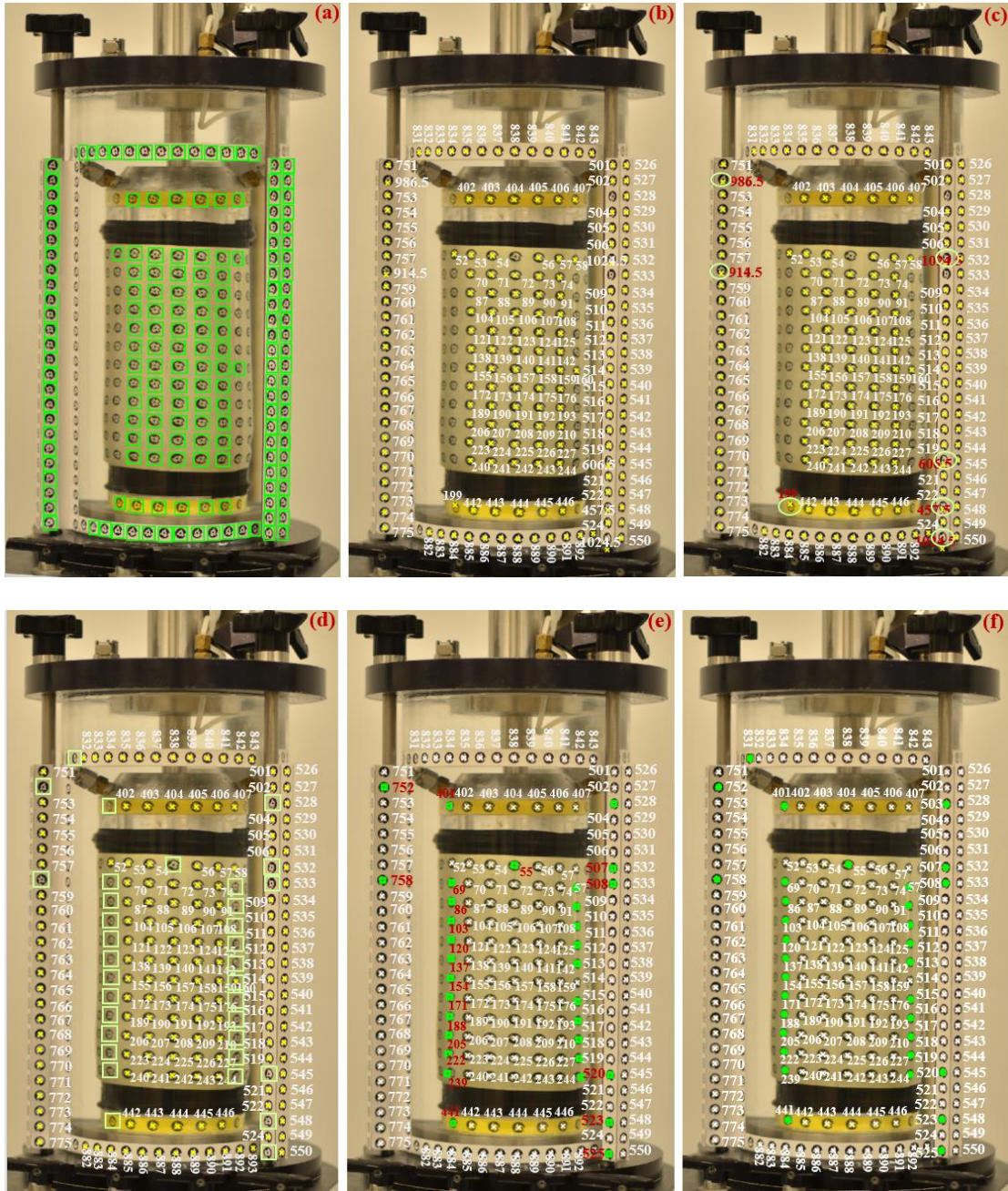
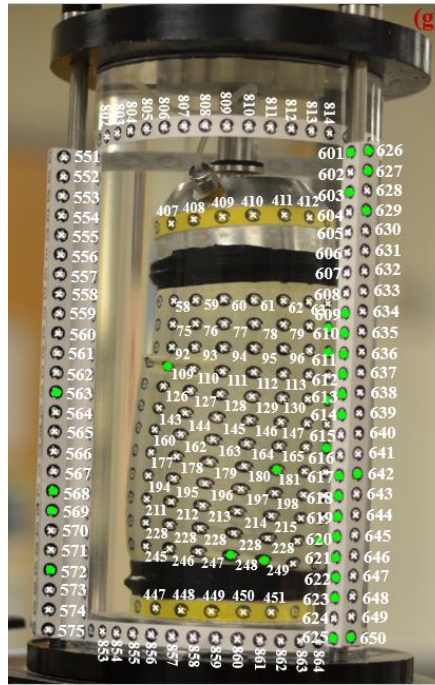


Figure 4. Coded target recognition and identification results. (a) Coded target recognition results using deep learning method; (b) initial IDs and centroid results; (c) identified outlier CT IDs; (d) identified missing CTs; (e) IDs results after interpolation and extrapolation and estimated centroids for missing CTs; (f) final IDs and centroid results after refining the pixel coordinates of CTs; and (g) results of a triaxial test image under loading and soil deformation conditions.



(g)

Figure 4. Coded target recognition and identification results. (a) Coded target recognition results using deep learning method; (b) initial IDs and centroid results; (c) identified outlier CT IDs; (d) identified missing CTs; (e) IDs results after interpolation and extrapolation and estimated centroids for missing CTs; (f) final IDs and centroid results after refining the pixel coordinates of CTs; and (g) results of a triaxial test image under loading and soil deformation conditions. (cont.)

embedded in a large blob for the CT in a binary image as shown in Figure 5c. This criterion can be used to reject outlier CT blobs. Then, the CT contour was obtained by detecting the boundary points of the CT. The CT contour result was shown in Figure 5d.

3.2.1.3. Ellipse fitting and CT center determination. The CT center was determined by fitting an ellipse to the outer boundary of the CT. The mathematical representation of an ellipse can be expressed by the following equation:

$$Ax^2 + Bxy + Cy^2 + Dx + Ey + F = 0 \quad (2)$$

where A, B, C, D, E, F are the ellipse parameters, which can be estimated by the least square method; (x, y) is a single measurement. The centroid of the ellipse that obtained from the ellipse fitting result is considered as the CT center. The cross in Figure 5a shows the CT center location.

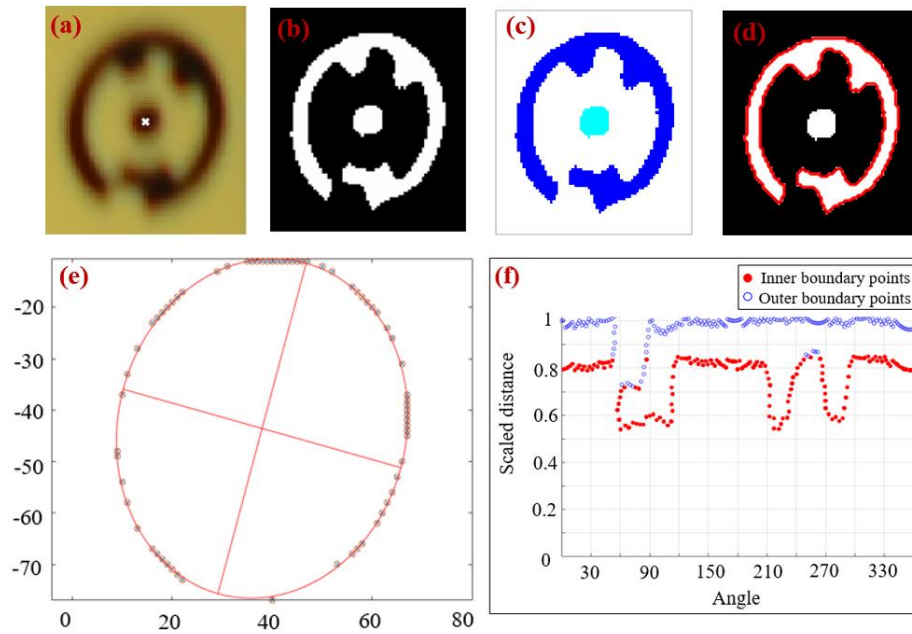


Figure 5. The proposed coded target identification method. (a) Original CT image; (b) binary CT image; (c) embedding criterion; (d) CT contours; (e) ellipse fitting; and (f) signature-based CT contour representation.

3.2.1.4. CT contour normalization. Typically, the circular CTs appear to be elliptical in the images under projective transformation. To obtain better decoding results, the elliptical CT contours were normalized to circular contours by using the following equation:

$$\begin{bmatrix} X_n \\ Y_n \end{bmatrix} = \begin{bmatrix} \frac{b}{a} & 0 \\ 0 & 1 \end{bmatrix} \begin{bmatrix} \cos \theta & -\sin \theta \\ \sin \theta & \cos \theta \end{bmatrix} \begin{bmatrix} X_i - X_0 \\ Y_i - Y_0 \end{bmatrix} \quad (3)$$

where X_n, Y_n = Normalized pixel coordinates of point I on the CT contour,

X_i, Y_i = original pixel coordinates of point I on the CT contour,

X_0, Y_0 = pixel coordinates of the ellipse centroid,

θ = the orientation angle of the ellipse, and

a, b = the major and minor axis lengths of the ellipse.

3.2.1.5. Signature-based CT contour representation and decoding. In the image processing, signature is a method for representing the contour of a bidimensional object by means of a one-dimensional function [25]. In this step, the signature was used to represent the CT contour for decoding purpose. The signature of the CT contour was obtained by computing the scaled distance from the centroid of the CT to its normalized contour as a function of the angle of the vector that leads from the centroid to the contour. The signature-based CT contour is shown in Figure 5f. In Figure 5f, the outer boundary points were used to determine the starting point, while the inner boundary points were used to decode CT numbers. Either 1 or 0 was assigned to each 30 degrees interval based on the number of points that larger than a threshold, for example, 0.75. The obtained 12-bit binary numbers were then converted to a decimal number, which corresponds to the ID number of the CT. The preliminary CT ID and centroid results are presented in Figure 4b.

3.2.2. Applying the Table Method. In Figure 4b, some false ID results were observed. The false CT identification results are inevitable due to several reasons, such as large projective distortion, unfavorable lighting conditions, and low-resolution, low-quality images, etc. The table method described in the Methodology section was applied

to automatically identify and reject the outlier CT IDs. The following steps were performed to utilize the table method:

3.2.2.1. Detect and remove the incorrect IDs. Figure 6a shows the preliminary ID results for the CTs on a cropped region of the membrane in another more representative image. Out of the 25 CTs in total in Figure 6a, 23 CTs were correctly recognized. Among these 23 recognized CTs, there were 22 CTs which had been correctly identified. There was one false CT ID, 170 (as denoted by a square), which should be 106 based on the look-up table.

The pseudo-code of the proposed algorithm for identifying outlier CT IDs is presented in Table 2. To use the table method, the normalized distances between each of the 23 recognized CTs and all the other CTs were computed using Equation 1. It is found that most of these normalized distances were in the range of 100 pixels to 130 pixels. The

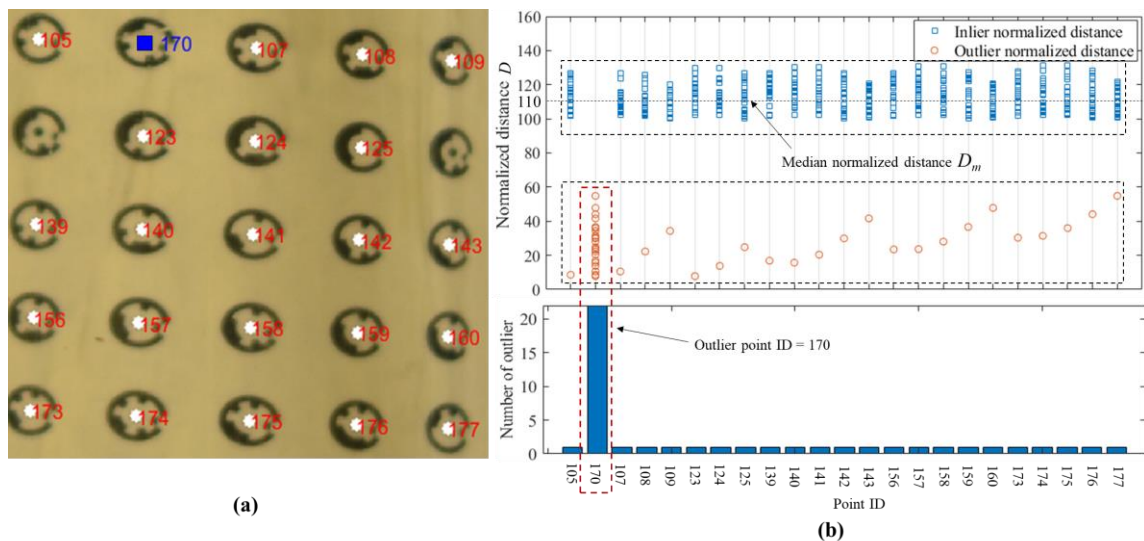


Figure 6. Identify outlier coded target IDs using table method. (a) Preliminary CT identification results; and (b) applying the table method to detect and correct outlier CT IDs.

Table 2. The pseudo code of the proposed algorithm for identifying outlier CT IDs.

Step	Procedure
1	Obtain the preliminary CT IDs and pixel coordinate results
2	Label each CT with row number and column number based on the look-up table
3	Compute the normalized distances between each CT and all other CTs
4	Determine the median of all the computed normalized distances
5	Identify the outlier normalized distances using threshold
6	Determine the number of outliers normalized distances for each CT
7	Identify and reject the outlier CT IDs

median normalized distance, D_m was determined to be 110 pixels, which was an estimated average spacing of any two adjacent CTs in the image. Then, an empirical threshold of 0.1 was used to classify all the normalized distances into inlier normalized distance and outlier normalized distance by using the following equation:

$$\frac{|D - D_m|}{D_m} < T \quad (4)$$

where D_m = the median normalized distance; D = the computed normalized distance, and T = the threshold, which is set to be 0.1.

Normalized distances that satisfy Equation 4 are defined as inlier normalized distances, while normalized distances that do not satisfy Equation 4 are defined as outlier normalized distances. Equation 3 was applied to all the 23 CTs and the results were presented in Figure 6b. CT ID 170 was identified to be an outlier point because this ID had 22 outlier normalized distances. Except ID 170, all the other CT ID had 22 inlier

normalized distances and 1 outlier normalized distance. Therefore, all the other CTs were inlier CTs.

It is noted that only the results of a cropped region of the membrane are presented here to demonstrate the effectiveness of the proposed table method due to the limited space. The same procedure can also be applied to the longitudinal stripes and transverse stripes that are shown in Figure 1b.

Figure 4c shows the identified outlier CT IDs. The ellipses represent falsely identified CT IDs from the preliminary CT identification results. In Figure 4c, it is found that seven CTs had been falsely identified. The determined CT centroids of some of these falsely identified CTs were not accurate from visual inspections, indicating that inaccurate CT centroids are often accompanied by false CT IDs due to low image qualities. These outlier CTs were removed and the new IDs and CT centroids results were presented in Figure 4d. As can be seen in Figure 4d, the ID results were all correct. However, 34 CTs were missing. The missing CTs were marked with squares. Most of the missing CTs were caused by the inability to recognize at the deep learning aided CT recognition stage. The removed outlier CTs were also regarded as missing CTs.

It is noted that only the results of a cropped region of the membrane are presented here to demonstrate the effectiveness of the proposed table method due to the limited space. The same procedure can also be applied to the longitudinal stripes and transverse stripes that are shown in Figure 1b.

Figure 4c shows the identified outlier CT IDs. The ellipses represent falsely identified CT IDs from the preliminary CT identification results. In Figure 4c, it is found that seven CTs had been falsely identified. The determined CT centroids of some of these

falsely identified CTs were not accurate from visual inspections, indicating that inaccurate CT centroids are often accompanied by false CT IDs due to low image qualities. These outlier CTs were removed and the new IDs and CT centroids results were presented in Figure 4d. As can be seen in Figure 4d, the ID results were all correct. However, 34 CTs were missing. The missing CTs were marked with squares. Most of the missing CTs were caused by the inability to recognize at the deep learning aided CT recognition stage. The removed outlier CTs were also regarded as missing CTs.

3.2.2.2. Interpolation/extrapolation. This step took advantage of both the prior knowledge of the geometric arrangement of the CTs and the IDs and centroids information of the CTs that were obtained from the previous step. As can be seen in Figure 4d, the CTs on the longitudinal stripes lied in a straight line even under projective transformation. In addition, a sufficient number of CTs had been correctly identified and their accurate centroid locations were known. This information was used in the 1-D linear interpolation to obtain accurate interpolation results. The same 1-D linear interpolation technique was also applied to the transverse annular stripes. The membrane was a more complicated case since there was a deformation of the soil specimen. To address this problem, 2-D extrapolation was performed on the membrane CTs based on the known IDs and centroids of the CTs that had been correctly identified in the previous step.

3.2.2.3. Assign correct IDs to the missing CTs. Since the IDs of the missing CTs can be accurately determined by interpolation/extrapolation, these IDs were assigned to the missing CTs directly without any computation for CT IDs. This CT assigning process not only saves computational cost but also ensures the high-accuracy IDs results.

Figure 4e shows the ID results after assigning correct IDs to the missing CTs. The squares represent the predicted locations of the CTs.

3.2.2.4. Search for the CTs near the predicted locations for missing CTs.

Based on the estimated centroid locations of the missing CTs that obtained from previous steps, it is easy to search for the CTs near the predicted locations for missing CTs.

3.2.2.5. Determine the accurate centroid of the missing CTs. Note that the interpolation/extrapolation process in step 2 can only obtain estimated centroid locations of the CTs. In this step, the accurate centroid location of the missing CTs can be obtained using the same techniques for determining the centroid locations of CTs. In Figure 4f, the missing CTs had been successfully recovered with both accurate CT IDs and centroid locations. The effectiveness of the proposed table method has been demonstrated particularly at recovering missing CTs on the membrane. The aforementioned two columns of missing CTs on the membrane had been recovered using the proposed table method.

Figures 4a-f present the CT recognition and identification results before the triaxial loading. To demonstrate the adaptability of the proposed method, the CT recognition and identification results after triaxial loading and soil deformation were presented in Figure 4g. Figure 4g demonstrates that the proposed method ensures accurate CT recognition and identification when the soil experiences large deformation.

3.3. STAGE 3: APPLICATION TO 3-D RECONSTRUCTION AND VOLUME MEASUREMENT OF SOILS SAMPLES

To further demonstrate the effectiveness of the proposed method, the CT recognition and identification results obtained by the proposed method had been

implemented into the 3-D reconstruction of soil specimen during triaxial testing. The 3-D model of the triaxial cell as well as the soil specimen can be obtained using the method described in Zhang et al. [1]. The meshes for the 3-D model of the soil specimen can be generated. This mesh can be used to calculate the volume of the specimen. Detailed procedures for calculating the volume based on the generated mesh can be found in Zhang et al. [1]. Therefore, the volume-change of the specimen can be obtained.

4. EXPERIMENTAL VALIDATION OF THE PROPOSED METHOD

This section describes the experiment conducted to demonstrate the performance of the proposed method in CT recognition and identification. The experiment validated the proposed method by 23 triaxial cell images. All the images were captured using the Nikon D7000 camera. To ensure a wide range of adaptability of the proposed method, all the images were taken under normal lighting conditions and real triaxial test environment. The table method for decoding CTs has also been implemented into the 3-D reconstruction of a sand specimen in the triaxial cell.

4.1. COMPARISON OF THE CT RECOGNITION AND IDENTIFICATION RESULTS OBTAINED BY THE PROPOSED METHOD AND SOFTWARE

To evaluate the effectiveness of the proposed method, the CT recognition and identification results obtained by the proposed method and a well-known photogrammetric software called PhotoModeler were compared. The statistics data of the comparison results were listed in Table 3. From the table, the faster R-CNN-based method shows promising CT recognition results especially for CTs on the pedestals and

membrane that were under immersed condition. The improvement percentages of the number of correctly recognized CTs on pedestals and membrane by faster R-CNN-based method and the software were 46.5% and 19.5%, respectively. This indicates that the proposed faster-RCNN-based method is effective and accurate in CT recognition. It is also found that the number of both correctly recognized and identified CTs on the membrane using the proposed method was 54.6% greater than the software, which was a significant improvement. This promising result is mainly due to the ability of the proposed method to identify outlier CT IDs and recover missing CTs based on the reliable interpolation/extrapolation technique.

Table 3. Comparison of CT recognition and identification results obtained by PhotoModeler and the proposed method.

Method Statistic data	PhotoModeler	The Proposed Method	Improvement Percentage (%)
Recognized CTs on membrane	1110	1327	19.5
Recognized CTs on pedestals	146	214	46.5
Recognized CTs outside the triaxial cell	2091	2135	2.1
Both recognized and identified CTs on membrane	990	1531	54.6
Both recognized and identified CTs on pedestals	130	199	53.1
Both recognized and identified CTs outside the triaxial cell	2049	2078	1.4
Total recognized CTs	3347	3676	9.8
Total both recognized and identified CTs	3169	3808	20.1
CT identification rate	94.6% (out of 3169)	100% (out of 3808)	-

Since all the outlier CT IDs can be identified, the proposed table can achieve a 100% identification rate (out of 3808 CTs) compared with PhotoModeler's 94.6% identification rate (out of 3169 CTs), as indicated in Table 3. In other words, the proposed method can identify more CTs with a higher accuracy. On the other hand, even if the increase in the identification rate from the commercial software to the proposed method is only 5%, it represents a significant increase in the identification efficiency. This is because even a small number of falsely identified CTs can directly cause failure in 3-D reconstruction. In order to perform 3-D reconstruction successfully, it is required to manually correct those falsely identified CTs, which is a rather tedious process. In fact, one limitation of the Zhang et al. [1]'s method is that it is computationally intensive. The results as shown in Table 3 are obtained from one loading step. In reality, a typical triaxial test involves 10 to 20 loading steps, each loading steps require about 20-50 images to reconstruct the 3-D models of the soil specimens, and on each image, about 150 to 250 points are processed. This means that, on average, about 100,000 CTs are needed to be correctly recognized and identified in one triaxial test. The time for processing all the images for one triaxial test can be reduced significantly by using the proposed table method which can automatically detect and correct falsely identified CTs. The total number of both correctly recognized and identified CTs using the proposed method was 3808, compared to 3169 by software, indicating that the proposed method is accurate and capable of identifying many more CTs compared to software. From Table 3, the proposed method outperformed PhotoModeler in terms of CT recognition and identification in all of the four aforementioned cases (longitudinal stripes and transverse stripes in the air,

transverse stripes and membrane in water), indicating that the proposed table method has the adaptability in different CT geometric arrangement and complex realistic scenarios.

4.2. IMPLEMENTATION OF THE PROPOSED METHOD INTO 3-D RECONSTRUCTION OF SOIL SPECIMEN

This section demonstrates the effectiveness of the proposed method by implementing it into the 3-D reconstruction of soil specimen during triaxial testing. In this section, a photogrammetry-based method introduced in Zhang et al. [1] was adopted to obtain the 3-D model of the soil specimen under refraction condition. A total of 23 triaxial test images were used for the validation test because 23 images were sufficient to secure a successful 3-D reconstruction project. The CT recognition and identification results obtained by the proposed method served as the input to 3-D reconstruction of the soil specimen. Figure 7a shows the 3-D model of the acrylic cell and camera locations. Figure 7b shows the generated 3-D model and meshes for the soil specimen. For the 3-D

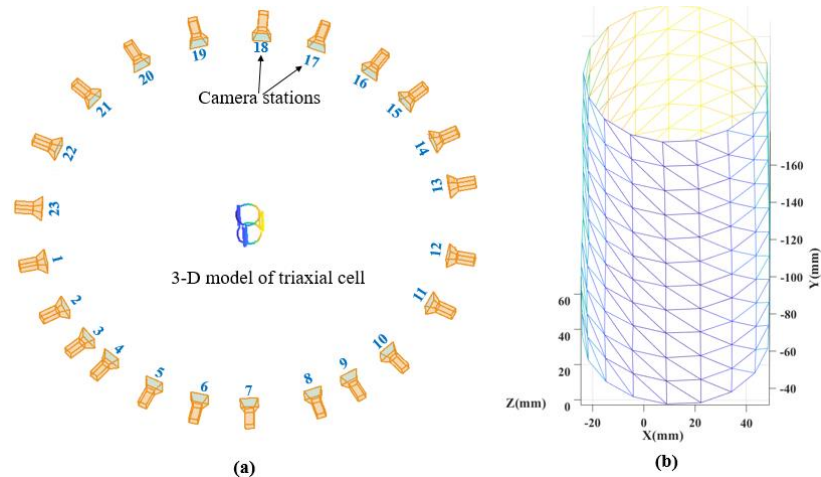


Figure 7. 3-D reconstruction results using the target recognition data. (a) 3-D models of the acrylic cell and camera stations; and (b) 3-D model and generated meshes for the soil specimen.

model of the soil specimen inside the triaxial cell, the 3-D location of each CT on the membrane was determined by six optical rays on average using a least-square optimization technique. As shown in Table 3, the proposed method has the potential to identify or recover more CTs compared with a commercial software. This means that more optical rays can be used to determine the 3-D locations of the CTs, which ensures high- accuracy 3-D locations of each CT. The 3-D models of the acrylic cell, soil specimen, and the 3-D camera locations in Figure 7 indicate that the proposed method is effective and accurate in terms of CT recognition and identification.

5. CONCLUSIONS

A table method for coded target identification with applications to the 3-D reconstruction of soil samples during triaxial testing was proposed. In this method, CT recognition was performed first using deep learning technique. The triaxial cell images required for training and validation were taken with a commercially available digital camera.

The proposed table method was especially strong at recognizing and identifying CTs on the membrane inside the triaxial cell under the immersed condition that makes detection difficult when using traditional methods. From the validation test results, the total number of both correctly recognized and identified CTs using the proposed method is 3808, compared to 3169 by software, indicating that the proposed method is accurate and capable of identifying many more CTs compared to software. The proposed method also enables automatic identification of outlier CT numbers, which is a huge advantage

since the tedious and prone-to-error manual corrections of false CT identifications can be eliminated. As far as the method in general goes, the proposed table method takes advantage of prior knowledge of the CT arrangement. The geometric arrangement of nearly all CTs is carefully designed before posting on the surfaces of measuring objects for the 3-D measurement purposes. Therefore, the proposed method has a wide application in most coded target-based photogrammetry tasks.

REFERENCES

1. Zhang X, Li L, Chen G, Lytton R (2015) A photogrammetry-based method to measure total and local volume changes of unsaturated soils during triaxial testing. *Acta Geotechnica* 10(1):55-82.
2. Li L, Zhang X (2019) Factors influencing the accuracy of the photogrammetry-based deformation measurement method. *Acta Geotechnica* 14(2): 559-574.
3. Salazar SE, Barnes A, Coffman RA (2015) Development of an Internal Camera-Based Volume Determination System for Triaxial Testing. *Geotechnical Testing Journal* 38(4):549-555.
4. Li L, Zhang X, Li P (2019) Evaluating a new method for simultaneous measurement of soil water retention and shrinkage curves. *Acta Geotechnica* 14(4): 1021-1035.
5. Fayek S, Xia X, Li L, Zhang X (2020) Photogrammetry-Based Method to Determine the Absolute Volume of Soil Specimen during Triaxial Testing. *Transportation Research Record*, 2020. 0361198120928339.
6. Knyaz VA, Sibiryakov AV (1998) Non-contact 3D model reconstruction using coded targets. *Image* 1(2).
7. Ahn SJ, Rauh W, Kim SI (2001) Circular coded target for automation of optical 3D-measurement and camera calibration. *International Journal of Pattern Recognition and Artificial Intelligence* 15(06):905-919.

8. Fernandez-Fernandez M, Alonso-Montes C, Bertelsen A, Mendikute A (2013) Industrial Non-intrusive Coded-Target Identification and Decoding Application. In Iberian Conference on Pattern Recognition and Image Analysis. Springer, Berlin, Heidelberg. pp. 790-797.
9. Shortis MR, Seager JW, Robson S, Harvey ES (2003) Automatic recognition of coded targets based on a Hough transform and segment matching. International Society for Optics and Photonics. In Videometrics VII, Vol. 5013, pp. 202-208.
10. Hattori S, Akimoto K, Fraser C, Ono T, Imoto H (2000) Design of coded targets and automated measurement procedures in industrial vision metrology. International Archives of Photogrammetry and Remote Sensing 33(5):72-78.
11. Forbes K, Voigt A, Bodika N (2002) An inexpensive, automatic and accurate camera calibration method. In Proceedings of the Thirteenth Annual South African Workshop on Pattern Recognition. pp. 1-6.
12. Xia R, Zhao J, Liu W, Wu JH, Fu SP, Jiang J, Li, J (2012) A robust recognition algorithm for encoded targets in close-range photogrammetry. Journal of information science and engineering 28:407-418.
13. Nyarko K, Thomas C, Torres G (2016) A robust close-range photogrammetric target extraction algorithm for size and type variant targets. In Automatic Target Recognition XXVI. International Society for Optics and Photonics. Vol. 9844, p. 984403.
14. Van Den Heuvel FA, Kroon R, Le Poole RS (1993) Digital close-range photogrammetry using artificial targets. International Archives of Photogrammetry and Remote Sensing 29:222-222.
15. Barazzetti L, Scaioni M (2010) Development and implementation of image-based algorithms for measurement of deformations in material testing. Sensors 10(8):7469-7495.
16. Bernat K, Tokarczyk R (2013) Automation of measurements of selected targets of photopoints in application to photogrammetric reconstruction of road accidents. Geomatics and Environmental Engineering 7.
17. Mendikute A, Zatarain M (2012) A machine vision approach for automated raw part alignment in machine tools. Modern Machinery Science Journal 1: 365-369.
18. Cheng J, Leng C, Wu J, Cui H, Lu H (2014) Fast and accurate image matching with cascade hashing for 3d reconstruction. In Proceedings of the IEEE Conference on Computer Vision and Pattern Recognition. pp. 1-8.

19. Soukup D, Huber-Mörk R (2014) Convolutional neural networks for steel surface defect detection from photometric stereo images. In International Symposium on Visual Computing. Springer, Cham. pp. 668-677.
20. Cha YJ, Choi W, Büyüköztürk O (2017) Deep learning-based crack damage detection using convolutional neural networks. *Computer-Aided Civil and Infrastructure Engineering* 32(5): 361-378.
21. Gao Y, Mosalam KM (2018) Deep transfer learning for image-based structural damage recognition. *Computer-Aided Civil and Infrastructure Engineering* 33(9):748-768.
22. Lee S, Ha J, Zokhirova M, Moon H, Lee J (2018) Background information of deep learning for structural engineering. *Archives of Computational Methods in Engineering* 25(1):121-129.
23. Hung TV, Viet VQ, Van Thuat D (2019) A deep learning-based procedure for estimation of ultimate load carrying of steel trusses using advanced analysis. *Journal of Science and Technology in Civil Engineering (STCE)-NUCE* 13(3):113-123.
24. Yu Y, Hur T, Jung J, Jang IG (2019) Deep learning for determining a near-optimal topological design without any iteration. *Structural and Multidisciplinary Optimization* 59(3):787-799.
25. Popescu C (2004) A Contour Based Descriptor for Object Recognition. SACI Transactions, Timisoara.

II. IMPROVED TABLE METHOD FOR CODED TARGET IDENTIFICATION WITH APPLICATION TO PHOTOGRAMMETRIC ANALYSIS OF SOIL SPECIMEN DURING TRIAXIAL TESTING

Xiaolong Xia¹, Xiong Zhang², Sara Fayek³, and Zhaozheng Yin⁴

¹Ph.D. candidate, Department of Civil, Architectural, and Environmental Engineering, Missouri University of Science and Technology, Rolla, MO 65409-0030. Email: xxrkq@umsystem.edu

²Ph.D. candidate, Department of Civil, Architectural, and Environmental Engineering, Missouri University of Science and Technology, Rolla, MO 65409-0030. Email: sfgbd@umsystem.edu

³(Corresponding Author) Professor, Department of Civil, Architectural, and Environmental Engineering, Missouri University of Science and Technology, Rolla, MO 65409-0030. Email: zhangxi@umsystem.edu

⁴Professor, Department of Computer Science, Stony Brook University, Stony Brook, NY 11794. Email: zyin@cs.stonybrook.edu

ABSTRACT

Accurate and efficient recognition and identification of coded targets are of great importance in coded target-based photogrammetry. Recently, a deep learning-based method has been utilized to recognize the coded targets. Then, a table method has been developed to decode the coded targets, identify falsely identified coded targets, and recover missing coded targets. This method takes advantage of the geometric arrangement of the coded targets. In this paper, an improved table method has been developed to improve the coded targets recognition and identification results. Blob analysis, instead of deep learning, is utilized to recognize coded targets. Then, the RANSAC algorithm was utilized to identify falsely identified coded targets. Based on

that, interpolation was performed on both the outside CT stripes and on membrane. Finally, the IDs of coded targets on the membrane are renumbered, which can increase the density of the coded targets on the membrane by three times. The effectiveness and accuracy of the proposed method are validated by implementing it into three-dimensional reconstruction of soil specimens during triaxial testing in geotechnical engineering. Experimental validation results indicate that the proposed method can achieve more accurate and more efficient coded target recognition and identification results.

1. INTRODUCTION

Close-Range Photogrammetry is a well-established three-dimensional (3-D) measurement technique that has found its applications in many different fields, such as industry, biomechanics, archaeology, architecture, aerospace engineering, accident reconstruction, hydraulic monitoring, as well as civil structural monitoring (1), etc. Recently, increasing attention has been paid to applications of photogrammetry to soil characterization in geotechnical community.

Zhang et al. (2) proposed a photogrammetry-based method which can correct for the ray refraction effects and measure both the global and localized 3-D deformations of soil specimens during triaxial testing. Only a single digital camera was required to capture images of the triaxial tests from any arbitrary locations and orientations. It was reported that the accuracy of point measurements in the triaxial tests ranges from 0.056 to 0.076 mm and the accuracy for total volume measurements is better than 0.25 %. Salazar et al. (3) developed an internal camera monitoring system which can measure the soil

volume and monitor the soil deformation during triaxial testing. The capability of determining total and localized strains, and total volume at any stage of triaxial testing was also validated. Li and Zhang (4) proposed a photogrammetry-based method to measure the soil shrinkage curve. In this method, the 3-D model of the soil specimen during drying was reconstructed, and the soil volume and deformation were calculated. The validation results from the shrinkage tests indicated that the proposed method is reliable and accurate for soil shrinkage curve measurement. Fayek et al. (5) developed a photogrammetry-based method for determining the top and bottom boundary planes between the two ends of soil specimen, and the top and bottom pedestals. Based on that, the absolute volume of the soil specimens with considerations of the soil ends were determined. Nishimura (6) adopted the ray tracing formulation by Zhang et al. (2) and proposed a stereophotogrammetry technique to derive accurate relative displacements of soil specimen in triaxial test. The accuracy, precision, and convenience of the proposed method were demonstrated.

One of the primary tasks of photogrammetry is to identify the homologous image points in multiple images from different views, which is popularly known as the correspondence problem (7). Coded targets (CTs) have been widely used in photogrammetry as a reliable tool to solve the correspondence problem and achieve high-accuracy 3-D measurements. A CT is a high contrast dot with a unique pattern around it that is often placed on the surface of the object to be measured. A more detailed description of the CT can be found in Xia et al. (8). Each CT has a unique shape which corresponds to a unique ID number. The process of determining the ID number of a CT is also known as CT identification, or decoding of the CT. The center of the CT is regarded

as the image point and point of interest. CTs are widely used in photogrammetry to solve the correspondence problem automatically due to its low cost and sub-pixel image point determination (9). The basics of CT algorithms consist of three phases. Phase 1 is called CT recognition which means to search for all CT candidates in the entire image. Phase 2 is called CT identification which is to decode the associated ID number of each CT. Phase 3 is called CT centroid determination which means to determine the accurate center of the CT.

The overall performance and accuracy of photogrammetry largely depend on the quality of the image point determination (7, 10). In the matter of coded target-based photogrammetry, the image point determination is directly linked to the performance of CT recognition and identification. Therefore, accurate and automatic CT recognition and identification are of primary importance in coded target-based photogrammetry. Many research efforts have been made to develop efficient CT recognition and identification algorithms in the past several decades. These algorithms can be broadly divided into three categories: (1) shape and structural descriptor methods; (2) template matching methods; and (3) deep learning methods. A more detailed review of these methods can be found in the Relative Work section. In spite of the availability of many CT recognition and identification algorithms, coded target-based photogrammetry often suffers from unavoidably unsatisfactory CT recognition and identification results. This is because the CTs are often subjected to a great perspective deformation, freely rotated with regard to image frames, and displayed very large-scale differences (11). In addition, the poor image quality, unfavorable light condition, scratches on the CTs, etc., can also result in low CT recognition and identification accuracies. In Xia et al. (8), it was reported that out

of the 197 CTs on a triaxial cell image, only 69.5% of the CTs had been correctly recognized and identified by a widely used photogrammetric software. 27.9% of the CTs were unrecognized, and 4.1% of the CTs were falsely identified. While the influence of unrecognized CTs on the subsequent photogrammetric analysis is relatively small, the false CT identification results can result in inaccurate 3-D reconstruction results or even failure of 3-D reconstruction (12). Therefore, manual correction is usually required to identify and correct those wrong CT IDs, which is tedious, time-consuming, and prone to error. The requirement of inefficient manual corrections deviates the original idea of CT as an efficient tool to automatically address the correspondence problem.

On the other hand, to date, almost all existing photogrammetry-based methods exhaustively search for every possible CT in the entire image and calculate the ID number of each candidate CT based solely on the CT recognition and identification algorithm (8). However, this method ignores the prior knowledge of the CT geometric arrangement. Actually, in almost every situation where the CTs are used, the IDs and geometric locations of the CTs are carefully designed and specified instead of randomly selected to ensure good representation of the objects to be measured. A table method has been proposed to recognize and decode the CTs by taking full advantage of the predesigned geometric arrangement of the CTs (8). Figure 1 shows the test setup of the method. In Xia et al. (8), a deep learning algorithm named faster R-CNN was utilized to recognize the CTs. A typical CT recognition result was shown in Figure 2. Then, the table method was applied and the normalized distances of the CTs were used to identify and reject the outlier CTs. Interpolation was also performed to recover more CTs. It was reported that there are significant improvements in terms of CT recognition and

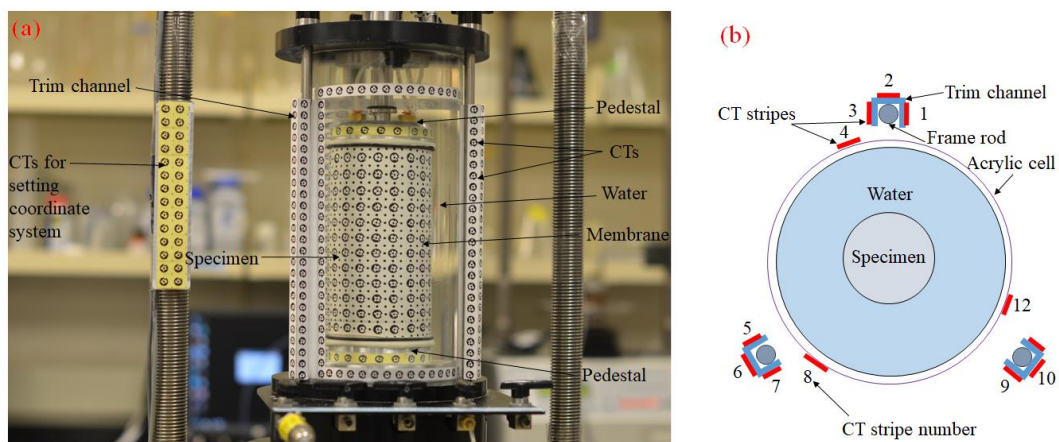


Figure 1. Triaxial test system. (a) System setup; and (b) the cross-section of the triaxial cell system (modified from Xia et al. (8))

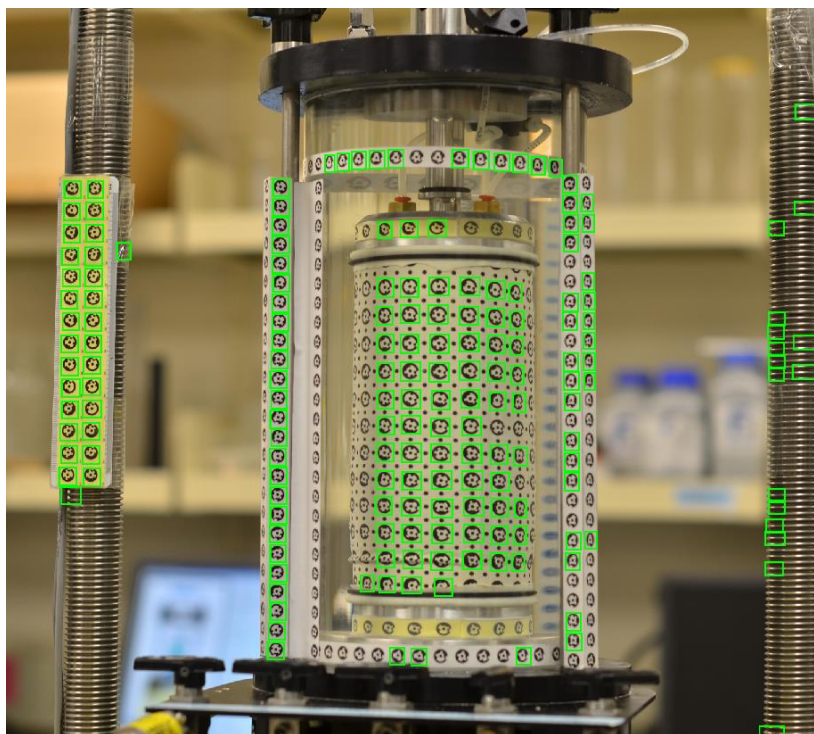


Figure 2. Coded target detection results using deep learning method.

identification results when comparing the proposed table method with a widely accepted photogrammetric software.

While the table method in Xia et al. (8) has some advantages over the other existing CT recognition and identification methods, it ignores the unique embedding feature of the CT. A Ringed Automatically Detected (RAD) coded target typically consists of a small solid dot which is embedded within a large ring with a unique shape. This is perhaps the most distinctive feature of the RAD CT and should be used to improve the efficiency and accuracy of CT recognition. In addition, the table method relies on a deep learning algorithm, faster R-CNN, to perform CT recognition, which requires time-consuming manual labeling of the groundtruth and preparation of the training data. It is not unusual to spend several days just to prepare the training data and train a deep learning model for the CT recognition. Furthermore, even though the faster-RCNN-based deep learning method seems a powerful tool for CT recognition, it only recognizes a limited number of CTs as shown in Figure 2. In Figure 2, only 161 out of 249 CTs were correctly recognized. In general, the robustness and performance of the deep learning methods for object detection are directly linked to the size of the training data. To improve the CT recognition results, more training data are needed which requires even longer time for labelling the groundtruth and preparing the training data. Moreover, the table method in Xia et al. (8) used the normalized distance to identify the wrong CT IDs which can lead to some inaccurate results due to the large perspective deformation of the objects (for example, membrane) in the image.

This paper aims to develop an improved table method with application to the 3-D measurement of soil specimens during triaxial testing. The proposed method not only retains all the merits of the table method in Xia et al. (8) but also has several improvements. These improvements include: (1) blob analysis that takes advantage of the

unique embedding feature of the CT instead of deep learning was utilized to recognize more CTs. (2) since no training data was required, the efficiency of CT recognition was greatly improved. (3) the RANSAC algorithm was used to identify the outlier CT IDs, which is more robust and accurate. (4) The number of points on the membrane is increased significantly to obtain more representative 3-D results for the soil specimen. The improved table method can improve the efficiency and accuracy of CT detection, which will further improve the photogrammetric analysis results for 3-D volume-change measurement during triaxial testing.

This paper first describes the principle of the proposed method, followed by a literature review on the CT recognition and identification methods. Then, the procedure of the proposed method was explained. After that, the design of validation experiment and experimental results are presented. Based on the analysis of the test results, some conclusions were made on the benefits of applying the improved table method to the 3-D measurement of soil specimens in real experimental conditions and other photogrammetric tasks.

2. RELATIVE WORK

In the past few decades, many CT recognition and identification methods have been developed. Apart from the abovementioned table method, other CT recognition and identification methods can be broadly divided into three categories: (1) The shape and structural descriptor methods; (2) template matching; and (3) deep convolution neural

network-based methods. Each of these methods will be discussed in the following section:

2.1. SHAPE AND STRUCTURAL DESCRIPTOR METHODS

Hattori et al. (13) developed a CT that consists of six retro-reflective circular dots, three of which define the origin and the coordinate axes, while the pattern of the rest represents the code. In this method, an image is first binarized by adaptive threshold values and then the blobs forming the code are extracted by an image dilation technique. The authors proposed that if six reflective targets merge to one segment, the group is regarded as a CT.

Ahn et al. (7) presented a circular coded target for automatic image point measurement and identification with application to optical 3-D measurement and camera calibration. We know from the given imaging conditions the approximate size of the image ellipse of the used point mark. The authors assumed that an image ellipse is the projection of an object circle onto the image plane. The authors believe that such an image ellipse is a relatively compact image feature for a natural scene, where the compactness can be represented by the form factor which is related to the perimeter and area of the ellipse. The form factor has a minimum value of 1 by a circular disc and is greater than 1 for all other geometric features. The CTs were then recognized and identified by using the criterion of form factor for the CTs.

Forbes et al. (14) used a combined features of the candidate regions to recognize CTs. These features include number of pixels, distance to image boundary, Euler number,

fit of best fit ellipse, contrast, and fit of best fit code. Rather than using the centre of the fitted ellipse as the centre of the imaged target, the intensity weighted centroid is used.

Shortis et al. (10) developed a coded target system that employs a Hough transform and segment matching to automatically recognize and identify the targets in digital images. Based on the structure of the CTs they used, they proposed that the following conditions must be satisfied to recognize a CT: (1) Each side must consist of one of the six segments. (2) Each corner must have a line touching it. (3) A coded target must be rotationally unique to all other coded targets.

Xia et al. (15) applied three restriction criteria based on length, shape, and embedding to restrict the set of candidate ellipses. Then the eligible central ellipses are extracted from input images. The corresponding encoded band patterns are obtained from the extracted ellipses, and then are used to modify the parameters of the extracted ellipses. Finally, the encoded targets are decoded through a certification and interpretation of the arrangement of the bit segments surrounding this encoded target.

Fernandez-Fernandez et al. (9) developed the shape and structural descriptor to recognize and decode CTs. The CT identification is done based on the analysis of the detected contour structures. The detected contours were analyzed to see whether they comply with the circularity factor. The minimum enclosing technique was used to distinguish those contours that are actually circles. A CT structure is formed by 3 concentric circles, so, all those circles that do not comply with this rule are discarded, and those that comply are classified as potential CT. A valid CT must follow some ratio descriptors, this is distance ratio among circles and diameter ratio of the central target. This is, this potential CT is compared to the values of the ideal CT pattern. If the ratios

are the same as in the ideal pattern, it is classified as CT and the surrounding area of interest is automatically computed. The authors reported promising CT recognition and identification results which allows the usage of the CTs within a real industrial machine.

2.2. TEMPLATE MATCHING

Van et al. (16) used the least square template matching method to search the targets. The template is a model of a reseau image. A binary image of an ideal reseau image (4 pixels wide and 100 pixels long) was generated and smoothed with a 2 x 2 averaging filter. It is shown that this procedure improves both precision and productivity of the photogrammetric process.

Barazzetti & Scaioni (17) used Least Squares Matching (LSM) to recognize targets with application to measurement of deformations in material testing. The LSM method ensures high precision measurements (up to ± 0.01 pixels) and is an optimal choice in the case of targets. However, it cannot be considered as an alternative to cross-correlation: cross-correlation provides good approximate values about target locations and LSM refines center coordinates. The authors claimed that the combined use of matching techniques is strictly mandatory in order to automate the whole analysis.

2.3. DEEP CONVOLUTIONAL NEURAL NETWORK-BASED METHODS

Shi & Zhang (18) designed and tested a set of novel Chinese character coded targets (CCTs). A Faster Region based Convolutional Neural Network (Faster R-CNN) is trained to locate and recognize the CCTs in motion blurred images. Experimental results

on both artificial and actual motion blurred images demonstrate the superiorities of the designed CCTs as well as the proposed localization and recognition pipeline.

Kniaz et al. (19) proposed a YOLO-Target Convolutional Network which was inspired by the popular deep learning object detection algorithm, YOLOv3 model. Firstly, it detects the bounding box of the coded target. Secondly, it estimates the position of the target center. The algorithm was evaluated using the generated dataset. It was reported that their model increased the target recognition mAP by 40% compared to the loading baselines.

Liu (20) proposed a target detection method based on a deep learning model to improve the target detection performance of robots in complex scenarios. In order to verify the effectiveness of the algorithm, a software system for target detection of intelligent robots was designed and implemented and excellent experimental results were reported by the authors.

Despite the availability of many CT recognition and identification methods mentioned above, as pointed out by some researchers, CT recognition and identification are still challenging since CTs were often subjected to a great perspective deformation and some incorrect CT IDs are inevitable (8, 11). Therefore, there is a clear need to develop alternative method that can be used for accurate and efficient recognition and identification of CTs with applications to coded target-based photogrammetry.

3. PROPOSED METHODOLOGY

In this study, the RANSAC algorithm was utilized to identify and reject wrong CT IDs. Figure 3 illustrates how the RANSAC algorithm identifies outlier point IDs, infers, and recovers missing points.

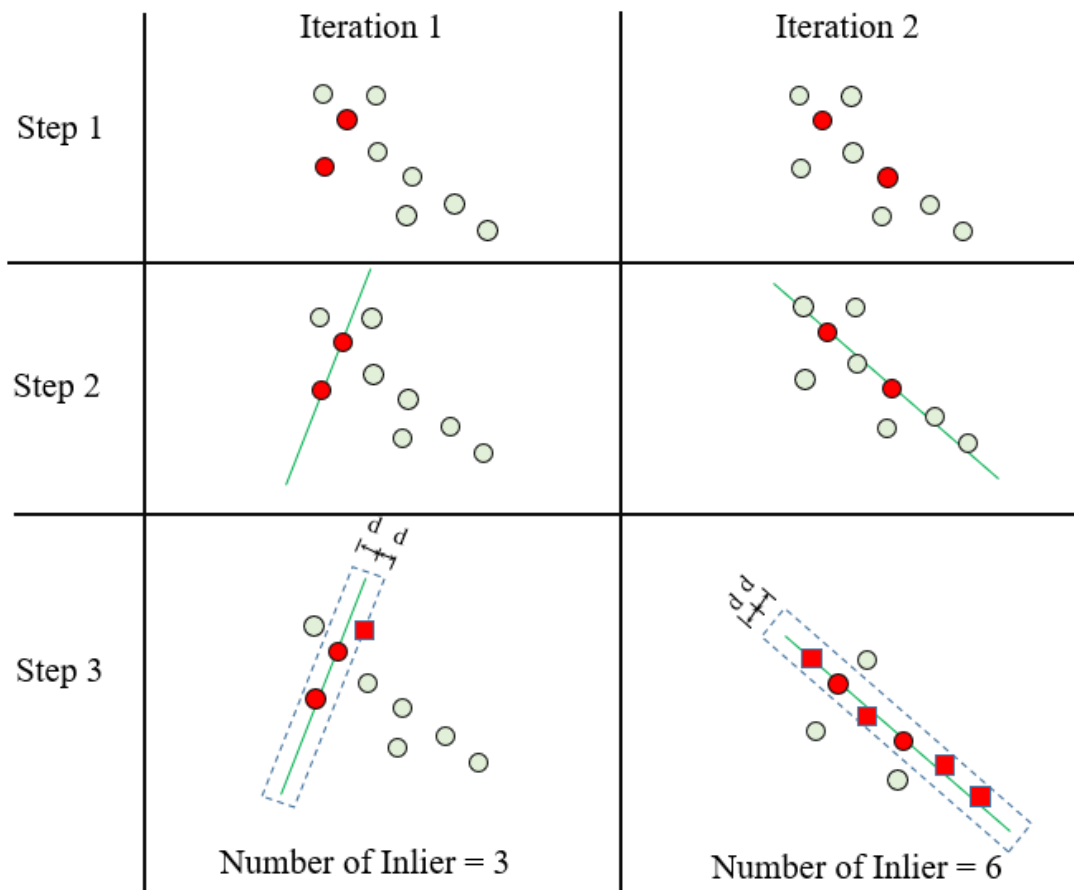


Figure 3. Schematic plot of the RANSAC algorithm. (Modified from Martinez-Camara, Marta, et al. (21))

Assume the initial ID results for a group of CTs on the membrane are obtained. As can be seen in Figure 1, all the CTs on the longitudinal CT stripes, transverse CT

stripes, and membrane are arranged roughly in different straight lines. This is very useful information regarding the geometric arrangement of the CTs that will be taken advantage of when applying the improved table method. The proposed method uses multiple iterations to identify outliers. Figure 3 shows an example of the comparison between two iterations. For the first iteration, two points (CTs) were randomly selected from all the points that have IDs on the same column or row. The model parameters for fitting a line to the two points can be estimated. Then the distances of the points to the fitted line can be calculated. The number of inliers was counted. The number of inliers for the first iteration is three. Then, the second iteration is performed by repeating the same steps as discussed previously. The number of inliers for the second iteration is 6. Then, the next iteration is executed. After a certain number of trials, the number of inliers for each iteration is evaluated. The model parameters that produce the most inliers represent the correct model. In the meanwhile, the outlier CT IDs were identified.

After the outlier CTs had been identified and rejected, the next step of the improved table method was to recover the missing CTs using the interpolation technique. The procedure in Xia et al. (8) was followed to perform the interpolation. However, different from the interpolation/extrapolation technique used in Xia et al. (8), only interpolation is performed, and the interpolation is based only on the predicted locations of nearby CTs. This can ensure more accurate interpolation results.

4. PROCEDURES OF THE PROPOSED METHOD

There are four phases in the proposed method. Phase 1 is image acquisition. Phase 2 is CT recognition. Phase 3 is CT identification and application of improved table method. Phase 4 is 3-D reconstruction application. In this paper, the detailed procedure of the proposed method was explained.

4.1. IMAGE ACQUISITION AND BLOB ANALYSIS

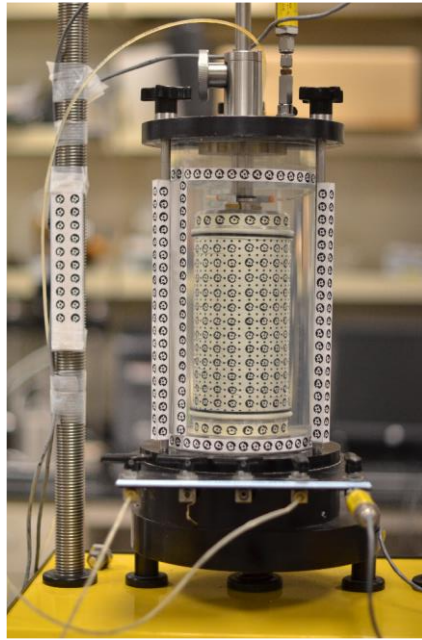
4.1.1. Experimental Setup. The experimental setup followed that used by Xia et al. (8) with some modifications and is shown in Figure 1a and Figure 1b. Three longitudinal CT stripes (with CT IDs ranging from 501 to 800) were attached to each of the three frame rods. Three longitudinal CT stripes and two (at the top and bottom) transverse circular CT stripes (with CT IDs ranging from 801 to 893) were attached to the acrylic cell. Two small annular CT stripes were attached to the top and bottom pedestals for top and bottom plane determination as proposed by Fayek et al. (5). The membrane was printed with CTs (with IDs ranging from 1 to 300, but only 52 to 255 are visible due to installation). It is noted that besides the CTs on the membrane, there are also solid dots between each two CTs. These solid dots are used to increase the number of CTs as will be explained in the Renumbering the CT IDs section.

4.1.2. Image Acquisition. Good image quality is vital to a successful photogrammetric project. Several factors influence the image quality, such as the image resolution, image capturing, shooting angles, the overlapping between images, and lighting condition, etc. In this study, a DSLR camera with an image resolution of 4928 by

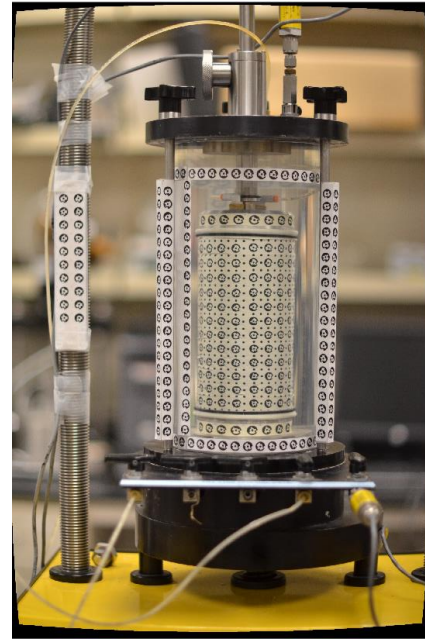
3264 was used. It is found that the image resolution is good enough since most CTs on the images can be clearly seen. Images were taken around the triaxial cell at around 16 different positions. These 16 positions were roughly in a circle. At each position, two images were captured at two different shooting angles. The abovementioned image capturing method is to ensure sufficient overlapping between images and various shooting direction, which are beneficial to 3-D reconstruction results. Each image was checked immediately after being captured to make sure every image is clear and in good quality. Normal light in the room should be sufficient to produce good images. Even though it might seem to have many requirements regarding the image acquisition, these requirements are all easy to achieve and can significantly contribute to good CT recognition, CT identification, and 3-D reconstruction results. A typical image of the triaxial system is shown in Figure 4a.

4.1.3. Image Idealization. It is important to correct the images for lens distortion (also referred to as image idealization) especially when the camera is wide angle camera and there is large images distortion. More discussion regarding image idealization can be found in Zhang et al. (2) and Xia et al. (8). Figure 4b. presents the triaxial cell image after correcting lens distortion.

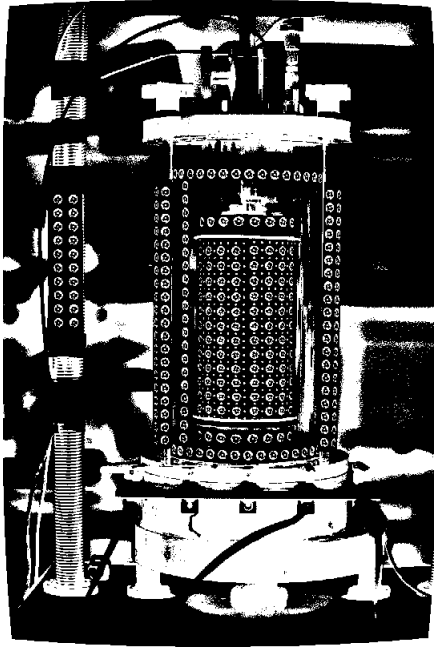
4.1.4. Image Binarization. After the image distortion was removed, image binarization was performed. Image binarization is an image processing technique that converts a grayscale image to black-and-white, which reduces the information contained within the image from 256 shades of gray to 2: black and white, a binary image. Image binarization is commonly performed in object extraction from an image. The image in Figure 4b is converted into a grayscale image. Then, a global threshold is computed from



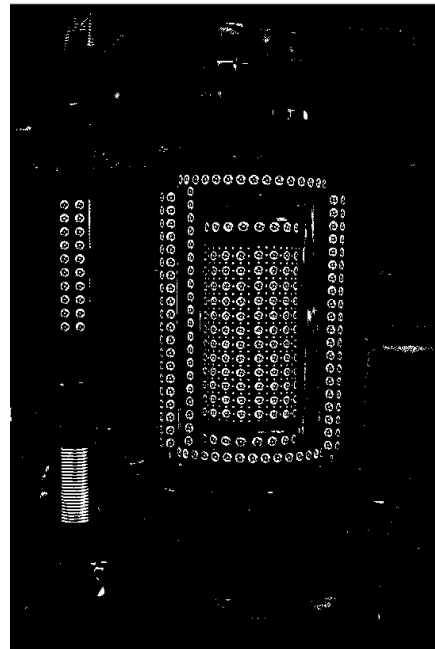
(a)



(b)

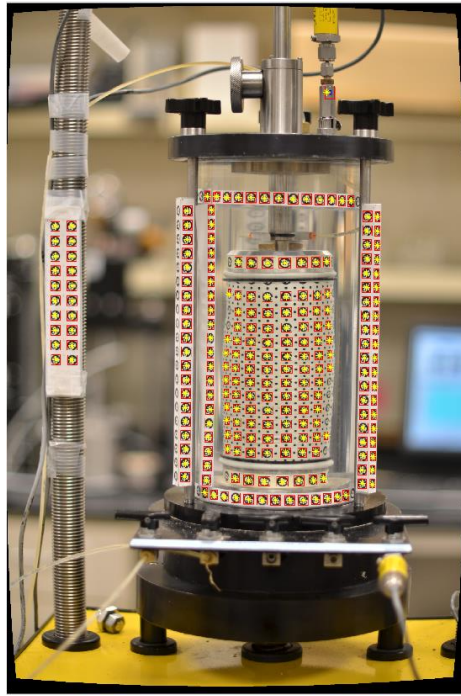


(c)

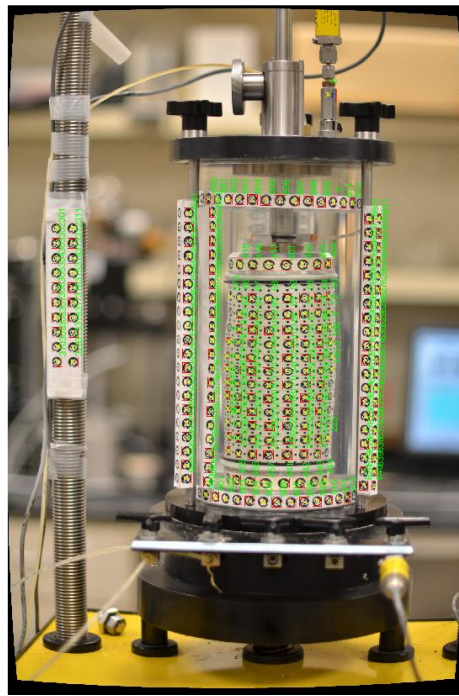


(d)

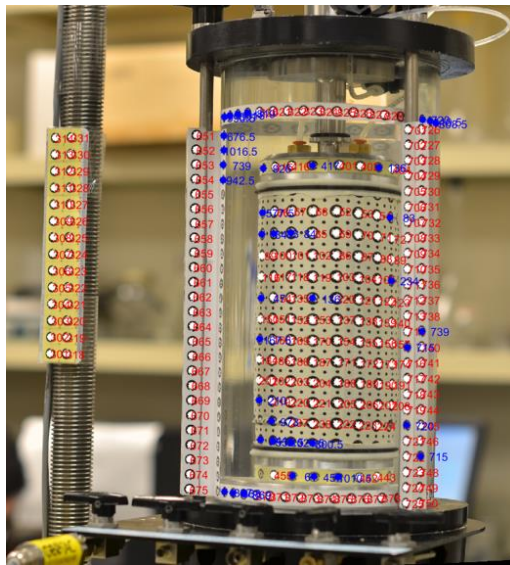
Figure 4. Procedure of the proposed method. (a) Original image; (b) undistorted image; (c) initial image binarization results; (d) refined image binarization results; (e) blob analysis-based coded target recognition results; (f) initial coded target identification results; (g) falsely identified coded targets; and (h) Final coded target identification results after applying the improved table method.



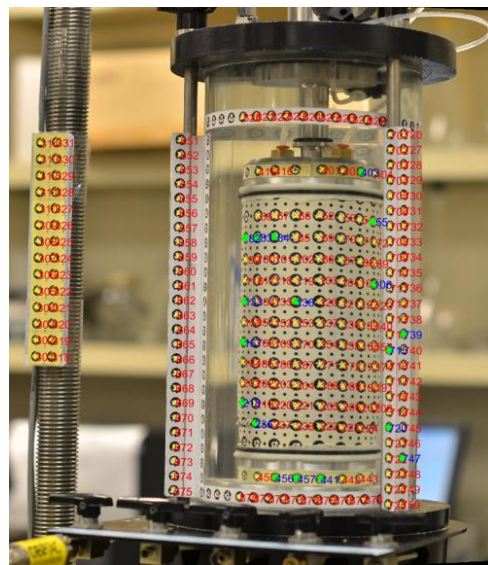
(e)



(f)



(g)



(h)

Figure 4. Procedure of the proposed method. (a) Original image; (b) undistorted image; (c) initial image binarization results; (d) refined image binarization results; (e) blob analysis-based coded target recognition results; (f) initial coded target identification results; (g) falsely identified coded targets; and (h) Final coded target identification results after applying the improved table method. (cont.)

the grayscale image using Otsu's method (22). This global threshold can be used to convert the grayscale image into a binary image. Figure 4c is the binary image of Figure 4b.

4.1.5. Blob Analysis. A blob means connected pixels in an image. Blob analysis is to calculate statistics for labeled regions in a binary image. A lot of important information can be extracted from the image, such as the quantities of the area, centroid, bounding box, label matrix, blob count of the blobs, etc. Blob analysis is an efficient tool to extract the CTs from the image. In our case, the area of the blob is an important feature. So, the area of each blob was computed.

This binary image Figure 4c is made up of thousands of blobs. As can be seen in Figure 4c, there are a lot of unwanted blobs which are not related to the CTs. Therefore, the initial screening test is performed to exclude the blobs that are either too small or too large. After the small and large blobs are removed, a cleaner binary image can be obtained as shown in Figure 4d.

In order to recognize CTs more accurately, a second screening test is required. The embedding criterion is used in the second screening test. Figure 5 illustrates the meaning of embedding criterion. The relative positions of two ellipses, e_i and e_j , can be categorized into three scenarios: (1) e_j is embedded in e_i (Figure 5a); (2) e_i is embedded in e_j (Figure 5b); and (3) neither e_i nor e_j is embedded in each other (Figure 5c). For a CT, it is very clear that there must be a small inner solid dot embedded in a larger annular dot. Therefore, the embedding criterion is chosen as the only criterion in the second screening test for CT recognition. Figures 5d and 5e show the CT recognition results using the embedding criterion. The small boxes represent the embedded inner dots and

the large boxes represent the large outer dots. Figure 4e shows the CT recognition results using blob analysis. Most CTs can be correctly recognized by using the embedding criterion. The results indicate that embedding criterion offers a robust solution to CT recognition.

4.1.6. Coded Target Identification. After the CTs have been recognized, it is important to decode each CT with its associated ID number. This process is called CT identification. A region of interest (ROI) that surrounds the CT was cropped based on the CT recognition results that obtained in the previous stage. All the operations in this phase will be performed over the CT ROI area. The detailed procedures for CT identification can be found in Xia et al. (8), while the primary steps are recalled here.

The original CT ROI image patch was first converted into a grayscale CT image. After that, a locally adaptive threshold for the grayscale CT image patch was computed based on the local mean intensity in the neighborhood of each pixel. Then, image binarization was performed by replacing all values above the locally adaptive threshold with 1s and setting all other values to 0s.

The next step is to use blob analysis to reject outlier CT blobs. Then, the CT contour was obtained by detecting the boundary points of the CT. The CT center was determined by fitting an ellipse to the outer boundary of the CT. The centroid of the ellipse that obtained from the ellipse fitting result is considered as the CT center. Typically, the circular CTs appear to be elliptical in the images under projective transformation. To obtain better decoding results, the elliptical CT contours were normalized to circular contours. A signature-based image processing technique is utilized

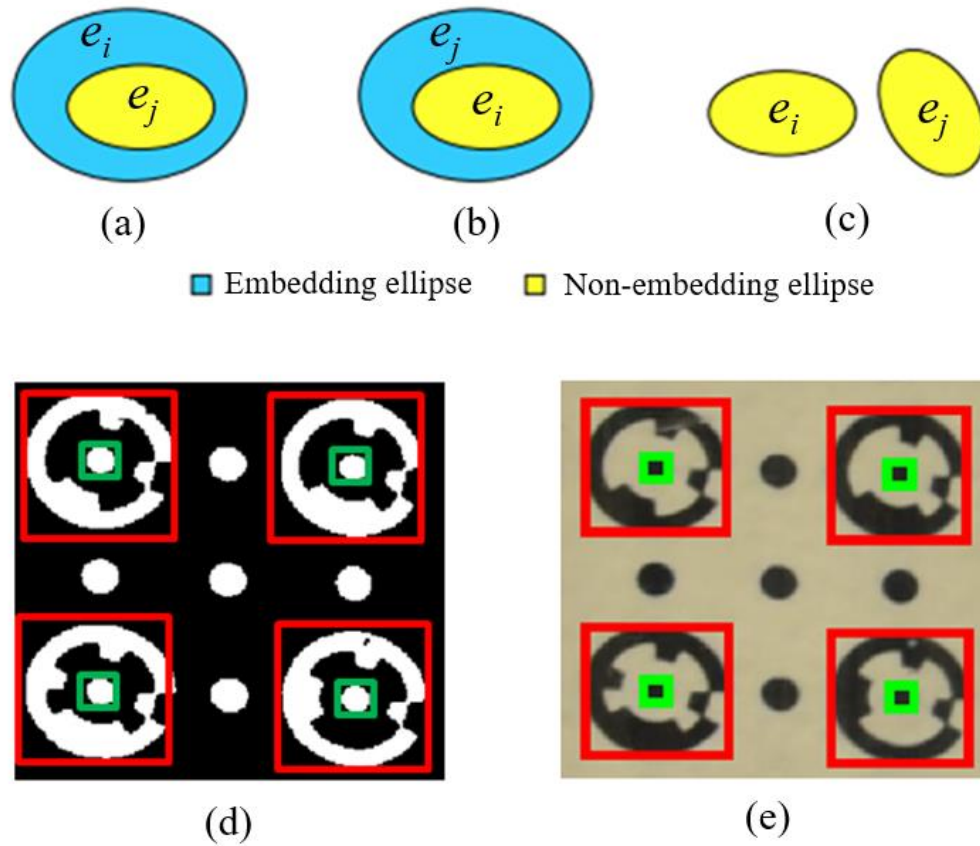


Figure 5. CT recognition using embedding criterion ((a) and (b) are modified from Xia et al. (15)).

to determine the 12-bit binary numbers for the CT. The obtained 12-bit binary numbers were then converted to a decimal number, which corresponds to the ID number of the CT. The preliminary CT ID and centroid results are presented in Figure 4f and Figure 7a.

4.2. APPLICATION OF IMPROVED TABLE METHOD

In Figure 4f, some false ID results were observed. The false CT identification results are inevitable due to several reasons, such as large projective distortion, unfavorable lighting conditions, and low-resolution, low-quality images, etc. The improved table method described in the Methodology section was applied to

automatically identify and reject the outlier CT IDs. The following steps were performed to apply the improved table method:

4.2.1. Step 1: Detect and Remove the Outlier IDs Using RANSAC Algorithm.

Figure 6a shows the preliminary ID results for the CTs on a cropped region of the membrane in a representative image. Out of the 21 CTs in total in Figure 6a, there were 20 CTs which had been correctly identified. There was one false CT ID, 53, which should be 139 based on the look-up table. The look-up table contains the information regarding the geometric arrangement of the CTs including the row number and column number of each CT and the associated IDs. Since the geometric design for the CTs is fixed, this look-up table is also fixed. From the look-up table, it is easy to obtain the row number and column number of the 21 CTs, which are shown in Figures 6b and 6c, respectively.

The next step is to select all the CTs that have the same column number and to identify any wrong IDs among these IDs. Figures 6c through 6h show an example of identifying the outlier ID using column number 2. All the CTs with column number 2 are selected first. Then, the first iteration was performed by selecting two points represented by the squares. Assume that a distance of d was used to define the inlier (Figure 6f). It is found that there are seven inliers for the first iteration. Then, the second iteration was performed by selecting two other points represented by the squares as shown in Figure 6g. The same procedure for iteration 1 was repeated for iteration 2. The number of inliers counted for iteration 2 is only 2. By performing a certain number of trials, it is found that the first iteration produces the most inliers. Therefore, the correct predicted line is shown in Figure 6f and it is easy to identify the wrong point that is not within the threshold distance d of the predicted line. The outlier CT ID is 53. This wrong ID can be easily

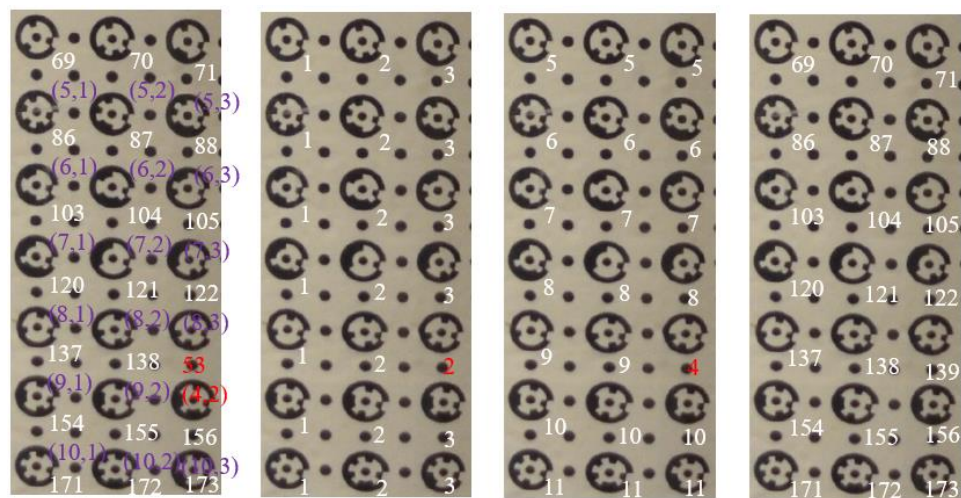
corrected as 139 by using the look-up table. The corrected ID results are shown in Figure 6d.

It is noted that only the results of a cropped region of the membrane are presented here to demonstrate the effectiveness of the proposed table method due to the limited space. The same procedure can also be applied to the longitudinal stripes and transverse stripes that are shown in Figure 1b. Figure 4g and Figure 7b show the identified outlier CT IDs. The ellipses represent falsely identified CT IDs from the preliminary CT identification results.

4.2.2. Step 2: Interpolation. This step takes advantage of both the prior knowledge of the geometric arrangement and the IDs and centroids information of the CTs that were obtained from the previous steps. As can be seen in Figure 4a, the CTs on the longitudinal stripes lie in a straight line even under projective transformation. In addition, a sufficient number of CTs had been correctly identified and their accurate centroid locations were known. This information was used in the 1-D linear interpolation to obtain accurate interpolation results. The same 1-D linear interpolation technique was also applied to the transverse annular stripes. The membrane was a more complicated case since there was a deformation of the soil specimen. To address this problem, 2-D interpolation was performed on the membrane CTs based on the known IDs and centroids of the CTs that had been correctly identified in the previous step.

4.2.3. Step 3: Assign Correct IDs to the Missing CTs. Since the IDs of the missing CTs can be accurately determined by interpolation, these IDs were assigned to the missing CTs directly without any computation for CT IDs. This CT assigning process not only saves computational cost but also ensures the high-accuracy IDs results. The CT

IDs results after assigning correct IDs to the missing CTs are shown in Figure 4h and Figure 7c.

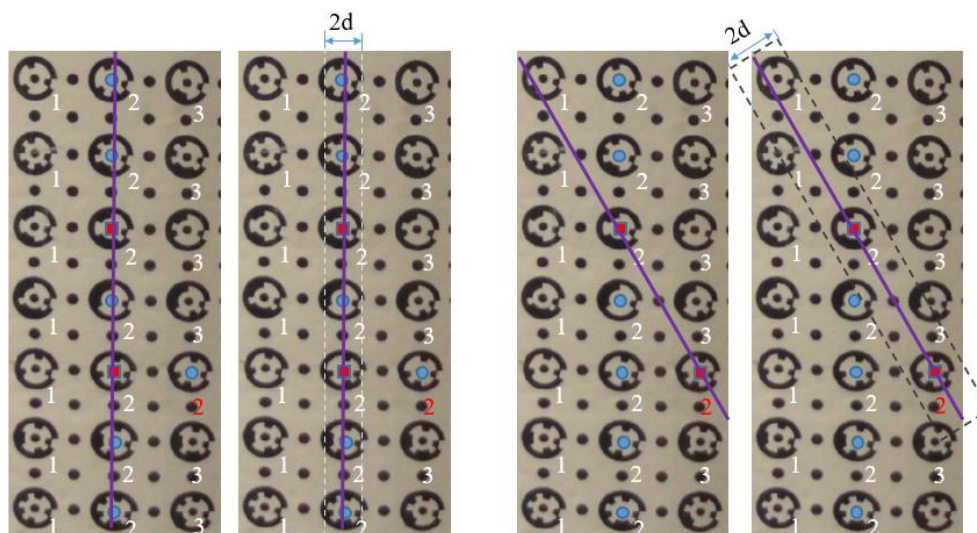


(a)

(b)

(c)

(d)



Number of inliers = 7

Number of inliers = 2

(e)

(f)

(g)

(h)

Figure 6. Identifying wrong CT IDs.

4.2.4. Step 4: Search for the CTs Near the Predicted Locations for Missing CTs.

CTs. Based on the estimated centroid locations of the missing CTs that obtained from previous steps, it is easy to search for the CTs near the predicted locations for missing CTs.

4.2.5. Step 5: Determine the Accurate Centroid of the Missing CTs.

It is noted that the interpolation process in step 2 can only obtain estimated centroid locations of the CTs. In this step, the accurate centroid location of the missing CTs can be obtained using the same techniques for determining the centroid locations of CTs. In Figure 4h, the missing CTs had been successfully recovered with both accurate CT IDs and centroid locations. The effectiveness of the proposed table method has been demonstrated particularly at recovering missing CTs on the membrane.

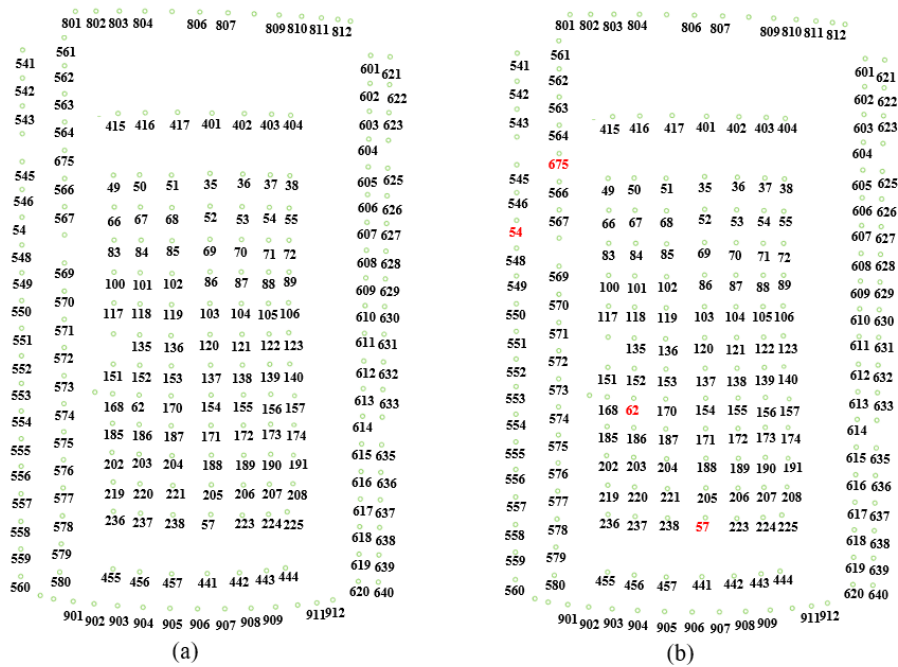


Figure 7. ID results before and after applying the improved table method. (a) Initial CT IDs on the triaxial test image; (b) Identified incorrect CT IDs; (c) Correct IDs results after interpolation

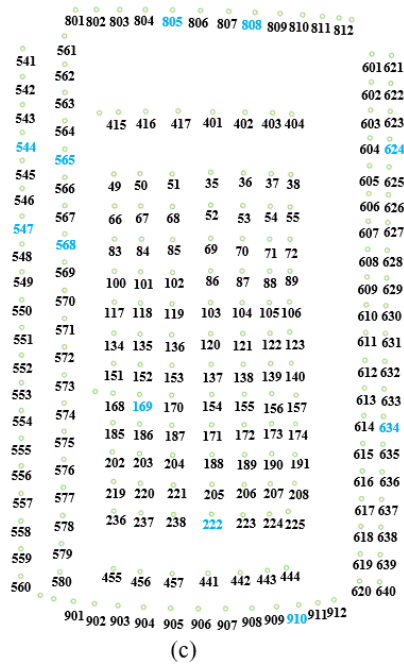


Figure 7. ID results before and after applying the improved table method. (a) Initial CT IDs on the triaxial test image; (b) Identified incorrect CT IDs; (c) Correct IDs results after interpolation. (cont.)

4.3. RENUMBERING THE CT IDS

Another improvement in the improved table method is the increased number of CTs achieved by simply renumbering of the CT IDs. The process of renumbering CT IDs is shown in Figure 8. Figure 8a shows the original IDs arrangement for the CTs on the membrane. There are 272 CTs in total ranging from 1 to 272. Figure 8b shows the new IDs of these 272 CTs. Each CT ID in the first table is converted into a new ID using the following equation:

$$ID_{new} = 4N(row - 1) + 2col \quad (2)$$

where ID_{new} is the new ID number for the CT; N is the number of columns in the table, $N = 17$ in the case of Figure 8; row is the row number of the CT; and col is the column number of the CT. The CT IDs are then rearranged to leave some space for the dots as

will be explained later. The renumbered CT IDs are shown in Figure 8c. The blank boxes in the third table are filled with other IDs for the solid dots on the membrane in Figure 4a. The ID numbers for these solid dots are also computed using Equation 2. The IDs for both the CTs and solid dots are shown in Figure 8d. Obviously, these IDs for the solid dots are not determined by any complicated decoding process but are computed using a very simple equation which can save a lot of computational efforts.

In addition, these solid dots with unique ID numbers can achieve the same purpose of CTs. There are 1088 ID numbers in total. Therefore, this simple renumbering process can increase the number of points (CTs and solid dots) by three times. Figure 9 shows an example of increasing the number of points on the membrane. A typical triaxial cell image is shown in Figure 9a. Figure 9b presents the enlargement of a small portion of the membrane. There are 12 CTs in Figure 9b. After renumbering the CT IDs and performing interpolation, the number of points increases to 48 as shown in Figure 9c. Since there are more CTs on the membrane, more representative 3-D point data for the soil specimen can be expected, which will potentially improve the accuracy of determining the volume and deformations of the soil specimens.

4.4. 3-D RECONSTRUCTION OF SOIL SPECIMEN

To further demonstrate the effectiveness of the proposed method, the CT recognition and identification results obtained by the proposed method had been implemented into the 3-D reconstruction of soil specimen during triaxial testing. The 3-D model of the triaxial cell as well as the soil specimen can be obtained using the method described in Xia et al. (23) and Zhang et al. (2). The meshes for the 3-D model of the soil

specimen can be generated. This mesh can be used to calculate the volume of the specimen. Detailed procedures for calculating the volume based on the generated mesh can be found in Fayek et al. (5). Therefore, the volume-change of the specimen can be obtained.

Original	1	2	3	4	...	14	15	16	17
1	1	2	3	4		14	15	16	17
2	18	19	20	21		31	32	33	34
3	35	36	37	38		48	49	50	51
4	52	53	54	55		65	66	67	68
5	69	70	71	72		82	83	84	85
6	86	87	88	89		99	100	101	102
7	103	104	105	106		116	117	118	119
8	120	121	122	123	...	133	134	135	136
9	137	138	139	140		150	151	152	153
10	154	155	156	157		167	168	169	170
11	171	172	173	174		184	185	186	187
12	188	189	190	191		201	202	203	204
13	205	206	207	208		218	219	220	221
14	222	223	224	225		235	236	237	238
15	239	240	241	242		252	253	254	255
16	256	257	258	259		269	270	271	272

(a)

New	1	2	3	4	...	14	15	16	17
1	2	4	6	8		28	30	32	34
2	70	72	74	76		96	98	100	102
3	138	140	142	144		164	166	168	170
4	206	208	210	212		232	234	236	238
5	274	276	278	280		300	302	304	306
6	342	344	346	348		368	370	372	374
7	410	412	414	416		436	438	440	442
8	478	480	482	484	...	504	506	508	510
9	546	548	550	552		572	574	576	578
10	614	616	618	620		640	642	644	646
11	682	684	686	688		708	710	712	714
12	750	752	754	756		776	778	780	782
13	818	820	822	824		844	846	848	850
14	886	888	890	892		912	914	916	918
15	954	956	958	960		980	982	984	986
16	1022	1024	1026	1028		1048	1050	1052	1054

(b)

Figure 8. Renumbering the CT IDs on the membrane.

Original								
1		1		2		3		4
2								
3		18		19		20		21
4								
5		35		36		37		38
6								
7		52		53		54		55
8								
9		69		70		71		72

⋮

24		188		189		190		191
25								
26		205		206		207		208
27								
28		222		223		224		225
29								
30		239		240		241		242
31								
32		256		257		258		259

⋮

14		15		16		17		
31		32		33		34		
48		49		50		51		
65		66		67		68		
82		83		84		85		

⋮

201		202		203		204		
218		219		220		221		
235		236		237		238		
252		253		254		255		
269		270		271		272		

(c)

New								
1	1	2	3	4	5	6	7	8
2	35	36	37	38	39	40	41	42
3	69	70	71	72	73	74	75	76
4	103	104	105	106	107	108	109	110
5	137	138	139	140	141	142	143	144
6	171	172	173	174	175	176	177	178
7	205	206	207	208	209	210	211	212
8	239	240	241	242	243	244	245	246
9	273	274	275	276	277	278	279	280

⋮

24	783	784	785	786	787	788	789	790
25	817	818	819	820	821	822	823	824
26	851	852	853	854	855	856	857	858
27	885	886	887	888	889	890	891	892
28	919	920	921	922	923	924	925	926
29	953	954	955	956	957	958	959	960
30	987	988	989	990	991	992	993	994
31	1021	1022	1023	1024	1025	1026	1027	1028
32	1055	1056	1057	1058	1059	1060	1061	1062

⋮

28	29	30	31	32	33	34		
62	63	64	65	66	67	68		
96	97	98	99	100	101	102		
130	131	132	133	134	135	136		
164	165	166	167	168	169	170		
198	199	200	201	202	203	204		
232	233	234	235	236	237	238		
266	267	268	269	270	271	272		
300	301	302	303	304	305	306		

⋮

810	811	812	813	814	815	816		
844	845	846	847	848	849	850		
878	879	880	881	882	883	884		
912	913	914	915	916	917	918		
946	947	948	949	950	951	952		
980	981	982	983	984	985	986		
1014	1015	1016	1017	1018	1019	1020		
1048	1049	1050	1051	1052	1053	1054		
1082	1083	1084	1085	1086	1087	1088		

(d)

Figure 8. Renumbering the CT IDs on the membrane. (cont.)

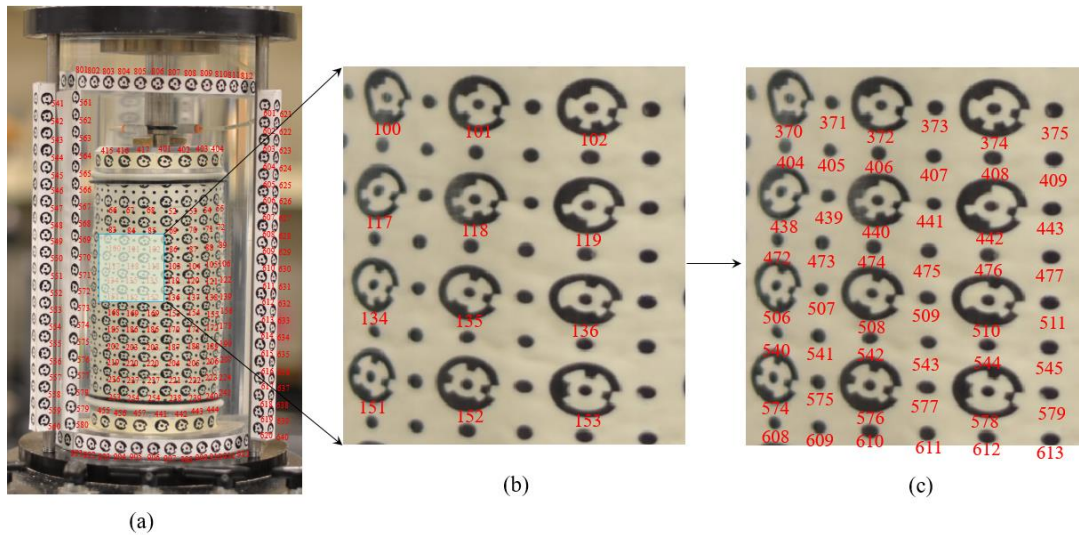


Figure 9. Interpolation of solid dots on the membrane. (a) Original CT IDs on the triaxial image; (b) the enlargement of a portion of the membrane CT IDs; and (c) The membrane CT IDs after interpolation.

5. EXPERIMENTAL VALIDATION OF THE PROPOSED METHOD

In this section, the effectiveness of the proposed method was demonstrated by implementing it into the 3-D reconstruction of soil specimen during triaxial testing. A total of around 35 triaxial test images were used for the validation test. All the images were captured using the Nikon D7000 camera. To ensure a wide range of adaptability of the proposed method, all the images were taken under normal lighting conditions and real triaxial test environment. The improved table method for decoding CTs has been implemented into the 3-D reconstruction of a sand specimen in the triaxial cell. A structure from motion photogrammetric method introduced in Xia et al. (23) was adopted to obtain the 3-D model of the acrylic cell in the air. Then, the ray tracing technique introduced in Zhang et al. (2) was utilized to obtain the 3-D model of the soil specimen

under refraction condition. The CT recognition and identification results obtained by the proposed method served as the input to 3-D reconstruction of the soil specimen.

Figure 10 shows the 3-D models of the acrylic cell, camera positions and soil specimen. In Figure 10 b, the dense 3-D point cloud on the membrane was obtained. About three times more 3-D points were obtained on the membrane for the soil specimen compared with the 3-D results on the membrane in Zhang et al. (2). This improvement is achieved by an interpolation and ID renumbering technique as introduced in the previous section. The meshes for the 3-D model of the soil specimen can be generated. Figure 10 c shows the 3-D meshes generated from Figure 10 b. These meshes can be used to calculate the volume of the specimen. The method proposed by Fayek et al. (5) was applied to determine the absolute volume of the soil specimen with consideration of the top and bottom soil specimen ends. The 3-D models of the acrylic cell, camera positions, and the soil specimen in Figure 10 indicate that the proposed method is effective and accurate in terms of CT recognition and identification.

6. CONCLUSIONS

An improved table method for coded target identification with applications to the 3-D reconstruction of soil samples during triaxial testing was proposed. In this method, CT recognition was performed first using blob analysis. The triaxial cell images were taken with a commercially available digital camera. The CT recognition and identification results have been implemented into 3-D reconstruction of the acrylic cell

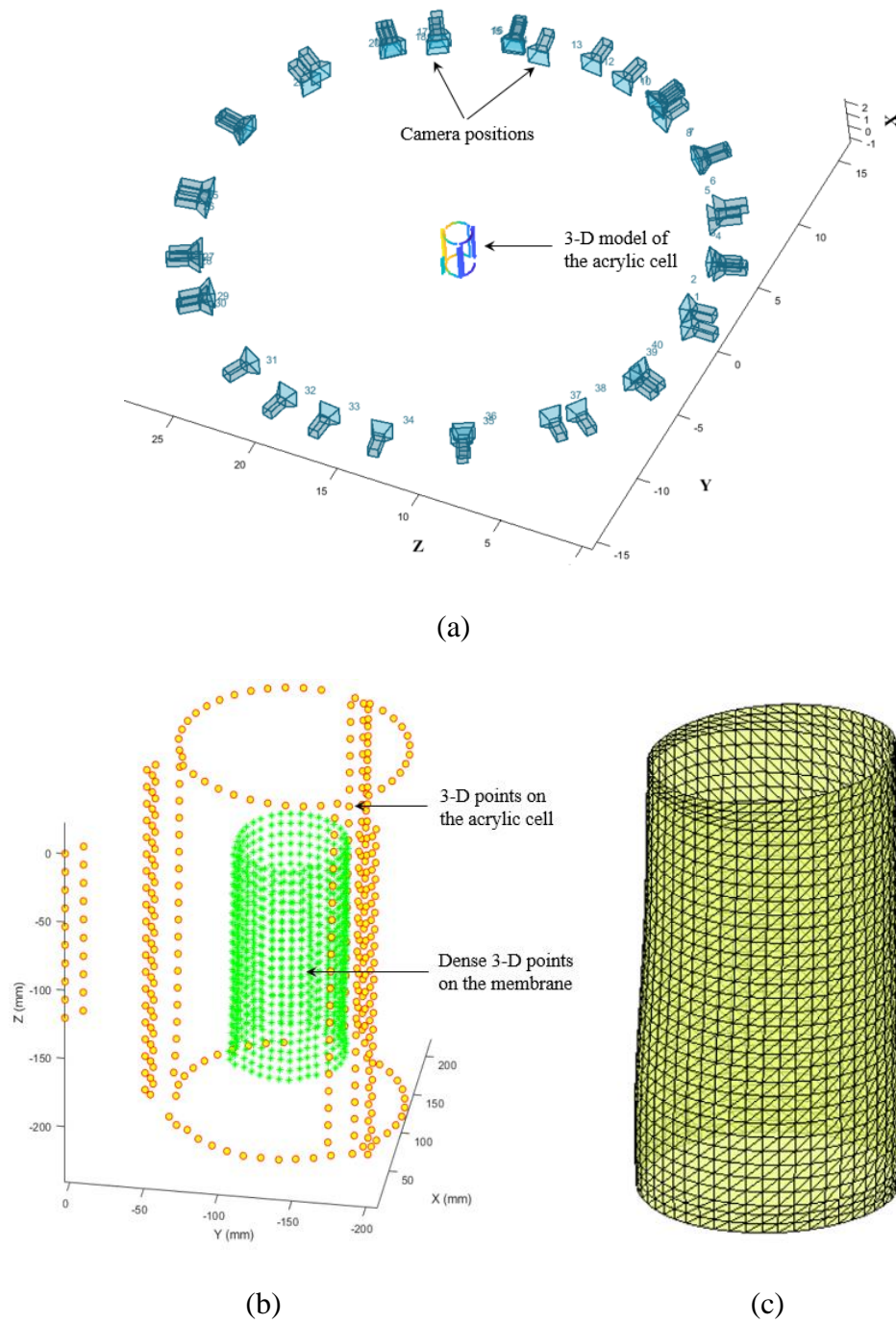


Figure 10. 3-D results using the input obtained from the proposed method. (a) 3-D model of the acrylic cell and camera positions; (b) Dense 3-D points on the membrane; and (c) Generated 3-D meshes.

and points on the soil specimens. It is found that there are several improvements in the improved table method. The embedding criterion and blob analysis are used to improve the CT detection accuracy and efficiency; The RANSAC algorithm was utilized to improve the results for identifying wrong CT IDs; The interpolation results are improved by using the predicted locations of nearby CTs; The number of points on the membrane is increased by three times and more representative 3-D results for the soil specimen can be obtained.

REFERENCES

1. Jiang, R., Jáuregui, D. V., & White, K. R. (2008). Close-range photogrammetry applications in bridge measurement: Literature review. *Measurement*, 41(8), 823-834.
2. Zhang, X., Li, L., Chen, G., & Lytton, R. A photogrammetry-based method to measure total and local volume changes of unsaturated soils during triaxial testing. *Acta Geotechnica*, 2015.10(1), 55-82.
3. Salazar, S. E., Barnes, A., & Coffman, R. A. Development of an Internal Camera-Based Volume Determination System for Triaxial Testing. *Geotechnical Testing Journal*, 2015.38(4), 549-555.
4. Li, L., & Zhang, X. A new approach to measure soil shrinkage curve. *Geotechnical Testing Journal*, 2018. 42(1), 1-18.
5. Fayek, S., Xia, X., Li, L., & Zhang, X. Photogrammetry-Based Method to Determine the Absolute Volume of Soil Specimen during Triaxial Testing. *Transportation Research Record*, 2020. 0361198120928339.
6. Nishimura, S. (2022). Characterisation of soil deformation over wide strain ranges in triaxial test with high-precision stereophotogrammetry. *Géotechnique*, 1-16.
7. Ahn, S. J., Rauh, W., & Kim, S. I. Circular coded target for automation of optical 3D-measurement and camera calibration. *International Journal of Pattern Recognition and Artificial Intelligence*, 2001. 15(06), 905-919.

8. Xia, X., Zhang, X., Fayek, S., & Yin, Z. (2021). A table method for coded target decoding with application to 3-D reconstruction of soil specimens during triaxial testing. *Acta Geotechnica*, 16(12), 3779-3791.
9. Fernandez-Fernandez, M., Alonso-Montes, C., Bertelsen, A., & Mendikute, A. Industrial Non-intrusive Coded-Target Identification and Decoding Application. In *Iberian Conference on Pattern Recognition and Image Analysis*, 2013. (pp. 790-797). Springer, Berlin, Heidelberg.
10. Shortis, M. R., Seager, J. W., Robson, S., & Harvey, E. S. Automatic recognition of coded targets based on a Hough transform and segment matching. In *Videometrics VII* (Vol. 5013, pp. 202-208). International Society for Optics and Photonics, 2003.
11. Bernat, K., & Tokarczyk, R. Automation of measurements of selected targets of photopoints in application to photogrammetric reconstruction of road accidents. *Geomatics and Environmental Engineering*, 2013. 7.
12. Cheng, J., Leng, C., Wu, J., Cui, H., & Lu, H. Fast and accurate image matching with cascade hashing for 3d reconstruction. In *Proceedings of the IEEE Conference on Computer Vision and Pattern Recognition*, 2014. (pp. 1-8).
13. Hattori, S., Akimoto, K., Fraser, C., Ono, T., & Imoto, H. Design of coded targets and automated measurement procedures in industrial vision metrology. *International Archives of Photogrammetry and Remote Sensing*, 2000. 33(5), 72-78.
14. Forbes, K., Voigt, A., & Bodika, N. An inexpensive, automatic and accurate camera calibration method. In *Proceedings of the Thirteenth Annual South African Workshop on Pattern Recognition*, 2002. (pp. 1-6).
15. Xia, R., ZHAO, J., Liu, W., Wu, J. H., Fu, S. P., Jiang, J., & LI, J. A robust recognition algorithm for encoded targets in close-range photogrammetry. *Journal of information science and engineering*, 2012. 28, 407-418.
16. Van Den Heuvel, F. A., Kroon, R. J. G. A., & Le Poole, R. S. Digital close-range photogrammetry using artificial targets. *International Archives of Photogrammetry and Remote Sensing*, 1993. 29, 222-222.
17. Barazzetti, L., & Scaioni, M. Development and implementation of image-based algorithms for measurement of deformations in material testing. *Sensors*, 2010. 10(8), 7469-7495.
18. Shi, Y., & Zhang, L. Design of Chinese Character Coded Targets for Feature Point Recognition under Motion-blur Effect. *IEEE Access*, 2020.

19. Kniaz, V. V., Grodzitskiy, L., & Knyaz, V. A. (2021). DEEP LEARNING FOR CODED TARGET DETECTION. *International Archives of the Photogrammetry, Remote Sensing & Spatial Information Sciences*.
20. Liu, L. (2022). A Deep Neural Network-Based Target Recognition Algorithm for Robot Scenes. *Scientific Programming*, 2022.
21. Martinez-Camara, M., Béjar Haro, B., Stohl, A., & Vetterli, M. (2014). A robust method for inverse transport modeling of atmospheric emissions using blind outlier detection. *Geoscientific Model Development*, 7(5), 2303-2311.
22. Otsu, N. (1979). A threshold selection method from gray-level histograms. *IEEE transactions on systems, man, and cybernetics*, 9(1), 62-66.
23. Xia X, Zhang X, Fayek S. (2022) “A Structure from Motion Photogrammetric Method to Measure the Volume-Changes of Unsaturated Soils during Triaxial Testing.” In preparation.

III. A STRUCTURE FROM MOTION PHOTOGRAMMETRIC METHOD FOR RECONSTRUCTING THE 3-D MODELS OF SOILS DURING TRIAXIAL TESTING

Xiaolong Xia¹, and Xiong Zhang²

¹Ph.D. student, Department of Civil, Architectural, and Environmental Engineering, Missouri University of Science and Technology, Rolla, MO 65409. Email: xxrkq@umsystem.edu

¹ (Corresponding Author) Professor, Department of Civil, Architectural, and Environmental Engineering, Missouri University of Science and Technology, Rolla, MO 65409. Email: zhangxi@umsystem.edu

ABSTRACT

Existing methods for measuring volume changes of unsaturated soil specimens during triaxial tests have several limitations. Recently a photogrammetry-based method has been proposed to overcome these limitations. Although this method has many advantages over existing methods, such as low cost, high accuracy, no requirements for camera positions, etc, it relies on a photogrammetric software PhotoModeler to detect coded targets which involves tedious and time-consuming manual corrections of coded target IDs and thus is not efficient to use. The objective of this study is to make the abovementioned photogrammetry-based method simpler, faster and more automatic to use. To this end, a table method has been adopted for the automatic decoding of coded targets. Based on the coded target detection results, a structure from motion 3-D reconstruction approach also has been proposed to reconstruct the 3-D models of the cylindrical soils specimen. Validation tests have been performed to validate the proposed approach.

1. INTRODUCTION

Measuring the deformation properties of soils is essential in understanding deformation and strength characteristics of soils. Conventional laboratory tests, such as triaxial tests, rely on local displacement sensors, such as linear variable differential transformer (LVDT), to measure axial and radial deformations/strains of the specimens during the tests. The triaxial cell and soil specimen usually become crowded with transducers. Generally, only a few measurements at a few locations can be made due to the limited space inside the cell.

During the past three decades, many research efforts have been made to develop alternative methods for measuring global and local deformational properties of both saturated and unsaturated soils during triaxial testing. The review of these methods is described in many literature (Zhang et al., 2015, Zhang et al., 2019, and Nishimura, 2022), and a short summary is presented below.

The double cell system (Bishop and Donald, 1961), also known as suction-controlled triaxial apparatus, is a widely accepted method for measuring the volume-changes of unsaturated soils. However, this method suffers several limitations, such as high-cost, only total volume-change measurement, and water absorption effect. Romero et al. (1997) used laser scanner to measure the deformations of the soils. It is non-contact and localized deformations can be made. However, the high-cost setup and sophisticated installation procedures limited the application of this method. Macari et al. (1997) proposed an alternative method which uses digital image analysis (DIA) with refraction correction to measure the localized deformations of the specimen. The measurement

accuracy is 0.2-0.3 mm, and it is low cost. However, this method requires accurate control of camera position, and several assumptions need to be made. For example, this method assumes that the camera shooting direction is exactly perpendicular to the specimen which is impossible to satisfy in actual practice. White et al. (2003) proposed a digital image correlation (DIC) method to measure the volume-changes of soils. The DIC method has gained a lot of interest and popularity in soil deformation measurements (Liu & Iskander, 2004; DeJong et al., 2006, Take., 2015). However, this method cannot be used in triaxial tests since it cannot consider the influence of refraction.

In most recent years, Zhang and co-workers (Zhang et al., 2015; Li et al., 2015; Li & Zhang., 2019; Fayek et al., 2020) have developed a photogrammetry-based method for measuring the volume-changes of unsaturated soils for triaxial tests. In this method, the refraction has been properly handled and corrected by using mathematically rigorous equations. The point accuracy in the air and volume measurement accuracy have been reported to be less than 0.076 mm and better than 0.25%, respectively. In this method, only one commercially available digital camera is needed to take images around the triaxial test apparatus from any arbitrary locations and orientations. While this method has significant merits in laboratory soil testing over existing methods, it is computationally intensive (Zhang et al., 2015). Furthermore, this method relies on a photogrammetric software to perform the coded target detection and photogrammetric analysis in the air. The limitations of using photogrammetric software to perform coded target include unsatisfactory coded target identification results and tedious and prone-to-error manual corrections, which has limited the application of this method. Therefore,

there is a clear need to develop an efficient and user-friendly photogrammetric method which is faster, highly automatic, and computationally efficient.

On the other hand, the advances in computer vision have offered great potential in the photogrammetric techniques. Recent developments in the computer vision algorithms have made it possible to reconstruct the three-dimensional models of a soil specimen using two dimensional images with a technique called Structure from Motion (SfM). This technique uses collections of 2-D images taken from a moving camera to reconstruct the 3-D model of the object. Contrary to conventional image-based methods, SfM technique is independent from the camera position and image perspective angles. In addition, the Computer Vision Toolbox and image Processing Toolbox were provided by several programming languages for researchers and program developers. From this point of view, SfM technique offers significant potential for developing a highly automatic and efficient method for non-contact volume-changes measurement of soil specimens.

In this paper, a customized SfM photogrammetric method has been developed for reconstructing the 3-D models and measuring the volume-changes of soils specimens in triaxial test. The difference between the proposed SfM photogrammetric method and conventional SfM will be elaborated. The technique allows researchers to rapidly create a three-dimensional model of the object, such as a soil specimen, without using expensive and complicated test equipment and software while maintaining the advantages of the current methods. The objective of this paper is to introduce and demonstrate the values of such merits of the proposed method for geotechnical research and practice.

2. METHOD

The proposed method is based upon conventional SfM. Therefore, the workflow of SfM is introduced first in this section. Then, the difference between the proposed customized SfM photogrammetric method and conventional SfM is described, and some merits of the proposed method are demonstrated.

2.1. STRUCTURE FROM MOTION WORKFLOW

2.1.1. Image Acquisition and Feature Point Extraction. Figure 1 illustrates the SfM process. The central issue that SfM addresses is determining the 3-D locations of the matching features identified in multiple images, captured from different locations and orientations. Matching features are the homologous feature points in multiple images. Therefore, the features in the individual image need to be extracted first. There are many algorithms available for feature extraction, such as SIFT, SURF, KAZE, and MSER. These algorithms use local features to deal with problems associated with scale changes, rotation, and occlusion. For example, SIFT detects features in each image that are invariant to all scales and locations (Lowe, 2004).

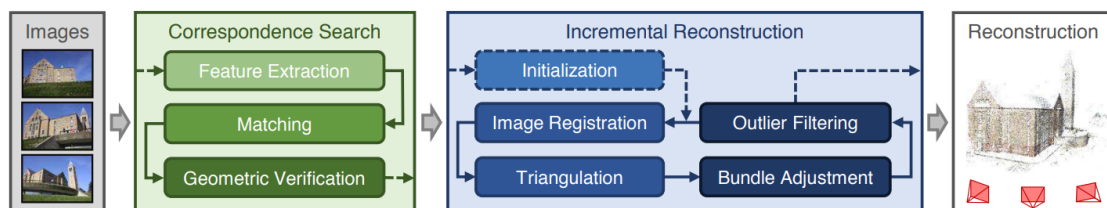


Figure 1. Structure from Motion pipeline (modified from Schonberger and Frahm (2016))

The SfM often requires sufficient image texture on the surface of the objects to be measured. This is because the number of matching features largely depend on the image texture and resolution. The range of natural textures, sharpness, and resolution of the image play a significant role in the quality of 3-D reconstruction results. It is important to ensure a wide range of natural scene texture, high sharpness, and good resolution of the image to produce more good quality matching features. Reducing the distance between the camera and the feature points on the object can increase the spatial resolution of the image and improve the density of the 3-D point cloud. After the features in the images are detected and extracted, feature matching algorithms are used to match the features between images.

A variety of image sensors can be utilized for SfM, such as inexpensive compact digital cameras, security cameras, and digital SLR cameras. Digital SLR cameras often achieve better reconstruction results due to their high image resolution. However, they are usually more expensive and require longer image processing time. It is difficult to determine the minimum number of images required for a successful 3-D scene reconstruction. However, each matching feature should be visible in at least three images. If possible, more images are recommended to ensure good overlap and redundancy which are beneficial to the 3-D construction results.

2.1.2. 3-D Point Cloud Generation. The matching features in a set of images are linked by point tracks. A point track is an object that stores the matching feature points from multiple views. These point tracks are used for 3-D point cloud generation. Before the 3-D point cloud can be generated, the camera poses need to be solved. Incremental SfM often initializes a “seed reconstruction” by selecting and processing two images.

Following that, more and more images can be added. For each added image, for following steps are performed: 1) the relative pose of the current view, which is the camera orientation and location relative to the previous view, is estimated; 2) the relative pose of the current view is transformed into the coordinate system of the first view of the sequence; 3) the camera pose and the image points of the current image are stored; 4) the outlier matches are removed; 5) the inlier matches between the previous and the current view are stored; 6) point tracks across all the views processed so far are established; 7) the initial 3-D points corresponding to the point tracks are computed by triangulation; 8) the camera poses and the 3-D points are refined by bundle adjustment function, and 9) the refined camera poses and 3-D points are updated and stored. The above steps produce a sparse point cloud. A dense point cloud can be further derived by detecting a dense set of matching features and tracking them across all views.

2.2. DIFFERENCES BETWEEN THE PROPOSED METHOD AND SfM

One noticeable advantage of the SfM method is its full automation, from feature point extraction to 3-D point cloud generation. However, one challenge of SfM is the mismatches of feature points which can cause inaccurate 3-D scene results or even failure in 3-D reconstruction. In this study, a hybrid approach is adopted and a customized SfM method has been developed by integrating the target-based point correspondence in conventional photogrammetry and the 3-D point cloud generation in SfM. This hybrid approach takes full advantage of the merits of both of the two methods while overcoming the limitations of each method. The differences between the proposed method and conventional SfM are listed in Table 1 and more details are discussed here.

Table 1. Comparison between conventional SfM and the proposed method.

	SfM	The proposed method	Improvements
Correspondence search	Feature extraction	CT recognition and identification	More accurate and robust, less computation
Camera pose estimation	The relative camera pose is computed	Absolute camera pose is computed using MSAC algorithm	More accurate camera pose estimation
Outlier removal in 3-D reconstruction stage	None	Robust outlier removal	More robustness

2.2.1. Feature Points vs. Coded Targets. One of the primary tasks in SfM is to find the point correspondences (also referred to as feature matches) in multiple images. However, bad feature matches are very common and can cause misregistration and failure in 3-D reconstruction. On the other hand, there are usually thousands of feature points on each image. The large number of feature points cause the feature matching process very slow especially when many images are processed. It is not uncommon to take several hours for a SfM software to complete the feature matching and 3-D reconstruction. To address the abovementioned limitations, coded targets are used to facilitate the accurate and rapid point correspondences search process. The difference in point correspondences between the proposed method and SfM are shown in Figure 2. A coded target is a high contrast dot with a pattern around it that is placed on the surface of an object to be measured. Each coded target has a unique associated ID number. These ID numbers can be automatically obtained by the coded target identification computer program. The computed ID numbers of coded targets are shown in Figure 2b. Since each coded target is identified with a unique ID number, the point matching process is

extremely simple and fast, and the chance of making mistakes is significantly reduced. In Xia et al. (2021), a table method was developed for automatically identifying the coded targets and a 100% detection rate can be achieved. Therefore, by using coded targets instead of natural random feature points in the images, the accuracy and efficiency of finding point correspondences can be greatly improved.

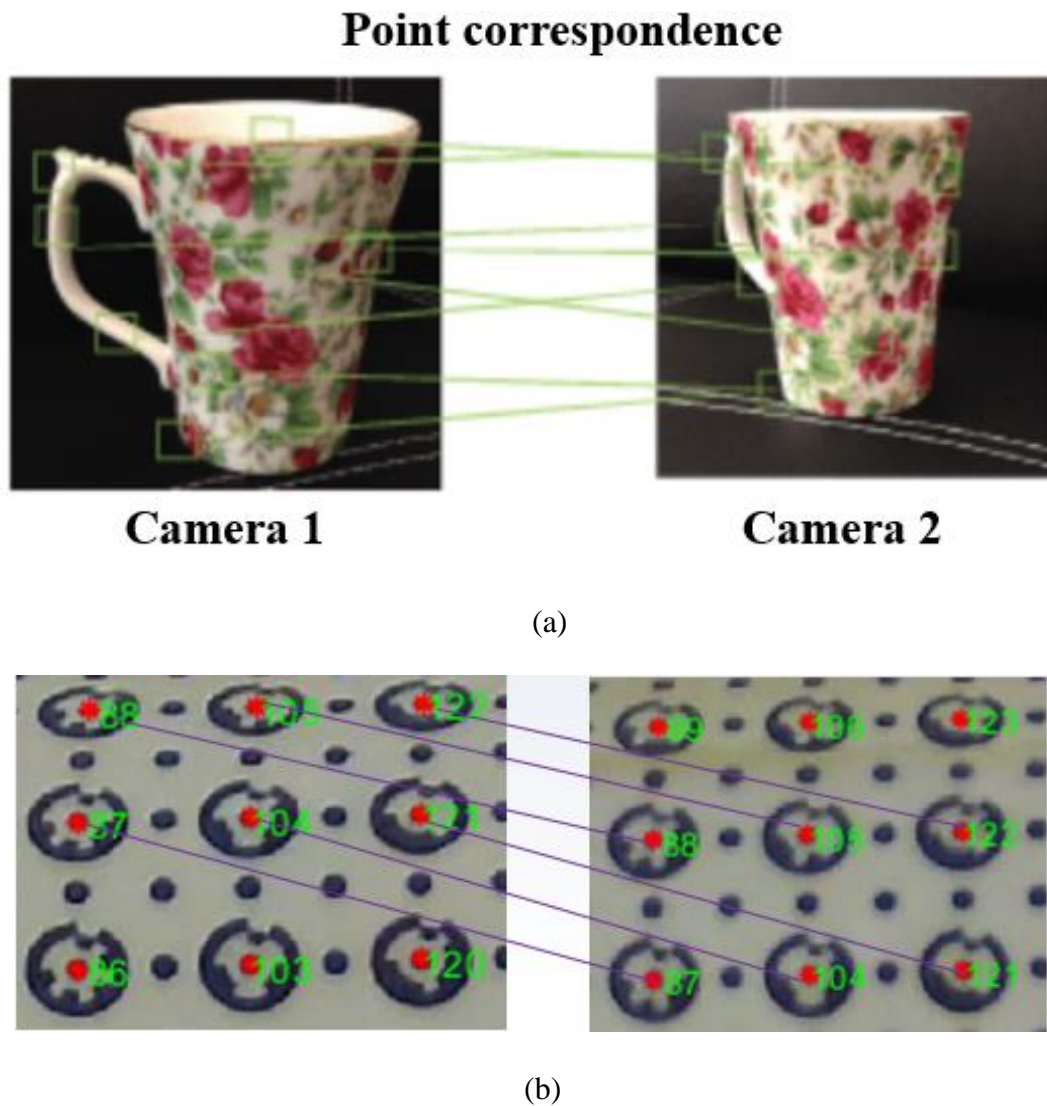


Figure 2. Comparison of point correspondences. (a) point correspondences in SfM, and (b) point correspondences in the proposed method.

Another advantage of coded target is its high marking precision. The differences between coded targets and feature points are listed in Table 2. As can be seen in the table, coded targets can achieve subpixel marking precision and the overall project accuracy of using coded targets is higher than using feature points. In terms of the volume-change

Table 2. Differences between coded targets and feature points.

	Coded target	Feature point
Point marking precision	Fractions of pixel precise	1 to 3 pixels precise
Underlying surface type	Anything	Must have some texture
Automatic setup of scale and coord system	Yes (optional)	No
Overall project accuracy	Can be very high accuracy	Good accuracy
Point density	Low density	High density

measurement of soils, subpixel marking precision is usually required to achieve high volume measurement accuracy. In this study, it is therefore proposed to adopt a hybrid approach. Coded targets are placed on the surfaces of the triaxial cell and soils specimen. The point correspondences are obtained by identifying the coded targets using the coded target identification algorithms. These point correspondences serve as input to 3-D reconstruction.

One limitation of using coded targets is the low point density. The point density can be improved by using smaller solid dots which can also be identified with a unique ID number. These solid dots have the same advantages as coded targets, such as sub-pixel

precision, but have much smaller sizes. Therefore, much more solid dots can be used and the point density can be improved.

2.3. A CUSTOMIZED SFM PHOTOGRAMMETRIC METHOD

The overview of the procedure of the proposed method is shown in Figure 3. There are four phases in the proposed method. Phase 1 is to use a commercially available digital camera to take a group of about 30-40 images around the triaxial test equipment. Phase 2 is to perform CT recognition. Phase 3 is to conduct CT identification. Phase 4 is to use the CT recognition and identification results from Phases 1-3 to perform 3-D reconstruction of the soil specimen. In this section, the detailed procedure of the proposed method was explained.

2.3.1. Triaxial Test Setup. The adopted triaxial apparatus is described by Xia et al., (2022) and shown in Figure 4. Conventional triaxial apparatus is used and some coded target stripes are placed on the acrylic cell, frame rods, and pedestals. One transverse annular coded target stripe was attached to the top of the acrylic cell, and one transverse annular coded target stripe was attached to the bottom of the acrylic cell. There are three longitudinal coded target strips on the acrylic cell which are next to the frame rods. To take full advantage of the space on the three U-channels, three longitudinal coded target stripes were attached to each of the U-channels. On the top and bottom pedestals, there are also two smaller transverse annular coded target stripes. These coded targets are used to determine the absolute volume of the soil specimen as will be discussed later. These coded target stripes are made with waterproof sticker to protect the coded targets immersed in water. Coded targets are printed directly on the membrane to

measure the 3-D points on the soil specimen. It is noted that all these coded targets stripes are inexpensive and easy to use. It only requires coded targets to be printed on commercially available stickers and attached them to the desired locations as described above. The coded target ID numbers for each coded target stripe and membrane are listed in Table 3.

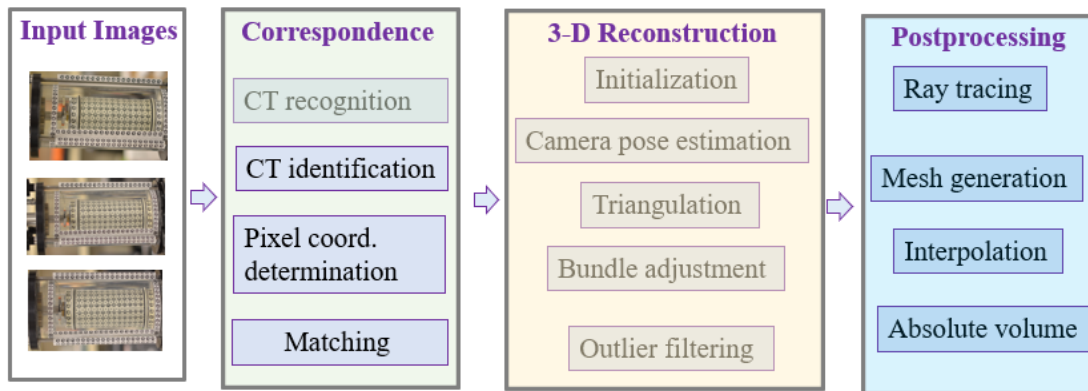


Figure 3. The procedures for the proposed method

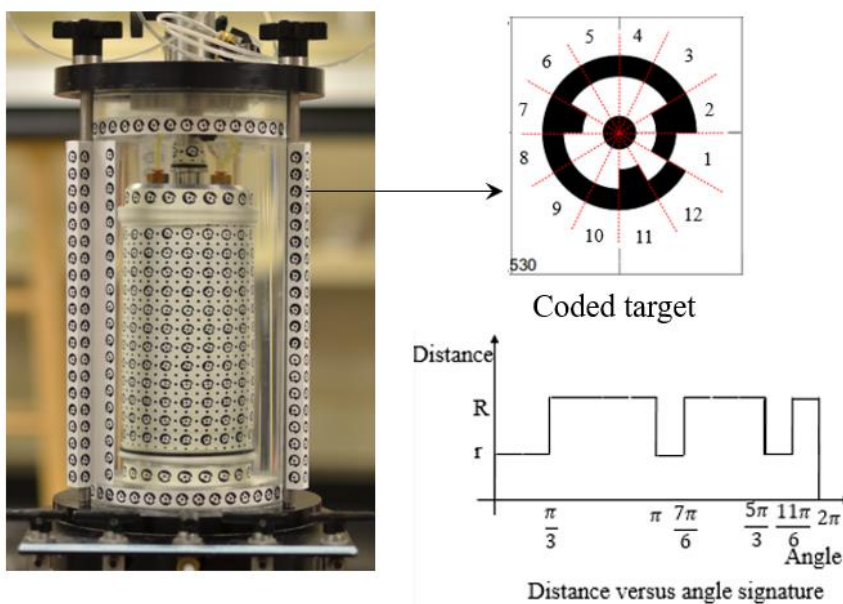


Figure 4. Triaxial test setup

Table 3. Coded target ID numbers for different coded target stripes.

	ID ranges	Total number of Coded targets
Membrane	1-255	255
Transverse annual stripes on the top pedestal	401-417	17
Transverse annual stripes on the bottom pedestal	441-457	17
Longitudinal stripes on the U-channels	501-560, 601-660,701-760	180
Longitudinal stripes on the acrylic cell	561-580, 661-680, 761-780	60
Top transverse annual stripes on the acrylic cell	801 -840	40
Bottom transverse annual stripes on the acrylic cell	901-940	40
Total	-	609

2.3.2. Image Acquisition Procedure. Good image quality is key to a successful photogrammetric project. Several factors influence the image quality, such as the image resolution, image capturing, shooting angles, the overlapping between images, and lighting condition, etc. In this study, a DSLR camera with an image resolution of 4928 by 3264 was used. It is found that the image resolution is good enough since most CTs on the images can be clearly seen. Images were taken around the triaxial cell at around 16 different positions. These 16 positions were roughly in a circle. At each position, two images were captured at two different shooting angles. The abovementioned image

capturing method is to ensure sufficient overlapping between images and various shooting direction, which are beneficial to 3-D reconstruction. Each image was checked immediately after being captured to make sure every image is clear. Normal light in the room should be sufficient to produce good images. Even though it might seem to have many requirements regarding the image acquisition, these requirements are all easy to achieve and can significantly contribute to good CT recognition, CT identification, and 3-D reconstruction results.

2.3.3. Code Target Recognition. It is important to correct the images for lens distortion (also referred to as image idealization) especially when the camera is wide angle camera and there is large images distortion. More discussion regarding image

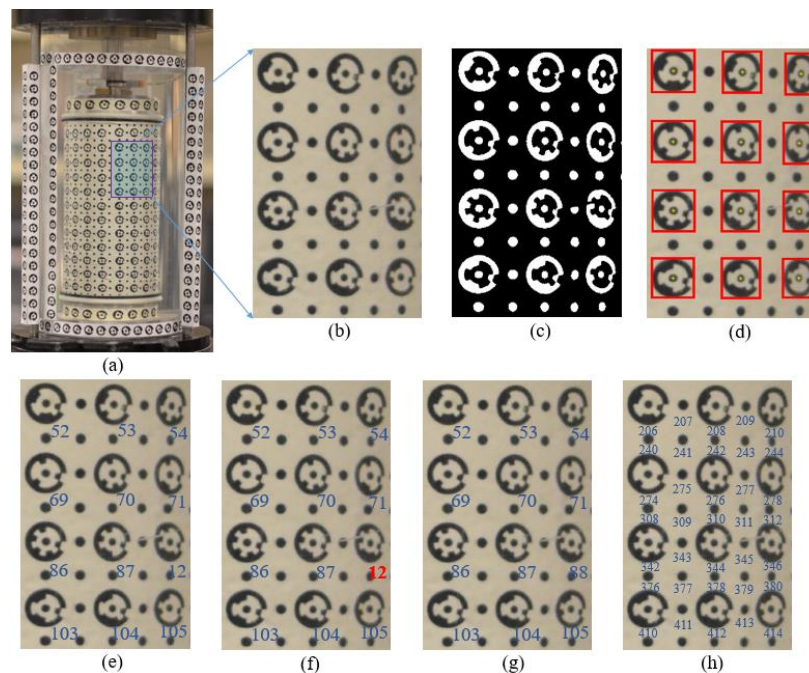


Figure 5. CT Recognition and decoding results. (a) the triaxial cell with CTs; (b) the enlargement of a portion of the rubber membrane; (c) binary image; (d) Recognized CTs by using the embedding feature; (e) initial CT IDs results; (f) Identification of outlier CT IDs; (g) ID results after correcting the wrong IDs; and (h) interpolating more points on the membrane.

idealization can be found in Zhang et al, (2015) and Xia et al, (2021). After the image distortion was removed, image binarization was performed. Image binarization is an image processing technique that converts a grayscale image to black-and-white, which reduces the information contained within the image from 256 shades of gray to 2: black and white, a binary image. Image binarization is commonly performed in object extraction from an image. Figure 5b is an enlargement of a portion of the rubber membrane and is used as an example to demonstrate and illustrate the proposed method. Figure 3c is the binary image of Figure 5b.

2.3.3.1. Blob analysis. A blob means connected pixels in an image. Blob analysis is to calculate statistics for labeled regions in a binary image. A lot of important information can be extracted from the image, such as the quantities of the area, centroid, bounding box, label matrix, blob count of the blobs, etc. Blob analysis is an efficient tool to extract the CTs from the image. In our case, the area of the blob is an important feature. So, the area of each blob was computed.

2.3.3.2. Blob filtering. It is obvious that most CTs have similar areas as shown in Figure 5c. Therefore, it is easy to remove any blobs that have either very large areas or very small areas. This can significantly reduce the search range of CTs. It is found that the CT has a unique feature: in each CT, one small blob is embedded in a large blob. This can be clearly seen in Figure 5c. For each binary CT in Figure 5c, the small blob is inside a large blob. This distinctive feature sets the CTs apart from almost all other blobs. Figure 5d presents the CTs found by using this embedding feature. The boxes in Figure 5d represent the bounding box of the CTs. It is shown that this distinctive feature is the most important and useful feature of the CTs when performing CT recognition. It is

found that most CTs can be successfully found and recognized by using the abovementioned blob filtering method based on area and the embedding feature.

2.3.4. Coded Target Identification. In this phase, the ID of each recognized CT was obtained. We started with determination of the initial CT IDs. Then, the RANSAC algorithm was used to identify and correct the wrong CT IDs. Finally, the interpolation technique was utilized to recover more CTs and more solid dots on the membrane. More detailed regarding these steps are explained as follows:

2.3.4.1. Initial ID determination. Each CT needs to be assigned a unique ID. The procedure for determining the initial CT IDs is briefly introduced here while a more detailed explanation can be found in Xia et al. (2021). The CT contour was identified by detecting the boundary of the CT. Then, ellipse fitting to the outer boundary of the CT was performed to obtain the orientation, major and minor axes of the CT. Then, the elliptical CT contour was normalized to circular contour by using equation. Finally, a signature-based CT contour representation technique was used to decode the CTs. In image processing, signature is a method for representing the contour of a bidimensional object by means of a one-dimensional function (Popescu, 2004). For each CT, the 12-bit binary numbers were obtained and converted to a decimal number, which corresponds to the ID number of the CT. Figure 5e shows the initial CT IDs results.

2.3.4.2. Outlier detection. As mentioned previously, the wrong CT IDs (outliers) are unavoidable due to poor image quality, inevitable scratches on the acrylic cell, unfavorable light conditions, etc. These wrong CT IDs will lead to inaccuracy or even failure in 3-D reconstruction. Manually correcting these wrong CT IDs is very tedious, time-consuming and prone to error since a lot of images are to be processed for a triaxial

test. There is a clear need to develop an efficient and accurate method for identifying the outlier CT IDs. In this study, the RANSAC algorithm was utilized to identify wrong CT IDs. The flowchart of the RANSAC algorithm is shown in Figure 6. Assume the initial ID results for a group of CTs on the membrane are obtained. One can take advantage of the information regarding the geometric arrangement of the CTs. The CT IDs design information is summarized in Table 3. To identify the wrong CTs, two points were randomly selected from all the points that have IDs on the same column or row. The model parameters for fitting a line to the two points can be estimated. Then the distances of the points to the fitted line can be calculated. The number of inliers was counted. After a certain number of trials, the model parameters that produce the most inliers represent the correct model. In the meanwhile, the outlier CT IDs were identified. In Figure 5f, ID 12 is an outlier and can be identified by using the RANSAC algorithm. The wrong ID can be corrected by using the predesign information of the triaxial cell. The ID results after correcting the wrong ID are shown in Figure 5g.

2.3.5. Interpolation. There might still be some missing CTs. Interpolation was performed to recover some missing CTs and find more CTs. Theoretically, a minimum of two correct CTs which did not belong to the same row and the same column were sufficient to infer both the IDs and the estimated pixel coordinates of all the other neighboring CTs. This is because one can take advantage of the prior knowledge of the geometric arrangement of the CTs and the accurate preliminary ID and pixel coordinate results after outlier IDs rejection (Xia et al, 2021). Interpolation was also performed on the membrane to find more solid dots. In Figure 3h, the solid dots are also detected and

decoded. This can significantly increase the number of points on the membrane and produce more representative 3-D results for the soil specimen.

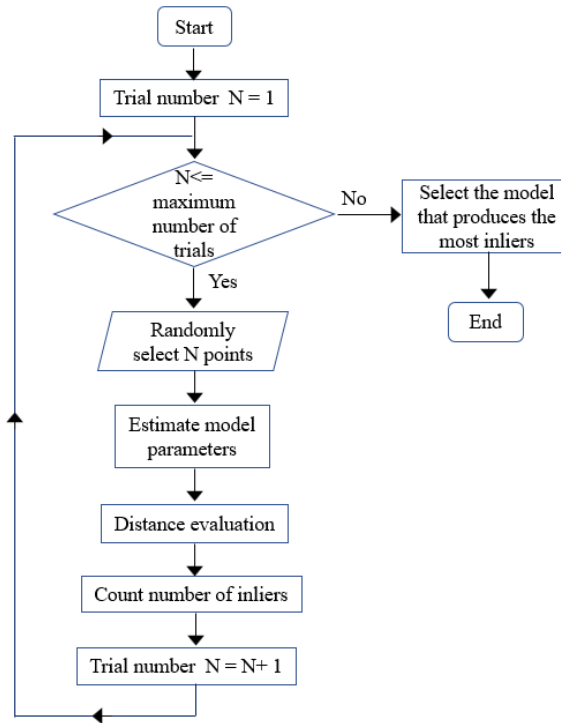


Figure 6. Flowchart for the RANSAC algorithm for detecting outlier CTs

2.3.6. 3-D Model Generation. Stage 1: Initialize 3-D reconstruction. The procedures are summarized as follows: (1) Choose two images that are likely to provide a stable estimate of relative pose; (2) Estimate the fundamental matrix F ; (3) Calculate the essential matrix E from F ; (4) Estimate the relative pose $[Rt]$ from E ; (5) Triangulate individual 3-D points Solve for the camera poses and 3-D points for the two cameras; (6) Perform bundle adjustment to refine points and poses.

Stage 2: Grow 3-D reconstruction. Solve for pose of additional camera(s) that observe reconstructed 3-D points. The process of solving for the camera poses is called

photo resection. An iterative approach is adopted to solve for the camera poses. In each iteration, the image that have the most triangulated points is selected to be processed.

Then, new 3-D points that are viewed in at least two cameras are solved. Bundle adjustment is performed again to minimize reprojection error.

Figure 7 shows the how the camera poses and 3-D points are solved by using the proposed method. In Figure 7a, the initialized 3-D points are solved by the first two cameras and a total of five 3-D points are obtained. Then, the 3-D reconstruction starts growing. A third camera is added in Figure 7b. In Figure 7c, four old points have new observations in the third image. These four points have both the 2-D pixel information and 3-D coordinates. Therefore, the camera pose for the third camera can be solved and the new points observed can be triangulated. The old structure is refined by triangulation over three views and the structure is extended as shown in Figure 7d. The updated structure is shown in Figure 7e. Following the same procedure, the fourth camera is added to the reconstruction. The camera pose for the fourth camera is solved using the common points between the fourth view and triangulated 3-D points. The structure is refined by triangulation over four views and extended. The extended structure is shown in Figures 7f and 7g.

Figure 8 shows the incremental 3-D reconstruction process. In Figure 8a, the structure is obtained through three cameras. One camera is added to the initial 3-D reconstruction. Only a small portion of the specimen is reconstructed. In Figure 8b, the fourth camera is added, and the structure is refined and extended by triangulation over four views. As more and more cameras are added, the structure keeps growing. In Figure

8c, seven cameras are added to the 3-D reconstruction and most of the soil specimen is reconstructed. A complete 3-D model of the soil specimen is shown in Figure 8d.

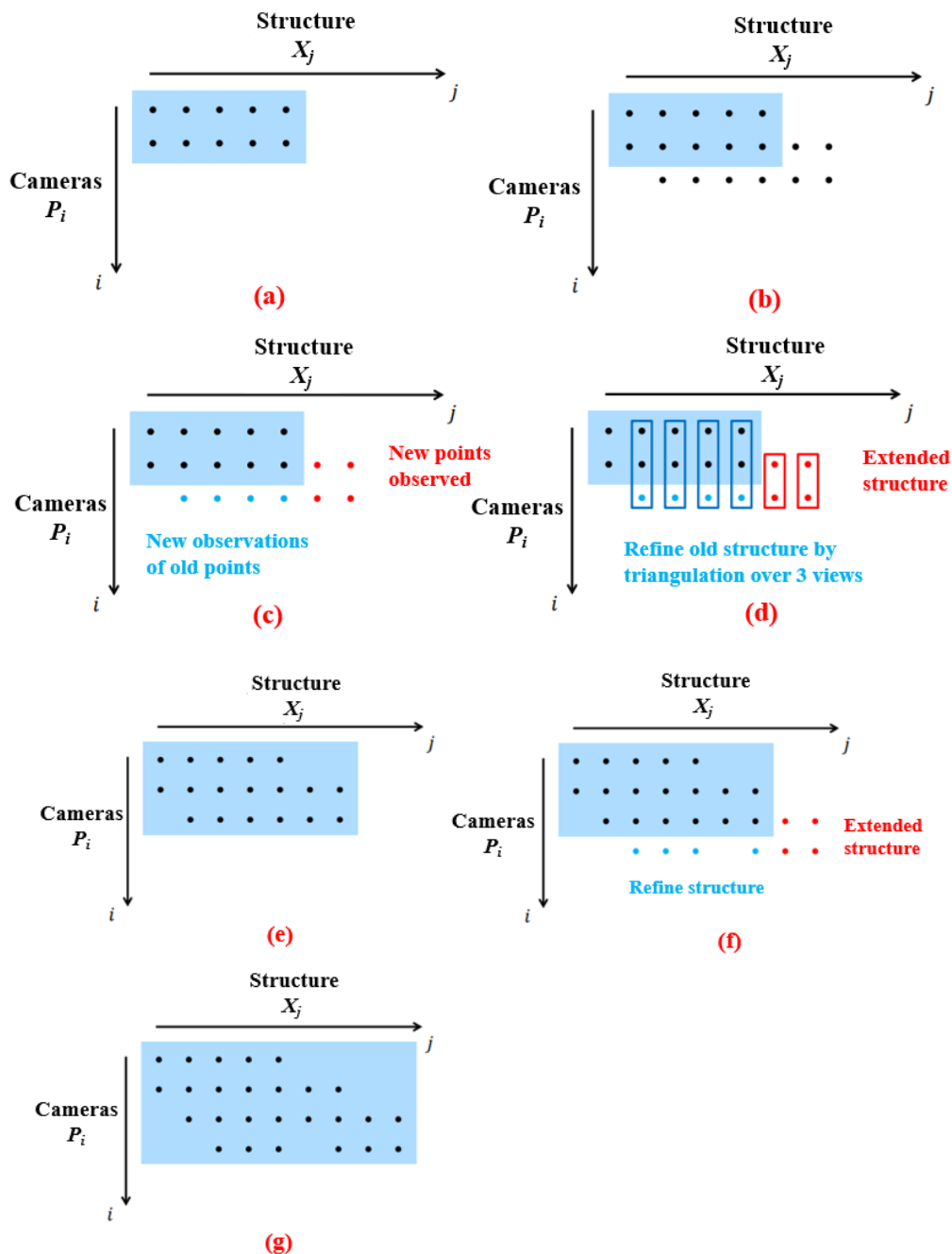
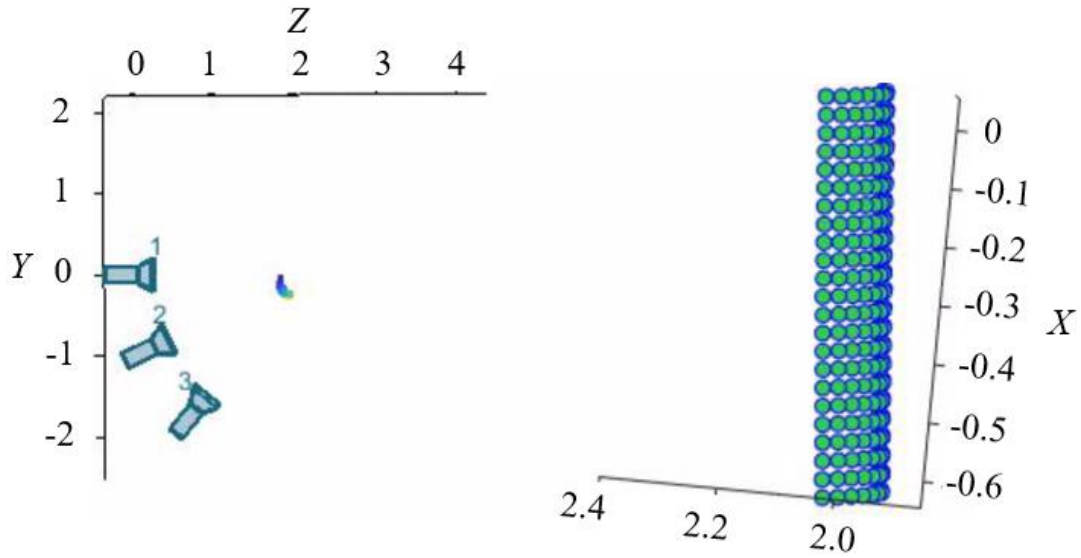
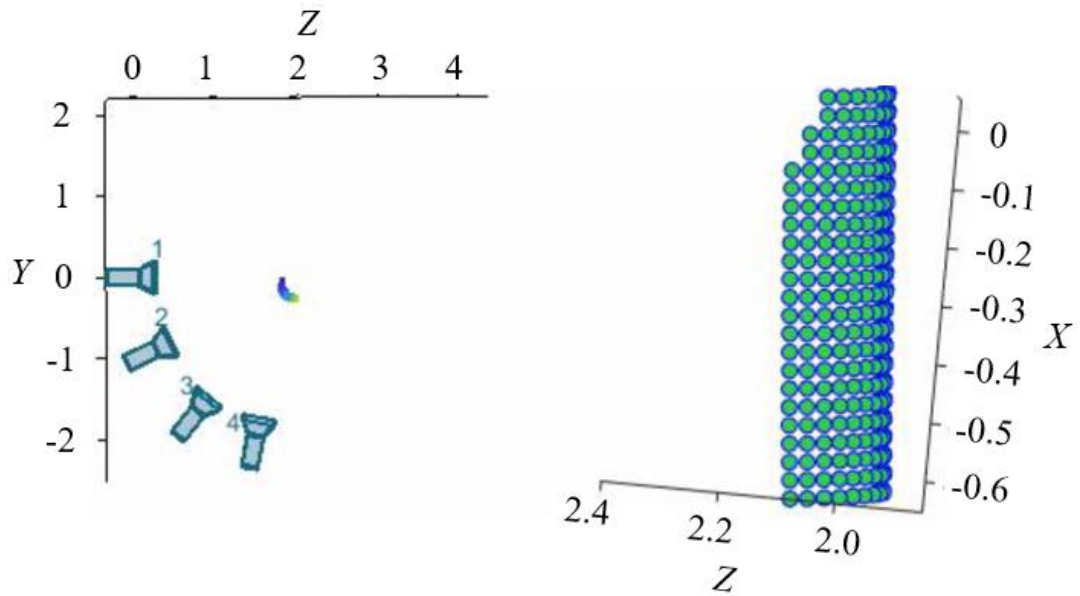


Figure 7. Schematic plot of the growing of 3-D reconstruction. (modified from Opsahl)



(a)



(b)

Figure 8. Incremental 3-D reconstruction. (a) One camera position is added to the initial 3-D reconstruction; (b) two camera positions are added to the initial 3-D reconstruction; (c) seven camera positions are added to the initial 3-D reconstruction; and (d) all camera positions and 3-D points are calculated.

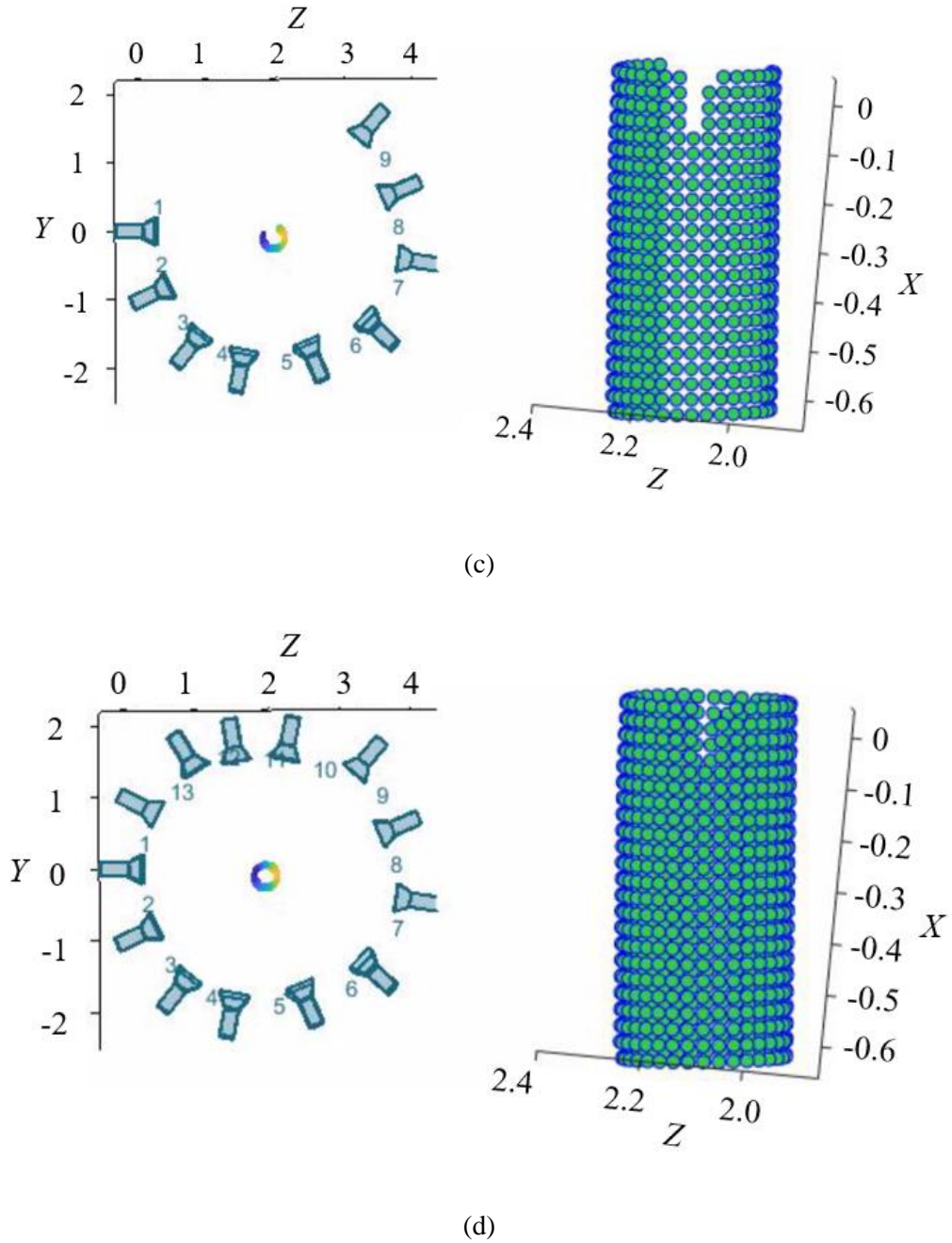


Figure 8. Incremental 3-D reconstruction. (a) One camera position is added to the initial 3-D reconstruction; (b) two camera positions are added to the initial 3-D reconstruction; (c) seven camera positions are added to the initial 3-D reconstruction; and (d) all camera positions and 3-D points are calculated. (cont.)

2.3.7. Outlier Rejection by Using Reprojection Error. One major challenge to 3-D reconstruction is the outlier. An outlier refers to an incorrect point correspondence which is caused by mismatch. In our case, outlier exists when there are incorrect ID numbers of the CTs/solid dots. The outlier can cause inaccurate 3-D reconstruction results or even failure in 3-D reconstruction (Xia et al., 2021). Outliers are unavoidable and need to be removed during the 3-D reconstruction to obtain accurate and reliable 3-D results. In this study, the reprojection error is used to identify and remove outliers. The meaning of reprojection error is illustrated in Figure 9. Point p is the detected point (CT/solid dot in our case) in the 2-D image. P is the corresponding 3-D point. p' is the back-calculated point that is determined by the camera parameters, camera pose, and 3-D point P . The difference between the detected point p and calculated point p' is called reprojection error.

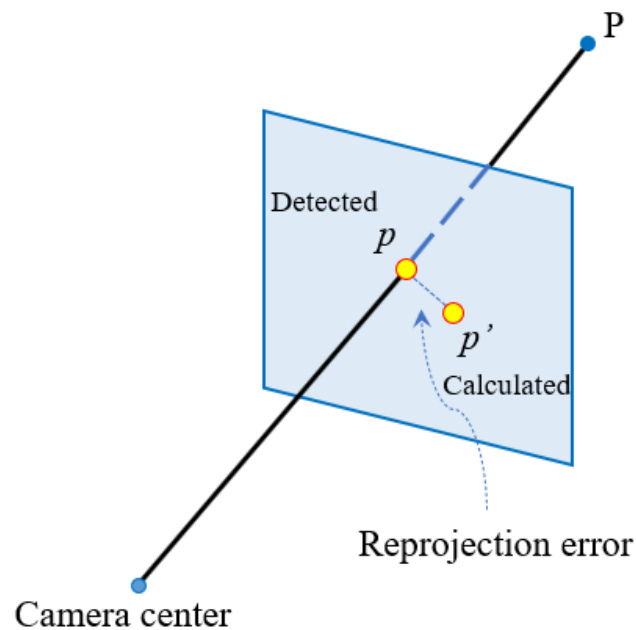


Figure 9. Reprojection error.

Outliers generally produce much larger reprojection error compared with inliers. Therefore, the reprojection error is a reliable way to remove outliers. In conventional SfM, the mean reprojection error for each 3-D point is calculated and used to reject outliers. However, each 3-D point is often determined by several 2-D image points and only one or two image points are incorrect. The removal of 3-D points directly can unnecessarily delete many 3-D points which can be corrected as good 3-D points. In this study, the reprojection error for each 2-D image point is calculated and evaluated after the 3-D results are obtained. Those image points with large reprojection error are removed before being used for the subsequent 3-D reconstruction process. Figure 10 shows the identified outliers under different scenarios. In the image on the left, two incorrect IDs, 507 and 601, are identified. In the image in the middle, one outlier, 310, is detected. The image on the right shows the ID results for the annular CTs, and two incorrect IDs, 815 and 404, are identified.

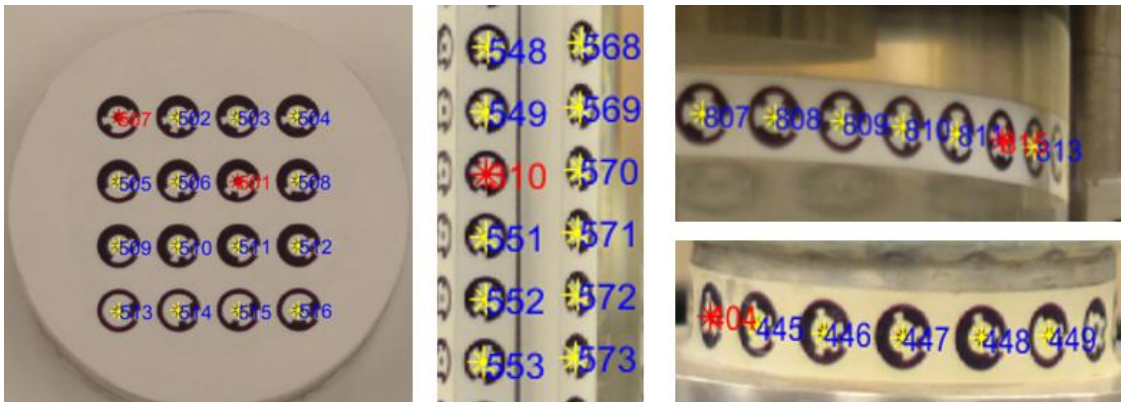


Figure 10. Outlier removal based on reprojection errors for individual image points.

2.3.8. Post-Processing and Absolute Volume Determination. The soil specimen is immersed in water and obvious refraction is observed. So, the optical ray no longer travels through a single line and the refraction needs to be taken into consideration. In this study, a ray tracing technique proposed in Zhang et al (2015) was utilized to correct the refraction and obtain the correct 3-D model of the soil specimen in water. After that, 3-D meshes were generated for the soil specimen. Figure 10 shows that ray tracing results and the 3-D model of the soil specimen obtained by the proposed method. The method in Fayek et al. (2020) is adopted to determine the absolute volume of the soil specimen.

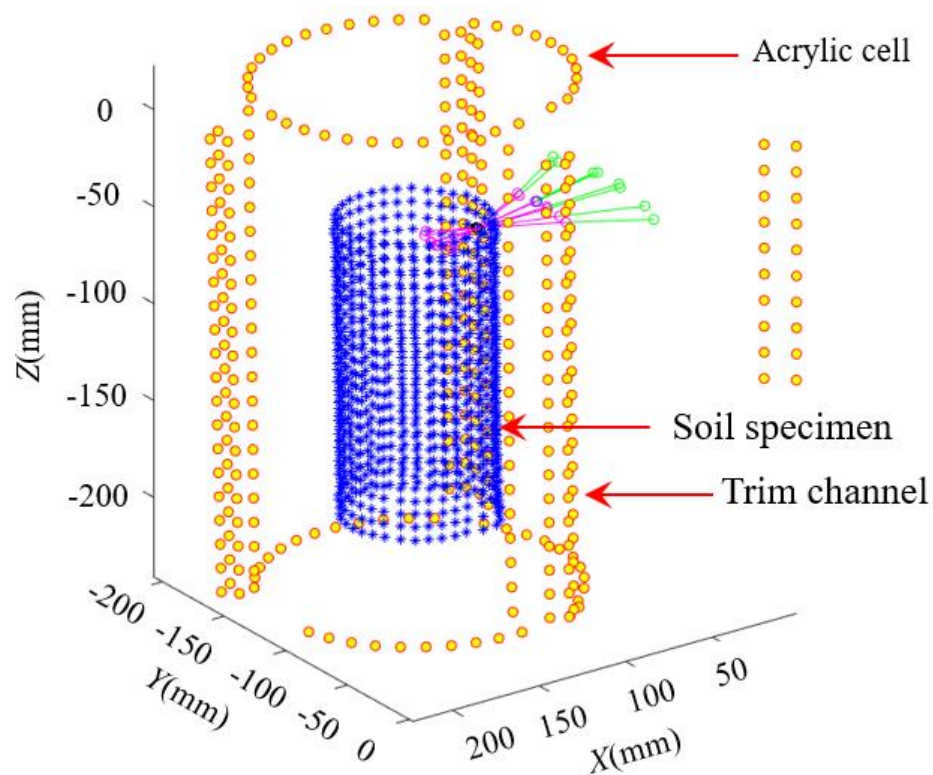


Figure 11. Postprocessing- ray tracing for determining 3-D points on specimen in water.

3. VALIDATION OF THE PROPOSED METHOD

A series of triaxial tests on Ottawa sand are performed to validate the effectiveness and precision of the proposed method. After the soil specimen was prepared in the air without installing the acrylic cell, an image set with about 30-40 images were captured. A second image set was taken after the acrylic cell was assembled. Then, carbon dioxide and water were flushed to the soil specimen to saturate the soil. After that, the back pressure was applied, and the degree of saturation was evaluated. Consolidation was performed at 50kPa, 100kPa, 150 kPa, and 200 kPa, respectively. Then, unloadings and reloadings were applied. Finally, the soil specimen was subjected to shearing at different strains. For each of these steps, an image set with about 30-40 images was capture for the subsequent analysis. The 3-D models of both the acrylic cell and soil specimen are obtained using the structure from motion photogrammetric method described in the previous section.

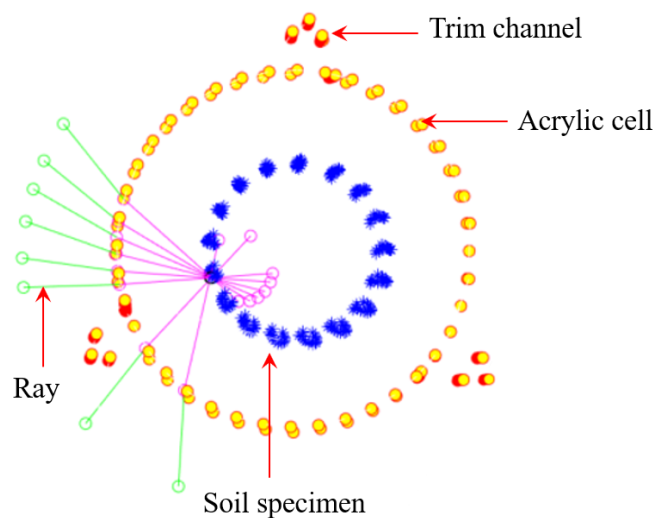


Figure 12. The reconstructed 3-D models of the acrylic cell and soil specimen.

Figure 12 shows the 3-D models of the acrylic cell and soil specimen. A representative 3-D point on the specimen was determined by eight rays as shown in Figure 12.

To evaluate the precision of the proposed method, the overall mean reprojection error for each image set is calculated and listed in Table 4. The overall mean reprojection ranges from 0.45 pixel to 1.37 pixels and the average mean reprojection error is 0.69 pixel for all the 16 image sets. The small mean reprojection errors indicate that the proposed method can achieve sub-pixel precision in terms of 3-D reconstruction results. In Table 4, each image set includes about 30-40 images, and a total of 480-640 images were processed for the 16 image sets. Each image set was processed by using the proposed method independently. The high precision of the proposed photogrammetric method obtained by evaluating the 16 image sets is also a strong indication of the repeatability and reproducibility of the proposed method.

4. CONCLUSIONS

Zhang et al., (2015) proposed a photogrammetry-based method which can be used to measure both the global and localized deformations of unsaturated soils. This method has the advantages of high accuracy, low-cost, both global and localized deformation measurements, and no need for controlling camera positions. However, this method relies on the photogrammetric software to perform target detection and photogrammetric analysis. However, the photogrammetric software often fails to produce satisfactory target detection results. Therefore, tedious manual corrections are required which is time-consuming and prone-to-error. In addition, the photogrammetry-based method requires

uses to have extensive training on both the photogrammetric software and the computer program developed by the authors. In this paper, an SfM photogrammetric method has been proposed which is fully automatic, more accurate in terms of target detection, faster and simpler. An efficient MatLab program has been developed to perform the all the tasks including target recognition and identification, 3-D reconstruction, and postprocessing. It is user-friendly since the program is fully automatically. It is fast since processing each image set takes only about three minutes. Considering that large number of images need to be processed for a triaxial test, the proposed method is efficient and can significantly reduce the time for processing the triaxial test images.

Table 4. Validation of the program on different image sets.

Image set	Overall mean reprojection error
1. Specimen in the air	0.45
2. Assembled triaxial cell	0.66
3. After flushing CO ₂	0.71
4. After flushing water	0.81
5. After applying back pressure	1.37
6. After evaluating saturation	0.49
7. Consolidation 50 kPa	0.55
8. Consolidation 100 kPa	0.45
9. Consolidation 150 kPa	0.57
10. Consolidation 200 kPa	0.54
11. Unloading consolidation 150 kPa	0.68
12. Unloading consolidation 100 kPa	0.89
13. Reloading consolidation 150 kPa	0.46
14. Reloading consolidation 200 kPa	0.77
15. Shearing 2% strain	1.13
16. Shearing 4% strain	0.54
	Average: 0.69

REFERENCES

1. Zhang, X., Li, L., Chen, G. and Lytton, R. (2015). "A photogrammetry-based method to measure total and local volume changes of unsaturated soils during triaxial testing." *Acta Geotechnica*, 10(1), pp.55-82.
2. Zhang, X., Li, L., & Xia, X. (2019). Recent advances in volume measurements of soil specimen during triaxial testing. *Japanese Geotechnical Society Special Publication*, 7(2), 31-37.
3. Nishimura, S. (2022). Characterisation of soil deformation over wide strain ranges in triaxial test with high-precision stereophotogrammetry. *Géotechnique*, 1-16.
4. Bishop AW, Donald IB (1961) The experimental study of partly saturated soil in the triaxial apparatus. In: *Proceedings of the 5th international conference on soils mechanic*, Paris, vol 1, pp 13–21.
5. Romero E, Facio JA, Lloret A, Gens A, Alonso EE (1997) A new suction and temperature controlled triaxial apparatus. In: *Proceedings of the 14th international conference on soil mechanics and foundation engineering*, Hamburg, vol 1, 185–188.
6. Macari EJ, Parker JK, Costes NC (1997) Measurement of volume changes in triaxial tests using digital imaging techniques. *Geotech Test J* 20(1):103–109.
7. White D, Take W, Bolton M (2003) Measuring soil deformation in geotechnical models using digital images and PIV analysis. In: *Proceedings of 10th international conference on computer methods and advances in geomechanics*, Tuscon, Ariz., Balkema, Rotterdam, The Netherlands, pp 997–1002.
8. Liu, J., & Iskander, M. (2004). Adaptive cross correlation for imaging displacements in soils. *Journal of computing in civil engineering*, 18(1), 46-57.
9. DeJong, J. T., White, D. J., & Randolph, M. F. (2006). Microscale observation and modeling of soil-structure interface behavior using particle image velocimetry. *Soils and foundations*, 46(1), 15-28.
10. Take, W. A. (2015). Thirty-Sixth Canadian Geotechnical Colloquium: Advances in visualization of geotechnical processes through digital image correlation. *Canadian Geotechnical Journal*, 52(9), 1199-1220.
11. Li, L., Zhang, X., Chen, G., & Lytton, R. (2015). Measuring unsaturated soil deformations during triaxial testing using a photogrammetry-based method. *Canadian Geotechnical Journal*, 53(3), 472-489.

12. Li, L., & Zhang, X. (2019). Factors influencing the accuracy of the photogrammetry-based deformation measurement method. *Acta Geotechnica*, 14(2), 559-574.
13. Fayek, S., Xia, X., Li, L., & Zhang, X. (2020). Photogrammetry-based method to determine the absolute volume of soil specimen during triaxial testing. *Transportation Research Record*, 2674(8), 206-218.
14. Lowe, D. G. (2004). Distinctive image features from scale-invariant keypoints. *International journal of computer vision*, 60(2), 91-110.
15. Schonberger, J. L., & Frahm, J. M. (2016). Structure-from-motion revisited. In *Proceedings of the IEEE conference on computer vision and pattern recognition* (pp. 4104-4113).
16. Xia, X., Zhang, X., Fayek, S., & Yin, Z. (2021). A table method for coded target decoding with application to 3-D reconstruction of soil specimens during triaxial testing. *Acta Geotechnica*, 16(12), 3779-3791.
17. Xia, X., Zhang, X., Fayek, S., & Yin, Z. (2022). An improved table method for coded target identification with application to photogrammetric analysis of soil specimens during triaxial testing. *Transportation Research Record*. (Under review)
18. Popescu C (2004) A contour-based descriptor for object recognition. *SACI Transactions*, Timisoara
19. Opsahl, T. Structure from Motion.
file:///S:/Spring%202022/Dissertation/lecture_8_2-structure-from-motion%20clear%20explanation.pdf. PowerPoint Presentation.

IV. USE OF LOW-COST SECURITY CAMERAS TO MEASURE AND TRACK THE VOLUME-CHANGES OF SOILS DURING TRIAXIAL TESTING

Xiaolong Xia¹, Sara Fayek², and Xiong Zhang³

¹Ph.D. candidate, Department of Civil, Architectural, and Environmental Engineering, Missouri University of Science and Technology, Rolla, MO 65409-0030. Email: xxrkq@umsystem.edu

²Ph.D. candidate, Department of Civil, Architectural, and Environmental Engineering, Missouri University of Science and Technology, Rolla, MO 65409-0030. Email: sfgbd@umsystem.edu

³(Corresponding Author) Professor, Department of Civil, Architectural, and Environmental Engineering, Missouri University of Science and Technology, Rolla, MO 65409-0030. Email: zhangxi@umsystem.edu

ABSTRACT

Photogrammetry-based methods have gained increasing interest in geotechnical engineering. Significant research efforts have been made to measure the soil deformations during triaxial testing. However, tracking the evolution of 3-D soil deformations during the whole testing process is still a challenge to researchers since conventional photogrammetry cannot be used for dynamic tests, such as the triaxial test in which the soil specimen is continuously deforming. This paper presents a feasibility study on developing a multi-camera-based photogrammetric method to track the evolution of 3-D soil deformations during triaxial testing. Coded targets and solid dots are utilized and posted on the acrylic cell and membrane to facilitate automatic point of interest detection. Thirteen low-cost surveillance cameras are installed to a steel ring around the triaxial test apparatus. The whole triaxial test process is videotaped by these surveillance cameras. The cameras are connected to two Network Video Recorders

(NVRs). The 3-D model of the soil specimen at the initial moment is obtained by processing the first image frame for each video using a structure from motion photogrammetric method. The pixel information and IDs of the points of interest at other moments are tracked through an efficient nearest point search method. The 3-D models of the soil specimen can readily be obtained for all other moments. A MatLab program has been developed to process the videos and extracted image frames automatically. A series of unconfined compression tests and triaxial test was performed to validate the concept of the proposed method. Experimental results indicate that the proposed method can obtain accurate 3-D models of the soil specimen at any time during the test. The overall reprojection error is less than 1 pixel. The proposed method can potentially be used to track the 3-D localized strain/deformations of the soil specimen at every moment during the triaxial testing.

1. INTRODUCTION

Measuring the soil deformations during triaxial testing is an important part of characterizing the stress-strain behavior of soils. A review of the method for volume measurement of soils during triaxial test can be found in Laloui et al., (2006), Zhang et al., (2015), and Nishimura (2022). It is found that all existing methods have limitations in measuring the volume-changes of soils (especially for unsaturated soils) during triaxial testing. In recent years, Zhang and coworkers (Zhang et al., 2015; Li et al., 2016; Fayek et al., 2020; Fayek et al., 2022) developed a photogrammetry-based method which can measure not only the 3-D full-field displacement, but also the absolute volume, tilting

and eccentricity of the soil specimen. This method has many advantages over existing methods, such as high accuracy (less than 0.076 mm for point measurement and better than 0.25% for soil volume measurement), low cost (< \$ 2K) and both global and localized deformation measurement. While this method is very useful, one limitation is the inability to continuously measure the deformations of the soil specimens during dynamic test, such as triaxial test, in which the soil specimen is continuously deforming. In Zhang et al. (2015), only one camera was used, and the method requires the test to be paused when taking images. However, for many tests, such as the triaxial tests on soils, the soil deformations are continuous. As a result, the tests cannot be paused during the test. Not to mention using this method to perform dynamic tests. Therefore, there is a clear need to develop a system which can continuously measure the 3-D full-field deformations of soil specimens during triaxial testing.

An alternative method for continuously measuring and tracking the deformations of soil specimen is to use multiple digital SLR cameras. However, generally 12-24 cameras are required, which can cause high cost. On the other hand, the potential of using low-cost security cameras in measuring the volume-changes of unsaturated soils during triaxial testing has been largely unexplored. The objective of this paper is to overcome the above limitations by using the low-cost security cameras to continuously measure the 3-D full-field deformations of the soil specimens during triaxial testing.

The total cost of the security camera system is about \$ 2K (about \$ 160 for each camera). One can take full advantage of the automatic data acquisition of the security camera system. However, there are some potential problems raised as summarized as follows: (1) the relatively low-resolution of the security cameras. Most commercially

available security cameras have a resolution equal or smaller than 4K. 4K refers to a horizontal display resolution of approximately 4000 pixels. For example, a typical 4K resolution is 3840 pixels by 2160 pixels which is only about half of the digital SLR camera resolution. The low resolution of security cameras can directly cause unfavorable coded target and solid dot recognition and identification results, which will further influence the subsequent 3-D reconstruction and volume measurement results; (2) the large image distortion. Security cameras are generally designed to keep property safe and need to have a much larger field of view angle to have more coverage of an entire area. These cameras are also referred to as wide angle cameras which often have field of views between 60 and 110 degrees. However, the large field of view often causes large image distortion. Large image distortion without being properly handled can undoubtedly influence the measurement results; (3) the unknown accuracy of the security camera system. Based on the abovementioned discussion, both the low image resolution and large image distortion of security cameras can potentially cause inaccurate coded target and solid dot detection results and 3-D measurement accuracy. Therefore, the accuracy of the security cameras system is one of the major concerns that needs to be addressed; (4) a high-efficiency computer program is required to process the large video files. This study aims at addressing each of the above issues and demonstrating the potential of the proposed method to continuously track the 3-D localized strain/deformations of the soil specimen during the triaxial testing.

2. PROPOSED METHOD

2.1. MULTI-CAMERA SYSTEM SETUP AND SECURITY CAMERA DESCRIPTION

The multi-camera system setup is shown in Figure 1. A total of thirteen low-cost security cameras are used in this study. It is noted that the cameras in this study are used as representative security cameras to demonstrate the ability of the proposed method and one can have more options to use other security cameras for the proposed method. All the thirteen cameras are controlled and managed by a 16-channel 4K UHD Network Video Recorder (NVR) from Lorex. The NVR with 4TB hard disk drive (HDD) can record from and manage the sixteen security cameras at resolutions up to 3840×2160 . Equipped with two SATA ports, this NVR can support up to 16TB of internal storage (4TB is preinstalled). H.265 and H.264 video codecs keep file sizes manageable while maintaining the best quality possible. The NVR offers a reliable way to achieve

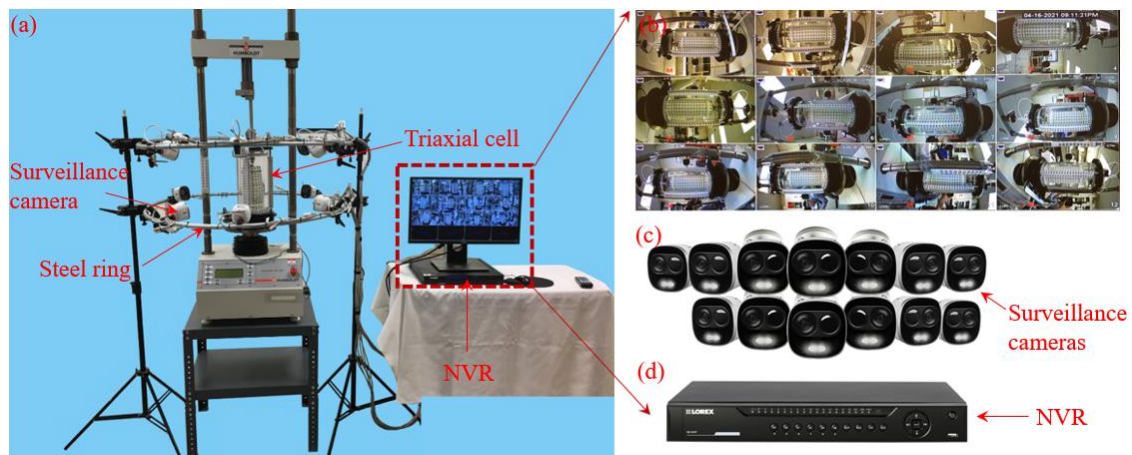


Figure 1. Multi-camera system setup for the proposed method: (a) the multi-camera system; (b) the screen that shows captured images of the triaxial cell;(c) surveillance cameras; and (d) NVR

synchronization of image and video generation which is very important in video-based tracking method. Each camera has an 8 MP 1/2.3" image sensor with a focal length of 4.0 mm according to the specifications. It is noted that all these cameras have fixed focal lengths. The lens field of view is 93 degrees. The streaming resolution of the cameras is 3840×2160 at 15 fps. The information regarding the NVR and the security cameras are listed in Table 1.

Table 1. The multi-camera system information.

NVR Information		Security Camera Information	
Number of Channels	16 (Video)	Sensor	8 MP 1/2.3"
Playback Resolution	3840×2160 (8 MP)	Focal length	4.0 mm
Recording Resolution	1080p, 720p, 3MP, 4MP, 8Mp at 30 fps	Fixed lens	Yes
PTZ support	Yes	Lens Field of View	Diagonal: 93°
Playback Speeds	16×	Maximum Aperture	f/2
IP Camera Support	16		
Throughput	320 Mb/s (Networking)	Shutter Speed	1/12000 to 1/5 second

The design choices to be considered when designing the multi-camera network involve a tradeoff. Since a change in one camera parameter often affects another, these parameters need to be considered simultaneously. Additionally, the optimal camera parameters are highly application dependent. Here, a few of the most important parameters for the security cameras are described

2.1.1. Field of View and Image Distortion. This parameter describes the maximum area of a sample that a camera can image. It is related to both focal length of the lens and the sensor size. A wide field of view provides greater coverage, while a narrow field of view produces more image details. The wide field of view is more popular in camera network design since less cameras are needed to achieve sufficient overlap and coverage. The field of view for the selected cameras in this study is 93 degrees. This relatively large field of view can provide large coverage across the entire triaxial test system.

However, one limitation for wide fields of view is the tendency to produce more distorted images. Especially for a fish-eye lens, the images are largely distorted, and proper camera calibration and distortion correction are required to achieve accurate measurement results. The procedures for security camera calibration were similar to those for digital SLR cameras and standard camera model was used as well. A checkerboard was placed on a flat surface. Then, multiple images were taken around the checkerboard from different orientations. These images were processed using MatLab Camera Calibrator App using standard camera model. Standard camera model was selected because the field of view of the lens of the selected cameras is relatively small compared with wide-angle security cameras. Figure 2 shows the security camera calibration images. Detected corners on the original distorted checkerboard image was shown in Figure 2a. As can be seen in Figure 2a, there is obvious distortion in the original image obtained the security camera. The undistorted checkerboard image after distortion correction was shown in Figure 2b.

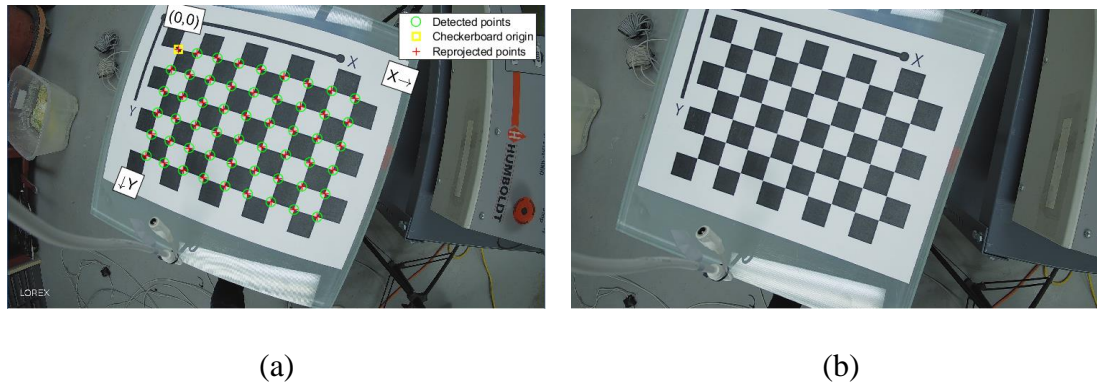


Figure 2. Camera calibration images for security cameras: (a) detected corners on the original distorted checkerboard image; (b) undistorted checkerboard image.

2.1.2. Image Resolution. This parameter describes the total number of pixels on the image sensor. Image resolution is an important parameter that needs to be considered since it is one of the major factors in 3-D measurement accuracy. A low resolution of 640×480 pixels (VGA resolution), is usually found in low-cost webcams (Katz, 2010). In recent years, security cameras with a 4K resolution are readily available. 4K cameras are more attractive since this relatively higher resolution tends to produce better quality images and better coded target/solid dot recognition and identification results. In this study, the selected security cameras have a 4K resolution (3840×2160 pixels). This resolution is smaller than the Digital Single-Lens Reflex (DSLR) Nikon camera with a resolution of 4928×3264 pixels that was used in previous studies (Zhang et al., 2015; Fayek et al., 2020). These 4K security cameras cost only about \$ 160 each.

2.2. THE CODED TARGET/SOLID DOT DESIGN FOR THE TRIAXIAL TEST

Figure 2 shows the design of coded targets and solid dots for the triaxial test. A coded target (CT) is a high contrast dot with a unique pattern around it that is placed on the surface of an object in the scene. Each CT has a unique associated ID number. The

process of determining the ID number of a CT is called CT identification or decoding. CT is a reliable tool for facilitating the automatic target recognition and identification in photogrammetry due to its sub-pixel target detection accuracy. However, there are two

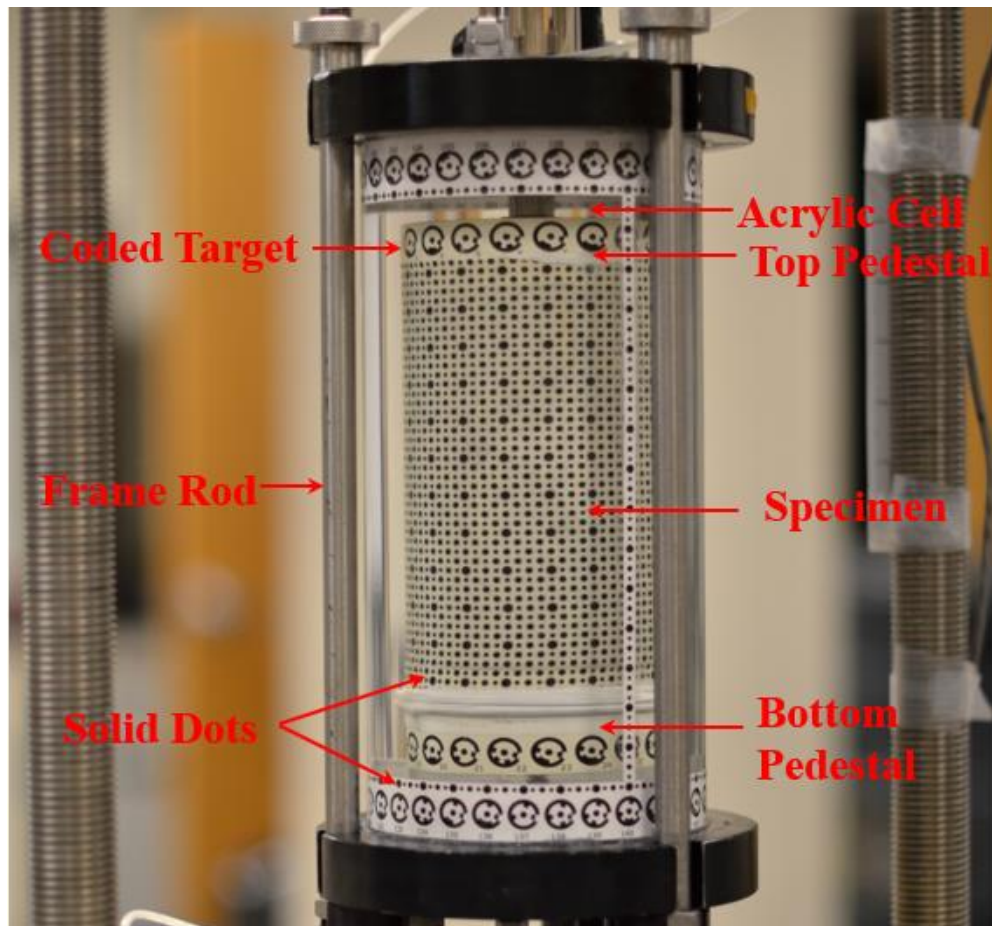


Figure 3. Coded target and solid dot stripes posted on the triaxial cell

limitations with the use of CTs. Firstly, CT identification is often performed by specific CT identification algorithms and sometimes can be time-consuming especially when there are significant number of images or large videos to be processed. In addition, only a limited number of CTs can be used due to the relatively large dimension of the CT. The

limited number of CTs on the rubber membrane can significantly limit the point density on the membrane. In many cases, more CTs or targets are required to achieve more accurate and representative 3-D results.

To overcome the abovementioned limitations, a hybrid approach is therefore adopted. In this approach, both CTs and solid dots are used. A solid dot is a simple dot that has a much smaller dimension than a CT. When carefully labelled or coded, the solid dot has the same function as the CT. Due to its small dimension, use of solid dots can significantly increase the point density. In Figure 2, a total of 92 CTs and 4260 solid dots are posted on the acrylic cell or printed on the rubber membrane. The ID design for these CTs and solid dots are listed in Table 2. In this hybrid approach, a relatively small number of CTs are used to improve the efficiency and reduce the processing time for target recognition and identification. Automatic recognition and marking of solid dots are generally simpler and faster than CTs as will be explained in later section.

2.3. PROCEDURES FOR THE PROPOSED METHOD

In this study, a three-phase multi-camera-based photogrammetric method was proposed. The flowchart for the proposed method was shown in Figure 3 (More details in Figure 3 will be explained later). In the first stage, the video acquisition and image preprocessing are introduced. In the second phase, after the first frame of each video is extracted, these first frames will be processed to initialize the pixel coordinates of the CTs/solid dots and 3-D results. Figure 4 shows the video processing process. In the third phase, a fast and efficient target tracking method is utilized to track the pixel coordinates and 3-D point based on the initialized target location results in phase 2.

Table 2. The predesigned ID lookup table.

Region	Stripe	Start ID	End ID	Number of Points
Pedestal	Top annular CT stripe	1	16	16
	Bottom annular CT stripe	17	32	16
Acrylic cell	Top annular CT stripe	101	130	30
	Bottom annular CT stripe	131	160	30
	Top annular solid dot stripe	161	280	120
	Bottom annular solid dot stripe	281	400	120
	Longitudinal solid dot stripe 1	401	460	60
	Longitudinal solid dot stripe 2	461	520	60
	Longitudinal solid dot stripe 3	521	580	60
Membrane	Annular solid dot stripe	1001	4840	3840
-	-	-	-	Total:4352

2.3.1. Video Acquisition. Before the test, the camera locations are carefully adjusted to make sure good quality videos are obtained. Generally, the largest image distortion is found on the edges of an image and the center of the image has the smallest image distortion. To reduce the influence of image distortion, the triaxial cell location is adjusted manually to the center of the image. The thirteen cameras are evenly distributed

2.3.2. Initialization of the Target Locations in 2-D Images and 3-D Space.

After the first frame for each video is extracted, the CTs/solid dots detection is performed for each of these images using the target recognition and identification algorithms. The

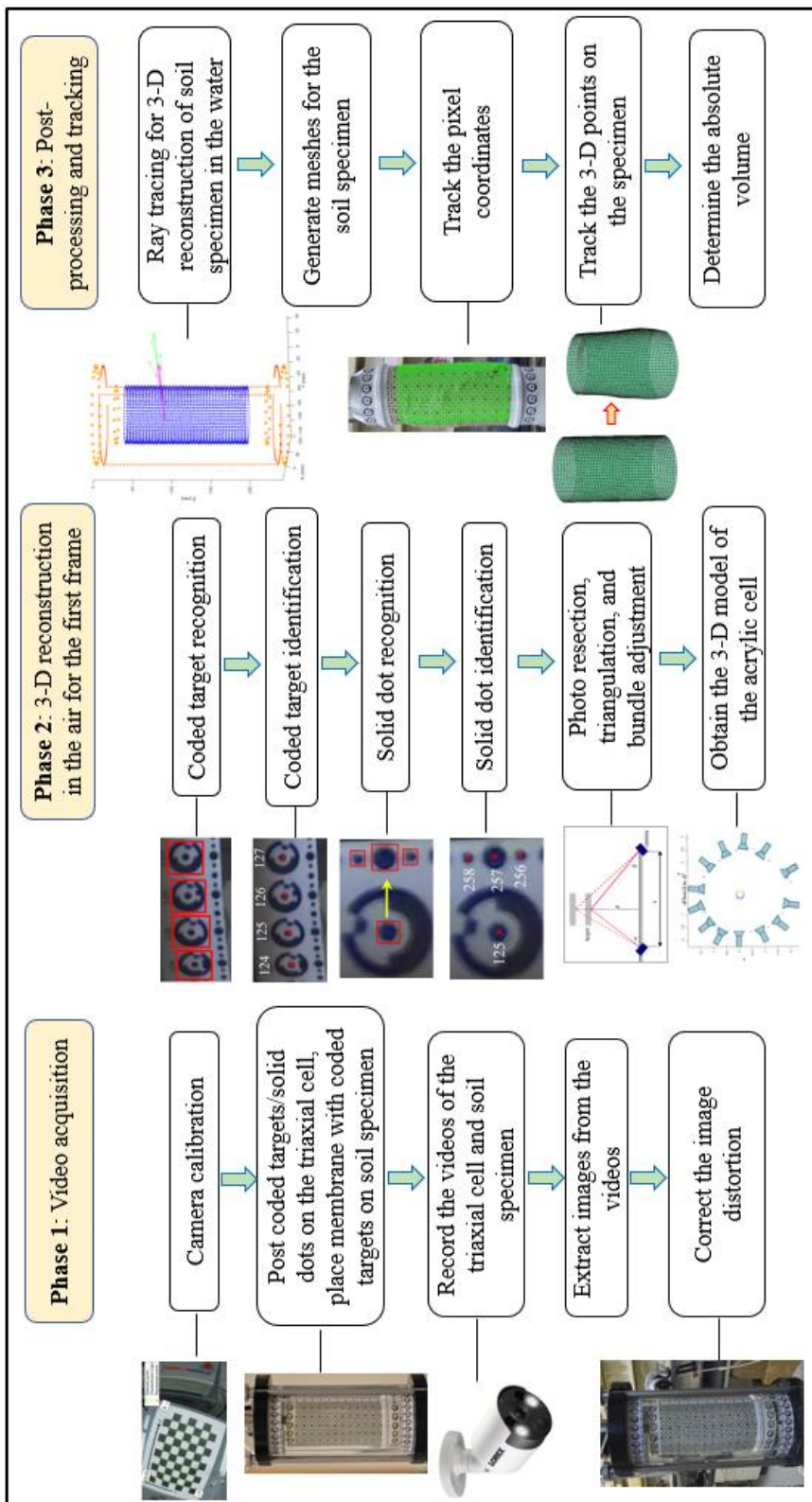


Figure 4. Flowchart for the proposed multi-camera photogrammetric method.

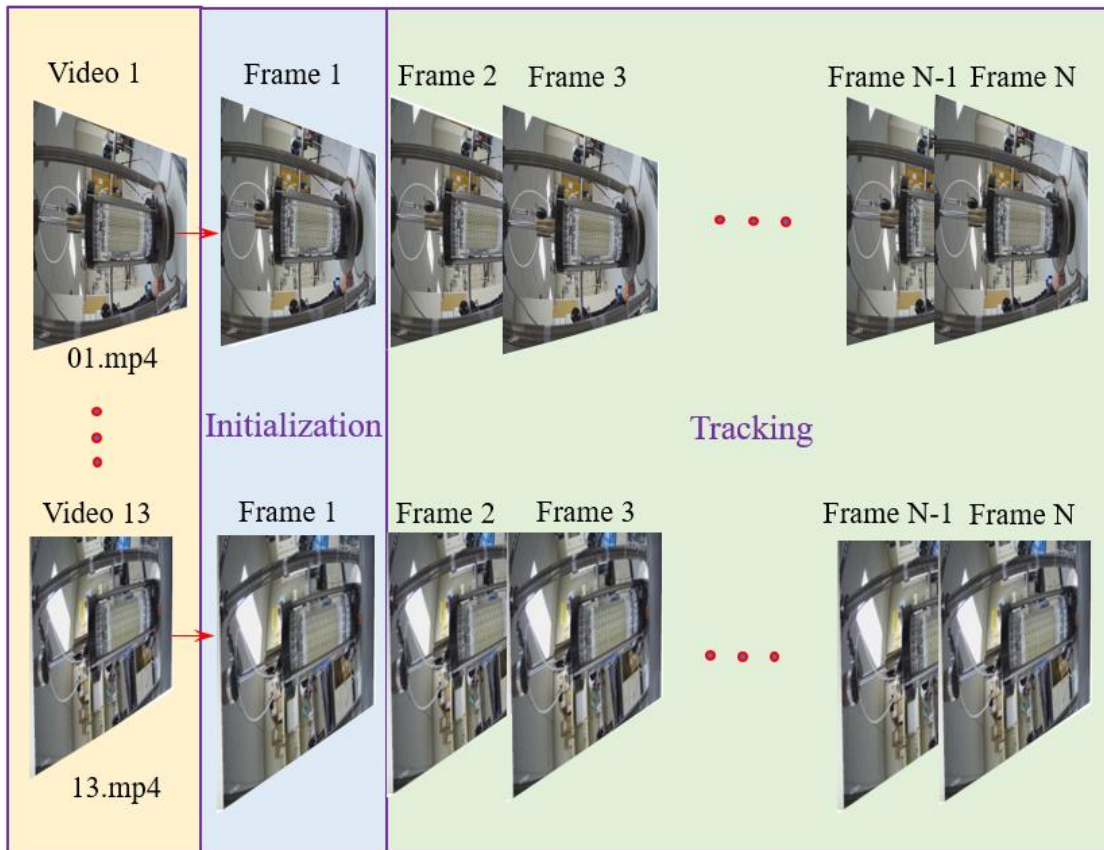


Figure 5. Schematic representation of the video processing.

method in Xia et al., (2021) is adopted to perform CT identification. Figure 6 shows the automatic recognition and identification of the solid dots on the acrylic cell and membrane. Figure 6a is a typical triaxial cell image. A small image patch on the top annular CT/solid dot stripe is selected to illustrate the proposed solid dot decoding method. The enlargement of this image patch is shown in Figure 6b. Assume the CT locations (denoted by the cross at the center of the CT) and IDs (114, 115, and 116) are already obtained using the CT identification algorithm proposed in Xia et al., (2021), the solid dots locations can be easily predicted by moving the CT centers down a distance of $D1$. $D1$ can be obtained from the predesigned geometrical information regarding the

relative location between the CTs and solid dots. Before the CTs and solid dots are posted to the acrylic cell, how relative location of each CT and solid dot compared with other CTs and solid dots are carefully designed and known. One can take advantage of this redesigned geometric information to predict the solid dot centers. Then, a nearest point

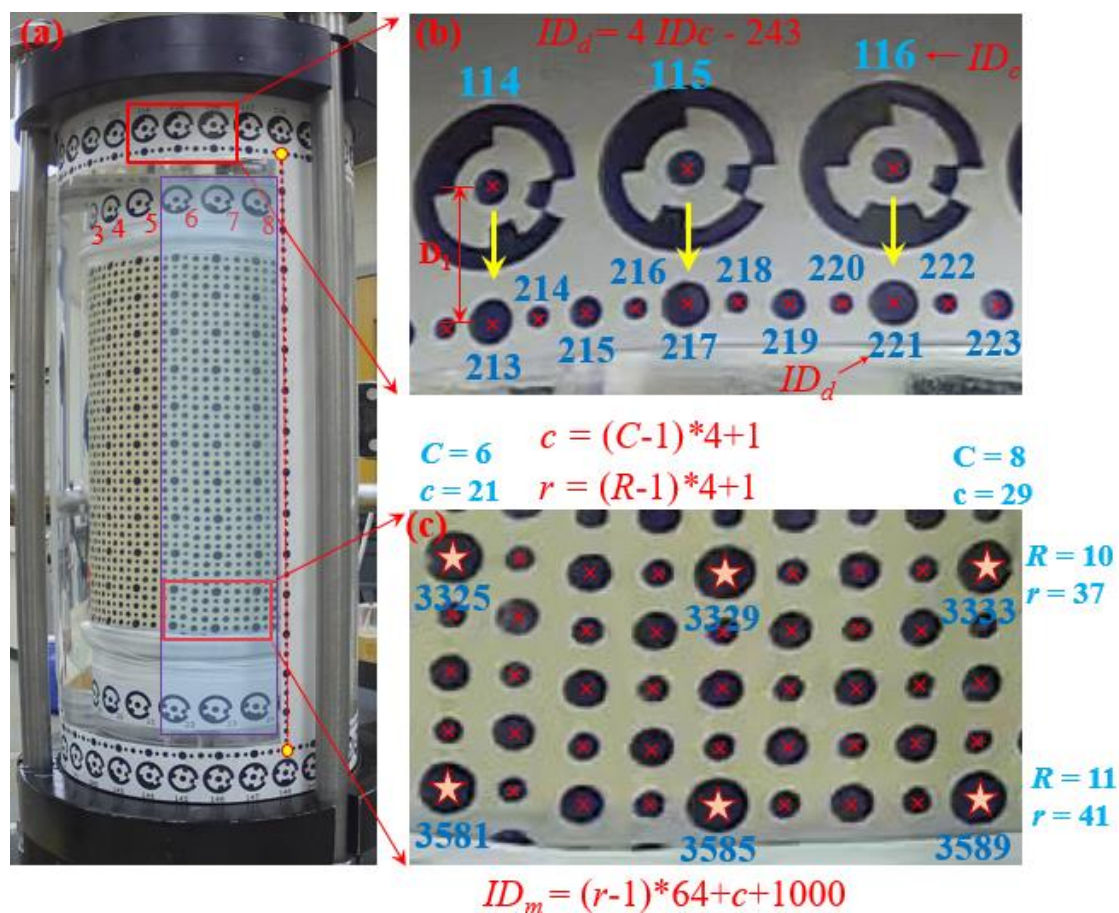


Figure 6. Automatic recognition and identification of the solid dots on the acrylic cell and membrane.

search is conducted to search the nearest point in the initial solid dot detection results compared with the predicted solid dot location. Therefore, the accurate solid dot locations

can be obtained. To label each of the solid dots automatically, the following equation is applied:

$$ID_d = 4 ID_c - 243 \quad (1)$$

where ID_c represents the ID number of the CT, and ID_d represents the ID number of the solid dot that corresponds to the CT. For example, after translating CT 114 to the solid dot directly below CT 114, an ID number 213 is automatically assigned to this solid dot. Each of the solid dots that is directly below the CTs are slightly larger than other solid dots as shown in Figure 6b. These solid dots are labeled by using the simple equation (1). The locations and ID numbers of the smaller solid dots that are between the larger solid dots can be readily obtained by one-dimensional interpolation. It is worth noting that all the solid dots are automatically labeled without using complex target identification algorithms. Instead, simple equation (1) and 1-D linear interpolation are applied, which can significantly reduce the image processing time and reduce the chance of errors.

Similarly, the solid dots on the longitudinal stripe as shown in the vertical line in Figure 6a can also be recognized and identified based on the CT recognition and identification results. The locations of the uppermost and downmost solid dots on this stripe can be predicted and refined according to the pixel coordinates of the CTs directly above or below the two solid dots. The solid dots in the middle of the longitudinal stripe can be obtained using a linear interpolation technique.

Figure 6c shows an enlargement of an image patch on the membrane. This image patch is selected to illustrate how the solid dots on the membrane are automatically recognized and identified. Firstly, based on the ID s of CTs on the top and bottom pedestals, the pedestal CT pairs are found. A pedestal CT pair means that the CT ID s

difference between the two CTs is 16 and the paired CTs are located at similar horizontal locations but on the top and bottom pedestals, respectively. From each CT pair, a polygon can be defined to include all the solid dots on the membrane. Then, the eleven largest solid dots are detected by selecting eleven solid dots with the largest area. This process is repeated for each of the pedestal CT pairs and all the larger solid dots on the membrane can be obtained. The next step is to detect the smaller solid dots through a 2-D interpolation method based on the larger solid dots. Finally, the ID numbers of the solid dots on the membrane are automatically assigned by using the following equations:

$$c = (C-1) \times 4 - 1 \quad (2)$$

$$r = (R-1) \times 4 - 1 \quad (3)$$

$$ID_m = (r-1) \times 64 + c + 1000 \quad (4)$$

where C is the column number of the pedestal CT pairs which is also the CT IDs on the top pedestal; R is the row number of the large solid dots without considering the small solid dots ranging from 1-11. c and r are the column number and row number of the solid dots on the membrane. ID_m is the ID number of the solid dots on the membrane. In Figure 6c, the C, R, c, r, and ID_m values of the six large solid dots are presented as an example.

The CT and solid dot IDs and pixel information serve as input to a 3-D reconstruction program to obtain the 3-D model of the acrylic cell in the air. In this study, a structure from motion photogrammetric method proposed by Xia et al., (2022) is adopted to obtain the 3-D model of the acrylic cell. The soil specimen is immersed in water during triaxial testing, and the refraction effect needs to be addressed. To deal with the refraction problem, a ray tracing technique (Zhang et al. 2015) was adopted to obtain the 3-D model of the triaxial soil specimen in water. A scale and a global 3-D coordinate

system were also defined in the analysis. All of the above- mentioned procedures were completed by a MatLab program developed by the authors so that the computation process is highly automatic and fast.

2.3.3. Tracking the Target Locations in 2-D Images and 3-D Space. As can be seen in Figure 5, all the frames except for the first frames are processed by a tracking method. An efficient target tracking method is necessary due to at least two reasons: (1) the deformation of the soil specimen is very small comparing the two adjacent frames. The selected security cameras have a frame rate of 15 frames per second. Therefore, the difference between the two adjacent frames is very small. There is no need to compute the target locations by using a “brute-force” method, for example, relying on solely the conventional target recognition and identification algorithms to compute the pixel coordinates and 3-D locations of the CTs/solid dots. A simple tracking technique should be sufficient to obtain the target locations in a much easier way. (2) Depending on the total testing period and frame rate, the video files can be very large, and thousands of frames need to be processed. Conventional “brute-force” target recognition and identification algorithms which compute the pixel information and ID numbers for each of the targets can be extremely inefficient.

In this paper, an efficient and fast target tracking method is utilized to determine the target locations. Figure 7 shows a schematic plot of the target tracking method. The initial pixel locations of the targets for the first frame (time = 0s) are obtained by using the method described previously and are shown in Figure 8a. The next frame to be processed depends on the time step we select for video processing. In our case, a time step of 5s is selected so that obvious displacements of the targets can be observed in the

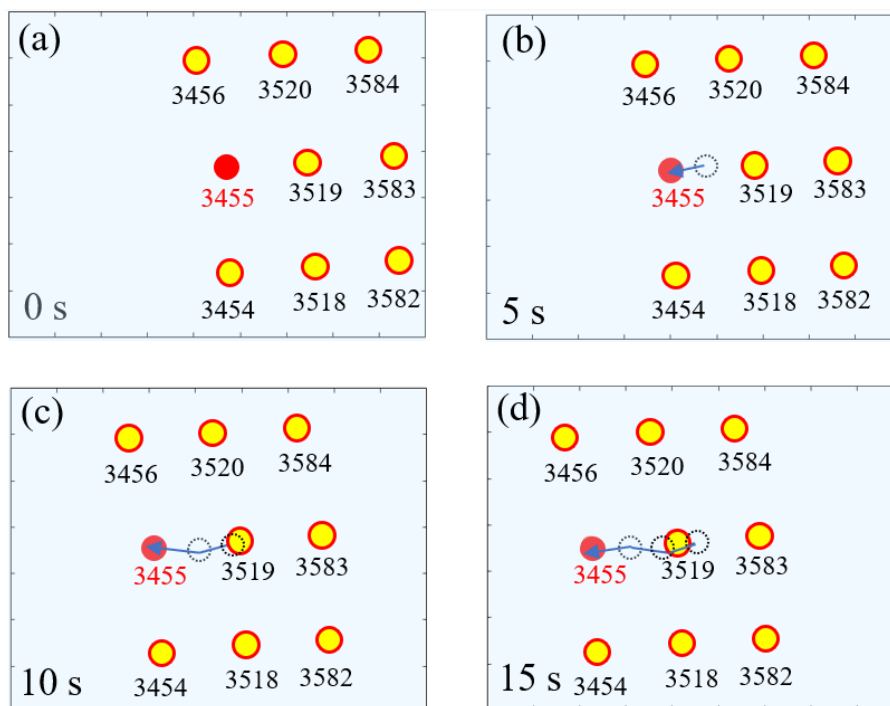


Figure 7. Schematic plot of the target tracking method.

figure. Figure 8b represents the pixel locations of the targets at time $T = 5s$. The shaded circles represent the pixel coordinates of the targets at current moment ($T = 5s$), while the circle with dotted line denotes the target location for solid dot 3455 at previous moment ($T = 0s$). To predict the new location of each target, a nearest point search is performed to find the nearest point between the previous location of this target and all the solid dots at the current moment. Thus, the accurate pixel location of the target at the current moment can be obtained. The IDs of these solid dots keep the same during the tracking process. Figures 8c and 8d show the pixel locations of the targets at moments $T = 10s$ and $T = 15s$, respectively. The changes in pixel location for solid dot 3455 are continuously tracked. This simple target tracking method saves a lot of processing time. A Matlab program has

been developed for tracking and the tracking of targets on each frame takes only about one second.

3. PRELIMINARY RESULTS AND DISCUSSION

A triaxial test was performed on a kaolinite clay sample to validate the concept of the proposed method. Thirteen security cameras are used to record the videos during the triaxial testing. The abovementioned method was applied to process the videos and obtain the continuous 3-D deformations of the soil specimen at every moment during the triaxial testing.

3.1. INITIAL 3-D RECONSTRUCTION RESULTS

Figure 8 shows the initial 3-D results for the acrylic cell and camera stations for the first frames which represent the initial moment $T = 0s$. The positions of the security cameras and 3-D model of the acrylic cell are obtained using the proposed method. It was found that the mean reprojection error for the 3-D reconstruction is only 0.29 pixel. Mean reprojection error indicates the difference between points' calculated 3-D position and their marked position on images. The small mean reprojection error obtained indicates that the proposed method is accurate in terms of the 3-D results. Since the security cameras are installed on a ring and are approximately equally spaced, the camera stations presented in Figure 8 agree well with the actual camera stations. It can also be seen that the top view of the 3-D model of the acrylic cell shows a very good circular shape. This agrees very well with the actual circular shape of the acrylic cell as well. Therefore, the

proposed method gives accurate and promising results regarding the 3-D model of the acrylic cell in the air.

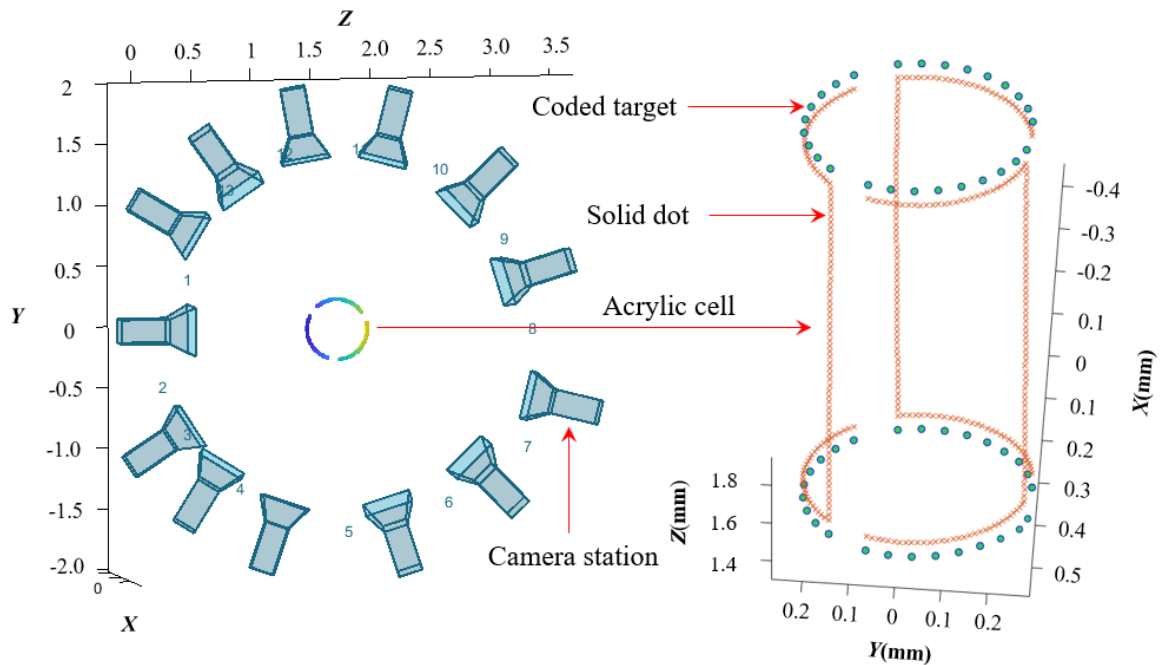


Figure 8. 3-D reconstruction results in the air for the first frames.

3.2. POSTPROCESSING AND RAY TRACING RESULTS

After refraction correction, the 3-D model of the soil specimen in the water is also obtained. Figure 9 shows the ray tracing results and the top view of the 3-D model of the soil specimen. A representative solid dot on the membrane is used as an example. For this point (solid dot), five rays are used simultaneously to determine the 3-D coordinates of this point in space. It is also found most of the points on the membrane are determined by five rays. This indicates that thirteen security cameras are sufficient to ensure reliable 3-D results for the soil specimen in water.

After the 3-D coordinates of the solid dots on the soil specimen are obtained, post-processing can be performed to generate 3-D meshes for the soil specimen. Then, a method for determining the absolute volume of the soil specimen proposed by Fayek (2020) can be adopted to calculate the absolute volume of the soil. By comparing the analysis results between different moments, the volume-changes for the specimen can be obtained. The top and bottom boundaries for determining the absolute volumes of the soil specimen are shown in Figure 9.

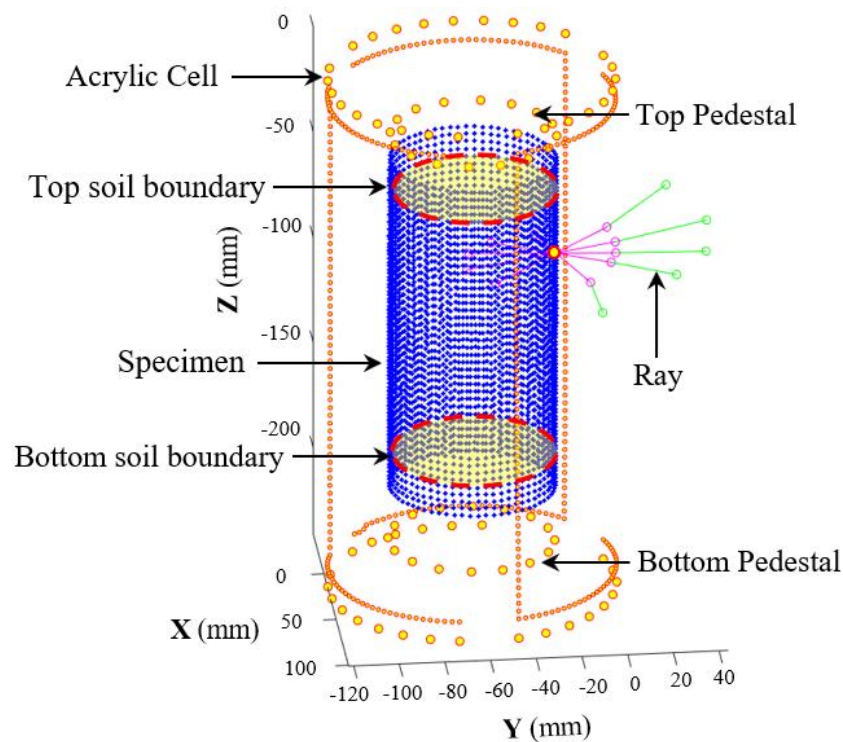


Figure 9. 3-D models of the acrylic cell and soil specimen.

3.3. CONTINUOUS 3-D DEFORMATIONS

One major advantage of the proposed method is its ability to continuously measure and track the 3-D deformations of the soil specimen during the whole triaxial

testing. Figure 10 shows the 3-D models of the soil specimen different moments and axial displacements. It is worth noting that although only the 3-D models at six moments are presented in Figure 10, the 3-D results at any time during the triaxial testing are obtained and made into a movie to display the whole 3-D deformation process.

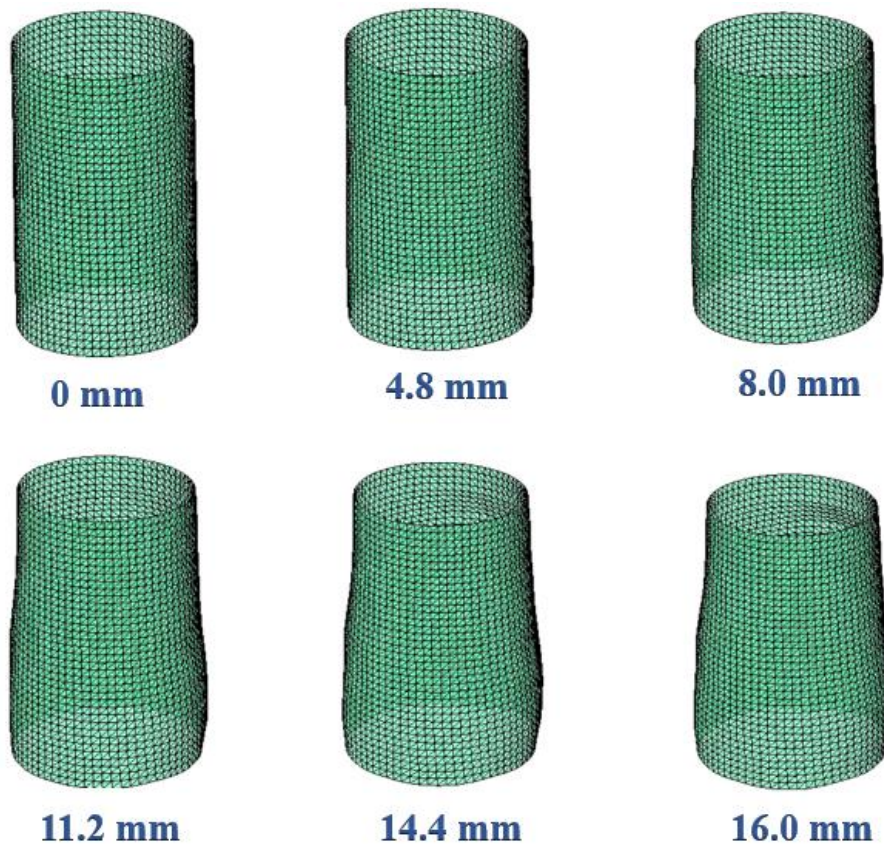


Figure 10. 3-D models of unconfined compression test soil specimen at different axial deformations.

As can be seen in Figure 10, the deformations became larger and larger over time. It was also found that the deformations of the soil specimen are non-uniform. The deformations at the lower portion of the specimen are much larger than those at the top of

the soil specimen. The proposed method can measure both the global and localized deformations of the soil specimen.

It is noted that the above results were obtained using the standard camera calibration parameters. However, the security cameras used in this study have a field of view angle of 93 degrees and should be considered as fisheye cameras. The results presented in this paper shows the preliminary 3-D reconstruction results. In the future, the fisheye calibration parameters will be used instead of the standard camera calibration results. Although the standard camera calibration parameters are used in this study, the proposed method still shows promising 3-D reconstruction and ray tracing results. More accurate results regarding the 3-D models of the acrylic cell and soil specimen can be expected in the future work. The preliminary results regarding the 3-D model of acrylic cell and soil specimen can also be used in the postprocessing processes to obtain the absolute volumes and volume changes of the soil specimen during triaxial testing and these results will be reported in the future work.

4. CONCLUSION

This paper presents a feasibility study on developing a multi-camera-based photogrammetric method which can measure the continuous deformations of both saturated and unsaturated soils during triaxial testing. The following conclusions are made:

- (1) The preliminary results indicate that the proposed method can obtain accurate 3-D model of the soil specimen using relatively low-cost security cameras. The

large image distortion caused by the wide-angle security cameras is corrected by camera calibration. The mean reprojection error is only 0.29 pixel. Each security camera costs only about \$ 160 and the multi-camera system costs about \$ 2K.

- (2) The proposed method can be used to track the 3-D localized strain/deformations of the soil specimen at every moment during the triaxial testing. It is found that the deformations of the soil specimen are non-uniform. The lower part of the specimen experienced larger deformations.
- (3) The proposed method is highly efficient and automatic. All the computation is conducted by a computer program. The tracking of each target takes only about one second.

REFERENCES

1. Bishop AW, Donald IB. (1961). "The experimental study of partly saturated soil in the triaxial apparatus." In: Proceedings of the 5th international conference on soils mechanic, Paris, vol 1, pp 13–21.
2. Fayek, S., Xia, X., Li, L., & Zhang, X. (2020). "Photogrammetry-Based Method to Determine the Absolute Volume of Soil Specimen during Triaxial Testing." *Transportation Research Record*, 2674(8), 206-218.
3. Katz, I. (2010). "Design and Performance of Multi-Camera Networks." Stanford University.
4. Li, L., Zhang, X., Chen, G., and Lytton, R. (2015). "Measuring unsaturated soil deformations during triaxial testing using a photogrammetry-based method." *Canadian Geotechnical Journal*, 53(3), 472-489.
5. Ng CWW, Zhan LT, Cui YJ. (2002). "A new simple system for measuring volume changes in unsaturated soils." *Can Geotech J*, 39(3), 757–764.

6. Romero E, Facio JA, Lloret A, Gens A, Alonso EE. (1997). “A new suction and temperature controlled triaxial apparatus.” In: Proceedings of the 14th international conference on soil mechanics and foundation engineering, Hamburg, vol 1, 185–188.
7. White D, Take W, Bolton M. (2003) “Measuring soil deformation in geotechnical models using digital images and PIV analysis.” In: Proceedings of 10th international conference on computer methods and advances in geomechanics, Tuscon, Ariz., Balkema, Rotterdam, The Netherlands, 997–1002.
8. Xia X, Zhang X, Yin Z. (2020) “A Photogrammetric Computer Vision Approach for 3D Reconstruction and Volume-Change Measurement of Unsaturated Soils.” In Geo-Congress 2020: Geo-Systems, Sustainability, Geoenvironmental Engineering, and Unsaturated Soil Mechanics 2020 Feb 21 (pp. 387-393). Reston, VA: American Society of Civil Engineers.
9. Xia X, Zhang X, Fayek S, and Zhao Z. (2021a). “A Table Method for Coded Target Decoding with Application to 3-D Reconstruction of Soil Specimens during Triaxial Testing.” *Acta Geotechnica*. Under review.
10. Xia X, Zhang X, Fayek S. (2021b) “A Computer Vision Photogrammetric System to Measure the Volume-Changes of Unsaturated Soils during Triaxial Testing.” In preparation.
11. Zhang, X., Li, L., Chen, G. and Lytton, R. (2015). “A photogrammetry-based method to measure total and local volume changes of unsaturated soils during triaxial testing.” *Acta Geotechnica*, 10(1), pp.55-82.

**V. A MULTI-CAMERA BASED PHOTOGRAMMETRIC METHOD FOR
THREE-DIMENSIONAL FULL-FIELD DISPLACEMENT MEASUREMENTS
OF GEOSYNTHETICS DURING TENSILE TEST**

Xiaolong Xia¹, Xiong Zhang², and Chunmei Mu³

¹Ph.D. candidate, Department of Civil, Architectural, and Environmental Engineering, Missouri University of Science and Technology, Rolla, MO 65409-0030. Email: xxrkq@umsystem.edu

²(Corresponding Author) Professor, Department of Civil, Architectural, and Environmental Engineering, Missouri University of Science and Technology, Rolla, MO 65409-0030. Email: zhangxi@umsystem.edu

³Associate Professor, College of Civil and Architectural Engineering, Guilin University of Technology, Guilin, Guangxi 541004, P.R.China, Email: mchm@glut.edu

ABSTRACT

Conventional methods for measuring the deformational response of geosynthetics, such as the linear variable differential transformers (LVDTs), strain gauges, and extensometers have several limitations in fully determining the complete strain distribution in geosynthetics. This paper presents a multi-camera based photogrammetric method to track the 3-D full-field displacements of geosynthetics during tensile tests. The proposed method extends the conventional one-camera based photogrammetry for static object measurements to multi-camera-based photogrammetry for object measurements with continuous movements or deformations. It is non-contact, cost-effective, highly accurate, and capable of measuring the 3-D full-field displacements of the geosynthetics. A tensile test on a geogrid specimen was performed to verify the effectiveness and accuracy of the proposed photogrammetric method. The results from the tensile tests

using both the proposed method and conventional methods, such as machine-controlled displacement measurements and extensometer, were presented and compared. It was observed that the average absolute difference between the proposed photogrammetric method and the machine-controlled movements of the bottom clamp was 0.25%, and the average absolute error was 0.038 mm. The average difference in measurements made by the proposed method and extensometer was 0.05%. It was further found that the proposed method can provide more comprehensive input, such as the complete strain and modulus distributions in the geosynthetics, for a probability-based geosynthetics design.

1. INTRODUCTION

Geosynthetics have been extensively used as a reinforcement for a variety of geotechnical applications, such as soil stabilization, mechanically reinforced retaining walls and slopes, etc. The modulus and tensile strength are indispensable parameters in the design applications of geosynthetics. The wide-width tensile test or grab tensile test is usually used to determine the tensile strength, failure strain, and deformation modulus of geosynthetics. The continuous and complete measurements of the displacements of geosynthetics at all locations (also referred to as full-field displacement) during tensile tests are essential for the above-mentioned purposes and provide important information about the mechanical behavior of the geosynthetics. However, the conventional mechanical strain measurement systems can only measure displacements/strains at a few locations with limited ranges. The inability to detect zones of varying strains and identify potential local failure zones as well as the inaccurate determination of strains may lead to

either an unconservative design of the structure or possible catastrophic failures (Aydilek et al., 2004). Over the past decade, numerous efforts have been made to develop alternative methods for displacement/strain measurements of geosynthetics during tensile tests. This paper reviews the methods used for displacement/strain measurements of geosynthetics during tensile tests and the methods developed for other purposes but can potentially be used for measuring the displacement/strain of geosynthetics. It was found that all existing methods had limitations. Thus, it remains a major challenge for researchers to develop alternative methods to more accurately measure the three-dimensional (3-D) full-field displacement/strain of geosynthetics during tensile tests.

In this paper, a photogrammetry-based method is developed to track the 3-D full-field displacement/strain of geosynthetics during tensile tests. This method takes advantage of conventional photogrammetry in which there is no need for the manual control of camera stations and still maintains a high measurement accuracy. Furthermore, it overcomes an important limitation of conventional photogrammetry for 3-D reconstruction for static objects only. Two commercially available digital cameras were used to take images of the geosynthetics specimen during the tensile tests. The experimental setup and procedures were introduced for a validation test. Finally, the results from the tensile tests using both the proposed method and conventional methods were presented to demonstrate the accuracy and advantages of the proposed method. It was found that more comprehensive measurement data regarding the complete strain distribution and deformational modulus of the geosynthetics at all locations could be obtained.

2. LITERATURE REVIEW

The literature review includes two parts: the review of (1) methods used for measuring displacement/strain of geosynthetics in tensile tests, and (2) non-contact methods that can potentially be used to measure the complete displacement/strain distribution of geosynthetics. A detailed discussion of these methods is presented below.

2.1. METHODS FOR MEASURING DISPLACEMENT/STRAIN OF GEOSYNTHETICS.

Methods specifically designed for displacement/strain measurement of geosynthetics, often considered as conventional methods, can be classified into four categories: (1) crosshead extension method, (2) contact extensometer, (3) strain gauge, and (4) LVDT.

2.1.1. Crosshead Extension Method. The crosshead extension method is commonly used to measure overall strain by measuring the separation distance between two tension grips during a tensile test. Skochdopole et al. (2000) performed a tensile testing on woven and knit geotextiles and geogrids, using roller grips and wedge grips. Crosshead extensions during testing were recorded. However, the authors pointed out that the strains measured by this method did not represent the actual strains at all. This was due to the fact that, during the tensile test, the specimen was often wound around a drum at each end. During the test, the specimen wound tighter around the drums, which was referred to as seating. Therefore, the measured strain was actually a combination of seating and specimen elongation. In addition, the measured strain was the ratio of the crosshead displacement and the initial grip distance. Therefore, any slippage during the

testing will result in errors in the strain measurement. Another drawback of this method is that only the overall strains can be measured, and no information about the localized strains are provided. Due to these limitations, crosshead extension method cannot be utilized to measure an accurate and complete strain distribution of geosynthetics.

2.1.2. Contact Extensometer. A contact extensometer is often a clip-on extensometer which has two edges that are attached mechanically to a specimen. Contact extensometers provide accurate strain measurement in numerous applications where high-precision strain measurement (mostly ASTM-based tests) is required. However, this method has several disadvantages as well. Knife-edge contact points can lead to stress concentrations on the specimen, which may cause premature failure of the specimen. Slippage may also occur as knife-edges become dull over time. For geogrid specimen, attachment of the extensometer to the specimen can increase the stiffness and modulus of the test specimen and the weight of the contact extensometer itself can distort specimens and, therefore, causes misleading results. The process of attaching a clip-on type of contacting extensometer relies on an operator's skill. In addition, high energy released when a specimen fails can cause damage to contact extensometers. To protect the extensometer, the test must be stopped at certain points before specimen failure to remove the extensometer. Therefore, only a limited range of strains can be measured by a contact extensometer. In addition, it can potentially introduce even more variability in the test results. All these drawbacks are inherent in contact extensometers. Even though several contact extensometers have been designed to minimize their limitations, none of the above-mentioned limitations can be eliminated by using contact extensometers.

2.1.3. Strain Gauge. Strain gauge is another widely used contact method for strain measurement. It is a wafer-like device that can be mounted on specimen to measure applied strain by converting the mechanical displacements into changes in electric resistance. Since this method requires the attachment of strain gauge to specimen at specific and predesigned locations, only the strains at limited number of locations within the specimen can be measured. Apart from that, the strain gauge easily detaches from the specimen when large strains occur. Furthermore, the attachment of a strain gauge to a specimen can stiffen the geosynthetics material. Therefore, the stiffening causes the measured strains to be different from the actual strains. In addition, the measured strains are influenced by many other factors, such as the data logger, gauge factors, quality of bonding between strain gauge and geosynthetics, and temperature (Gallage and Jayalath, 2019). Therefore, although commonly used in strain measurement, this method cannot be used to accurately measure full-field strain distribution in geosynthetics.

2.1.4. LVDT. LVDT is another conventional contact method that can be used to measure the displacement of geosynthetics materials. LVDTs measure displacements by converting linear motion into electrical signals. While commonly used in many industrial and scientific applications, LVDT has several disadvantages when used for tensile testing. LVDT displaces yarns and rupture filaments in a geosynthetic specimen, which alters both the elongation and ultimate load of the specimen. In addition, there is usually a certain amount of looseness or 'play' in the LVDT device when attaching it to a geosynthetic specimen, which directly influences its strain measurement results. This 'play' also causes an inconsistency in the starting point. Since the starting point continuously changes during the tensile test, it must be manually and carefully set by the

operator. Moreover, the additional weight of the LVDT itself leads to fluctuations in measured strains because the LVDT naturally tends to pull itself downward. This has been especially noticed when higher load levels and loose constructions geotextile fabrics are used (Skochdopole et al., 2000).

2.2. METHODS THAT CAN POTENTIALLY BE USED FOR MEASURING DISPLACEMENT/STRAIN OF GEOSYNTHETICS

In recent years, non-contact methods have been gaining more popularity in many geotechnical engineering applications and can potentially be used to measure the displacement of geosynthetics during tensile tests. These non-contact methods include video extensometer, laser extensometer, image-based particle tracking method, and conventional photogrammetry.

2.2.1. Video Extensometer. The video extensometer measures displacements by monitoring the separation of two contrasting gauge marks placed on a specimen (Jones 2000). The gauge marks can be in the form of dots or lines and are applied to the specimen using a wide variety of methods. Prior to running a test, the software uses a neural network to search the image for marks that are compatible with a library of acceptable marks. Image processing algorithms then track the center of the marks, which ensures accurate displacement measurement even if the gauge marks were distorted during a test involving high elongation. Jones (2000) used video extensometry to measure the strain of three different geotextiles during tensile tests by tracking two contrasting lines placed on the specimen. Depending on the lens selection, a calibration procedure was needed for a particular optical field of view. The geotextiles were tested in their machine and cross-machine directions, and the displacements were measured with a

conventional direct contact extensometer and a non-contact image-based video extensometry technique. The results showed that the image-based methodology for measuring displacements had accuracy values in the range of 86–100% relative to the extensometer.

2.2.2. Laser Extensometer. Laser extensometer is another non-contact method which uses a laser scanner to measure the spacing between the reflective tape strips on a sample. Skochdopole et al. (2000) used a laser extensometer with a separation capacity of 280 mm to determine the displacements and strains in wide-width tensile tests conducted on geosynthetics. In general, the calculated strains were comparable with those obtained using the crosshead extension method. Laser extensometer has many advantages over contact methods. It can eliminate any stresses being introduced to the specimen by knife edges associated with extensometer types. It is also easy to set up and align. In addition, laser extensometer can measure high elongation of samples. However, this method can only measure the overall strain at the locations within two reflective strips. The full-field strain distribution cannot be obtained.

2.2.3. Image-Based Tracking Techniques. Image-based tracking techniques identify and track the movement of particles in a series of captured digital images. These techniques have been receiving increased attention in geotechnical engineering.

Raschke et al. (1996) developed an image-based technique to track the movements of granular soil particles from video images captured through a transparent planar viewing window. A thresholding technique was used to segment the individual particle trajectories. However, this method required the plane strain and certain axisymmetric test conditions.

Paikowsky and Xi (2000) developed a system that provided detailed tracking of a large number of particles for studying the fundamental mechanism of particulate materials through the use of charge-coupled device (CCD) cameras and semi-automatic image processing and analysis algorithms.

Alshibli and Sture (2000) used a video camera to record the sand specimen deformation during compression. The deformation of the sand specimen was monitored by tracking the displacement of the grid imprinted on the membrane surface.

Very few studies exist that applied image-based tracking techniques to the testing of geosynthetics. Aydilek et al. (2004) used an image-based tracking technique to measure strain distribution in geosynthetics during tensile test. This method employed a block-based matching technique using software. It was assumed that the image frames were composed of small moving patterns rather than particular objects in the images. The macroblock size, matching criterion, and search strategy were the factors that controlled the performance of the method. Localized strain zones in a geosynthetic during tensile test were identified using the image-based tracking technique. It was also found that the strain values measured by the image-based method were comparable with the average strain values obtained by extensometer.

Mishra et al. (2017) used the particle image velocity (PIV) technique to capture the strain distribution in five types of geotextiles during tensile tests. An inexpensive complementary metal-oxide semiconductor camera was used in this method. The images were processed by an open source module called GeoPIV-RG. The authors reported that the method could give accurate measurements of deformation patterns within an acceptable tolerance.

None of the above-mentioned image-based particle tracking methods mentioned camera calibration, which is an indispensable step for all image analysis methods. This is due to the fact that all image-based methods implicitly assume the camera as a pinhole camera with fixed focal length, while commercially available cameras often have multiple lenses. As a result, the images captured with these cameras have distortions at different locations. Camera calibration is necessary to correct such image distortions. Moreover, all the above-mentioned image-based particle tracking methods used zoom-lens cameras whose focal lengths can change during the tests. Generally, image-based tracking technique compares the same region or pattern in one image frame and the next image frame, and if the focal length of the camera used is not fixed, a small amount of movement of the testing sample will cause the focal length to change, which can lead to misleading results in the image analysis process. Furthermore, most existing image-based methods often use 2D images taken from one single camera. As a result, the assumption that the installed geosynthetics are initially planar and maintain as a plane during the testing period is needed. In addition, existing image-based methods require accurate control of the camera position. The shooting directions are also required to be exactly perpendicular to the assumed plane. All these requirements are nearly impossible to achieve as will be shown in later discussions. The inability to satisfy all these requirements may lead to unreliable or misleading results.

2.2.4. Conventional Photogrammetry. Photogrammetry is defined as the science and technology of obtaining reliable information about physical objects through the processes of recording, measuring, and interpreting photographic images.

Conventional one-camera-based photogrammetry has been widely used for 3-D reconstruction and deformation measurements in multiple fields, such as surveying, geology and mining, agriculture, architecture, and civil engineering. Only one camera is needed to take multiple images of a stationary object and the 3-D measurement results can be obtained. However, conventional photogrammetry can only be used for 3-D reconstruction of stationary objects. It cannot be used for dynamic tests, such as the tensile test in which the object is continuously deforming. Consequently, conventional one-camera-based photogrammetry is not applicable to the strain/displacement measurement of geosynthetics during the tensile test. The proposed multi-camera-based photogrammetric method aims to overcome the limitation of conventional one-camera-based photogrammetry and track the continuous deformation of geosynthetics during the tensile test.

3. THEORETICAL BASIS OF THE PROPOSED METHOD

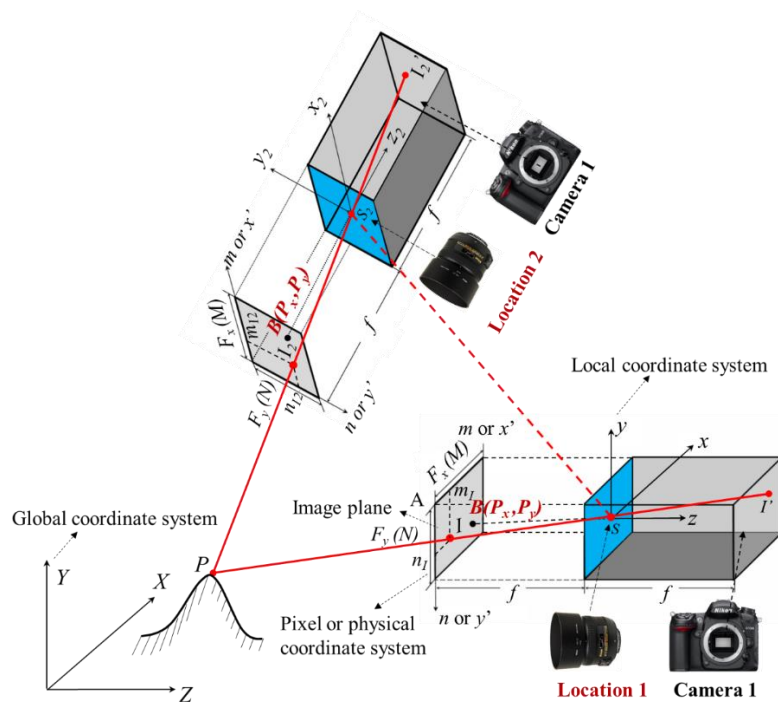
To overcome the above-mentioned limitations, a multi-camera-based photogrammetric method is proposed to measure the accurate 3-D full-field deformation of geosynthetics during tensile test. The proposed photogrammetric method extends the conventional one-camera-based photogrammetry for static object measurements to multi-camera-based photogrammetry for object measurements with continuous movements and/or deformation. The theoretical basis of the proposed multi-camera based photogrammetric method is explained in detail in this section.

3.1. DETERMINATION OF THE 3-D POSITIONS AND ORIENTATIONS OF THE CAMERAS

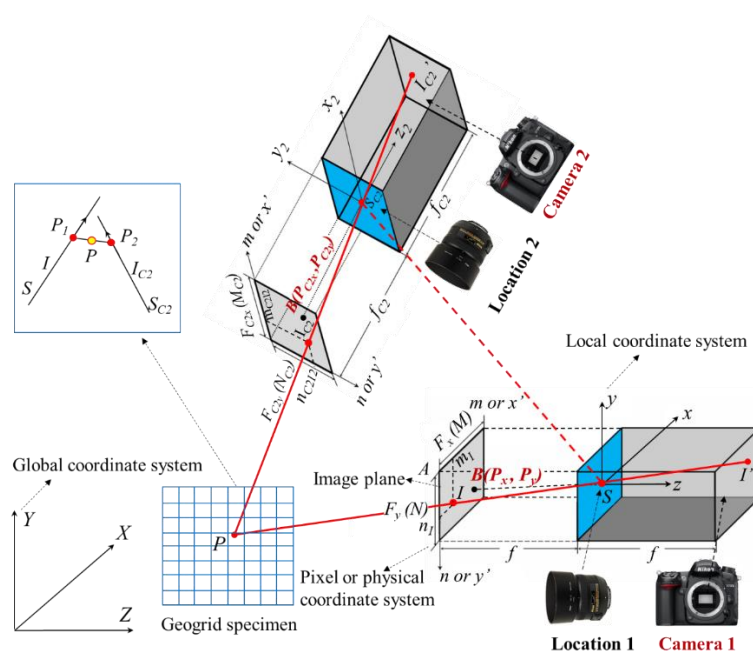
Figure 1a shows the principle of determining the 3-D positions and orientations of the camera using conventional photogrammetry. Assume that point I' in Figure 1a is the image point of an object point P in an image taken by a camera at location 1. In photogrammetry, the image plane in Figure 1a is depicted at the left side of the pinhole S (perspective center of the camera), rather than at the right, as it would have been the case with the image sensor of an actual camera. This allows one to work with image geometry as if on a right-reading paper print or film dispositive rather than on a photographic negative. The new image point is point I on the left image plane. The object point P, the image point I in the image plane, and the perspective center of the camera S lie on the same line of sight in 3-D space as shown in Figure 1a.

In the image plane, two 2-D coordinate systems can be set, one is the pixel coordinate system mAn and the other is the physical coordinate system $x'Ay'$. The upper left corner of the image plane (point A in Figure 1a) is defined as the origin of both coordinate systems. In the image plane, the dimensions of the sensor sizes in the x' and y' directions are F_x and F_y , respectively. The total numbers of pixels in the x' and y' directions are M and N , respectively. Therefore, for the image point I with pixel coordinates, the relationship between the pixel coordinate system and the physical coordinate system can be expressed as follows:

$$\begin{bmatrix} x'_I \\ y'_I \end{bmatrix} = \begin{bmatrix} F_x/M & 0 \\ 0 & F_y/N \end{bmatrix} \begin{bmatrix} m_I \\ n_I \end{bmatrix} \quad (1)$$



(a)



(b)

Figure 1. Principles of the proposed photogrammetric method: (a) principle of conventional photogrammetry (modified from Zhang et al. (2015)), and (b) principle of the proposed mid-point method

where x'_I, y'_I are the coordinates of point I (mm) in the physical coordinate system $x'Ay'$, and F_x, F_y are the format sizes of the image sensor in the x' and y' directions, respectively (mm).

A 3-D coordinate system called the local coordinate system xyz is also constructed as shown in Figure 1a. The pinhole S is defined as the origin of the local coordinate system. Suppose the projection of the pinhole S in the physical coordinate system is a point with coordinates of (P_x, P_y) , as point B shown in Figure 1a, and the focal length of this camera is f , the coordinates of image point I in the 3-D local coordinate system can be calculated as follows:

$$\begin{bmatrix} x_I \\ y_I \\ z_I \end{bmatrix} = \begin{bmatrix} x'_I - P_x \\ -y'_I + P_y \\ -f \end{bmatrix} \quad (2)$$

where x_I, y_I, z_I are the coordinates of point I in the local coordinate system (mm).

Normally multiple images are taken at different locations and orientations using the SAME camera, and each image has its own local coordinate system. Conventional photogrammetry involves the analyses of multiple images taken by ONE CAMERA at different orientations. As a result, a global coordinate system is also needed so that all the images are analyzed in the same coordinate system. For convenience, uppercase X, Y, and Z are used to represent the coordinates of any point in this global system as shown in Figure 1a. Then, the coordinates of the image point I in the global coordinate system can be calculated as follows:

$$\begin{bmatrix} X_I \\ Y_I \\ Z_I \end{bmatrix} = R(\omega, \varphi, \kappa) \begin{bmatrix} x_I \\ y_I \\ z_I \end{bmatrix} + \begin{bmatrix} X_S \\ Y_S \\ Z_S \end{bmatrix} \quad (3)$$

where X_I, Y_I, Z_I are the coordinates of point I in the global coordinate system (mm); X_S, Y_S, Z_S are the global coordinates of the camera location; ω, φ, κ are the orientations of the camera. ω is the rotation about the x-axis, φ is the rotation about the y-axis, and κ is the rotation about the z-axis. They are right-hand system as defined in the conventional photogrammetry theory (Mikhail et al., 2001); and R is the rotation matrix which is defined as

$$R = \begin{pmatrix} \cos \kappa \cos \varphi & -\sin \kappa \cos \varphi & \sin \varphi \\ \cos \kappa \sin \omega \sin \varphi + \sin \kappa \cos \omega & -\sin \kappa \sin \omega \sin \varphi + \cos \kappa \cos \omega & -\sin \omega \cos \varphi \\ -\cos \kappa \cos \omega \sin \varphi + \sin \kappa \sin \omega & \sin \kappa \sin \omega \cos \varphi + \cos \kappa \sin \omega & \cos \omega \cos \varphi \end{pmatrix} \quad (4)$$

The same object point P appears as an image point I2 in the second image taken at location 2 with the same camera as shown in Figure 1a. The coordinates of I2 in the global coordinate system can be calculated using the same procedures described above as follows:

$$\begin{bmatrix} X_{I2} \\ Y_{I2} \\ Z_{I2} \end{bmatrix} = R_2(\omega_2, \varphi_2, \kappa_2) \begin{bmatrix} x_{I2} \\ y_{I2} \\ z_{I2} \end{bmatrix} + \begin{bmatrix} X_{S2} \\ Y_{S2} \\ Z_{S2} \end{bmatrix} \quad (5)$$

where X_{I2}, Y_{I2}, Z_{I2} are the coordinates of point I2 in the global coordinate system (mm); X_{S2}, Y_{S2}, Z_{S2} are the global coordinates of camera location S2; $\omega_2, \varphi_2, \kappa_2$ are the camera orientation angles; and R_2 is the rotation matrix for the camera at location S2. In Figure 1a, three lines, SS_2 , SI , and S_2I_2 are in the same plane, which can be described as the following equation:

$$\overline{SS}_2 \cdot (\overline{SI} \times \overline{S_2I_2}) = 0 \quad (6)$$

Eq. (6) includes the following unknowns: Camera positions, $X_S, Y_S, Z_S, X_{S_2}, Y_{S_2}, Z_{S_2}$, and camera orientation angles, $\omega, \varphi, \kappa, \omega_2, \varphi_2, \kappa_2$. These unknowns can be solved by building a system of equations for multiple conjugate image points. Therefore, the 3-D positions and orientations of the camera can be determined. Once the camera positions and orientations are known, the 3-D coordinates of the object point P in the global coordinate system can be obtained from the two images. More details regarding the theory of conventional photogrammetry can be found in Mikhail et al. (2001).

3.2. A MID-POINT METHOD FOR 3-D RECONSTRUCTION OF MOVING GEOGRIDS DURING TENSILE TESTS

In the conventional photogrammetry as described above, only one camera is used to take at least two images at different locations and orientations to reconstruct the 3-D model of a static object. It cannot be used to reconstruct the 3-D model of objects during dynamic tests with continuous movements and/or deformation, such as the deforming geosynthetics in a tensile test. One possible solution is to use multiple cameras to overcome this limitation. For example, two or more cameras can be used to synchronously take images/videos of the same object during dynamic tests, as shown in Figure 1b. The locations and orientations of the two cameras can be calculated following the same procedures as those in the conventional one-camera photogrammetry. Once the locations and orientations of the two cameras are known, the images/videos taken by the two cameras at the same moment can be used to reconstruct the 3-D model of the object at that moment. It should be noted that although only two cameras were used in this

paper as an example, the same method described here can be easily applied to multi-camera-based tests and better results are expected.

As shown in Figure 1b, assume that the 3-D positions and the rotation matrix for

the first camera at location 1 are $S = \begin{pmatrix} X \\ Y \\ Z \end{pmatrix}$ and R , respectively, which can be obtained

by the method described in the previous section using the conventional photogrammetric analyses. The mathematical description of the light ray SI from the first camera is given by

$$\overline{SI} = \begin{pmatrix} X_I \\ Y_I \\ Z_I \end{pmatrix} - \begin{pmatrix} X_S \\ Y_S \\ Z_S \end{pmatrix} \quad (7)$$

where X_I, Y_I, Z_I are the coordinates of the point I in the global system (mm), as shown in Figure 1b; X_S, Y_S, Z_S are the coordinates of the pinhole S in the global coordinate system (mm), as shown in Figure 1b.

Point I also appears in the image as I_{C2} that is taken by the second camera at location 2 as represented by S_{C2} shown in Figure 1b. Similarly, points P , I_{C2} , and S_{C2} are on the same line, and one can obtain the equation for the light ray $PI_{C2}S_{C2}$ as follows:

$$\overline{S_{C2}I_{C2}} = \begin{pmatrix} X_{IC2} \\ Y_{IC2} \\ Z_{IC2} \end{pmatrix} - \begin{pmatrix} X_{C2} \\ Y_{C2} \\ Z_{C2} \end{pmatrix} \quad (8)$$

where $X_{IC2}, Y_{IC2}, Z_{IC2}$ are the coordinates of the point I in the global system for the second camera as shown in Figure 1b. The subscript C2 denotes the second camera.;

$X_{C_2}, Y_{C_2}, Z_{C_2}$ are the coordinates of the pinhole S_{C_2} for the second camera in the global coordinate system XYZ as shown in Figure 1b.

As a result, the unit direction vector passing points S and I is given by:

$$\vec{i} = \frac{\overline{SI}}{|\overline{SI}|} = \frac{1}{\sqrt{(X_I - X)^2 + (Y_I - Y)^2 + (Z_I - Z)^2}} \begin{pmatrix} X_I - X \\ Y_I - Y \\ Z_I - Z \end{pmatrix} \quad (9)$$

Similarly, the unit direction vector passing points S_{C_2} and I_{C_2} is given by:

$$\vec{i}_2 = \frac{\overline{S_{C_2}I_{C_2}}}{|\overline{S_{C_2}I_{C_2}}|} = \frac{1}{\sqrt{(X_{IC_2} - X_{C_2})^2 + (Y_{IC_2} - Y_{C_2})^2 + (Z_{IC_2} - Z_{C_2})^2}} \begin{pmatrix} X_{IC_2} - X_{C_2} \\ Y_{IC_2} - Y_{C_2} \\ Z_{IC_2} - Z_{C_2} \end{pmatrix} \quad (10)$$

Based on the mathematic description of the two light rays discussed in the previous section, the two light rays, namely SI and $S_{C_2}I_{C_2}$ in Figure 1b, can be expressed as two 3-D vectors as follows:

$$\text{Line 1 (} SI \text{ in Figure 1b): } L_1 = C + t\vec{i} \quad (11)$$

$$\text{Line 2 (} S_{C_2}I_{C_2} \text{ in Figure 1b): } L_2 = C_{C_2} + t_2\vec{i}_2 \quad (12)$$

where $C = \begin{pmatrix} X_S \\ Y_S \\ Z_S \end{pmatrix}$, $C_{C_2} = \begin{pmatrix} X_{C_2} \\ Y_{C_2} \\ Z_{C_2} \end{pmatrix}$; t and t_2 are two scalar parameters.

Due to unavoidable computational errors, it is most likely that the two lines SI and $S_{C_2}I_{C_2}$ will not intersect (as shown in the upper left panel of Figure 1b). Instead, they are skew lines SIP_1 and $S_{C_2}I_{C_2}P_2$ in the 3-D space. To solve this problem, a mid-point method is proposed to find the 3-D coordinates of the object point P . It is assumed that the object point P is the mid-point of the shortest line segment connecting the two lines as represented by P_1P_2 In Figure 1b. In other words, the mid-point is assumed to be “true”

location of point P . The mathematical procedure to find the mid-point is described as follows.

Assume that line P_1P_2 as shown in the upper left panel of Figure 1b is a line which is perpendicular to the two lines SI and $S_{C_2}I_{C_2}$, and P_1 and P_2 are the two intersecting points on the two lines, respectively. Consequently, the direction of line P_1P_2 can be calculated by the cross product of \vec{i} and \vec{i}_2 as follows:

$$\vec{n} = \vec{i} \times \vec{i}_2 \quad (13)$$

The normal to the plane IP_1P_2 has a normal as follows:

$$\vec{n}_1 = \vec{i} \times \vec{n} \quad (14)$$

Accordingly, the normal of the plane $I_{C_2}P_1P_2$ has a normal as follows:

$$\vec{n}_2 = \vec{i}_2 \times \vec{n} \quad (15)$$

The intersecting point between line SI and the plane $I_{C_2}P_1P_2$ is P_1 , and its coordinate can be solved as follows:

$$P_1 = C + \frac{(C_{C_2} - C) \cdot \vec{n}_2 \cdot \vec{i}}{\vec{i} \cdot \vec{n}_2} \vec{i} \quad (16)$$

Similarly, the intersecting point between line $S_{C_2}I_{C_2}$ and the plane IP_1P_2 is P_2 , and its coordinate can be solved as follows:

$$P_2 = C_{C_2} + \frac{(C - C_{C_2}) \cdot \vec{n}_1 \cdot \vec{i}_2}{\vec{i}_2 \cdot \vec{n}_1} \vec{i}_2 \quad (17)$$

Thus, the mid-point of the segment formed by the intersecting points P_1 and P_2 is given by

$$P = \frac{P_1 + P_2}{2} = \frac{C + C_{C2} \frac{(C_{C2} - C) \cdot \bar{n}_2 \cdot \bar{i} + (C - C_{C2}) \cdot \bar{n}_1 \cdot \bar{i}_2}{\bar{i} \cdot \bar{n}_2} + \frac{(C - C_{C2}) \cdot \bar{n}_1 \cdot \bar{i}_2}{\bar{i}_2 \cdot \bar{n}_1}}{2} \quad (18)$$

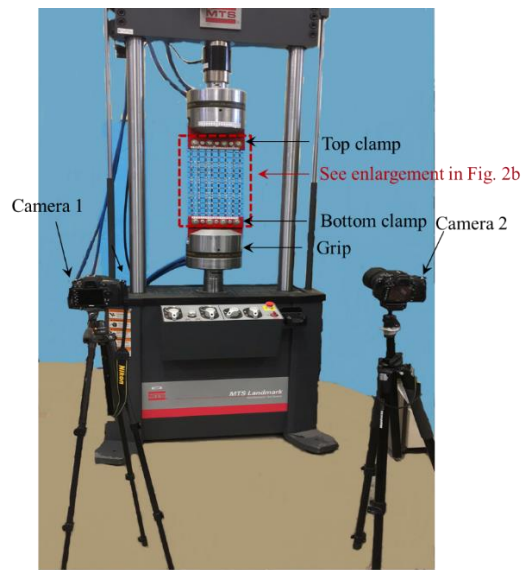
In Equation (18), P represents the coordinates of the object point in the 3-D space. The global coordinate system is used in Equations (16)-(18). By using the method described above, the coordinates of all the points on an object can be calculated and the 3-D model of the object can be obtained. During a dynamic test, an object can be continuously moving/deforming. Two digital cameras can be used to take videos of the testing process. By using the proposed method, the 3-D models of the moving/deforming object could be obtained.

Figure 1b describes the two-camera scenario. In the upper left panel of Figure 1b, there are two rays, P_1I and P_2I_{C2} . If there are N cameras (N is greater than two), there are N light rays, $P_1I, P_2I_{C2}, \dots, P_nI_{Cn}$. If there is no error, all these light rays will converge to the same point P . However, errors unavoidably exist in the measurement and computational processes and it is very likely that these N light rays will not intersect in the 3-D space. A least-square optimization technique is proposed in Zhang et al. (2015) to address this problem. It was considered that although the N light rays might not intersect with each other, each light ray represents an estimate of the light source of the object point P . As a result, the “true” location of point P should be close to those rays and has the shortest distances to those rays. It is therefore postulated that if the sum of square of a point’s distances to all the rays is the minimal, the point is the light source where all the rays are generated. More details regarding the least-square optimization technique can be found in Zhang et al. (2015).

4. EXPERIMENTAL DESIGN

4.1. SPECIMEN PREPARATION AND TEST METHOD

Figure 2a shows an experimental setup of a tensile test to validate the proposed method. An MTS Landmark 370 load frame equipped with a rated loading capacity of 250 kN was used to perform the tensile test for geosynthetics. Biaxial geogrids (BasXgrid 11) were used as a representative geosynthetic to demonstrate the effectiveness and accuracy of the proposed method, although the same method can be



(a)

Figure 2. Geogrid tensile test setup and the geogrid specimen: (a) geogrid tensile test setup for the deformation analysis using the photogrammetric method and conventional methods, (b) geogrid specimen with coded targets attached, (c) a typical coded target, and (d) enlarged extensometer with coded targets measured by both extensometer and the proposed photogrammetric method.

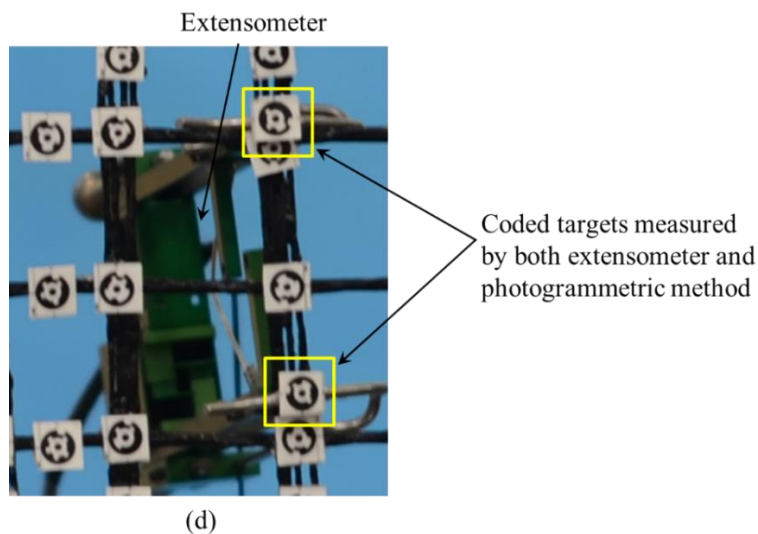
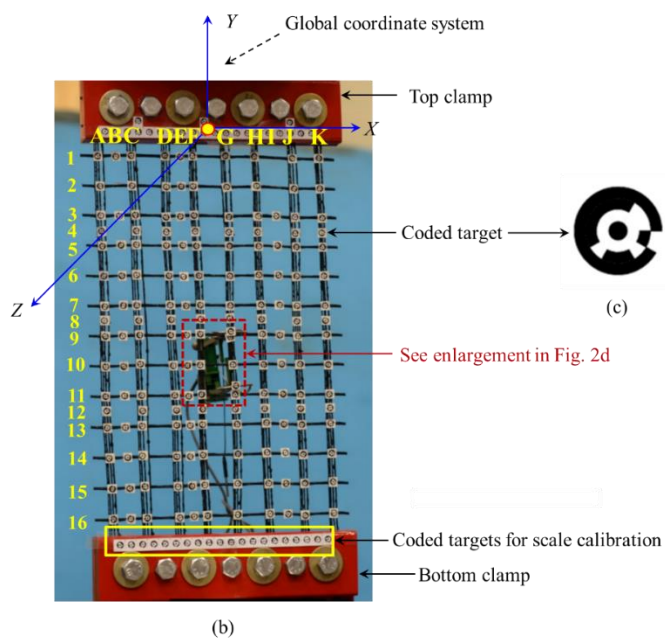


Figure 2. Geogrid tensile test setup and the geogrid specimen: (a) geogrid tensile test setup for the deformation analysis using the photogrammetric method and conventional methods, (b) geogrid specimen with coded targets attached, (c) a typical coded target, and (d) enlarged extensometer with coded targets measured by both extensometer and the proposed photogrammetric method. (cont.)

easily applied to a wide range of other geosynthetics. The material properties of the geogrids used in the tests are listed in Table 1. The dimensions of the specimen were

selected in accordance with ASTM D6637/D6637M-15 (2015), which were approximately 25 cm in width and 35 cm in length. Customized clamps were used to fix the top and bottom edges of the specimens to the machine as shown in Figures. 2a and 2b. These clamps were used to minimize the slippage of the specimen during the tensile test.

Table 1. Properties of the test geogrid specimen.

Material	Mass per unit area (g/m ²)	Aperture size (mm)	Tensile modulus (at 1% strain)	Wide width tensile strength (kN/m)			
				At 1% strain	At 2% strain	At 5% strain	At ultimate
Polyester	405	25.4	437	4.3	7.3	13.4	29.2

To employ the proposed method, some coded targets were placed at different locations in the geogrid sample as shown in Figure 2b. A coded target is a high contrast dot, which is automatically recognized by a computer algorithm. Figure 2c shows an enlarged coded target. The outer ring of the coded target was used to define the identification number based upon if there is a protrusion at every 30-degree interval, and each coded target is different with a unique identification number. (Fernandez-Fernandez et al., 2013; Xia et al., 2021) The centroid of the inner solid round point is used to define the location of the coded target. Since the centroid of the coded target is a mathematic point without physical dimension, the coded target can be used to achieve a sub-pixel accuracy. A total of forty coded targets were also attached to the clamps at both ends of the specimen to measure the displacements of the clamps as shown in Figure 2b. During the test, the top grip of the MTS machine is fixed, and the bottom grip is moveable to apply the desired displacement or load for the tensile test. Consequently, the coded

targets posted on the top clamp, which are always fixed together with the top grip during the test, were used to set up the global coordinate system as shown in Figure 2b. In this way, all the measurements could be made in the same coordinate system and comparisons among measurements can be performed.

To compare the accuracy of the proposed method with conventional methods, an extensometer was mounted to the middle of the back of the specimen, and two coded targets were placed on both ends of the extensometer. Figure 2d shows the enlarged image of the extensometer with two coded targets attached. The displacements of these two coded targets were measured by both extensometer and the proposed photogrammetric method, so the results obtained from the two methods can be compared.

4.2. CAMERA CALIBRATION AND IMAGE IDEALIZATION

Camera calibration in the context of 3-D scene reconstruction is the process of determining the internal camera geometric parameters and optical characteristics (intrinsic parameters) (Tsai, 1987). Camera calibration is a necessary step in most 3-D scene reconstruction to extract precise and reliable 3-D metric information from images. In the photogrammetry, the cameras are assumed to be the pinhole cameras. However, a commercial camera is not pinhole camera. This is because a commercial camera often uses multiple lenses for focusing light and its aperture is not a single point. These lenses often slightly bend the light rays either outwards or inwards, which results in distorted images (images subjected to barrel or pincushion distortions). In addition, the focal length and the format size of the image sensor can be different from the specifications in the user's manual. All these can lead to inaccurate 3-D reconstruction results if the camera is

not calibrated. In order to achieve highly accurate measurements, the camera needs to be calibrated for the photogrammetric analyses. The camera calibration parameters can be used to correct lens distortion and measure the size of an object in world units. There are many commercial or free software options that can be used for camera calibration, such as Camera Calibrator in Matlab (Zhang, 2000), FAUCCAL, and Agisoft PhotoScan. Since camera calibration is a well-established technique, the details and procedure of camera calibration are not elaborated in this paper. After camera calibration, the obtained camera parameters were then used to correct the image distortions. In this process, the distorted images (either barrel shape or pincushion shape) were converted into undistorted images, which reflected its true shape. This process is called image idealization. Image idealization was performed on each of the processed images.

It is worth noting that there are no specific requirements for the cameras' focal lengths for the proposed method. In this study, two existing digital cameras readily available in the laboratory—a Nikon D7000 and a Nikon D7100—were used to validate the proposed method. The focal lengths of the lens of the two cameras were 50 mm and 80 mm, respectively, according to their specifications. The camera parameters before and after calibration are listed in Table 2. As can be seen in Table 2, before idealizations, the

Table 2. Parameters of the cameras used in this study.

Camera IDs	Focal length(mm)	Format size		Principal point		Radial distortion			Tangential distortion	
		Width(mm)	Height(mm)	P _x (mm)	P _y (mm)	K ₁	K ₂	K ₃	P ₁	P ₂
Before idealization										
Camera 1	55.774	24.002	15.990	12.417	7.984	6.222×10^{-5}	0	0	2.205×10^{-5}	2.130×10^{-5}
Camera 2	83.340	36.003	24.000	18.228	11.893	2.551×10^{-5}	0	0	3.363×10^{-6}	4.688×10^{-6}
After idealization										
Camera 1	55.774	25.151	16.657	12.575	8.328	0	0	0	0	0
Camera 2	83.340	36.887	24.589	18.443	12.295	0	0	0	0	0

focal lengths of the two cameras are 55.774 and 83.340 mm respectively, which are different from the 50 and 80 mm in the specifications provided by the manufacturer. The format sizes are 24.00mmX15.990 mm and 36.003mmX24.000mm, which are also different from 24.0 mmX16.0 mm and 36.0mmX24.0mm as given in the user's manuals for the two cameras. In addition, the principal points of the two cameras are not exactly at the centers of the image sensors, either. Furthermore, there are radial and tangential distortions for the images taken by these two cameras, as indicated by the non-zero parameters of K1, P1, and P2 in Table 2. As can be seen in Table 2, after image idealization, the principal points of the two cameras are exactly at the centers of the image sensors and there is no distortion any more as indicated by all zeros for the radial and tangential distortion parameters.

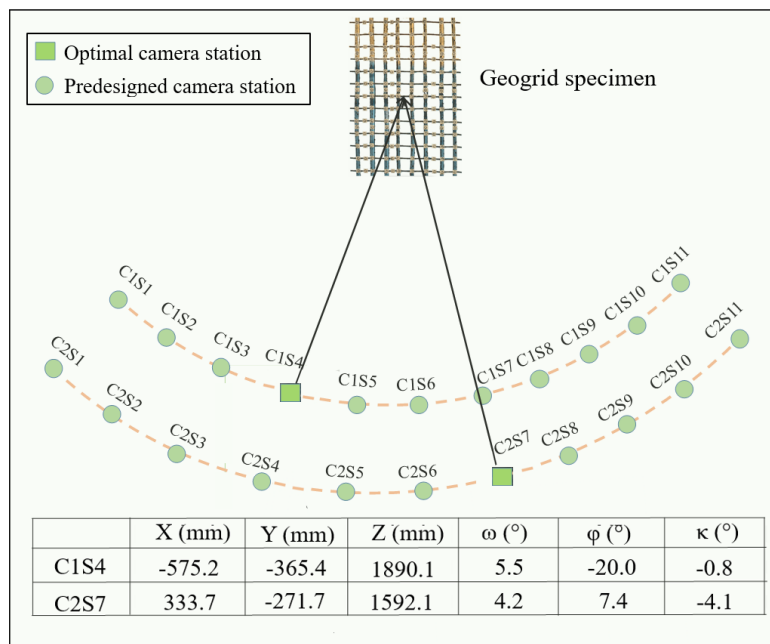
4.3. DETERMINATION OF THE OPTIMAL CAMERA STATIONS AND ORIENTATIONS

The proposed method uses two cameras to take images with overlapping for 3-D reconstruction. To achieve successful 3-D photogrammetric reconstruction, the images taken by the two cameras had to satisfy two requirements: (1) the stations and shooting directions of the two cameras must be close enough to achieve sufficient overlap, and (2) the differences in the stations and shooting directions of the two cameras should be large enough to ensure the successful application of the photogrammetric method.

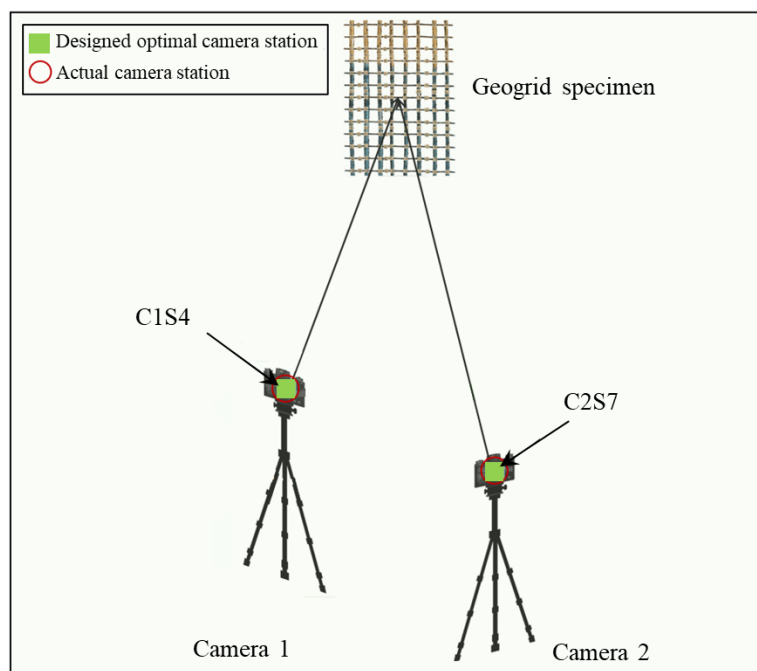
Consequently, there exists an optimal camera position and orientation for each of the two cameras. These optimal camera positions and orientations satisfy both the two aforementioned requirements and can thus produce more accurate 3-D reconstruction

results. The procedures for determining the optimal camera positions and orientations were as follows:

- (1) Draw two concentric arcs on the floor in front of the geogrid specimen as shown in Figure 3a. The centers of the two concentric arcs were approximately set at the origin of the global coordinate system as shown in Figure 2b. Two arcs were needed to ensure good image quality due to the different camera focal lengths.
- (2) Select a group of predesigned camera positions on the first arc as shown in Figure 3a. These camera positions were equally distributed from the leftmost to the rightmost. In Figure 3, the subscripts of C and S denote the camera IDs and the camera station IDs, respectively. For example, C1S1 denote the first camera station of the first camera. The predesigned shooting directions for the cameras are represented by lines connecting the cameras and the center of the arc, as denoted by the solid lines in Figure 3a.
- (3) Fix the first camera on the tripod at a height of approximately the same as the center of the geogrid specimen and take images of the whole testing system at the predesigned camera positions.
- (4) Perform a photogrammetric analysis to back-calculate the actual camera positions and orientations and reconstruct the 3-D model of the testing system from which the 3-D coordinates of the coded targets on the specimen could be obtained as shown in Figure 4a.
- (5) Repeat Steps (3) and (4) for the second camera. Figure 4b shows the photogrammetric analysis results obtained from the second camera.

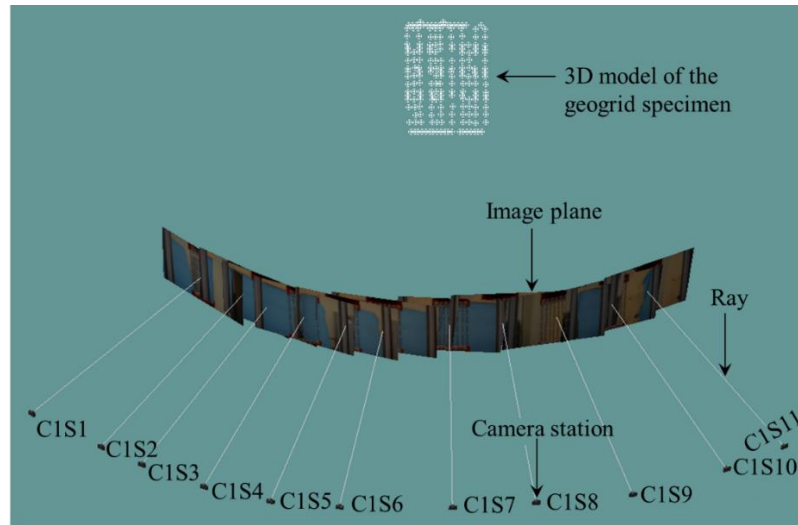


(a)

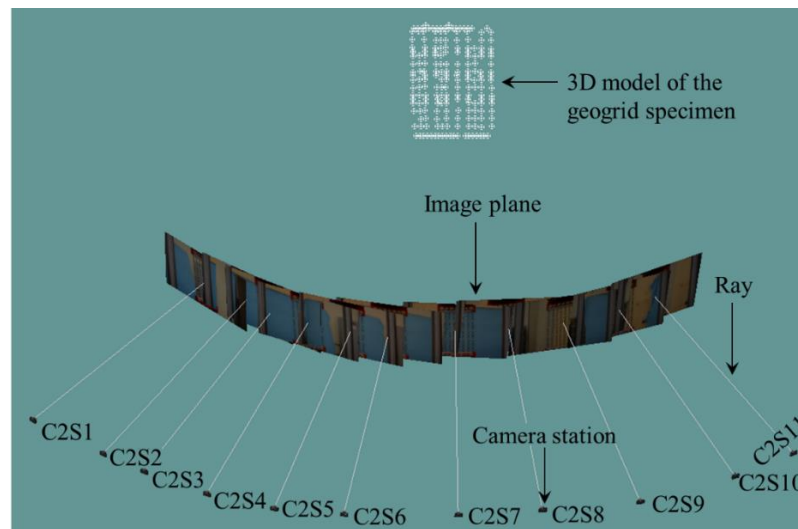


(b)

Figure 3. Determination of the camera stations and shooting directions: (a) determination of the optimal camera stations and shooting direction, and (b) determination of the actual camera stations and shooting directions



(a)



(b)

Figure 4. 3-D models of the geogrid specimen and the camera stations. (a) 3-D model of the geogrid specimen and the camera stations for the first camera; (b) 3-D model of the specimen and the camera stations for the second camera

- (6) Randomly select two images taken by the two cameras at different locations such as C1S4 and C2S7 as shown in Figure 3b and use the method described in the “Theoretical Basis of the Proposed Method” section to calculate the 3-D coordinates of all coded targets. It was noted that the global coordinate system

used in steps (4) to step (5) must be the same, namely the global coordinate system as shown in Figure 2b, so that the results could be compared.

(7) Calculate the difference in the coded targets' coordinates between step (6) and step (4) or between step (6) and step (5). The camera positions and orientations which could produce the smallest overall differences with the results from step (4) or (5) are selected as the optimal camera positions and orientations for the two cameras.

(8) Once the optimal combination of camera positions was determined such as C1S4 and C2S7 as shown in Figure 3a, the two cameras were set up at the optimal positions and fixed as shown in Figure 3b. Two images were taken to replace the original images to repeat the two photogrammetric analyses as described in steps (4) and (5) from which the two camera positions can be accurately determined.

4.4. DATA COLLECTION REGARDING THE TENSILE TEST ON THE GEOGRID SPECIMEN

After the two cameras were fixed at the corresponding optimal locations, the cameras were ready for capturing images of the tensile test. The selected displacement rate for the tensile test was 2.54 mm/min. During the test, the two cameras took images synchronously using a wireless shutter remote-release control device. This device decreases the chances of damaging image integrity and quality caused by camera vibration when pressing the camera shutter button. Each camera took one image of the tensile test for every minute. This image acquisition rate was selected so that sixty images captured by the two cameras could properly record the whole testing process. The image

frames were saved into a file and processed by the proposed photogrammetric method from which the complete 3-D displacement/strain could be obtained. The extensometer was removed at the fifteenth minute to avoid being damaged. All the procedures of the proposed method had been implemented into a computer program, and the calculation was done by the program. The purpose of this paper is to validate the concept of the proposed method using images taken by two digital cameras. In reality, multiple cameras can be used to videotape the whole testing process and the same method can be applied to achieve better results. More research is on-going along this direction.

5. RESULTS AND DISCUSSION

The optimal camera positions and orientations are schematically shown in Figure 3. The rectangular boxes, C1S4 and C2S7, denote the optimal camera locations that were obtained using the method described previously. The two solid lines represent the optimal camera orientations. The 3-D camera positions (denoted by X, Y, and Z) and orientations (denoted by directional angles) for C1S4 and C2S7 are listed in the table in Figure 3a.

5.1. VALIDATION OF ACCURACY OF THE PROPOSED METHOD

The proposed photogrammetric method requires a scale to determine the 3-D real-world coordinates of the points on the geogrid specimen. This scale must be consistent with the actual size of the geogrids. The MTS Landmark 370 load frame machine has been calibrated with high accuracy of 1/1000 of an inch. Therefore, the controlled movements of coded targets posted on the bottom movable clamp in Figure 2b were used

for scale calibration for the proposed photogrammetric method. The 3-D coordinates of these points over time were calculated using the proposed photogrammetric method, for which the displacements of these points could be obtained. Eight images were taken for scale calibration. The average displacements of the points obtained by the photogrammetric method for these images were compared with the machine-controlled displacements of bottom clamp at the same moment, and the scale of the photogrammetric analyses was determined.

During the tensile test, the bottom clamp in Figure 2a was firmly attached to the grip. Therefore, a comparison between the machine-controlled movements of the bottom clamp and the displacement results obtained by the proposed method at different stages of the tensile test was conducted to verify the accuracy of the photogrammetric method. It should be noted that the images used for verifying the accuracy of the proposed method are different from those used for scale calibration so that more convincing results and conclusions can be obtained.

Figure 5 shows the comparison of the displacement results from the proposed method and the machine-controlled movements of the bottom clamp over a period of 25 minutes with an interval of 1 minute. The average displacement difference between the two methods was 0.25% and the average absolute displacement difference was 0.038mm. In comparison, Aydilek et al. (2004) reported an average accuracy of 8% when comparing their image-based method and extensometer. It is therefore concluded that the proposed method at the present version shows much higher accuracy than the existing

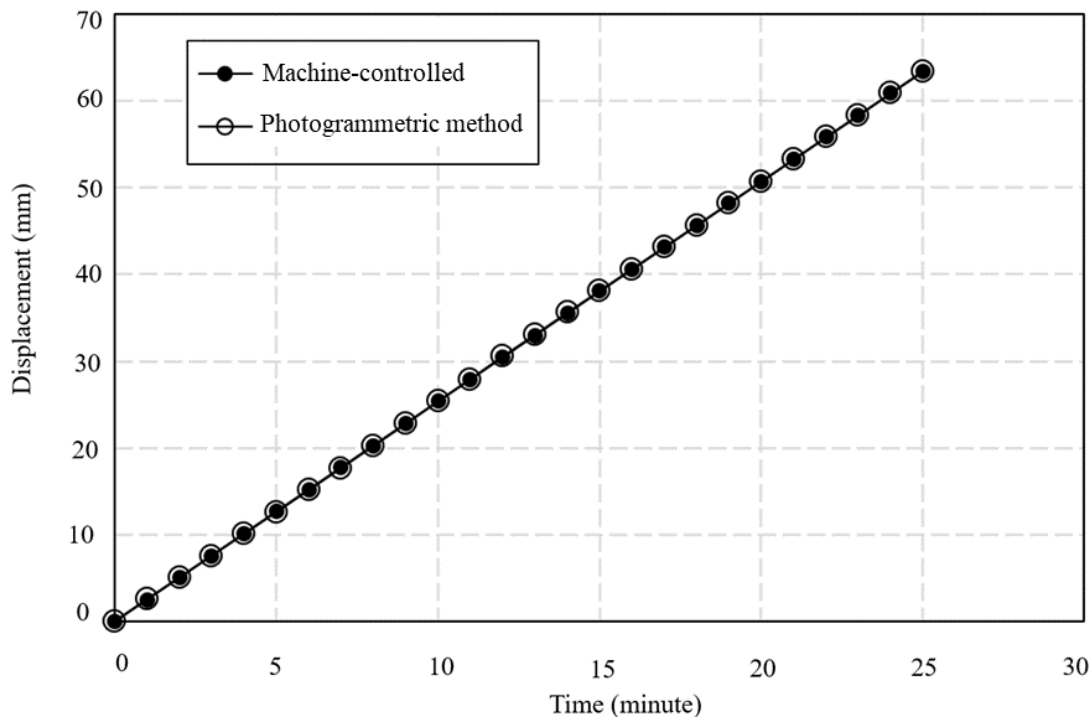


Figure 5. Comparison of the displacements obtained by machine-controlled bottom clamp movements and the proposed method

method. In this paper, only two cameras are used. If more cameras are used with the least square optimization technique as proposed in Zhang et al. (2015), even higher accuracy is expected.

There are several reasons the proposed photogrammetric method achieved such high accuracy. First, the proposed method used the cameras with fixed focal lengths. This means that the focal lengths of the cameras remained unchanged during the tests, which contributed to the high accuracy of the proposed method. Secondly, the cameras used for tensile the test were calibrated. As discussed previously, camera calibration is important for eliminating the image distortions and obtaining the optical camera parameters which are of great importance in accurately back-calculating the camera

positions and determining the 3-D coordinates of the objects. Many existing image-based methods do not use calibrated cameras, which can lead to unreliable results. Thirdly, the coded targets were used in the photogrammetric method. As discussed previously, the location of a coded target is represented by the centroid of the solid round point, which is a mathematical point without physical dimension. In this way, its accuracy can be less than one pixel, which is far more accurate than other existing methods in marking the points of interest in images. The high-accuracy coded target positions undoubtedly contributed to the high accuracy of the back-calculated camera positions and the subsequent displacement/strain results of the geogrid specimen. Finally, the camera positions and shooting directions were back-calculated using the proposed method rather than manually controlled, leading to mathematical solution with much higher accuracy.

The high accuracy of the proposed photogrammetric method obtained by the above comparison is also a strong indication of the repeatability and reproducibility of the proposed method since the measurements made for the geogrid specimen are independent of each other. In other words, Figure 5 actually presents 26 independent measurements against the machine-controlled displacements. For any data point in Figure 5, two images were taken synchronously from two optimal camera stations, namely C1S4 and C2S7, to reconstruct the 3-D model of the geogrid specimen. These images were taken at different times and with different degree of deformations of the geogrids. As a result, the measurements made by the proposed photogrammetric method are independent of each other. They are also independent of the machine-controlled displacements as shown in Figure 5. The high accuracy as indicated by the comparison for multiple stages measurements clearly indicated that the test results are repeatable and reproducible.

5.2. COMPARISON OF THE ACTUAL AND THE PREDESIGNED CAMERA STATIONS AND SHOOTING DIRECTIONS

As discussed previously, most existing image-based methods require manual control of the camera positions and shooting directions. Figure 6 compares the predesigned (or manually controlled) and actual (or back-calculated) camera positions for Camera 1 for analyses performed in Figure 4a. The actual shooting directions and the predesigned shooting directions are also shown in Figure 6. In Figure 6, the round points and dashed lines represent the predesigned camera positions and shooting directions, respectively. The square points and solid lines represent the actual camera positions and shooting directions, which were back-calculated using the photogrammetric analysis in step (8). In Figure 6, “PD” and “CS” represent predesigned camera station and actual camera stations. As shown in the table in Figure 6, the actual camera positions deviated from the predesigned camera positions with an averaged distance of 53.9 mm, and the average deviation of the shooting direction was 1.1 degrees. This is due to the fact that the perspective centers and shooting directions of the cameras were unknown and impossible to be accurately controlled. This was the reason why in the “Introduction” section, it was concluded that the existing image-based methods with manual camera position control can lead to unreliable results.

5.3. EVALUATION OF THE FULL-FIELD DISPLACEMENT OF GEOGRIDS

Conventional methods use the machine-controlled grip movement as the overall displacement of the geosynthetic in the tensile test. One major limitation of this method is that, although the movements of the grip can be accurately controlled by the machine, if there is specimen slippage at the grip faces, then the obtained results are misleading. In

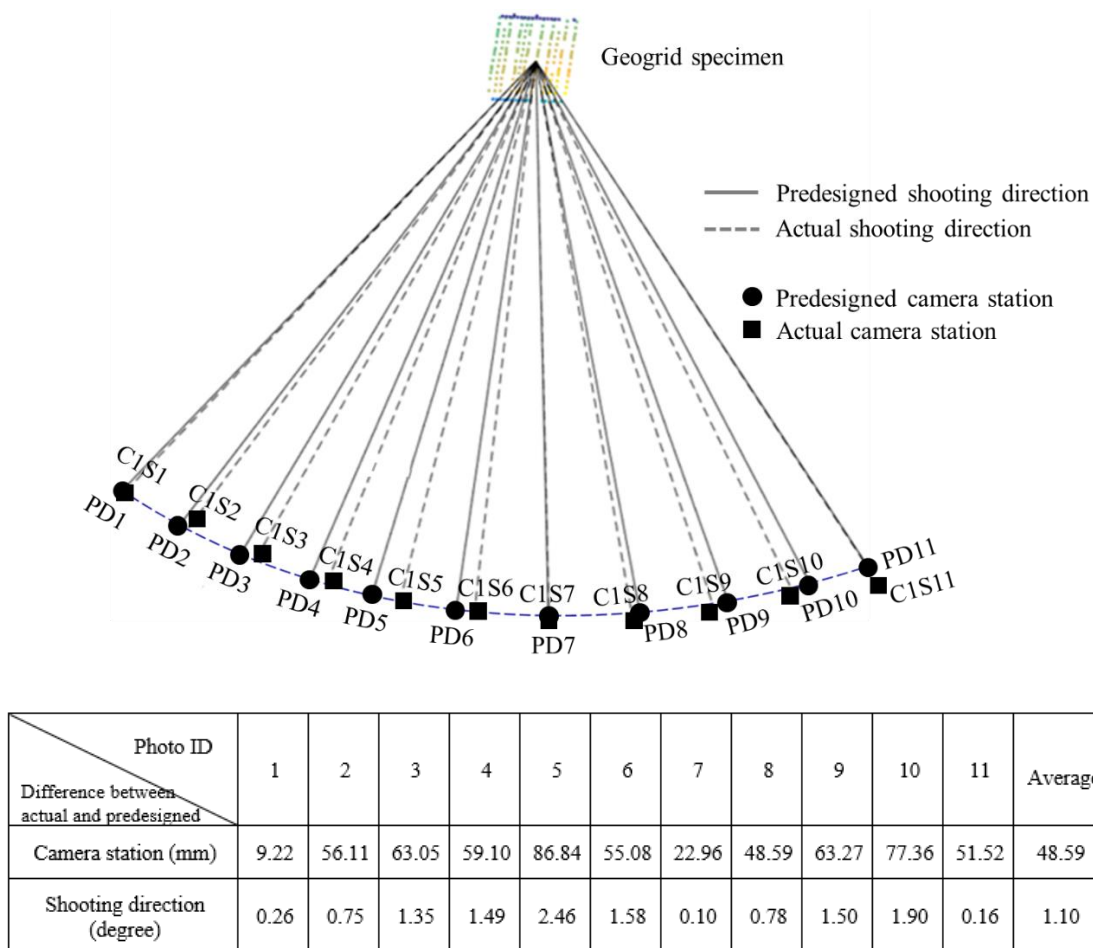


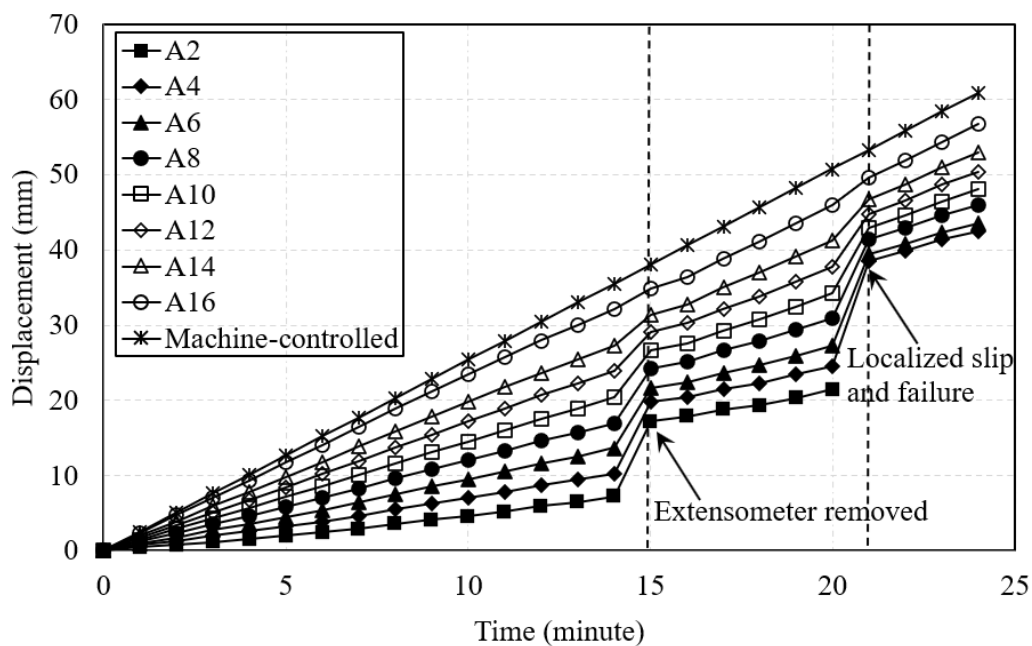
Figure 6. Comparison of the actual and predesigned camera stations and shooting directions for camera

contrast, the method proposed in the paper can not only provide the accurate measurements for the grip (or bottom clamp) movements, but also the full-field displacements of geosynthetic at any location and any moment.

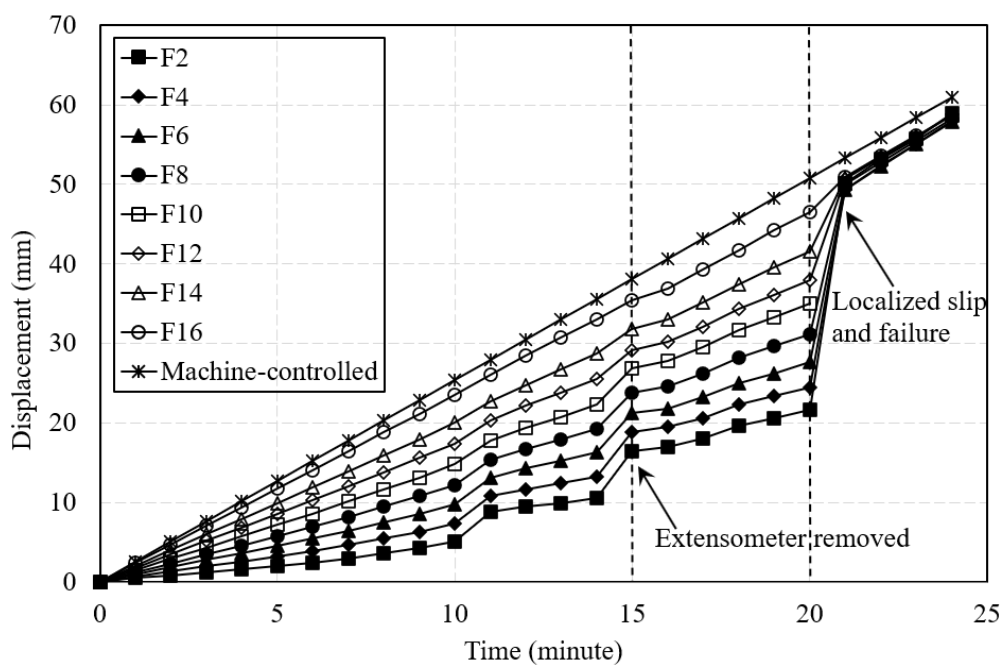
The 3-D coordinates of the coded targets placed on the geogrid specimen were calculated using the proposed multi-camera based photogrammetric method. By comparing the 3-D coordinates of the same points on the specimen at different times with

their initial values, the full-field displacements of the geogrid during the tensile test were thus obtained. The results are presented in this section.

Figures 7a through 7e show the variations in the displacements of the geogrids over time. In this paper, the displacements of four longitudinal ribs, namely longitudinal ribs A, F, G, J, and the ninth transverse rib as labelled in Figure 2b are selected as representatives to demonstrate the ability of the proposed method to measure the full field displacements of the geosynthetics during the tensile test. The variations in the displacements of longitudinal rib A with time are shown in Figure 7a. As exemplified in Figure 7a, the points at the lower locations experienced larger displacements. For example, the displacements of A4 were larger than those of A2. A16 experienced the largest displacements. This result was reasonable because the lower points had accumulative displacements that were transmitted from the displacements of the upper points. In Figure 7a, a sudden change in the displacement was observed when the testing time was 15 minutes for almost all points. This was attributed to the removal of the extensometer from the geogrid specimen to protect the extensometer from damage after testing for 15 minutes. Another interesting phenomenon in Figure 7a was that the responses of different points to the disturbance caused by the extensometer dismounting differed. The lower the point, the smaller effects the extensometer disturbance had. The extensometer disturbance caused the largest effects on A2, while the effect on A16 was almost negligible. This indicated that the mechanical interruption can cause localized deformation of the geogrid specimen, and the deformation of the geogrid was not uniform. This is further exemplified by the following information. In Figure 7a, the

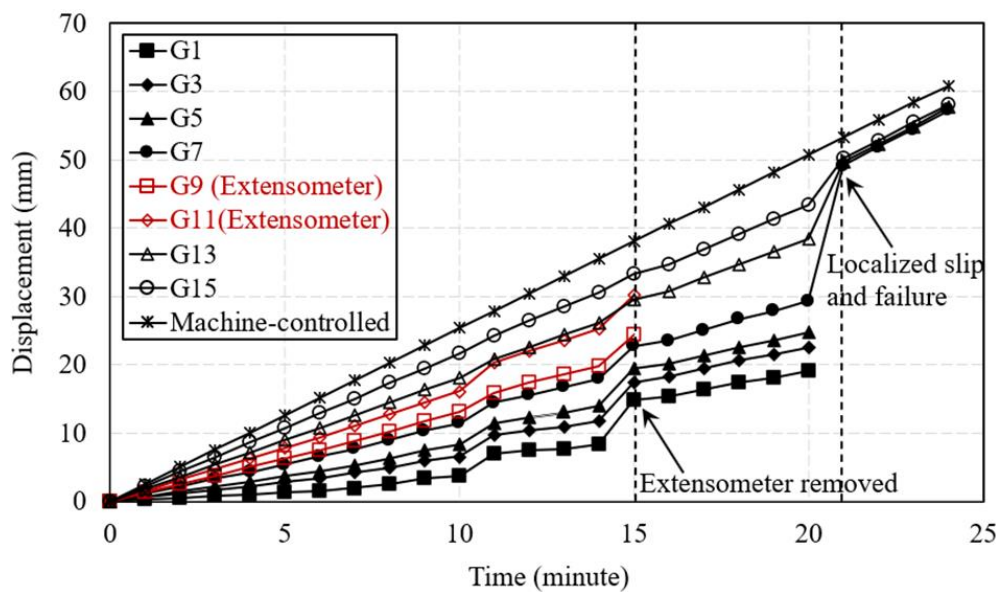


(a) longitudinal rib A

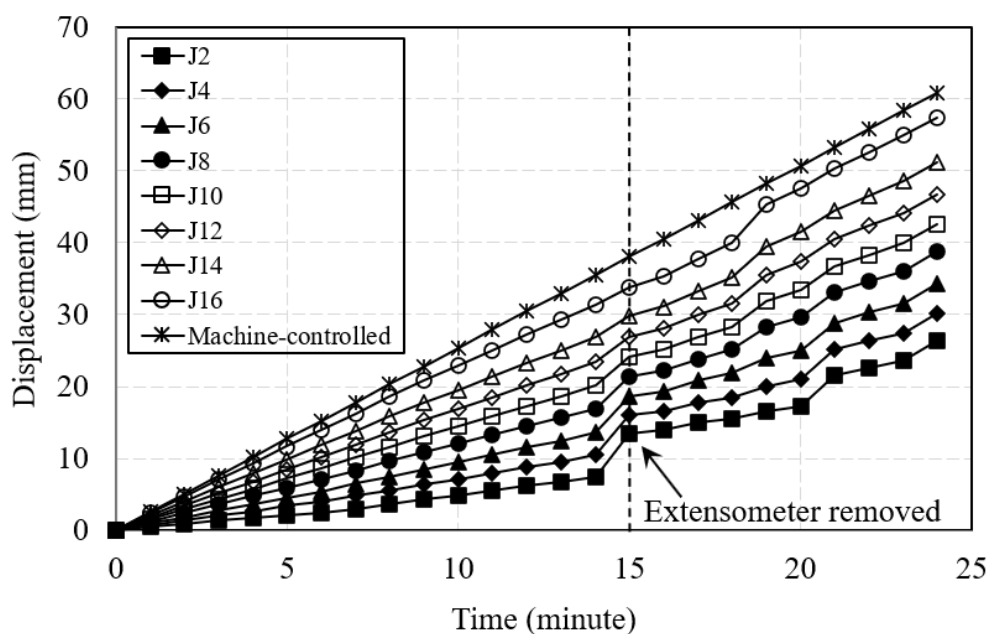


(b) longitudinal rib F

Figure 7. Displacement-time relationship curves of the geogrid specimen: (a) longitudinal rib A, (b) longitudinal rib F, (c) longitudinal rib G, (d) longitudinal rib J, and (e) the 9th transverse rib.

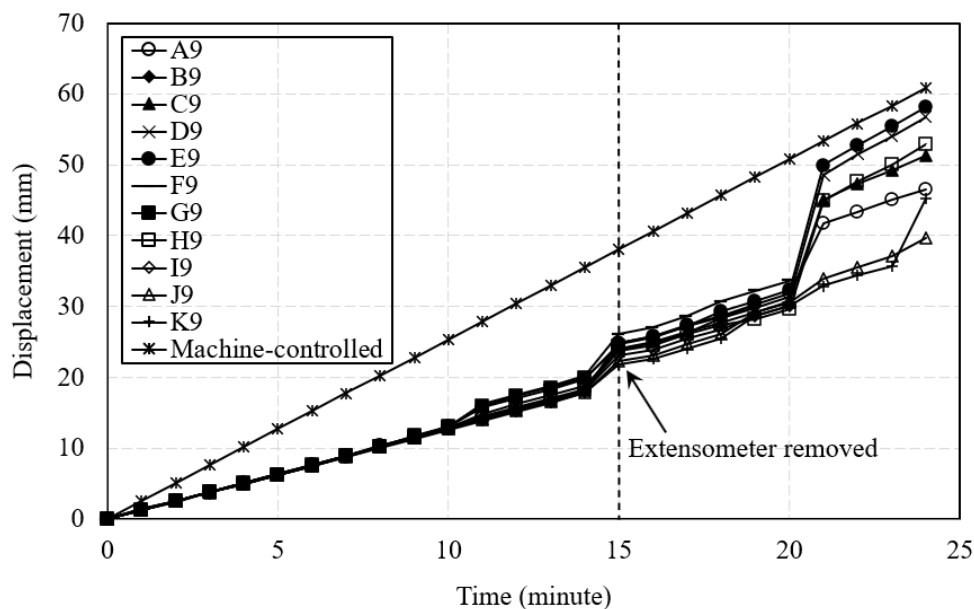


(c) longitudinal rib G



(d) longitudinal rib J

Figure 7. Displacement-time relationship curves of the geogrid specimen: (a) longitudinal rib A, (b) longitudinal rib F, (c) longitudinal rib G, (d) longitudinal rib J, and (e) the 9th transverse rib. (cont.)



(e) the 9th transverse rib

Figure 7. Displacement-time relationship curves of the geogrid specimen: (a) longitudinal rib A, (b) longitudinal rib F, (c) longitudinal rib G, (d) longitudinal rib J, and (e) the 9th transverse rib. (cont.)

localized slip and failure that caused a sudden decrease in the displacements were observed when the testing time exceeded 20 minutes.

Figure 7b shows the displacement versus time curves for the longitudinal rib F, which reports similar results to those for longitudinal rib A. The disturbance caused by extensometer dismounting led to a jump in displacements for all the points. In contrast to longitudinal rib A and after exceeding 20 minutes test time, all the points converged into one point and had almost the same displacements. This is due to the fact that the top portion of the geogrid specimen experienced a localized slip and failure after 20 minutes had elapsed. As a result, this longitudinal rib on the geogrid experienced rigid translation instead of continuous elongation. This explanation is supported by Figure 8 which show

the pictures of the top portion of the geogrid specimen before the test (Figure 8a) and after 21 minutes of testing (Figure 8b). As shown in Figure 8b, it is clear that the top of longitudinal rib F reached failure (marked by a small ellipse), and one transverse rib slipped out of the clamp, which was marked by a long ellipse. A jump in the displacement was also observed at time = 10 minutes for points F2, F4, F6, F8, and F10. This might be caused by specimen disturbance during the testing.

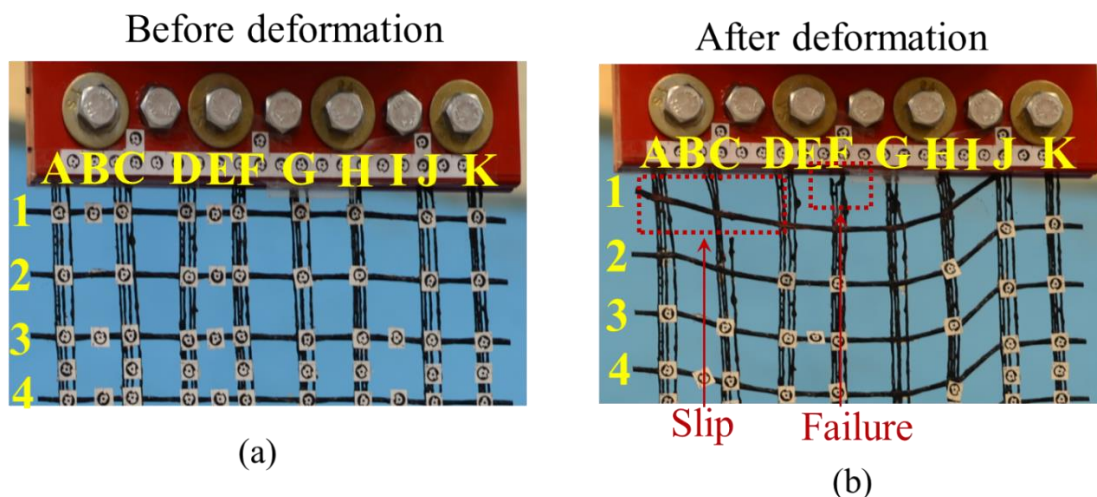


Figure 8. Images of the observed localized slip and failure of the geogrid specimen: (a) the top portion of the geogrid specimen before the deformation, and (b) the top portion of the geogrid specimen after deformation and the observed localized slip and failure

Figure 7c shows the displacement curves of the longitudinal rib G over time, which contain two points measured by both extensometer and the proposed photogrammetric method. The displacements measured by the extensometer at points G9 and G11 had similar displacements to other points before time =10 minutes. After testing time exceeded 10 minutes, the displacements measured by the extensometer at points G9 and G11 were similar to those at elevation above the extensometer such as G1 through

G7, but deviated from those measured at elevations lower than the extensometer such as points G13, G15 and machined controlled displacements. Such differences can be attributed to the disturbances caused by the extensometer. This demonstrated the advantages of the proposed method as a non-contact method over the conventional extensometer method. There is no disturbance caused by the proposed method. If there is any abnormality at any location, they can be captured by the proposed method. It was also noted that the displacements of G1, G3, G5, and G7 were missing after the testing time exceeded 20 minutes. This was due to the fact that some coded targets on the geogrid began to peel off the geogrid specimen as the deformation of the geogrid became larger and larger. This issue can however be easily resolve using better methods to post the coded targets.

Figure 7d presents the variations in the displacements of longitudinal rib J as time progressed. Similar to other longitudinal ribs, extensometer disturbance induced localized deformation was continuously observed in this longitudinal rib. However, as shown in Figure 7d, after the testing time exceeded 20 minutes the displacement curves of the points were separated from each other, and all the points had independent displacements. It seemed that the localized slip and failure as discussed previously had very limited influence on the displacement of this longitudinal rib. These discussions were supported by the visual observations of the images taken before and after the localized failure as shown in Figures. 8a and 8b, respectively. In Figure 8b, no localized failure was found in longitudinal rib J. However, the localized slip and failure detected in other longitudinal ribs still had a small influence on the displacements of this longitudinal rib. Therefore, a small jump in displacement after testing time exceeded 20 minutes was observed.

To evaluate the displacements of the points along the transverse direction, the 9th transverse rib as shown in Figure 2b, was selected as a representative to demonstrate the displacements of the points on different transverse ribs. The corresponding results are shown in Figure 7e. Since all the points were on the same rib, their displacements were expected to be the same or at least very similar pattern. This was true for the first 5 minutes. However, a discrepancy appeared between time = 10 and time = 15 minutes. The differences continued to increase after the extensometer was removed at time = 15 minutes. Starting from time = 20 minutes the differences became even larger and could be roughly divided into two categories. The first category involved A9, C9, D9, E9, and H9 and was affected by a jump in the displacement, which occurred 21 minutes after the testing started. As discussed previously, the localized slip and failure at the top of the geogrid specimen were detected after 21 minutes at longitudinal ribs of C, D, E, and F as shown in Figure 8b. A9 and H9 did not fail, but the displacements along these two ribs were influenced because they were close to the failure zone. Therefore, the points in the first category experienced the localized deformation caused by the localized slip and failure. The second category contained J9 and K9, which were far away from the failure zone and whose displacements were not affected. The results indicate that the proposed photogrammetric method was capable of capturing the localized displacements of the geogrids. In comparison, the results also demonstrated that when conventional contact methods, such as LVDT and extensometer are used, they can only measure displacements at limited locations and their measurements are not representative for two reasons: (1) the installation of sensor can unavoidably result in disturbances of the testing specimen, and (2) localized displacements always exist in the specimen.

The displacement data of longitudinal ribs B, C, D, E, H, I, and K were also obtained, and similar test results and phenomena were observed. However, to avoid unnecessary over-length these results were not reported in this paper.

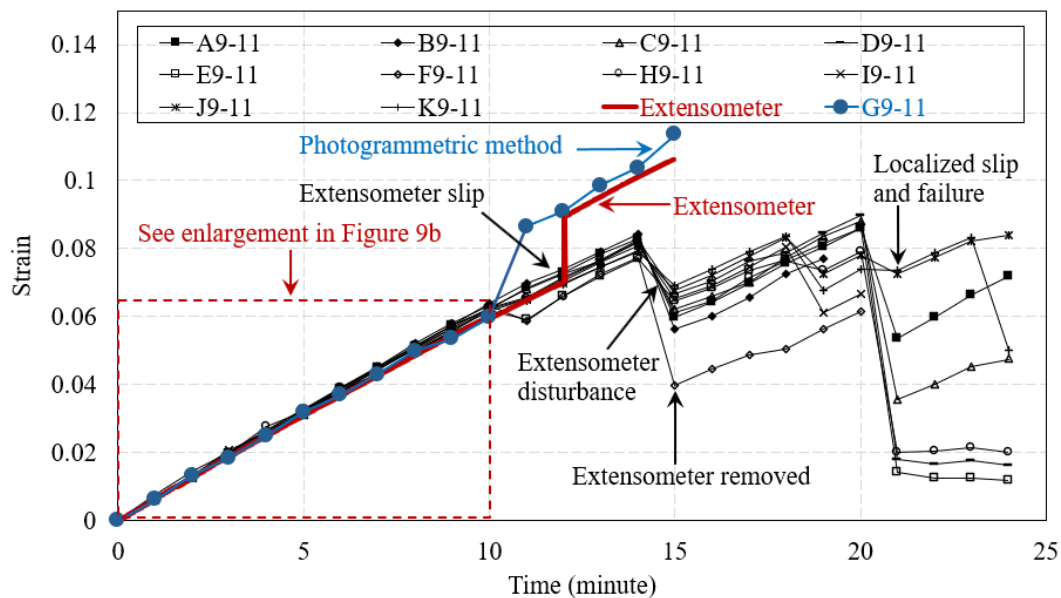
5.4. EVALUATION OF THE FULL-FIELD STRAIN IN GEOGRIDS

The proposed method can also be used to evaluate the localized strains in the geosynthetic specimen. By comparing the displacements between any two adjacent points at different times, the strain at the small segment can be calculated. For example, A9-11 represents the segment formed by point A9 and A11. The localized strain was calculated as follows:

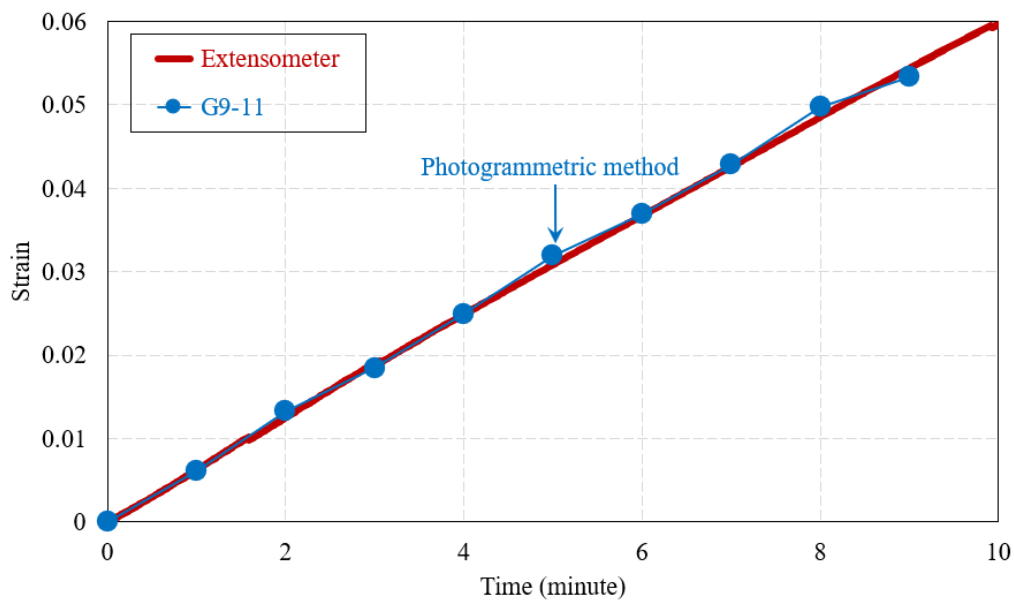
$$\varepsilon = \frac{L_t - L_0}{L_0} \quad (19)$$

where L_0 is the initial length of segment A9-11, and L_t is the length of segment A9-11 at testing time t .

Figure 9 shows the localized strains in the segments between the 9th and 11th transverse ribs. These two transverse ribs were selected because the two measuring points of the extensometer, namely G9 and G11, were also on these two transverse ribs so that the results from the photogrammetric method and the extensometer could be compared. The measured results by the two methods agreed very well for all segments in the first 10 minutes. Figure 9b shows an enlargement of Figure 9a for testing time between 0 and 10 minutes for the measurements of points G9 and G11 made by the proposed



(a) Comparison of the vertical strains at different locations



(b) enlarged vertical strain versus time curves for time = 0 to 10 minutes

Figure 9. Comparison of the vertical strains obtained by the extensometer and the proposed photogrammetric method.

photogrammetric method and extensometer. As shown in Figure 9b, the average difference in measurements of G9 and G11 made by the proposed method and extensometer was 0.05%, indicating that the proposed method can produce high-accuracy results which are comparable to those made by the extensometer. In other words, using 160 coded targets as indicated in Figure 2 is equivalent to having installed more than 100 extensometers at different locations of the specimen. It is noted that the strain measurements made by the proposed photogrammetric method are independent of each other and are also independent of the extensometer-measured strains as shown in Figure 9b. The high accuracy of the proposed photogrammetric method obtained by the above comparison is also a strong indication of the repeatability and reproducibility of the proposed method.

Immediately after 10 minutes, there was a jump in the strain at G9-11 measured by the two coded targets posted on the extensometer, likely due to a slippage of extensometer. This slippage was not picked up by the extensometer until time = 12 minutes. The differences in measurements made by the extensometer and the proposed method were about 0.2% after slippage.

In addition, after testing time exceeded minutes, the extensometer was removed to prevent it from possible damages due to large deformation. However, the displacements of the specimen at different locations could still be monitored by the proposed method until the specimen completely failed. This is a strong evidence that the proposed photogrammetric method is capable of overcoming the major limitations of the extensometer method.

Figure 10 shows the strain distribution contours of the geogrid specimen at different times. Figure 10 was obtained in the following way. Firstly, the localized strains at different locations of the geogrid specimen were calculated using Equation 19. Then, the contours were obtained by linearly interpolating the vertical strains at different locations. It should be noted that although Figure 10 shows the strain distribution within the entire specimen plane, only the strain data for the transverse and longitudinal geogrid ribs were meaningful. As shown in Figure 10, the strain distribution was dynamic and changed over time. During the first stage (testing time = 0 to 5 minutes), the strains were relatively uniformly distributed within the test specimen. However, the strain distribution kept changing after that (testing time = 7 to 11 minutes). As can be seen in Figure 10, at time = 7 minutes, there was an obvious low strain region identified at the middle region of the specimen where the extensometer was located. Such a small strain was mainly attributed to the existence of the extensometer. After that, the strain distribution became uniform again at testing time 11 to 14 minutes, but the strain localization was identified again after testing time = 15 minutes. In a summary, Figure 10 indicated that (1) the strain distribution during the tensile test is not uniform with space or time. As a result, one cannot use strains measured at one or a few points to represent the strain development for the whole specimen, and (2) installation of a sensor on the specimen can cause disturbance of the strain field of the specimen during the tensile test and the obtained results do not represent the actual behavior of the geosynthetic.

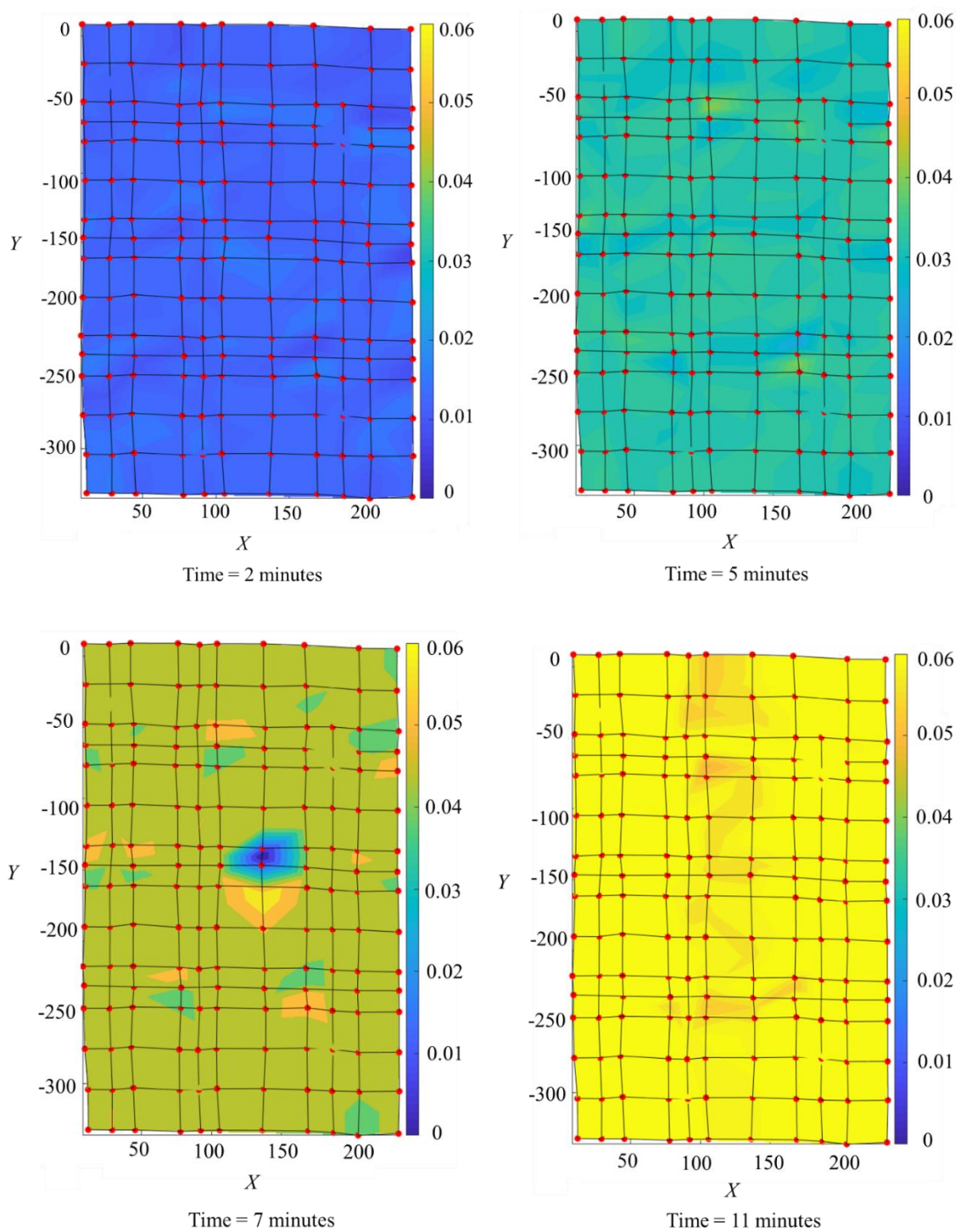


Figure 10. Contour plots of the strain distribution at different times during the tensile test

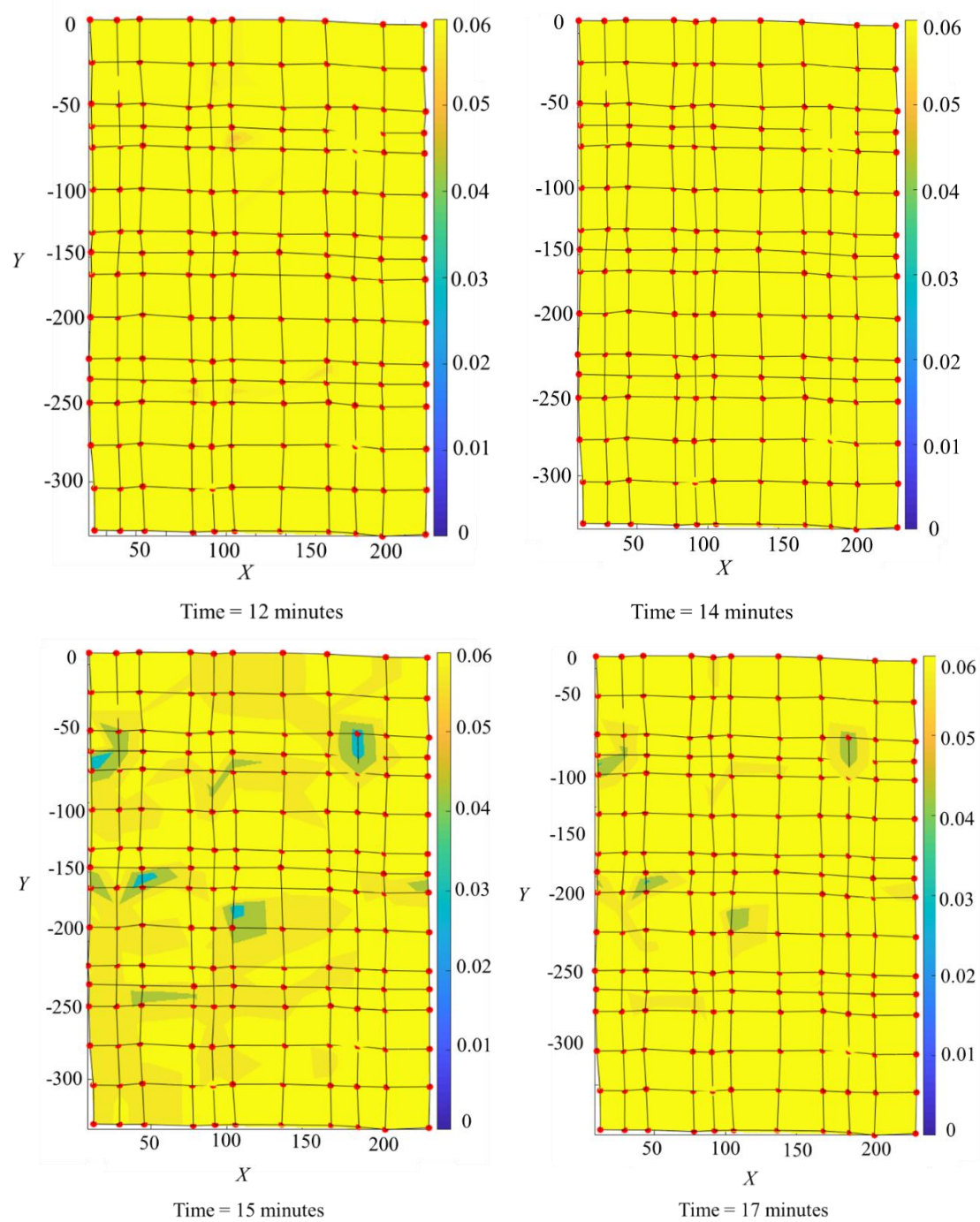


Figure 10. Contour plots of the strain distribution at different times during the tensile test.
(cont.)

5.5. EVALUATION OF THE MODULUS DISTRIBUTION OF THE GEOGRIDS

Figure 11 shows the load versus strain curves of the geogrid specimen at different locations. In Figure 11, the load versus strain curves of three representative longitudinal ribs A3-4, E2-3, and F15-16 are presented. A3-4 denotes the load-strain relationship of the segment between points A3 and A4. As can be seen in Figure 11, almost all the segments had similar load-strain curve trends but with different quantities in terms of modulus and tensile strength. These different quantities indicated that the modulus and tensile strength varied at different locations of the geogrids, meaning that the modulus of the geogrids was not uniform within the entire specimen.

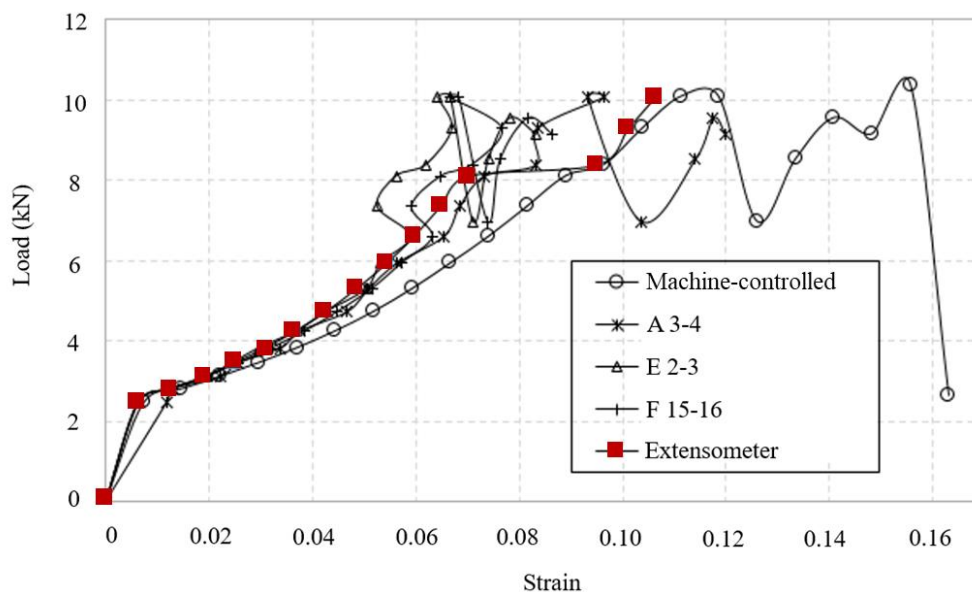


Figure 11. Load-strain curves of the geogrid specimen at different locations

To calculate the localized modulus of the specimen, the modulus of each segment was calculated in accordance with ASTM D6637/D6637M-15 (2015). The following equation was used to calculate the modulus:

$$J_{\text{sec}} = (\alpha_f \times 100) / \varepsilon_p \quad (18)$$

where J_{sec} is the secant modulus, at corresponding elongation (1% average strain was selected in this study); α_f is the force per unit width at the designated percent strain 1%, which can be obtained from the load versus strain curves; ε_p is the strain computed from previous sections. It should be noted that in ASTM D6637/D6637M-15 (2015), the equation used for calculating the secant modulus of the geogrid specimen assumes that the strain in the specimen is uniform at all locations, thus it can only calculate an average and overall modulus of the specimen. However, in this study, different strains with respect to the same force per unit width were observed at different locations as shown in Figure 11. By using the proposed photogrammetric method and using Eq. (18) the modulus and tensile strength at any locations of the geogrid could be obtained.

Figure 12 shows the contour plot of the modulus distribution of the test geogrid specimen. It clearly shows that the modulus varied at different locations in the geogrid specimen. The values of the modulus ranged from 231.9 kN/m to 338.1 kN/m. The center, where the extensometer was installed, and the specimen had lower moduli. This indicates that boundaries effect and sensor installation influence the modulus measurements. Figure 13 shows the modulus histogram for the geogrid specimen. The average modulus was 278.6 kN/m and the standard deviation of the modulus was 11.4 kN/m. In conventional design and applications of geosynthetics/geogrids, only one averaged value for the modulus of the material is used. However, the proposed method provided statistical data regarding the modulus to better characterize the mechanical

properties of the specimen. As a result, the proposed method can be used to provide a more comprehensive input for a probability-based geosynthetics design.

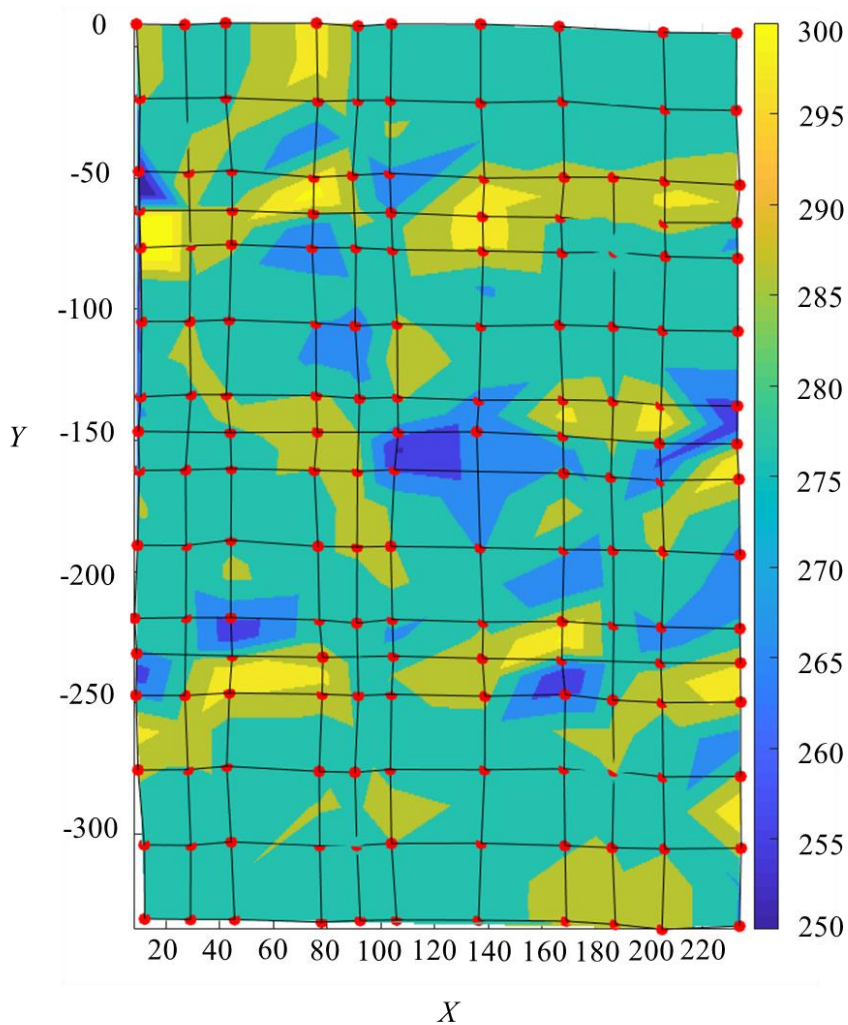


Figure 12. Contour plot of the modulus distribution of the test geogrid specimen.

5.6. EVALUATION OF THE PLANAR ASSUMPTION

Another advantage of the proposed photogrammetric method is that it can reconstruct the 3-D models of the specimen during the dynamic testing and the results can be used to calculate the 3-D displacements of the geogrid specimens. Figure 14

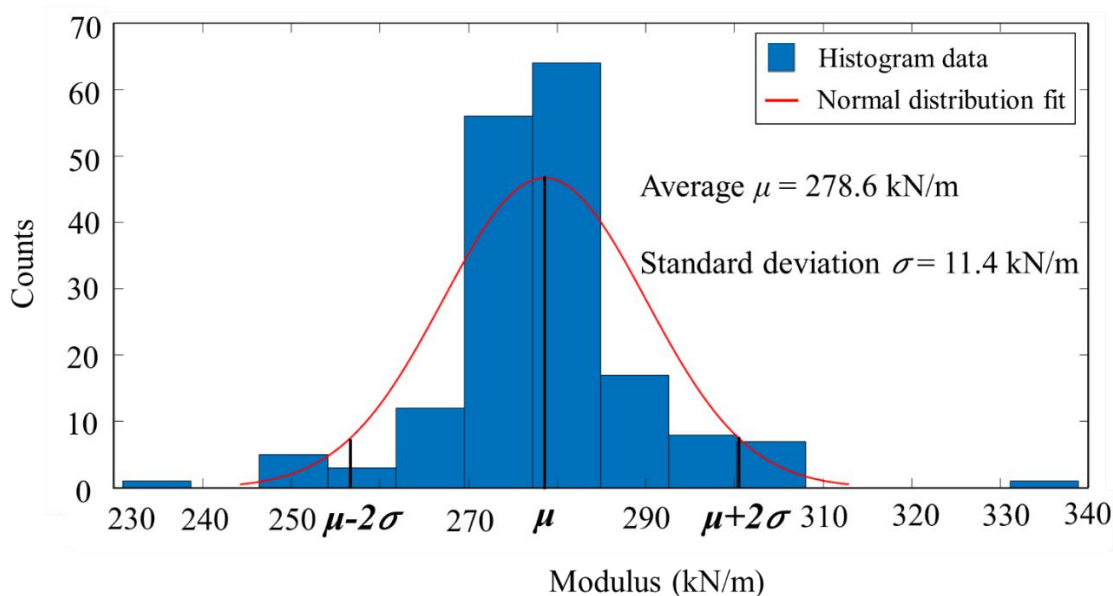
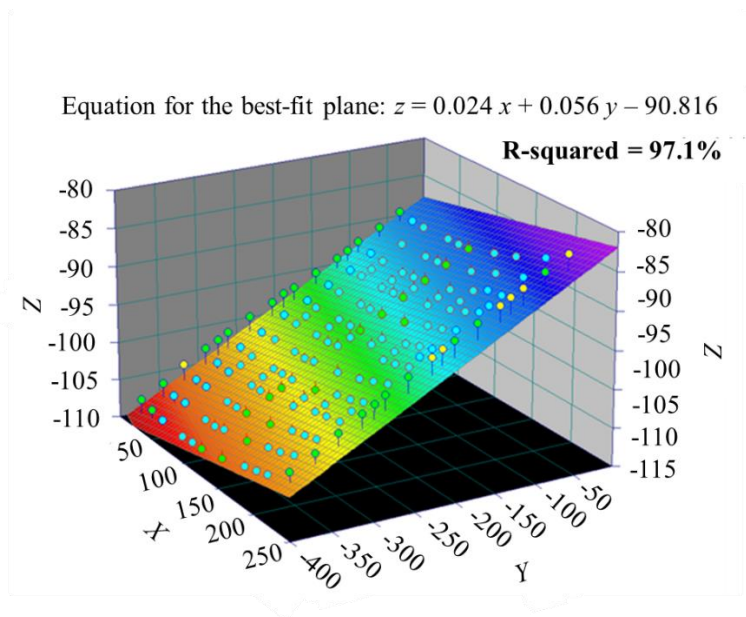
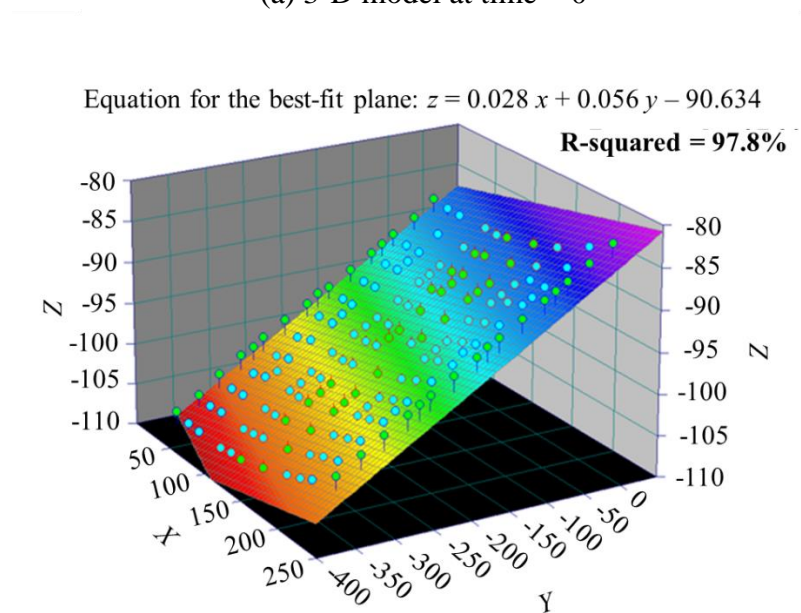


Figure 13. Histogram plot of the modulus distribution of the test geogrid

shows the 3-D models of the geogrid at time = 0, 10 minutes, 20 minutes, and 24 minutes, respectively. The scattered points in Figure 14 represent the coded targets that were placed on the geogrid specimen. The scattered points were used to best fit planes at different times and the equations for the planes and R-squared are also shown in Figure 14. As can be seen in Figures 14a through 14d, the points were not perfectly fallen on a plane in any of the figures. This can be further demonstrated by Figure 15 in which the R-squared values of the best-fit planes at testing time 0 to 24 minutes are presented. The R-squared of the best-fit plane was 97.1% at $t = 0$ as shown in Figures 14a and Figure 15, indicating that the geogrid specimen was initially not in the same plane. In Figure 15, as time increased, the R-squared increased first, and then began to decrease at $t = 20$ minutes. This could be explained as follows: initially, the geogrid specimen was not



(a) 3-D model at time = 0



(b) 3-D model at t = 10 minutes

Figure 14. 3-D models of the geogrid specimen at various times.

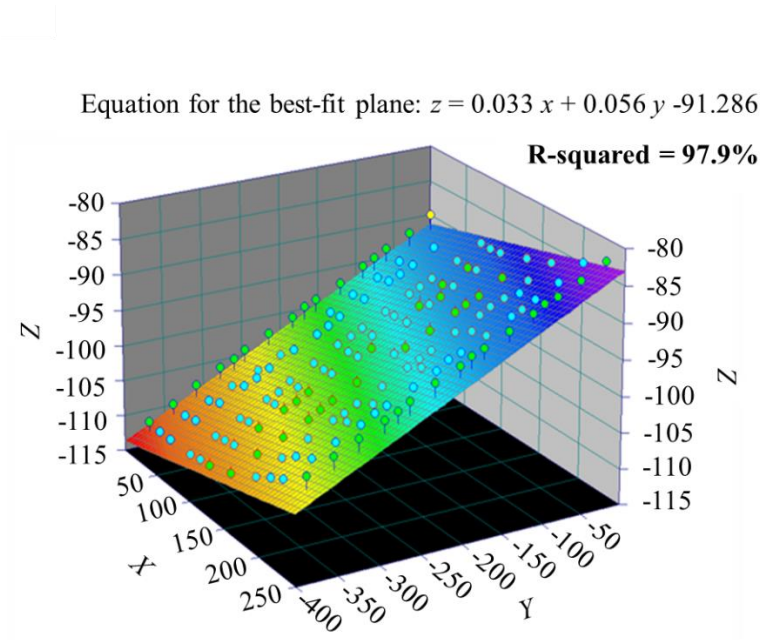
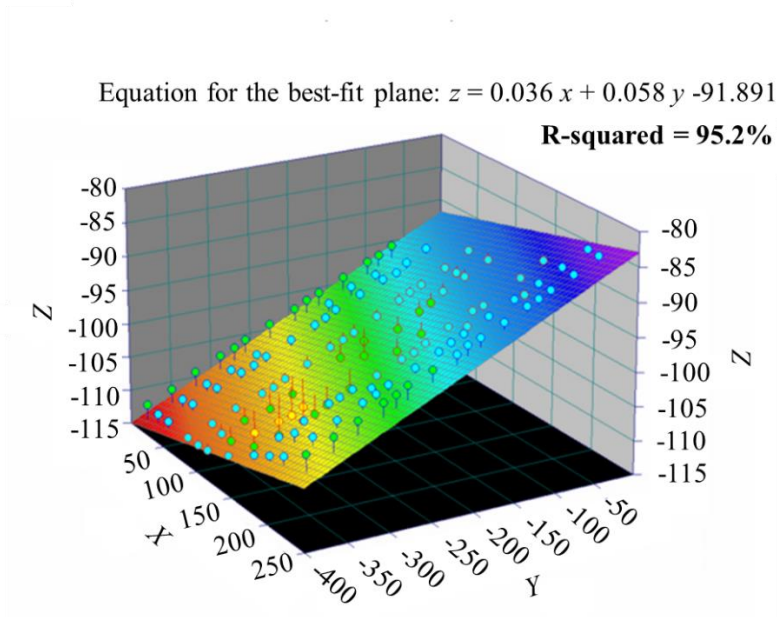
(c) 3-D model at $t = 20$ minutes(d) 3-D model at $t = 24$ minutes

Figure 14. 3-D models of the geogrid specimen at various times. (cont.)

installed in a perfect plane with a R-squared far away from 100%. As the applied load increased with time, the specimen was stretched under tensile stress, and became more

like a plane. Therefore, the R-squared of the best-fit plane of the specimen increased from an initial value of 97.1% to 97.9% at $t = 20$ minutes. After testing time exceeded 20 minutes, the R-squared decreased due to the failure of the geogrid specimen. R-squared of the best-fit plane for the last image was only 95.2 % compared with the initial R-squared of 97.1% as shown in Figures 14a, 14d, and Figure 15. The normal to the planes was used to calculate the rotational angles of the best-fit planes during the test. It was found that the best-fit plane of the geogrid specimen at 24 minutes rotated 0.67 degrees, compared with its initial position, as shown in Figure 15. As discussed previously, conventional methods assume that the geosynthetics were initially in one plane and stayed in the same plane during the whole test (Aydilek et al. 2004). However, this assumption was proven to be invalid by the above evaluation of the 3-D displacements of the geogrid specimen using the proposed photogrammetric method. In conclusion, the results shown in Figures 14 and 15 demonstrate that the geogrid specimen was neither initially in one plane nor did it maintain a plane during the tensile test. In fact, the geogrid underwent significant out-of-plane deformations during the test. Therefore, the planar assumption in the existing methods for measuring the deformations of geogrids is invalid.

6. CONCLUSIONS

In this paper, a multi-camera-based photogrammetric method was proposed to measure the 3-D full-field displacement of geosynthetics. A tensile test was performed on

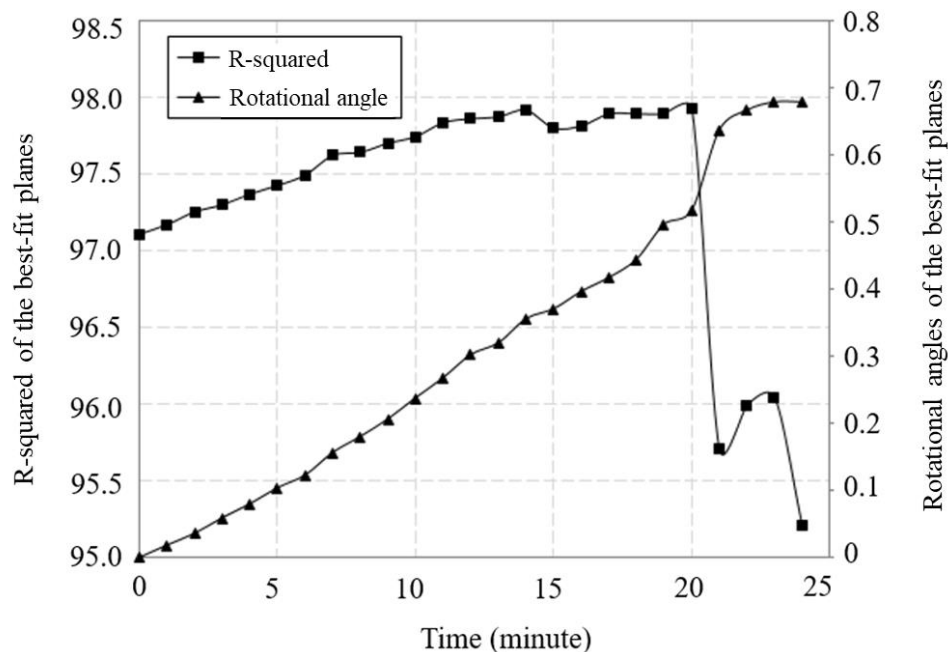


Figure 15. R-squared and rotational angles of the best-fit planes of the geogrid specimen over time.

geogrid specimen to verify the effectiveness and accuracy of the proposed method. The main findings of this study are summarized as follows:

- (1) The proposed photogrammetric method extended the conventional one-camera-based photogrammetry to multi-camera-based photogrammetry. This method can be used in dynamic tests where the objects are continuously moving/deforming, such as tensile tests on the geosynthetics, which cannot be done by using the conventional one-camera-based photogrammetry.
- (2) The proposed method is a non-contact, low-cost, and highly accurate method. It only requires two commercially available digital cameras that cost about \$2000. The average absolute difference in displacements obtained by the proposed photogrammetric method and the machine-controlled movements of the bottom

clamp was 0.25%, and the average absolute error was 0.038 mm. The average difference in measurements made by the proposed method and extensometer was 0.05%.

- (3) Strain localization existed in the tested geogrid specimen during the tensile test.

The proposed photogrammetric method is capable of identifying localized strains. The localized strains are attributed to many factors, such as manufacturing defects, improper installation and alignment, the disturbance caused by sensor dismounting, and localized slip and failure during the tensile test. Since these factors are unavoidable, the strain localization should be identified and paid special attention.

- (4) Existing image-based methods for measuring the deformational properties of geosynthetics often require the camera positions and shooting directions to be controlled manually by the users, and it is often assumed that the geosynthetics specimen is initially in a single plane and maintains in the same plane during the whole testing period. However, this research demonstrated that neither the requirement nor the assumption can be satisfied. The results in this paper indicated that the average difference in camera stations between actual camera stations and predesigned camera stations was 53.9 mm, and the average difference in shooting directions was 1.1 degrees. It was also found that the geogrid specimen was not initially in one plane, and the geogrid specimen plane continuously rotated during the tensile test. As a result, the use of the existing image-based methods may lead to unreliable and inaccurate results in a tensile test for geosynthetics. This limitation can be overcome by the proposed

photogrammetric method in which the camera stations and shooting directions are back calculated and no manual control of camera stations or shooting directions is required.

- (5) Conventionally, the modulus of the geosynthetic specimen is assumed to be uniform within the whole specimen, and only one overall modulus can be obtained. This study shows that the moduli at different locations in the specimen were dissimilar. The proposed photogrammetric method is capable of calculating the moduli at all locations in the specimen. The proposed photogrammetric method is equivalent to having installed many mechanical sensors on the geosynthetics with high accuracy and large measurement ranges. The associated cost is negligible since it only requires posting of some coded targets at the points of interest. As a result, the proposed method can provide a more comprehensive input regarding the deformational and strength properties, such as displacements, strains, moduli, and tensile strength at any locations of the geosynthetics, for a probability-based geosynthetics design.
- (6) The results show that the moduli of the geogrid specimen ranged from 231.9 kN/m to 338.1 kN/m. The average modulus was 278.6 kN/m and the standard deviation of the modulus was 11.4 kN/m. The proposed photogrammetric method can potentially improve the current design methods of geosynthetics applications from a statistical perspective.
- (7) One limitation of the proposed method could be its intensive computation requirement. However, a computer program has been developed to perform the required calculations in a few minutes.

REFERENCES

1. ASTM D6637/D6637M-15 Standard Test Method for Determining Tensile Properties of Geogrids by the Single or Multi-Rib Tensile Method, West Conshohocken, PA, 2015.
2. Alshibli, K.A. and Sture, S., 2000. Shear band formation in plane strain experiments of sand. *Journal of Geotechnical and Geoenvironmental Engineering*, 126(6), pp.495-503.
3. Aydilek, A.H., Guler, M., and Edil, T. B. 2004. Use of image analysis in determination of strain distribution during geosynthetic tensile testing. *Journal of Computing in Civil Engineering*, 18(1), 65-74.
4. Fernandez-Fernandez, M., Alonso-Montes, C., Bertelsen, A., and Mendikute, A., 2013. Industrial Non-intrusive Coded-Target Identification and Decoding Application. In *Iberian Conference on Pattern Recognition and Image Analysis*. Springer, Berlin, Heidelberg. 790-797.
5. Gallage, C. and Jayalath, C. 2019. Use of Particle Image Velocimetry (PIV) technique to measure strains in geogrids. In *E3S Web of Conferences (Vol. 92, p. 12007)*. EDP Sciences.
6. Hryciw, R. D. and Raschke, S. A. 1996. "Development of computer vision technique for in situ soil characterization." *Transportation Research Record*, 1526(1), 86-97.
7. Jiang, R., Jáuregui, D. V., and White, K. R. 2008. Close-range photogrammetry applications in bridge measurement: Literature review. *Measurement*, 41(8), 823-834.
8. Jones, D. 2000. Wide-width geotextile testing with video extensometry. *Grips, Clamps, Clamping Techniques, and Strain Measurement for Testing of Geosynthetics*. ASTM International.
9. Kutay, M. E., Murat, G., and Aydilek, A. H. 2006. Analysis of factors affecting strain distribution in geosynthetics. *Journal of geotechnical and geoenvironmental engineering*. 132(1), 1-11.
10. Mikhail, E. M., Bethel, J. S., and McGlone, J. C. 2001. *Introduction to modern photogrammetry*. New York, 19.

11. Mishra, S. R., Mohapatra, S. R., Sudarsanan, N., Rajagopal, K., and Robinson, R. G. 2017. A simple image-based deformation measurement technique in tensile testing of geotextiles. *Geosynthetics International*, 24(3), 306-320.
12. Paikowsky, S. G. and Xi, F. 2000. Particle motion tracking utilizing a high-resolution digital CCD camera. *Geotechnical Testing Journal*, 23(1), 123-134.
13. Raschke, S. A., Hryciw, R. D., and Donohoe, G. W. 1996. Micro deformations in sands by digital image processing and analysis. *Transportation Research Record*, 1548(1), 31-37.
14. Skochdopole, T. R., Cassady, L., Pihs, D., and Stevenson, P. E. 2000. Comparative Study of Roller and Wedge Grips for Tensile Testing of High Strength Fabrics with Laser Extensometry: Comparisons to LVDT and Crosshead Extension. Grips, Clamps, Clamping Techniques, and Strain Measurement for Testing of Geosynthetics. ASTM International.
15. Tsai, R. 1987. A versatile camera calibration technique for high-accuracy 3D machine vision metrology using off-the-shelf TV cameras and lenses. *IEEE Journal on Robotics and Automation*, 3(4), 323-344.
16. Wolf, P. R. and Dewitt, B. A., 2004. *Elements of Photogrammetry with Application in GIS (3rd International Edition)*. McGraw-Hill Press, Melbourne. ISBN 10, 0-071.
17. Xia, X., Zhang, X., Fayek, S., & Yin, Z. (2021). A table method for coded target decoding with application to 3-D reconstruction of soil specimens during triaxial testing. *Acta Geotechnica*, 16(12), 3779-3791.
18. Zhang, X., Li, L., Chen, G., and Lytton, R., 2015. A photogrammetry-based method to measure total and local volume changes of unsaturated soils during triaxial testing. *Acta Geotechnica*, 10(1), 55-82.
19. Zhang, Z. 2000. A flexible new technique for camera calibration. *IEEE Transactions on pattern analysis and machine intelligence*, 22(11), 1330-1334.

VI. A LOW-COST PHOTOGRAMMETRIC METHOD FOR MEASURING AND TRACKING THE CONTINUOUS 3-D FULL-FIELD DEFORMATIONS OF GEOSYNTHETICS DURING TENSILE TEST

Xiaolong Xia¹, and Xiong Zhang²

¹Ph.D. candidate, Department of Civil, Architectural, and Environmental Engineering, Missouri University of Science and Technology, Rolla, MO 65409-0030. Email: xxrkq@umsystem.edu

²(Corresponding Author) Professor, Department of Civil, Architectural, and Environmental Engineering, Missouri University of Science and Technology, Rolla, MO 65409-0030. Email: zhangxi@umsystem.edu

ABSTRACT

Existing methods have limitations in measuring the continuous and complete displacements of geosynthetics at all locations during tensile test. This paper presents a low-cost photogrammetric method for continuously measuring and tracking the 3-D full field displacements and complete strains of geosynthetics during the tensile test. A series of tensile tests were performed on six geogrid specimens to verify the effectiveness and accuracy and demonstrate the advantages of the proposed photogrammetric method. The results from the tensile tests using both the proposed method and the machine-controlled displacement measurements were presented and compared. It was observed that the average absolute difference between the proposed photogrammetric method and the machine-controlled movements of the bottom clamp was 0.14 mm. The proposed method is non-contact, cost-effective, accurate, and capable of measuring the 3-D displacements of the geosynthetics at any locations within the geosynthetics and at any moment during tensile test. The proposed method can also identify any localized strains at any location

within the specimen. The proposed photogrammetric method is equivalent to having installed several hundred of LVDTs and extensometers on the geosynthetics with high measurement accuracy. The proposed photogrammetric method can be used in dynamic tests where the objects are continuously moving/deforming, such as tensile tests on the geosynthetics, which cannot be done by using the conventional one-camera-based photogrammetric method.

1. INTRODUCTION

Geosynthetics have been widely used in a diverse range of geotechnical applications, such as embankment, roads, mechanically reinforced retaining walls and slopes, etc. The deformational modulus and tensile strength are essential parameters in the engineering designs of geosynthetics. The wide-width tensile test is the most commonly used test to determine the load-displacement relationship of the geosynthetics from which the deformational modulus, tensile strength, and failure strain are calculated. It is of great significance to measure the continuous and complete displacements of geosynthetics at all locations (also referred to as full-field displacement) during the whole process of tensile test for the abovementioned purposes.

In the recent decade, many conventional contact methods have been utilized to measure the displacements/strains of geosynthetics. These methods are briefly discussed here while a more detailed review of these methods can be found in Xia et al. (1). Crosshead extension method is commonly used to measure the overall deformations of geosynthetics by measuring the separation distance between the two tension grips.

Skochdopole et al. (2) performed a tensile test on woven and knit geotextiles and geogrids using the crosshead extension method. It was pointed out that the measured strain obtained by this method was actually a combination of seating and specimen elongation. In addition, no information about the localized strains can be provided as this method only measures the overall displacements/strains of geosynthetics. Contact extensometer is also commonly used to provide accurate strain measurements. The use of extensometer requires the attachment of extensometer to the specimen at limited number of predesigned locations. In addition, the extensometer needs to be removed during the test to avoid being damaged which will limit the measurement ranges of the extensometer. Strain gauge is another widely used contact method that has been used to measure the displacements/strains of geosynthetics. The measured strains by strain gauge are easily influenced by many factors, such as the strain gauge weight, data logger, quality of bonding between the strain gauge and the specimen (3). LVDT has also been extensively used in the displacement measurements. However, the additional weight of LVDT can lead to inaccurate measured strains in the geosynthetics. All the abovementioned contact methods can only measure the displacements/strains of geosynthetics at limited locations with limited measurement ranges. Aydilek et al. (4) pointed out that the inability to detect zones of varying strains and identify potential failure zones as well as the inaccurate determination of strains may lead to either an unconservative design of the structure or possible catastrophic failures.

There are methods developed for other purposes but can potentially be used for measuring the varying displacement/strain of geosynthetics with larger measurement ranges. Jones (5) used a non-contact image-based video extensometry technique to

measure the strain of geotextiles during tensile test. It was reported that this method had accuracy values in the range of 86%-100 compared to the extensometer. Many researchers used image-based tracking techniques to track the movements of particles (6-8). Aydilek et al. (4) measured the strain distribution in geosynthetics during tensile test using an image-based method tracking method. However, the abovementioned image-based tracking methods often use 2-D images captured from a single camera and it is usually required to make an assumption that the specimen is initially planar and must maintain as a plane during the test. Additional assumptions that the shooting direction should be exactly perpendicular to the specimen and the camera positions can be accurately controlled are also required. However, all these assumptions are nearly impossible to achieve. Moreover, these methods used zoom-lens and failed to perform camera calibration which can also lead to inaccurate or unreliable results.

To overcome the abovementioned limitations, a multi-camera-based photogrammetric method (1) has been proposed recently to measure the 3-D full-field displacement of the geosynthetics. This method extends the conventional photogrammetry using one camera for static object measurements to multi-camera-based photogrammetry for continuous deformation measurements. The results from the tensile test using both the proposed method and conventional methods were compared to demonstrate the accuracy and advantages of the proposed method. It was found that the proposed method can provide more comprehensive input, such as the complete strain and modulus distributions in the geosynthetics, for a probability-based geosynthetics design. However, only two cameras were used in this method and this method is unable to continuously track the deformations of geosynthetics at every moment during the entire

testing process. In addition, the potential of using low-cost surveillance cameras to measure and track the 3-D deformations of geosynthetics during the whole tensile test remains largely unexplored.

In this paper, six low-cost surveillance cameras were utilized to measure and track the 3-D full-field deformations of geosynthetics during the tensile test. A structure from motion photogrammetric method has been developed to obtain the 3-D model of the geosynthetics at the initial moment during the test. Then, an accurate and fast tracking technique was applied to obtain the 3-D model of the geosynthetics at any time during the test. A series of tensile tests on six different geogrid specimens were performed. The accuracy and the advantages of the proposed method are presented and demonstrated.

2. MATERIALS AND METHOD

2.1. SPECIMEN PREPARATION AND TEST METHOD

Figure 1 shows an experimental setup for the tensile test. An MTS Landmark 370 load frame equipped with a rated loading capacity of 250 kN was used to perform the tensile test for geosynthetics. Biaxial geogrids (Miragrid BXG110 and Miragrid BXG120) were used as a representative geosynthetic to demonstrate the effectiveness and accuracy of the proposed method, although the same method can be easily applied to a wide range of other geosynthetics. The material properties of the geogrids used in the tests are listed in Table 1. The dimensions of the specimen were selected in accordance with ASTM D6637/D6637M-15 (9), which were approximately 25 cm in width and 35 cm in length. Customized clamps were used to fix the top and bottom edges of the

Table 1. Properties of the Tested Geogrid Specimens.

Specimen	Shear Rate (mm/min)	Model	Tensile Strength (kN/m)	Rib Thickness (mm)	Grid Aperture Size (mm)
S1	4	BXG 110	12.4	0.76	25.4
S2	5				
S3	6				
L1	4	BXG 120	19.2	1.27	
L2	5				
L3	6				

specimens to the machine as shown in Figure 1c. These clamps were used to minimize the slippage of the specimen during the tensile test.

A total of six inexpensive surveillance cameras (Figure 1a) were used in this study. Each camera costs only about \$ 130. All these cameras were controlled by a Network Video Recorder (NVR) as shown in Figure 1b to achieve camera synchronization. The information regarding the NVR and the camera parameters are listed in Table 2.

To employ the proposed method, a total of 268 solid dots were placed at the junctions and the midpoint of the two neighboring junction points as shown in Figure 2a. As can be seen in Figure 2a, there are 15 columns (denoted by A to O) and 23 rows (denoted by 1 to 23) of solid dots. These solid dots have the same dimensions and can be easily printed on the stickers and placed on the geogrid specimen. Each solid dot can be automatically recognized by the computer program. There is a unique ID number ranged from 1 to 345 for each solid dot. The ID numbers for the solid dots are shown in

Table 2. Summary of the Information Regarding the 4K UHD NVR Multi-Camera System.

NVR		Surveillance Camera	
Number of Channels	8 (Video)	Sensor	8 MP 1/2.3"
Playback Resolution	3840 × 2160 (8 MP)	Focal length	4 mm
W × D × H (mm)	424 x 99 x 266	Maximum Aperture	f/2
Recording Resolution	1080p, 720p, 3MP, 4MP, 8Mp at 15 fps	Lens Field of View	Horizontal: 93°
Playback Speeds	16×	Shutter Speed	1/12000 to 1/5 second
IP Camera Support	16		
Storage	Up to 1 HDD (SATA)	Number of Camera Used	6

Figure 2b. A total of sixteen coded targets were also attached to the clamps at both ends of the specimen to measure the displacements of the clamps as shown in Figure 2a. A coded target (CT) is a high contrast dot, which is automatically recognized by a computer algorithm. The outer ring of the coded target was used to define the identification number based upon if there is a protrusion at every 30-degree interval, and each coded target is different with a unique identification number (1, 10). The centroid of the inner solid round point is used to define the location of the coded target. Since the centroid of the coded target is a mathematic point without physical dimension, the coded target can be used to achieve a sub-pixel accuracy. During the test, the top grip of the MTS machine is fixed, and the bottom grip is moveable to apply the desired displacement or load for the tensile test. Consequently, the coded targets posted on the top clamp, which are always fixed together with the top grip during the test, were used to set up the global coordinate

system as shown in Figure 1c. In this way, all the measurements could be made in the same coordinate system and comparisons among measurements can be performed.

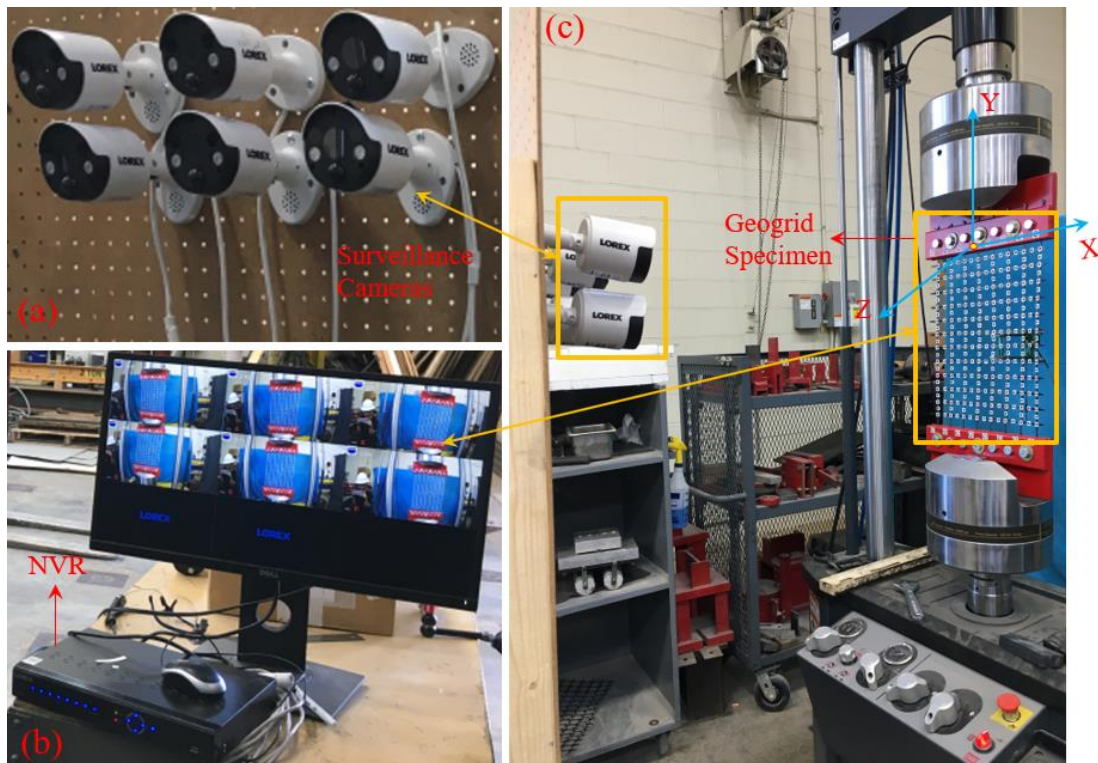


Figure 1. Multi-Camera System Setup for the Tensile Test.

2.2. CAMERA CALIBRATION AND IMAGE DISTORTION CORRECTION

Camera calibration is the process of determining the camera geometric parameters and optical characteristics (intrinsic parameters) (11). Camera calibration is an important step in accurate 3-D photogrammetric measurements. It is necessary to obtain the camera parameters and correct image distortion in order to obtain accurate 3-D measurement results. The significance and procedures for cameras calibration can be found in Zhang et al. (12) and Xia et al. (1). It is worth noting that one of the challenges of using

surveillance cameras in photogrammetric analysis is that surveillance cameras are often wide-angle cameras and there is usually much larger image distortion compared with other digital cameras such as digital single-lens reflex camera. Therefore, particular attention should be paid to the image distortion produced by surveillance cameras. In this study, the cameras have a horizontal field of view of 93 degrees, which is relatively small compared with other surveillance cameras. This relatively small field of view angle is beneficial for the photogrammetric analysis as the image distortion can be easily corrected. Camera calibration was performed on each of the six surveillance cameras and the image distortion of each image was corrected by following the procedure in Xia et al. (1). The camera calibration parameters are listed in Table 3.

Table 3. Camera Calibration Parameters.

Camera ID	Focal Length (Pixel)		Principal Point (Pixel)		Radial Distortion			Tangential Distortion	
	f_x	f_y	P_x	P_y	R_1	R_2	R_3	T_1	T_2
1	2628.6	2627.6	2067.8	1120.0	-0.366	0.016	0.202	0.0004	-0.0013
2	2603.5	2601.6	1999.5	1097.8	-0.362	-0.055	0.553	0.0005	1.19E-05
3	2622.7	2623.7	1967.4	1115.9	-0.401	0.280	-0.360	-0.0014	0.0006
4	2606.2	2608.6	2031.8	1040.1	-0.387	0.188	-0.103	-0.0006	0.0006
5	2631.4	2631.9	1935.4	1067.5	-0.403	0.257	-0.233	-0.0008	0.0008
6	2606.5	2622.4	1996.3	1150.4	-0.351	-0.195	0.896	-0.0034	0.0009

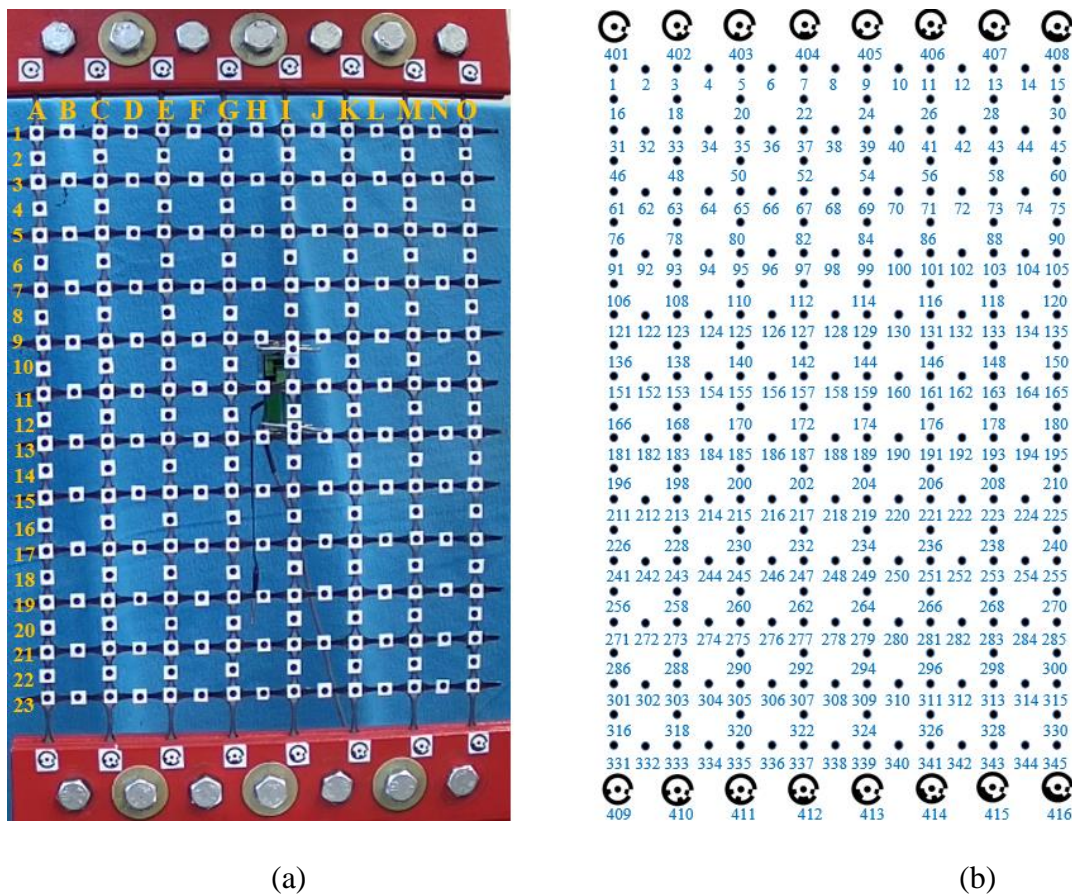


Figure 2. IDs Design for the Coded Targets and Solid Dots.

2.3. VIDEO ACQUISITION

After the geogrid specimen is installed on the MTS Landmark load frame, the locations and orientations of the six cameras are adjusted so that the specimen is almost in the center of the video and good quality images can be extracted from the videos. Then, the cameras are fixed at the corresponding optimal locations and used to videotape the tensile test simultaneously. All the video data with exact time information are managed and saved in the NVR. Therefore, camera synchronization can be achieved by using the same exact time for all the six cameras when extracting videos from the NVR.

The cameras have a frame rate of 15 frames/second. Assume that the tensile test duration is 10 minutes, then, 9000 image frames can be extracted from the videos, which means that the 3-D full-field displacements/strains of the geogrid specimen at 9000 different moments during the test can be obtained by the proposed method.

2.4. AUTOMATIC RECOGNITION AND DECODING OF CTS AND SOLID DOTS

After the test, the videos for the six cameras are exported from the NVR using a USB drive. The first image frame, representing the initial moment of the test, is extracted from the videos for each of the cameras for image analysis. The CTs on the top and bottom clamps are automatically recognized and decoded by the method proposed in Xia et al. (13). Simple and fast image processing algorithms for solid dot recognition and decoding have been developed in this study to facilitate the automation and improve the efficiency of the proposed method. Figure 3a is the original image for the geogrid specimen. After image distortion correction, the image is converted into a binary image as shown in Figure 3b. There are a lot of unnecessary and unwanted objects (also referred to as blobs) in Figure 3b. The solid dots can be correctly recognized by applying the following area and roundness criteria:

$$A_s \leq A_d \leq A_l \quad (1)$$

$$R_s \leq R_d \leq R_l \quad (2)$$

where A_d is the area (number of pixels) of the solid dots, A_s and A_l are the smaller and larger thresholds for the solid dot area. The typical values for A_s and A_l are 40 and 180, respectively. R_d is the roundness of the solid dots. R_s and R_l are the smaller and larger thresholds for the solid dot roundness. The typical values for R_s and R_l are 0.7 and 1.3,

respectively. The thresholds A_s , A_l , R_s , R_l can be slightly different for the images extracted from different cameras. Figure 3b shows the solid dot detection results after applying the abovementioned criteria.

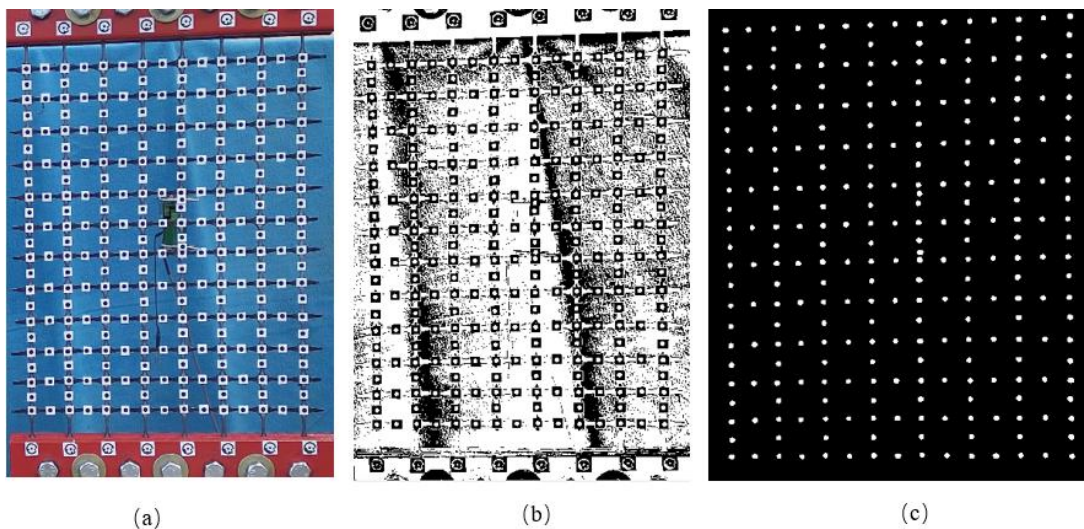


Figure 3. Image processing results for solid dot recognition.

After the solid dots are recognized, another image processing algorithm has been developed to automatically label each solid dot with a unique ID number (also referred to as decoding or identification). The decoding of the solid dots is illustrated in Figure 4. Figure 4a shows the ID labelling for the first column of the solid dots. The first column of solid dots (column A) can be easily detected and labelled based on the locations of the leftmost CT on both top and bottom clamps. Then, the locations of solid dots on column C can be predicted by translating column A to the right with certain number of pixels. Then, by comparing the predicted locations and the pixel locations of all the solid dots the accurate locations for each solid dot in column C can be obtained and the IDs can be easily assigned. The IDs on column C is shown in Figure 4b. By repeating this process,

the IDs of solid dots on columns E, G, I, K, M, and O can also be readily obtained. The decoding for the rest of columns can be done by using the pixel locations and IDs information for column A through column O. The final decoding results are shown in Figure 4d. It is noted that different from Xia et al. (1) in which CTs were used on the geogrid specimen, only solid dots were placed on the geogrid specimen. The use of solid dots and the abovementioned simple and fast image processing algorithms for solid dots recognition and decoding can significantly reduce the processing time.

2.5. MULTI-CAMERA-BASED STRUCTURE FROM MOTION PHOTOGRAMMETRY

Structure from Motion (SfM) is the process of estimating and creating the three-dimensional structure of a scene from a set of 2-D images generally captured by a moving camera. SfM has a variety of applications in many fields, such as computer vision, geoscience, architecture, and agriculture, etc. The SfM process is depicted in Figure 5 and detailed description of SfM can be found in Hartley & Zisserman (14). Assume that the 3-D model of a cubic is to be reconstructed by the SfM method. Images of the cubic were captured from three different locations and orientations by one moving camera. The corners of the cubic are the points of interest and are also referred to as feature points. The feature points were automatically detected by feature detection algorithms/detectors, such as Harris, and Shi & Tomasi corner detectors, and SURF, SIFT, KAZE blob detectors. SfM requires point correspondences between images. The point correspondences are found either by matching features or tracking points from the previous image to the current image. Then, a 3-D reconstruction project is initialized by

considering only two images as a ‘seed’. After the relative location and orientation of the second image relative to the first image are determined, more and more images can be

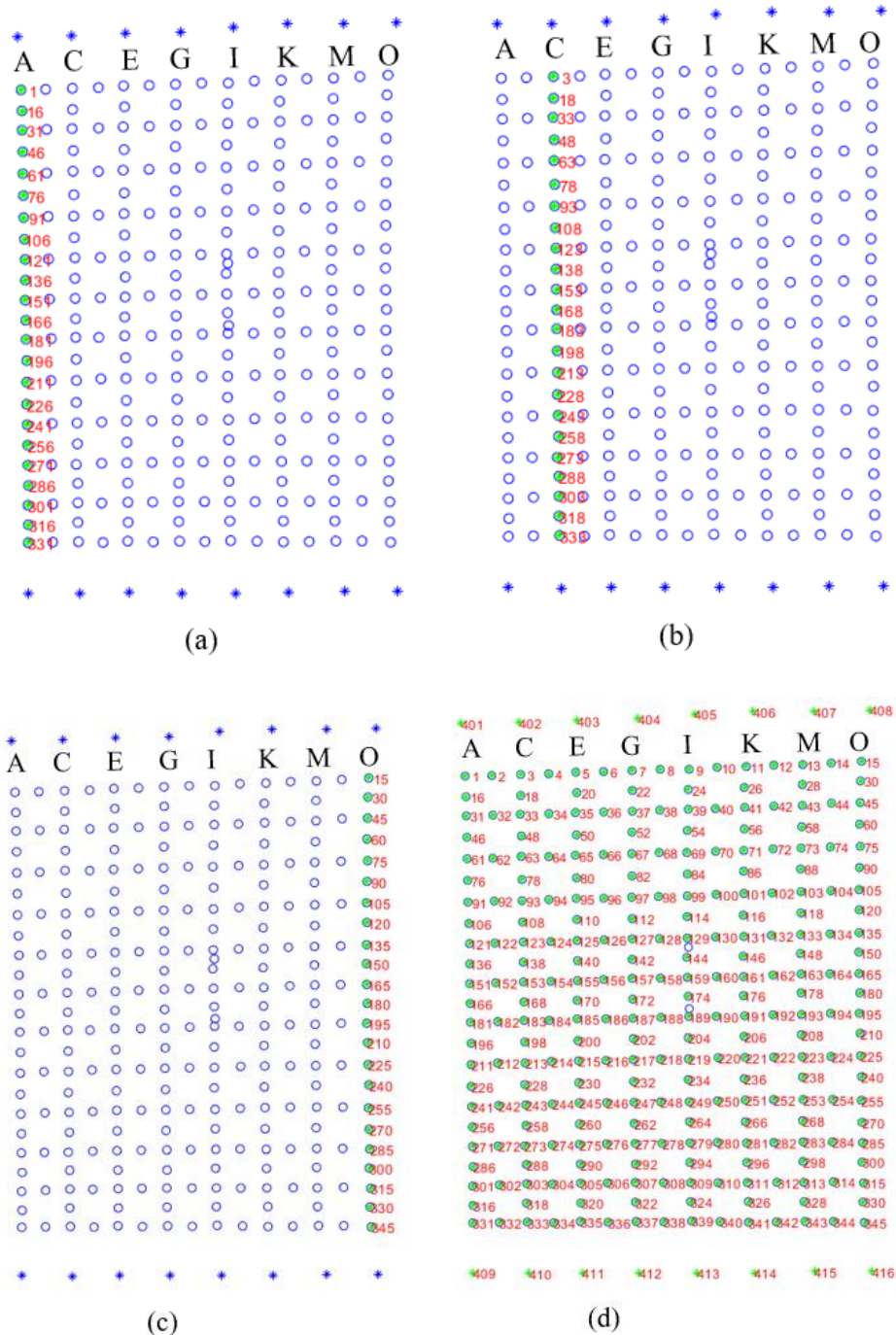


Figure 4. Automatic decoding of solid dots.

added to the 3-D reconstruction and finally all the corresponding camera stations and 3-D points can be solved. Bundle adjustment is often used in SfM to adjust and optimize the camera positions and 3-D points. In Figure 5, after the feature points between different images are matched, the 3-D reconstruction can be performed by using the abovementioned method and the 3-D points for the corners of the cubic can be obtained.

In this paper, a multi-camera-based structure from motion method is proposed based on conventional SfM. There are two major differences between the proposed photogrammetric method and conventional SfM: (1) Conventional SfM uses only one moving camera to capture the images of a static object. Therefore, it can only be used in 3-D reconstruction of a static object. However, in many dynamic tests, such as tensile test on geosynthetics, the object to be measured is continuously moving. To overcome this limitation, the proposed method utilizes multiple (six) surveillance cameras to videotape the whole process of a dynamic test, such as tensile test on geosynthetics. (2) Conventional SfM relies on random feature points detected in the images to find the point correspondences. However, as pointed out by some researchers (15-16), how to deal with the mismatches or outliers caused by incorrect point correspondences is still a challenge in SfM approaches. The proposed method uses solid dots as a more efficient and reliable way to find the point correspondences, which enables accurate and efficient photogrammetric analysis for the displacement/strain measurement of geosynthetics. The pixel locations and IDs of the solid dots obtained in previous section are used to perform 3-D reconstruction of the geogrid specimen. Therefore, the 3-D model of the geogrid specimen at the initial moment of the test can be obtained.

2.6. TRACKING THE PIXEL COORDINATES AND 3-D LOCATIONS OF THE SOLID DOTS

In this step, a fast and efficient target tracking technique has been developed to obtain the 3-D models of the geogrid specimen at any time during the whole testing process. This is achieved by taking full advantage of the pixel coordinates and IDs of the solid dots and camera locations for the first image frame which represents the initial moment of the test. It is assumed that the cameras are fixed during the test and the movement of the solid dots from previous image frame to the

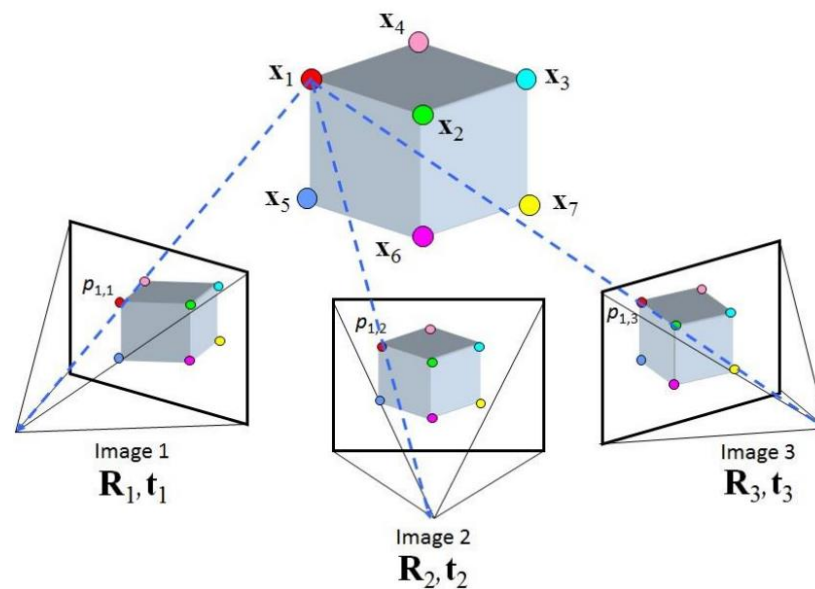


Figure 5. Structure from Motion (SfM) process (modified from Ozgur and Fatih (17))

current image frame is very small. Therefore, for the rest of the image frames extracted from the videos, there is no need to repeat the steps in previous sections but only a simple tracking process is needed. The tracking of pixel coordinates of three solid dots is illustrated in Figure 6. The three solid dots on the top of the specimen are used as an

example. Assume the second image frame is at $T = 1$ s, since the movement between image 2 and image 1 is very small the pixel coordinates of the three solid dots on image frame 2 are those points/blobs that are closest to the pixel locations of the three solid dots on image frame 1. Therefore, the accurate pixel coordinates and IDs of solid dots on image frame 2 can be easily obtained without any further computation. Then, for image frame 3 at $T = 2$ s, the same method is applied, and this process is repeated until the last image frame is analyzed and tracked. In Figure 6, the pixel locations of the three solid dots at three different moments are presented. Since the cameras are assumed to be fixed

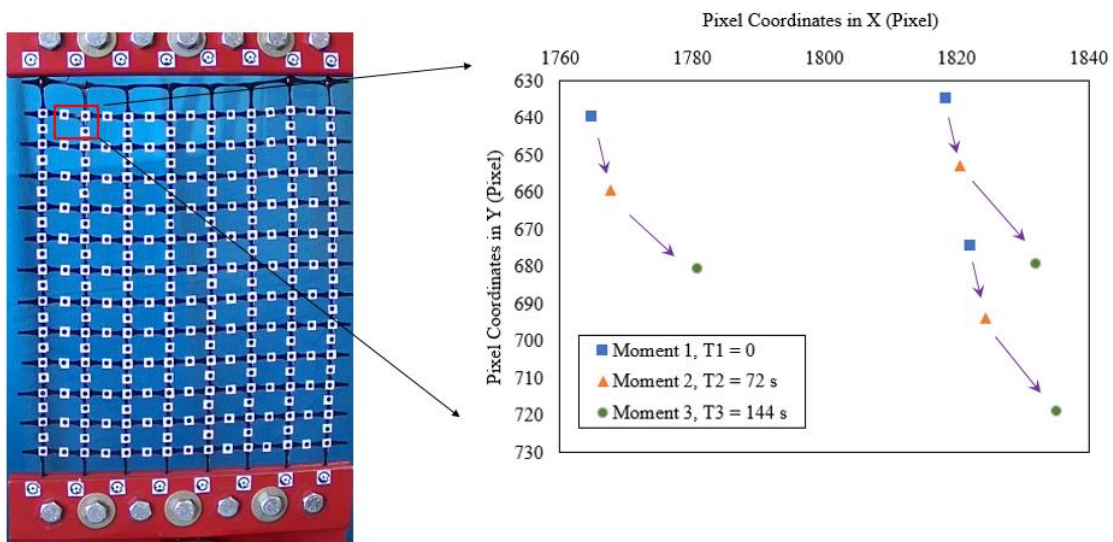


Figure 6. Tracking the solid dot pixel coordinates.

during the test, the camera stations obtained from the first image frame for each camera are used to perform triangulation and obtain the 3-D model of the geogrid specimen at any moment. It is noted that this simple tracking technique is very efficient to use since

each image frame other than the first image frame can be analyzed within one second by the computer program.

3. RESULTS AND DISCUSSION

3.1. VALIDATION OF ACCURACY OF THE PROPOSED METHOD

The 3-D models for the geogrid specimen and surveillance cameras at the initial moment obtained by the proposed method are shown in Figure 7. The 3-D locations of both the CTs and the solid dots are obtained. The CTs on the bottom clamp (shown in Figure 7) are used to validate the accuracy of the proposed method. These CTs are selected for validation purpose because the CTs are posted on the bottom clamp and will move with the bottom clamp during the tensile test. By comparing the displacements of the CTs on the bottom clamp obtained from the proposed method and the machine-controlled bottom clamp displacements, the accuracy of the proposed method can be verified.

Figure 8 shows the comparison of the displacement results from the proposed method and the machine-controlled movements of the bottom clamp over a period of 8 minutes with an interval of 8 seconds. The average absolute displacement difference between the two methods is 0.14 mm.

3.2. EVALUATION OF THE FULL-FIELD DISPLACEMENT OF GEOGRIDS

Conventional contact methods assume that the displacements of the geosynthetics are uniform and use the displacement of the machine-controlled grip as the overall

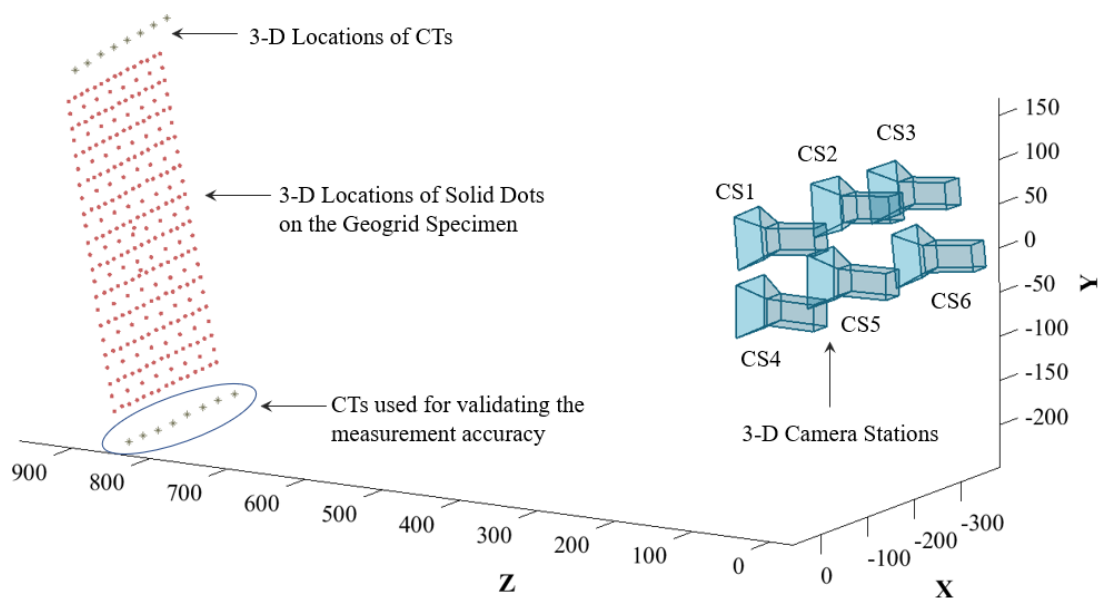


Figure 7. 3-D models for the geogrid specimen and surveillance cameras at the initial moment.

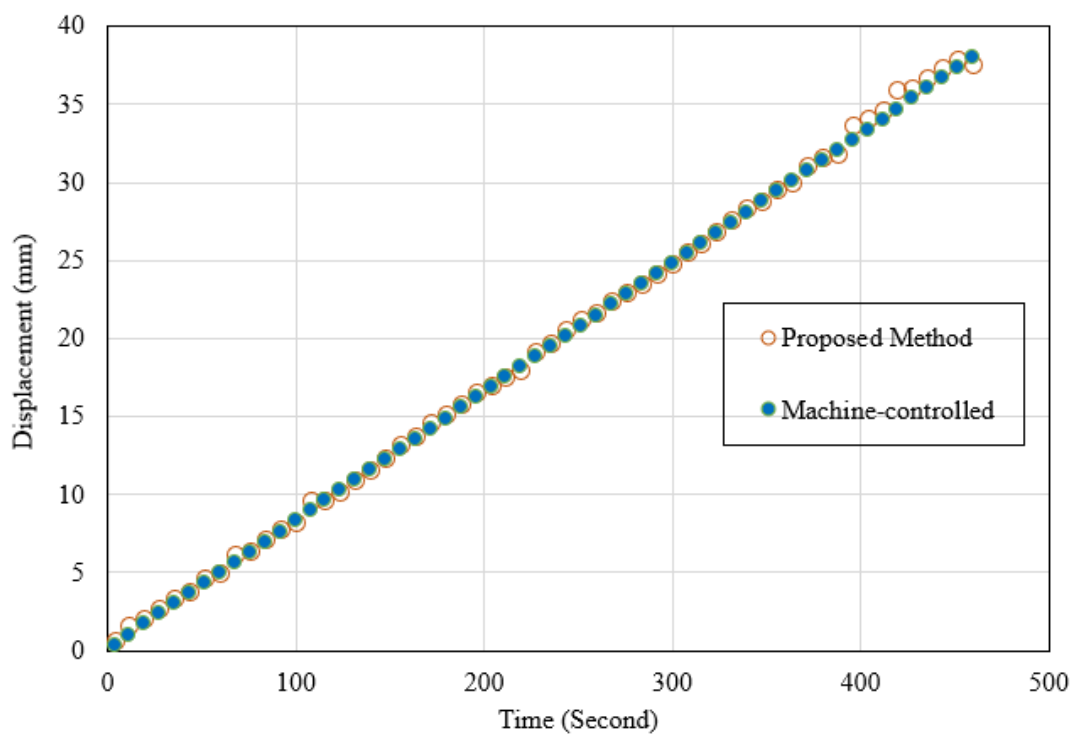


Figure 8. Comparison of the displacements obtained by the bottom clamp movements and the proposed method.

displacement of the geosynthetics. However, it is demonstrated in the following sections that the deformations/displacements of the geosynthetics are nonuniform, and the proposed method can measure the displacements of the geosynthetics at all locations and at any moment during the test. In this paper, the displacements of longitudinal rib A are selected as representatives to demonstrate the capability of the proposed method to measure the full-field displacements of geosynthetics during tensile test. The variations in the displacements of longitudinal rib A with time are shown in Figure 9.

As can be clearly seen from Figure 9, the displacements of rib A at different vertical locations are different even though they are in the same longitudinal rib. This is strong evidence that the displacements of the geosynthetics are nonuniform. It can also be observed in Figure 9 that the points at lower locations experienced larger displacements. For example, the displacements of A9 were larger than those of A1. A23 experienced the largest displacements. This result can be reasonably explained as due to the fact that the lower points had accumulative displacements that were transmitted from the displacements of the upper points. It is also found that the curve for A23 is much higher than the curves for other points. This might be caused by the slip of the last row of the geogrid specimen and the large localized strains developed on the last row of the specimen. This hypothesis will be verified in the later section. The displacement data of longitudinal ribs B through O were also obtained, and similar test results and phenomena were observed. However, to avoid unnecessary over-length these results were not reported in this paper.

3.3. EVALUATION OF THE FULL-FIELD STRAINS IN THE GEOGRID SPECIMEN

This section demonstrates the capability of the proposed method to identify the localized strains at any locations within the geosynthetic specimen. The method proposed by Xia et al. (1) was adopted to calculate the strains in the geosynthetics. By comparing the displacements between any two adjacent points (solid dots) at different moments, the strain in the segment formed by these two points can be calculated.

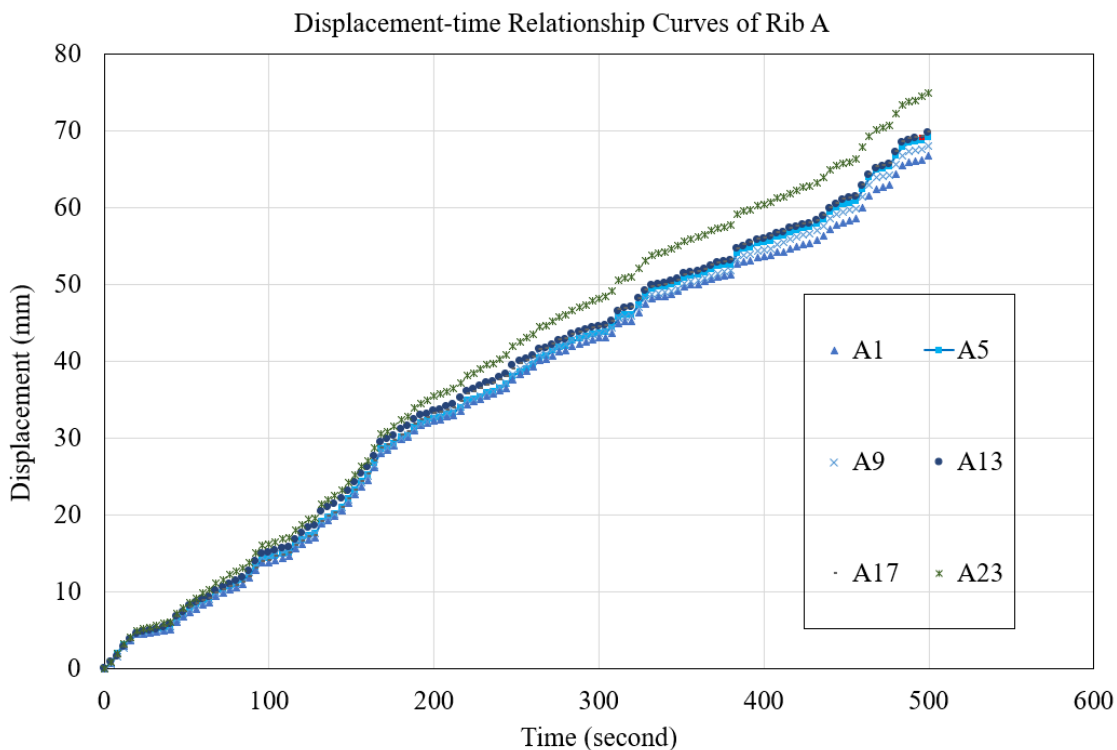


Figure 9. Displacement-time Relationship Curves for Rib A.

Although the complete strain distributions of all the six geogrid specimens were obtained, the full-field strain distribution results for geogrid specimen L3 are used as representatives to demonstrate the method. After the localized strains at different

locations of the geogrid specimen were calculated, the strain contours were obtained by linearly interpolating the vertical strains at different locations. The strain distribution contours of the geogrid specimen L3 at different moments is shown in Figure 10. It is worth mentioning that although Figure 10 shows the strain distribution within the entire specimen plane, only the strain data for the transverse and longitudinal geogrid ribs were meaningful. As shown in Figure 10, the strain distribution was dynamic and changed over time. At time $T1 = 54$ s (Figure 10 a), even though no obvious strains were observed, it is noticed that the strains on the top of the specimen are negligible while some small strains were developed in other locations. At time $T2 = 160$ s (Figure 10b), the strains are much larger than those at time $T1 = 54$ s. It can be seen in Figure 10b that the strains within the geogrid specimen are nonuniform. The lower points have larger strains compared with the upper points. At times $T3 = 302$ s (Figure 10c) and $T4 = 418$ s (Figure 10d), obvious localized strains at the bottom of the geogrid specimen are observed. The strains at the top of the specimen increased but are much smaller than the strains at the bottom of the specimen. At time $T5 = 507$ s (Figure 10e), the localized strains at the bottom of the specimen further increased but a redistributed strains were identified at time $T6 = 531$ s (Figure 10f). This might be caused by a stress redistribution after one or two longitudinal ribs reached failure during $T5$ to $T6$. The large localized strains identified at the bottom of the geogrid specimen during the late stage of the test is consistent with the results in Figure 9 in which the curve for A23 is much higher than the curves for other points. Figure 10 indicated that the strain distribution during the tensile test is not uniform with space or time. As a result, one cannot use strains measured at one or a few points to represent the strain development for the whole specimen. The proposed

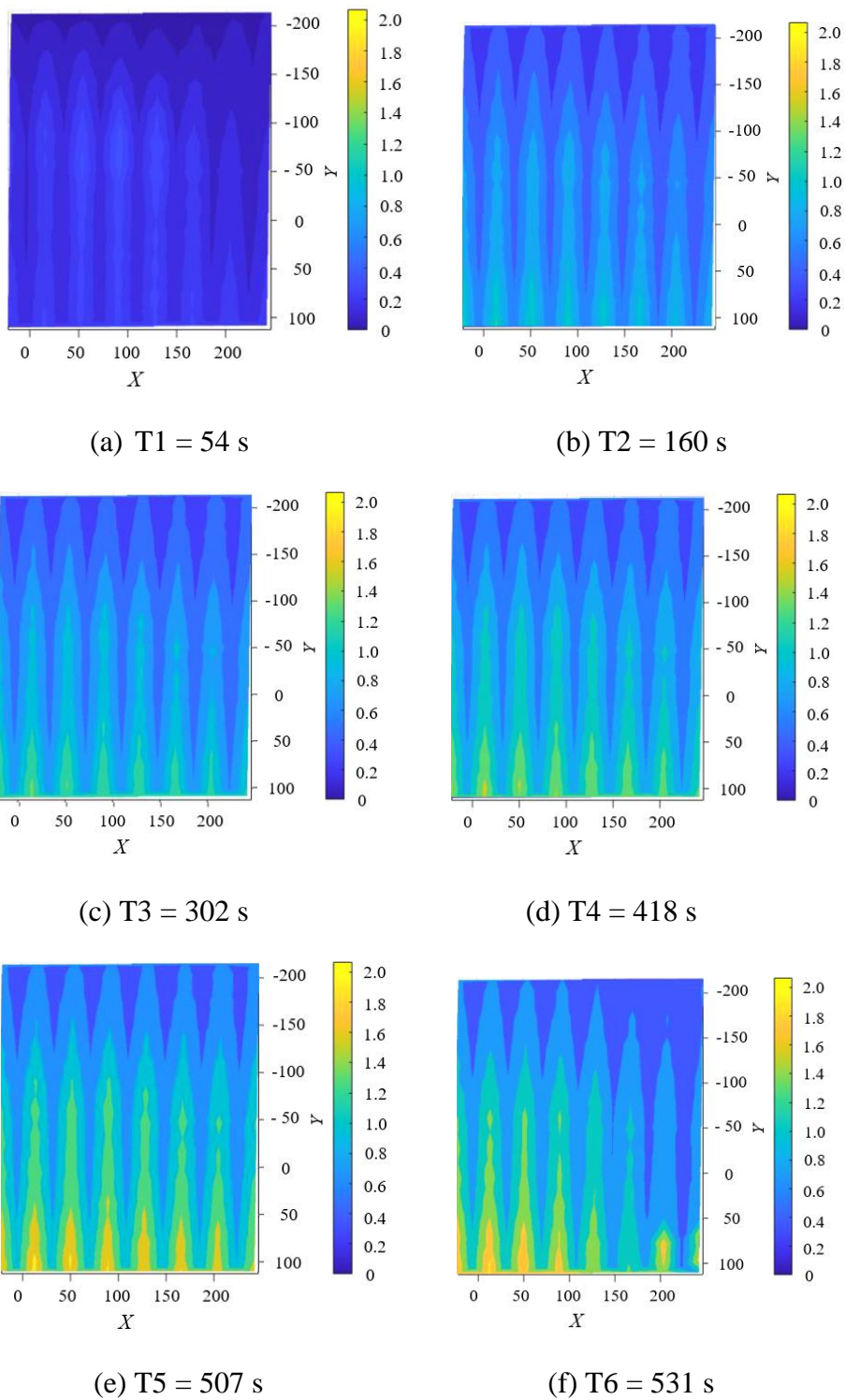


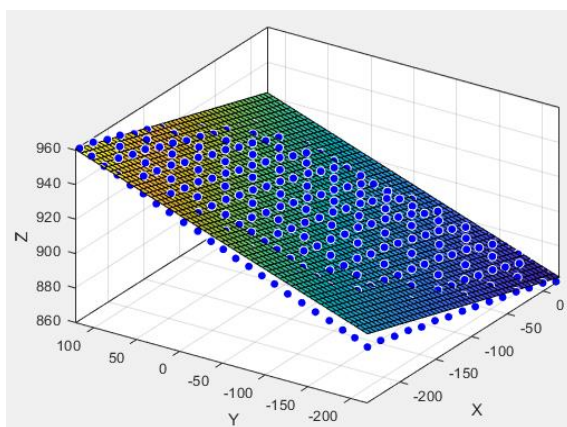
Figure 10. Changes in full-field strains in geogrid specimen L3 over time.

method uses 268 solid dots which is equivalent to having installed 268 LVDTs and 268 extensometers/strain gauges to the specimen and much more comprehensive data regarding the complete strain distributions within the entire geogrid specimen can be obtained.

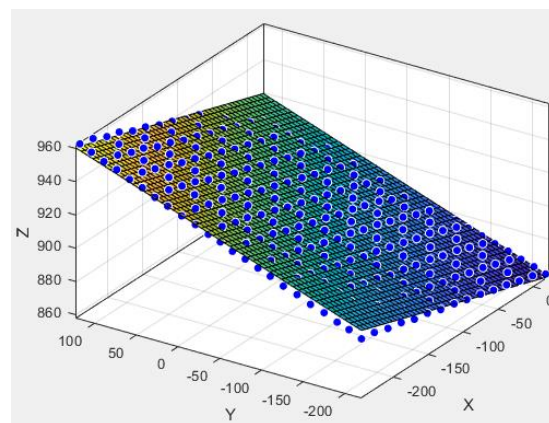
3.4. EVALUATION OF THE PLANAR ASSUMPTION

Another advantage of the proposed photogrammetric method is that it can reconstruct the 3-D models of the specimens during the dynamic testing and the results can be used to calculate the 3-D displacements of the geogrid specimens. Figure 11 shows the 3-D models of the geogrid specimen at time = 8 s, 48 s, 200 s, and 512 s, respectively. The scattered points in Figure 11 represent the solid dots that were placed on the geogrid specimen. The scattered points were used to best fit planes at different times. As can be seen in Figures 11a through 11d, the points were not perfectly fallen on a plane in any of the subfigures. This can be further demonstrated by Figure 12 in which the R-squared values of the best-fit planes at testing time 0 to 529 s are presented. The R-squared of the best-fit plane was 96.5% at $t = 0$ as shown in Figure 12, indicating that the geogrid specimen was initially not in the same plane. In Figure 12, as time increased, the R-squared increased first, and then began to decrease at $t = 514$ s. This could be explained as follows: initially, the geogrid specimen was not installed in a perfect plane with a R-squared far away from 100%. As the applied load increased with time, the specimen was stretched under tensile stress, and became more like a plane. Therefore, the R-squared of the best-fit plane of the specimen increased from an initial value of 96.5% to 99.8% at $t = 514$ s. After testing time exceeded 514 s, the R-squared decreased due to

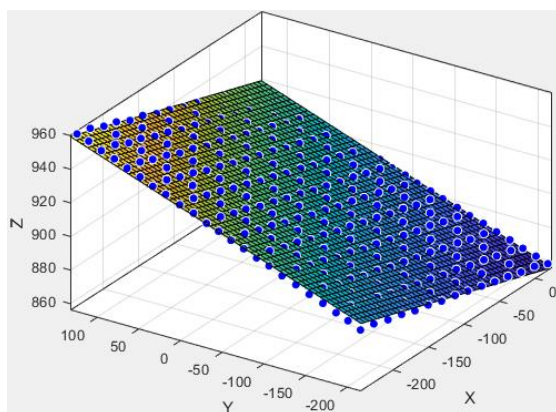
the failure of the geogrid specimen. As discussed previously, conventional methods assume that the geosynthetics were initially in one plane and stayed in the same plane during the whole test (4). However, this assumption was proven to be invalid by the above evaluation of the 3-D displacements of the geogrid specimen using the proposed photogrammetric method. In conclusion, the results shown in Figures 11 and 12 demonstrate that the



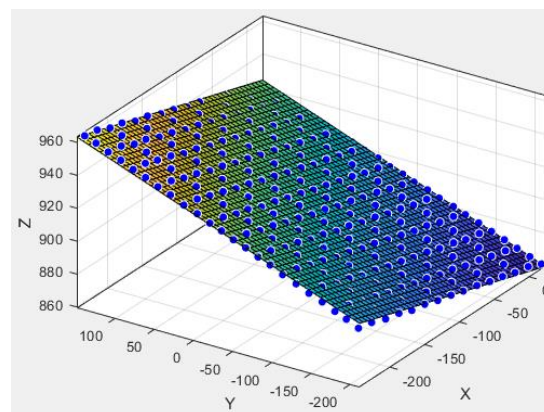
(a) $T1 = 8 \text{ s}$, $R_Squared = 97.1 \%$



(b) $T2 = 48 \text{ s}$, $R_Squared = 99.32 \%$



(c) $T3 = 200 \text{ s}$, $R_Squared = 99.64 \%$



(d) $T4 = 512 \text{ s}$, $R_Squared = 99.76 \%$

Figure 11. Changes in the 3-D models and R-squared of the fitting planes for the geogrid specimen over time.

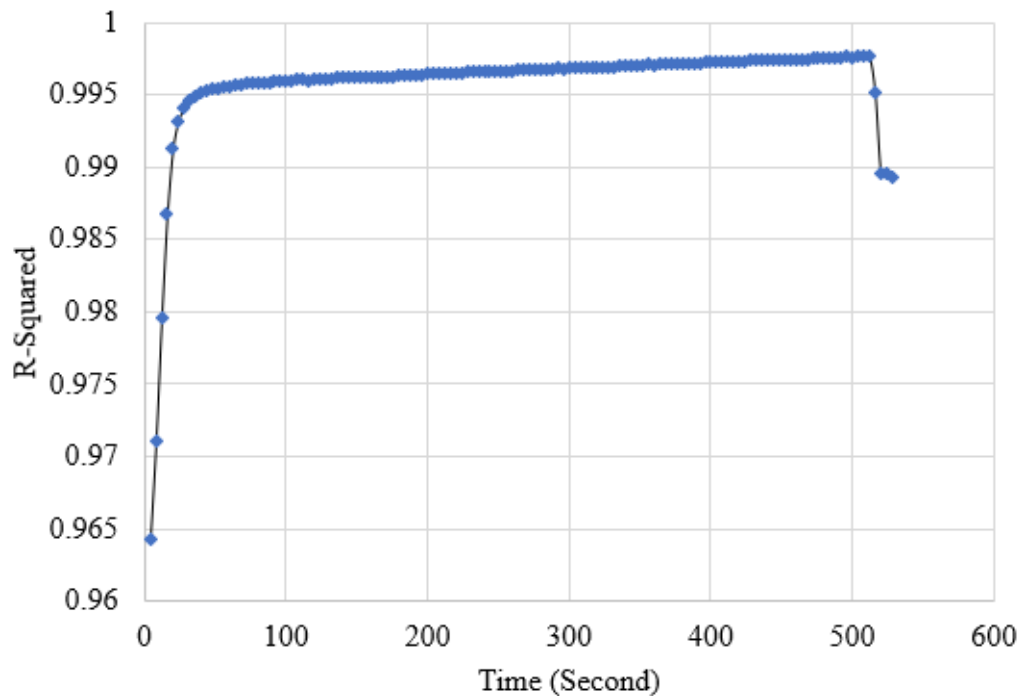


Figure 12. Changes in the R-squared of the fitting planes for the geogrid specimen during the entire tensile test.

geogrid specimen was neither initially in one plane nor did it maintain a plane during the tensile test. In fact, the geogrid underwent significant out-of-plane deformations during the test. Therefore, the planar assumption in the existing methods for measuring the deformations of geogrids is invalid.

4. CONCLUSIONS

In this paper, a multi-camera-based photogrammetric method was proposed to measure the 3-D full-field displacements of geosynthetics. A series of tensile tests were conducted on six geogrid specimens to verify the effectiveness and accuracy and

demonstrate the advantages of the proposed method. The main findings of this study are summarized as follows:

- (1) The proposed photogrammetric method can be used in dynamic tests where the objects are continuously moving/deforming, such as tensile tests on the geosynthetics, which cannot be done by using the conventional one-camera-based SfM. A fast-tracking technique has been developed to track the deformations of the geosynthetics at any moment during the test.
- (2) The proposed method is a non-contact, low-cost, and highly accurate method. It only requires several low-cost surveillance cameras that cost about \$1000. The average absolute difference in displacements obtained by the proposed photogrammetric method and the machine-controlled movements of the bottom clamp was 0.14 mm.
- (3) Strain localization existed in the tested geogrid specimens during the tensile tests. The proposed photogrammetric method can identify localized strains. The localized strains are attributed to many factors, such as manufacturing defects, improper installation and alignment, the disturbance caused by sensor dismounting, and localized slip and failure during the tensile test. Since these factors are unavoidable, the strain localization should be identified and paid special attention.
- (4) Existing image-based methods for measuring the deformational properties of geosynthetics often assumed that the geosynthetics specimen is initially in a single plane and maintains in the same plane during the whole testing period. However, this research demonstrated that neither the requirement nor the

assumption can be satisfied. The results in this paper indicated that the geogrid specimen was not initially in one plane, and the geogrid specimen plane continuously rotated during the tensile test. As a result, the use of the existing image-based methods may lead to unreliable and inaccurate results in a tensile test for geosynthetics. This limitation can be overcome by the proposed photogrammetric method in which the camera stations and shooting directions are back-calculated and no manual control of camera stations or shooting directions is required.

- (5) The proposed photogrammetric method is equivalent to having installed several hundreds of LVDTs and extensometers on the geosynthetics with high measurement accuracy. The associated cost is negligible since it only requires printing and posting of some solid dots at the points of interest. As a result, the proposed method can provide a more comprehensive input regarding the deformational and strength properties, such as displacements, strains, and tensile strength at any locations of the geosynthetics.
- (6) Computer programs have been developed for automatic recognition and decoding of solid dots, fast tracking of the pixel coordinates and 3-D locations of the solid dots, and calculation of the complete strain distributions. This method is easy to use since all the required calculation is done by the computer program in a few hours.

REFERENCES

1. Xia, X., Zhang, X., & Mu, C. (2021). A multi-camera based photogrammetric method for three-dimensional full-field displacement measurements of geosynthetics during tensile test. *Geotextiles and Geomembranes*, 49(5), 1192-1210.
2. Skochdopole, T. R., Cassady, L., Pihs, D., and Stevenson, P. E. (2000). Comparative Study of Roller and Wedge Grips for Tensile Testing of High Strength Fabrics with Laser Extensometry: Comparisons to LVDT and Crosshead Extension. Grips, Clamps, Clamping Techniques, and Strain Measurement for Testing of Geosynthetics. ASTM International.
3. Gallage, C. and Jayalath, C. (2019). Use of Particle Image Velocimetry (PIV) technique to measure strains in geogrids. In *E3S Web of Conferences* (Vol. 92, p. 12007). EDP Sciences.
4. Aydilek, A.H., Guler, M., and Edil, T. B. (2004). Use of image analysis in determination of strain distribution during geosynthetic tensile testing. *Journal of Computing in Civil Engineering*, 18(1), 65-74.
5. Jones, D. (2000). Wide-width geotextile testing with video extensometry. Grips, Clamps, Clamping Techniques, and Strain Measurement for Testing of Geosynthetics. ASTM International.
6. Raschke, S. A., Hryciw, R. D., and Donohoe, G. W. (1996). Micro deformations in sands by digital image processing and analysis. *Transportation Research Record*, 1548(1), 31-37.
7. Paikowsky, S. G. and Xi, F. (2000). Particle motion tracking utilizing a high-resolution digital CCD camera. *Geotechnical Testing Journal*, 23(1), 123-134.
8. Alshibli, K.A. and Sture, S., (2000). Shear band formation in plane strain experiments of sand. *Journal of Geotechnical and Geoenvironmental Engineering*, 126(6), pp.495-503.
9. ASTM D6637/D6637M-15 Standard Test Method for Determining Tensile Properties of Geogrids by the Single or Multi-Rib Tensile Method, West Conshohocken, PA, 2015.
10. Fernandez-Fernandez, M., Alonso-Montes, C., Bertelsen, A., and Mendikute, A., (2013). Industrial Non-intrusive Coded-Target Identification and Decoding Application. In *Iberian Conference on Pattern Recognition and Image Analysis*. Springer, Berlin, Heidelberg. 790-797.

11. Tsai, R. (1987). A versatile camera calibration technique for high-accuracy 3D machine vision metrology using off-the-shelf TV cameras and lenses. *IEEE Journal on Robotics and Automation*, 3(4), 323-344.
12. Zhang, X., Li, L., Chen, G., and Lytton, R., 2015. A photogrammetry-based method to measure total and local volume changes of unsaturated soils during triaxial testing. *Acta Geotechnica*, 10(1), 55-82.
13. Xia, X., Zhang, X., Fayek, S., & Yin, Z. (2021). A table method for coded target decoding with application to 3-D reconstruction of soil specimens during triaxial testing. *Acta Geotechnica*, 16(12), 3779-3791.
14. Hartley, R., & Zisserman, A. (2003). *Multiple view geometry in computer vision*. Cambridge university press.
15. Wang, L., Ge, L., Luo, S., Yan, Z., Cui, Z., & Feng, J. (2022). TC-SfM: Robust Track-Community-Based Structure-from-Motion. *arXiv preprint arXiv:2206.05866*.
16. Chen, Y., Wang, Y., Lu, P., Chen, Y., & Wang, G. (2018). Large-scale structure from motion with semantic constraints of aerial images. In *Chinese Conference on Pattern Recognition and Computer Vision (PRCV)* (pp. 347-359). Springer, Cham.
17. YILMAZ, Ö. and KARAKUŞ, F., 2016. Stereo and KinectFusion for continuous 3D reconstruction and visual odometry. *Turkish Journal of Electrical Engineering and Computer Sciences*, 24(4), pp.2756-2770.

SECTION

2. CONCLUSIONS AND RECOMMENDATIONS

2.1. CONCLUSIONS

A review of the existing methods for soil deformation measurement in the triaxial test has indicated that it remains a great challenge for researchers to measure the deformations of unsaturated soils during triaxial testing. The photogrammetry-based method (Zhang et al., 2015, Li et al., 2015, Fayek., 2020) can measure the volume-changes, absolute volume, eccentricity, and tilting of unsaturated soils with refraction correction. However, this method cannot satisfy the need to continuously measure the deformations of soil specimens during the dynamic tests, such as triaxial test. The main objective of this research is to develop a new structure from motion photogrammetric method that can continuously measure and track the 3-D deformations of both saturated and unsaturated soils. The dissertation can be divided into four sections. The first three sections include developments of :1) a table method for target decoding; 2) a single-camera-based SfM photogrammetric method, and 3) a multi-security camera system to continuously measure the soil deformation. In addition to these three sections, the multi-camera-based SfM photogrammetric method for soil deformation measurement has extended its application to tensile test on geosynthetics. A low-cost security camera system has been developed to continuously measure and track the 3-D full-field displacements/strains of geosynthetics. The conclusions for each section have been summarized as follows:

2.1.1. A Table Method for Coded Target Decoding. Accurate recognition and decoding of CTs are of great importance in coded target-based photogrammetric 3-D measurements. Incorrect CT decoding results can lead to inaccurate 3-D measurement results or even failure in 3-D reconstruction. Existing photogrammetry-based methods often rely on a photogrammetric software to manually correct the incorrect CT decoding results, which is highly inefficient and time-consuming. In fact, at almost any time when CTs are used, the ID numbers and geometric locations of the CTs are carefully prescribed ahead of time instead of being arbitrarily posted to obtain the best representation of the targeted objects to be reconstructed. Therefore, a table method for coded target decoding with applications to the 3-D reconstruction of soil samples during triaxial testing was proposed. This method takes full advantages of the predesigned geometric information of the CTs. In this method, CT recognition was performed first using blob analysis based on the unique embedding feature of the CTs. The RANSAC algorithm was utilized to identify incorrect CT IDs. The validation test results indicate that the proposed method is accurate and capable of identifying more CTs compared to the software. The proposed method also enables automatic identification of outlier CT numbers, which is a huge advantage since the tedious and prone-to-error manual corrections of false CT identifications can be eliminated.

2.1.2. Development of a Single-Camera-Based SfM Photogrammetric Method. A review of current methods for soil deformation measurement indicates that there are no available methods which can efficiently and rapidly measure the volume-changes of unsaturated soils with refraction correction. There is a clear need to develop an efficient and user-friendly photogrammetric method which is faster, highly automatic,

and computationally efficient. SfM is a 3-D reconstruction technique which has received numerous attentions in computer vision community and has the potential to rapidly obtain the 3-D models of the soil specimen. In this study, a hybrid approach and customized SfM method has been proposed. It integrates the target recognition and identification in photogrammetry community and SfM procedures for 3-D structure generation in computer vision community. The proposed method does not rely on any commercial software. Instead, it has been implemented into an efficient MatLab program to conduct all the computation within three to five minutes for processing one image set for a triaxial test. Considering that large number of images need to be processed for a triaxial test, the proposed method is efficient and can significantly reduce the time for processing the triaxial test images.

2.1.3. Development of a Multi-Security Camera System to Continuously Measure the Soil Deformations. One limitation of existing methods is the inability to continuously measure and track the deformations of the soil specimens during triaxial test. In this study, a multi-camera based SfM method has been proposed. Thirteen low-cost security cameras are used to continuously measure the 3-D full-field deformations of soil specimens during triaxial testing. The large image distortions have been corrected by camera calibration. Validation results indicate that: 1) the proposed method can obtain accurate 3-D model of the soil specimen using relatively low-cost security cameras. The mean reprojection error is only 0.29 pixel. Each security camera costs only about \$ 160 and the multi-camera system costs about \$ 2K; 2) the proposed method can be used to track the 3-D localized strains/deformations of the soil specimen at any moment during the triaxial testing. It is found that the deformations of the soil specimen are non-uniform.

The lower part of the specimen experienced larger deformations; and 3) the proposed method is highly efficient and automatic. All the computation is conducted by a computer program. The tracking of each target takes only about one second.

2.1.4. Continuous 3-D Full-Field Displacements/Deformations Measurement for Geosynthetics. Existing methods have limitation in continuous and complete measurements of the displacements of geosynthetics at all locations. In this study, a multi-security camera based photogrammetric method has been developed to measure the 3-D full-field displacements of geosynthetics. A series of tensile tests were conducted on different types of geogrid specimens to verify the effectiveness and accuracy of the proposed method. The validation test results demonstrate that the proposed method has the following advantages: 1) it can be used in dynamic tests where the objects are continuously moving/deforming, such as tensile tests on the geosynthetics. A fast-tracking technique has been developed to track the deformations of the geosynthetics at any moment during the test; 2) The proposed method is a non-contact, low-cost, and highly accurate method. The multi-security camera system requires only five to eight low-cost security cameras that cost about \$1 K; 3) Strain localization existed in the tested geogrid specimens during the tensile tests. The proposed method can identify localized strains at any locations within the specimen; 4) the geogrid specimen was not initially in one plane, and the geogrid specimen plane continuously rotated during the tensile test. As a result, the use of the existing image-based methods which assume that the specimen is initially in a plane and maintains in the same plane may lead to unreliable and inaccurate results in a tensile test for geosynthetics. This limitation can be overcome by the proposed photogrammetric method in which the camera stations and shooting directions

are backcalculated and no manual control of camera stations or shooting directions is required; and 5) the proposed photogrammetric method is equivalent to having installed several hundreds of LVDTs and extensometers on the geosynthetics with high measurement accuracy.

2.2. RECOMMENDATIONS

The following recommendations are made for the future research:

- (1) Further research is needed to apply the proposed method to constitutive modeling of soils. The proposed method can be used in triaxial tests on both saturated and unsaturated soils. By combining the proposed method with Fayek et al., (2020) and Fayek et al., (2022) more comprehensive soil properties can be obtained, such as absolute volume, 3-D full-field displacements/strains, tilting and eccentricity of soil specimen, etc. These new soil deformation measurements will contribute to more accurate characterization of the stress-strain behavior of both saturated and unsaturated soils.
- (2) Use of the proposed multi-camera based SfM photogrammetric method to perform dynamic (cyclic) triaxial testing on soils. Dynamic Triaxial testing is used to evaluate the strength and deformation properties of soils under cyclic loading conditions. These conditions might include earthquakes, passing vehicles and trains, vibration machines, etc. Conventional dynamic triaxial testing often uses displacement sensors to measure the displacements of the soil specimen. However, the triaxial cell and soil specimen often becomes crowded when the local transducers are used. Moreover, only a few locations

of the specimen can be measured. The proposed multi-camera system is very promising in continuously tracking the 3-D full-field deformations of the soil specimen during dynamic triaxial testing.

- (3) The tensile test results on the geogrid specimens indicate that the proposed multi-camera-based method can provide more comprehensive input, such as the complete strain and modulus distributions in the geosynthetics. In the future, more tensile tests can be done on geosynthetics to obtain more data regarding the complete strain and modulus distributions in the geosynthetics. Then, recommendations will be made for a probability-based geosynthetics design.

BIBLIOGRAPHY

1. Bishop AW, Donald IB (1961) The experimental study of partly saturated soil in the triaxial apparatus. In: Proceedings of the 5th international conference on soils mechanic, Paris, vol 1, pp 13–21.
2. Romero E, Facio JA, Lloret A, Gens A, Alonso EE (1997) A new suction and temperature controlled triaxial apparatus. In: Proceedings of the 14th international conference on soil mechanics and foundation engineering, Hamburg, vol 1, 185–188.
3. Macari EJ, Parker JK, Costes NC (1997) Measurement of volume changes in triaxial tests using digital imaging techniques. *Geotech Test J* 20(1):103–109.
4. White D, Take W, Bolton M(2003) Measuring soil deformation in geotechnical models using digital images and PIV analysis. In: Proceedings of 10th international conference on computer methods and advances in geomechanics, Tuscon, Ariz., Balkema, Rotterdam, The Netherlands, pp 997–1002.
5. Liu, J., & Iskander, M. (2004). Adaptive cross correlation for imaging displacements in soils. *Journal of computing in civil engineering*, 18(1), 46-57.
6. DeJong, J. T., White, D. J., & Randolph, M. F. (2006). Microscale observation and modeling of soil-structure interface behavior using particle image velocimetry. *Soils and foundations*, 46(1), 15-28.
7. Take, W. A. (2015). Thirty-Sixth Canadian Geotechnical Colloquium: Advances in visualization of geotechnical processes through digital image correlation. *Canadian Geotechnical Journal*, 52(9), 1199-1220.
8. Zhang, X., Li, L., Chen, G. and Lytton, R. (2015). “A photogrammetry-based method to measure total and local volume changes of unsaturated soils during triaxial testing.” *Acta Geotechnica*, 10(1), pp.55-82.
9. Li, L., & Zhang, X. (2019). Factors influencing the accuracy of the photogrammetry-based deformation measurement method. *Acta Geotechnica*, 14(2), 559-574.
10. Salazar SE, Barnes A, Coffman RA (2015) Development of an Internal Camera-Based Volume Determination System for Triaxial Testing. *Geotechnical Testing Journal* 38(4):549-555.

11. Li L, Zhang X, Li P (2019) Evaluating a new method for simultaneous measurement of soil water retention and shrinkage curves. *Acta Geotechnica* 14(4): 1021-1035.
12. Fayek, S., Xia, X., Li, L., & Zhang, X. (2020). Photogrammetry-based method to determine the absolute volume of soil specimen during triaxial testing. *Transportation Research Record*, 2674(8), 206-218.
13. Knyaz VA, Sibiriyakov AV (1998) Non-contact 3D model reconstruction using coded targets. *Image* 1(2).
14. Ahn SJ, Rauh W, Kim SI (2001) Circular coded target for automation of optical 3D-measurement and camera calibration. *International Journal of Pattern Recognition and Artificial Intelligence* 15(06):905-919.
15. Fernandez-Fernandez M, Alonso-Montes C, Bertelsen A, Mendikute A (2013) Industrial Non-intrusive Coded-Target Identification and Decoding Application. In *Iberian Conference on Pattern Recognition and Image Analysis*. Springer, Berlin, Heidelberg. pp. 790-797.
16. Shortis MR, Seager JW, Robson S, Harvey ES (2003) Automatic recognition of coded targets based on a Hough transform and segment matching. *International Society for Optics and Photonics*. In *Videometrics VII*, Vol. 5013, pp. 202-208.
17. Hattori S, Akimoto K, Fraser C, Ono T, Imoto H (2000) Design of coded targets and automated measurement procedures in industrial vision metrology. *International Archives of Photogrammetry and Remote Sensing* 33(5):72-78.
18. Forbes K, Voigt A, Bodika N (2002) An inexpensive, automatic and accurate camera calibration method. In *Proceedings of the Thirteenth Annual South African Workshop on Pattern Recognition*. pp. 1-6.
19. Xia R, Zhao J, Liu W, Wu JH, Fu SP, Jiang J, Li, J (2012) A robust recognition algorithm for encoded targets in close-range photogrammetry. *Journal of information science and engineering* 28:407-418.
20. Nyarko K, Thomas C, Torres G (2016) A robust close-range photogrammetric target extraction algorithm for size and type variant targets. In *Automatic Target Recognition XXVI*. International Society for Optics and Photonics. Vol. 9844, p. 984403.
21. Van Den Heuvel FA, Kroon R, Le Poole RS (1993) Digital close-range photogrammetry using artificial targets. *International Archives of Photogrammetry and Remote Sensing* 29:222-222.

22. Barazzetti L, Scaioni M (2010) Development and implementation of image-based algorithms for measurement of deformations in material testing. *Sensors* 10(8):7469-7495.
23. Bernat K, Tokarczyk R (2013) Automation of measurements of selected targets of photopoints in application to photogrammetric reconstruction of road accidents. *Geomatics and Environmental Engineering* 7.
24. Mendikute A, Zatarain M (2012) A machine vision approach for automated raw part alignment in machine tools. *Modern Machinery Science Journal* 1: 365-369.
25. Cheng J, Leng C, Wu J, Cui H, Lu H (2014) Fast and accurate image matching with cascade hashing for 3d reconstruction. In *Proceedings of the IEEE Conference on Computer Vision and Pattern Recognition*. pp. 1-8.
26. Aydilek, A.H., Guler, M., and Edil, T. B. (2004). Use of image analysis in determination of strain distribution during geosynthetic tensile testing. *Journal of Computing in Civil Engineering*, 18(1), 65-74.
27. Jones, D. (2000). Wide-width geotextile testing with video extensometry. *Grips, Clamps, Clamping Techniques, and Strain Measurement for Testing of Geosynthetics*. ASTM International.
28. Raschke, S. A., Hryciw, R. D., and Donohoe, G. W. (1996). Micro deformations in sands by digital image processing and analysis. *Transportation Research Record*, 1548(1), 31-37.
29. Paikowsky, S. G. and Xi, F. (2000). Particle motion tracking utilizing a high-resolution digital CCD camera. *Geotechnical Testing Journal*, 23(1), 123-134.
30. Alshibli, K.A. and Sture, S., (2000). Shear band formation in plane strain experiments of sand. *Journal of Geotechnical and Geoenvironmental Engineering*, 126(6), pp.495-503.
31. Li, L., Zhang, X., Chen, G., & Lytton, R. (2015). Measuring unsaturated soil deformations during triaxial testing using a photogrammetry-based method. *Canadian Geotechnical Journal*, 53(3), 472-489.
32. Fayek, S., Zhang, X., Galinmoghdam, J., and Xia, X., (2022). Measuring Tilting and Eccentricity of Soil Specimen During Triaxial Testing Using a Photogrammetry-Based Method, *Geotechnical Testing Journal*. (Under Review)

VITA

Xiaolong Xia was born in Hubei, China. He received his Bachelor of Science in Civil Engineering from Wuhan University of Technology in June 2013. He obtained his Master of Science in Geotechnical Engineering from University of Chinese Academy of Sciences in June 2016. He enrolled in the Ph.D. program at Missouri University of Science and Technology in August 2016. He worked as a research and teaching assistant during his graduate studies at Missouri S&T. His dissertation title was “A Structure from Motion Photogrammetric Method for Continuously Measuring and Tracking the Deformations of Soils During Triaxial Testing.” In December 2022, he received his Doctor of Philosophy in Civil Engineering from Missouri S&T.